Chem. Rev. **1999,** *99,* 77–174

Metal Oxide Surfaces and Their Interactions with Aqueous Solutions and Microbial Organisms

Gordon E. Brown, Jr.*

Surface and Aqueous Geochemistry Group, Department of Geological & Environmental Sciences, Stanford University, Stanford, California 94305-2115

Victor E. Henrich*

Surface Science Laboratory, Department of Applied Physics, Yale University, New Haven, Connecticut 06520

William H. Casey

Department of Land, Air, and Water Resources, University of California, Davis, Davis, California 95616

David L. Clark

G.T. Seaborg Institute for Transactinium Science, Nuclear Materials Technology Division, Los Alamos National Laboratory, Los Alamos, New Mexico 87545

Carrick Eggleston

Department of Geology and Geophysics, University of Wyoming, Laramie, Wyoming 82071-3006

Andrew Felmy

Environmental Molecular Sciences Laboratory, Pacific Northwest National Laboratory, Richland, Washington 99352

D. Wayne Goodman

Department of Chemistry, Texas A&M University, College Station, Texas 77843-3255

Michael Grätzel

Institute of Chemical Physics, École Polytechnique Fédérale de Lausanne, CH-1015 Lausanne, Switzerland

Gary Maciel

Department of Chemistry, Colorado State University, Ft. Collins, Colorado 80523

Maureen I. McCarthy

Theory, Modeling and Simulation Group, Environmental Molecular Sciences Laboratory, Pacific Northwest National Laboratory, Richland, Washington 99352

Kenneth H. Nealson

Jet Propulsion Laboratory-183-301, California Institute of Technology, 4800 Oak Grove Drive, Pasadena, California 91109-8099

Dimitri A. Sverjensky

Department of Earth and Planetary Sciences, The Johns Hopkins University, Baltimore, Maryland 21218

Michael F. Toney

IBM Almaden Research Center, San Jose, California 95120

John M. Zachara

Environmental Molecular Sciences, Laboratory Pacific Northwest National Laboratory, Richland, Washington 99352

Received February 27, 1998 (Revised Manuscript Received November 9, 1998)

10.1021/cr980011z CCC: $35.00

Contents

1. Introduction

During the past decade, interest in chemical reactions occurring at metal oxide–aqueous solution interfaces has increased significantly because of their importance in a variety of fields, including atmospheric chemistry, heterogeneous catalysis and photocatalysis, chemical sensing, corrosion science, environmental chemistry and geochemistry, metallurgy and ore beneficiation, metal oxide crystal growth, soil science, semiconductor manufacturing and cleaning, and tribology. The metal oxide–aqueous solution interface is reactive due to acid–base, ligand-exchange, and/or redox chemistry involving protons (hydronium ions), hydroxyl groups, aqueous metal ions, and aqueous organic species and also complexes among these species. Interfacial localization of those species (adsorption) may result from electrostatic, chemical complexation, and hydrophobic interactions

Gordon E. Brown, Jr., received his B.S. in chemistry and geology in 1965 from Millsaps College, Jackson, MS, and his M.S. and Ph.D. in mineralogy and crystallography from Virginia Polytechnic Institute & State University in 1968 and 1970, respectively. He is currently the D. W. Kirby Professor of Earth Sciences at Stanford University and Professor and Chair of the Stanford Synchrotron Radiation Laboratory Faculty at SLAC.

Victor E. Henrich received his Ph.D. in physics from the University of Michigan in 1967. He is currently the Eugene Higgins Professor of Applied Science at Yale, and a Professor in the Departments of Applied Physics and of Physics. He is the co-author, with P. A. Cox of Oxford University, of *The Surface Science of Metal Oxides* (Cambridge University Press, 1994).

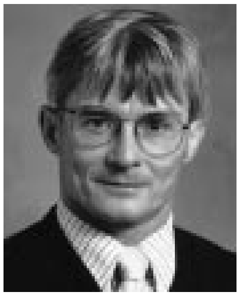

William H. Casey has appointments in the Department of Land, Air and Water Resources and in the Department of Geology at University of California, Davis; previously he was at Sandia National Laboratories. His research concerns the energetics and kinetics of the reactions between minerals and aqueous solutions, and in recent work, he has determined rate coefficients for dissociation of Al–O bonds in various dissolved aluminum complexes.

David L. Clark received a B.S. in chemistry in 1982 from the University of Washington and a Ph.D. in inorganic chemistry in 1986 from Indiana University under the direction of distinguished Prof. Malcolm H. Chisholm. He is presently the Director of the Glenn T. Seaborg Institute for Transactinium Science at Los Alamos National Laboratory.

between surface and sorbate. One very important, but only partly understood, aspect of oxide−aqueous solution interfaces is the nature of the interfacial

Carrick Eggleston graduated from Dartmouth College in 1983. He worked in the oil field and at a ski area before graduate school, received a National Science Foundation graduate fellowship, and received a Ph.D. from Stanford University in 1991. He is presently an Assistant Professor at the University of Wyoming.

Andrew R. Felmy is a Staff Scientist in the Environmental Dynamics and Simulation Directorate in the Environmental Molecular Sciences Laboratory at PNNL. He obtained his Ph.D. in 1968 under Professor John H. Weare from the Department of Chemistry at the University of California, San Diego in the theoretical physical chemistry group.

D. Wayne Goodman received his Ph.D. in physical chemistry from the University of Texas in 1974 and the following year, as a NATO Fellow, did postdoctoral study at the Technische Hochschule, Darmstadt, Germany. He is Professor of Chemistry at Texas A&M University and currently holds the Robert A. Welch Chair.

Michael Grätzel has been a Professor at the Institute of Physical Chemistry at the Swiss Federal Institute of Technology in Lausanne, Switzerland since 1977. He served as Head of the Chemistry Department from 1983 to 1985 and from 1991 to 1993.

solvent, in which the structure and properties of interfacial water are perturbed relative to bulk water (Figure 1). Oxide surface reactivity is exploited in many industrial processes involving catalysis and photolysis and is fundamental to environmental

Gary Maciel received a B.S. in chemistry at the University of California, Berkeley, in 1956. His Ph.D. studies were in physical organic chemistry at M.I.T., where his thesis supervisor was Professor F. D. Greene. He is currently a Professor of Chemistry at Colorado State University.

Maureen I. McCarthy received her Ph.D. from the University of Colorado in 1988 and was the Lady Davis Postdoctoral Fellow at the Hebrew University, Jerusalem, Israel, 1988–1991. She is the 1997–1999 recipient of the American Association for the Advancement of Science (AAAS) Defense Policy Fellowship, serving as Scientific Advisor for Strategic Arms Controls to the Under Secretary of Defense for Acquisition and Technology. She is currently on professional leave-of-absence from Pacific Northwest National Laboratory.

Kenneth H. Nealson received his B.S. degree in biochemistry (1965) and Ph.D. in microbiology (1969), both from the University of Chicago, after which he did postdoctoral work at Harvard University for three years. He recently took a position as Senior Research Scientist at the Jet Propulsion Laboratory and Faculty Associate at Caltech, where he is establishing the astrobiology group, with the goal of developing methods for life detection in extreme environments on earth and perhaps in samples returned from non-earth sites.

Dimitri A. Sverjensky is a Professor of Geochemistry in the Department of Earth and Planetary Sciences at the Johns Hopkins University. His early training in geology and chemistry was at the University of Sydney, Australia. He came to the United States for graduate studies and received a Ph.D. in the study of light stable isotope geochemistry and ore deposits from the Department of Geology and Geophysics at Yale University in 1980.

Micheal F. Toney received his Ph.D. in surface physics from the University of Washington in 1983. He then moved to the Riso National Laboratory in Denmark, as a NATO Postdoctoral Fellow, where he used surface X-ray diffraction to study semiconductor surface structure. In 1984 he joined the IBM Research Division in San Jose, CA where presently his research is concentrated on structural studies of metal multilayers and thin films with novel magnetic properties, which are important to IBM's magnetic recording technologies.

John M. Zachara received his Ph.D. in soil chemistry from Washington State University in 1986. Currently he is Chief Scientist and one of four Associate Scientific Directors of the William Wiley Environmental Molecular Sciences Laboratory (EMSL) at Battelle, Pacific Northwest National Laboratories.

chemistry and geochemistry. Indeed, hydrous oxides of Al, Fe, Mn, and aluminosilicates such as clays are ubiquitous in the natural environment, and their surface chemical properties control such important phenomena as nutrient and contaminant element release and uptake, pH buffering, water quality, and soil rheological properties. These surfaces function as templates for the growth of other solid phases and as a matrix for microflora. Polyvalent metal ions [e.g., Fe(III) and Mn(IV)] in the metal (hydr)oxide−aqueous solution interfacial region serve as terminal electron acceptors in the respiratory cycle of microorganisms common to soil, aquatic and marine sediments, and groundwater, a process of central importance to the global biogeochemical cycling of C, N, P, and other elements. Given the importance of metal oxide surfaces in these processes, surprisingly little is known about their atomic-scale structure and chemical reactivity, particularly in aqueous environments.

This review is the result of a workshop sponsored by the Chemical Sciences Division, U.S. Department of Energy, whose goals were to (1) review recent work and assess the state of knowledge in this interdisciplinary research field; (2) identify important problem areas and new research opportunities; (3) highlight the various scientific and technologic contexts where this knowledge is needed; and (4) evaluate the experimental and theoretical techniques needed to obtain the necessary information.

Chemical interactions at metal oxide−aqueous solution interfaces are relevant to an extremely broad

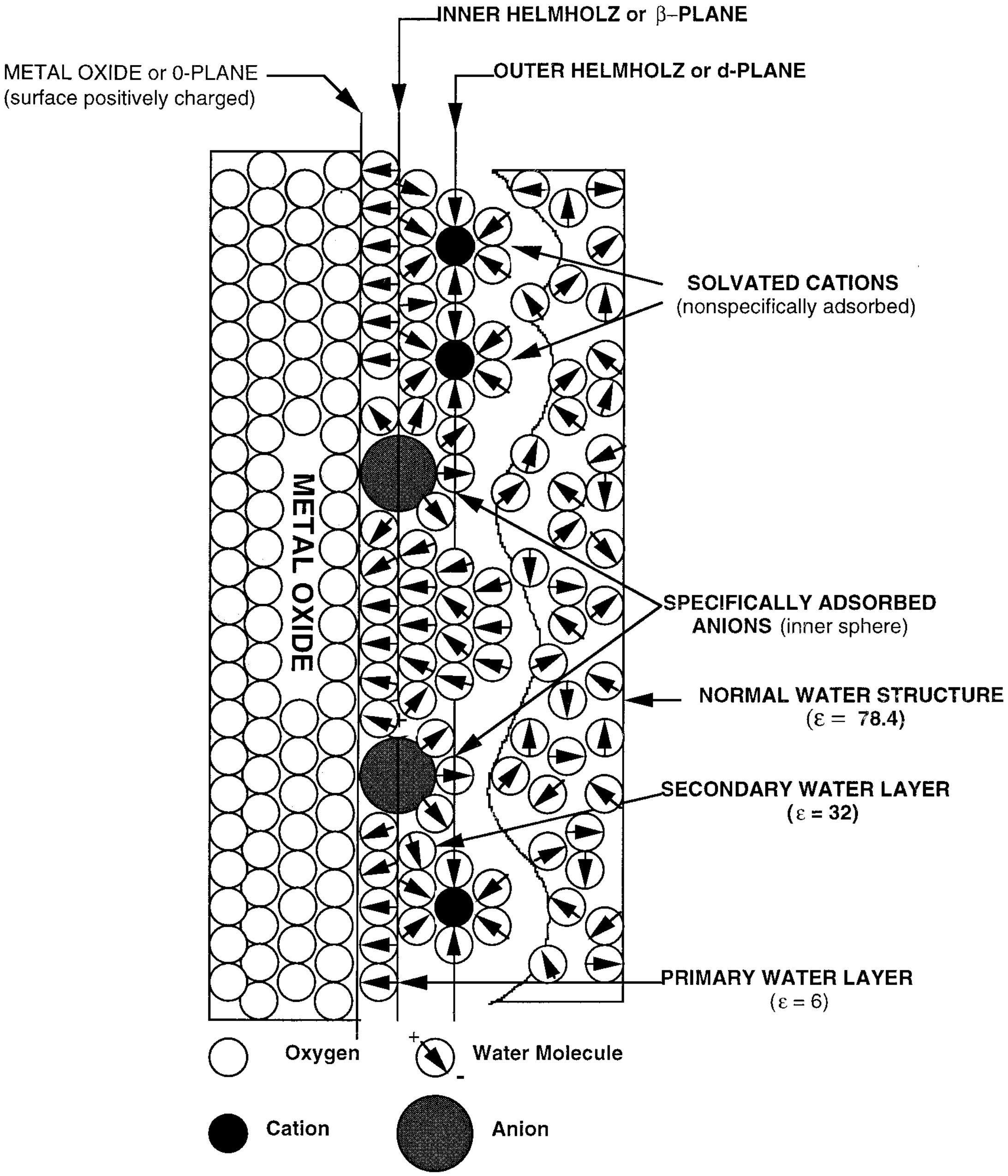

Figure 1. Schematic model of the electrical double layer (EDL) at the metal oxide–aqueous solution interface, showing elements of the Gouy–Chapman–Stern model, including specifically adsorbed anions and nonspecifically adsorbed solvated cations. The metal oxide, or zero-plane, is defined by the location of surface sites which may be protonated or deprotonated. The inner Helmholz plane, or β-plane, is defined by the centers of specifically adsorbed anions and cations. The outer Helmholz plane, or d-plane, corresponds to the beginning of the diffuse layer of counterions. Estimates of the dielectric constant, ϵ, of water are indicated for the first and second water layers nearest the interface and for bulk water.

range of disciplines. This review attempts to address the most important areas across the entire spectrum of physical, chemical, and biological sciences. However, a great deal of the current interest involves geochemical/environmental/soil systems,[1–9] and this review reflects that interest.

Chemical interactions at metal oxide–aqueous solution interfaces are extremely complex, and it is safe to say that understanding such interactions on a fundamental atomic level has not been achieved. Thus many workers in this field adopt a reductionist approach: the very complex problem is broken down into experimental and/or theoretical studies of simplified parts of the overall reaction, with the aim of defining the structure, bonding, composition, and physical form of reaction products (i.e., present as a true adsorption complex or a precipitate) and the effect of the reaction on the electronic and geometric structure of the oxide surface. This approach is essential for separating and understanding the effects of the many variables that ultimately control the structure and properties of the metal oxide surface, including its reactivity. For example, we cannot understand the basic physics and chemistry of water adsorption on oxide surfaces unless we have a thorough understanding of the atomic and electronic structure of the clean surfaces: to know what has happened, we need to know where we started. To understand chemisorption reactions of metal ions at metal oxide–aqueous solution interfaces at the atomic/molecular level, we must know a number of things, including: (1) the effect of water on the structure, composition, and reactivity of surface sites including defect sites; (2) the speciation of metal ions in solution; (3) how the solution species change when they react with the solid surface (e.g., do they hydrolyze in the electrical double layer?); (4) how many protons are released from the metal oxide surface during the sorption process and during possible hydrolysis of the metal ion in the double-layer region; (5) how sorption complexes bond to the surface; (6) the effects of sorption on surface atomic and electronic structure; (7) the effects of electron-transfer reactions between sorbate and surface; (8) how rapidly sorption complexes exchange ligands and diffuse on the metal oxide surface; and (9) how sorbates oligomerize. We should ideally have information from as many different physical and chemical points of view as possible, requiring a multidisciplinary approach and the application of a wide variety of techniques; the various techniques should also operate over different time domains of the chemical process. For researchers dealing with a specific problem, a clear understanding of what aspects of, e.g., UHV photoemission studies are likely to be relevant, and which are not likely to be so useful, is very important.

Some mutual skepticism exists between research communities regarding UHV (or ex situ) versus in situ techniques for studying many kinds of surfaces, of which metal oxides are only a small subset. Researchers working with in situ techniques and experiments tend to be suspicious about the relevance of UHV information to in situ situations, while those working with clean, well-defined surfaces in UHV tend to be skeptical that the fundamental physics of these surfaces can be understood in “dirty” in situ situations. There is truth in both views, and both UHV and in situ approaches are needed in order to ultimately understand how the fundamental physics and chemistry of these surfaces are related to their reactivity in “real” settings.

The term in situ, as used in this review, refers to measurements under ambient conditions (298 K and 1 atm), usually with the metal oxide surface in contact with a bulk aqueous solution. Dependent upon solution pH, ionic strength, and metal ion concentration, these conditions may simulate those under which chemical reactions between aqueous solution and metal oxide surfaces (e.g., chemisorption, corrosion, crystal growth, dissolution) occur during a particular type of natural or technological process. Even when not in contact with bulk aqueous solutions, a metal oxide surface in air under ambient conditions is often covered by several to many monolayers of water, depending upon the relative humidity of ambient air. For example, gravimetric studies of water on α-Al_2O_3 have shown that $\approx$2 monolayers (8.2 Å) of water cover the surface at a relative humidity of 50%, whereas $\approx$8 monolayers (32 Å) are present at 80% relative humidity at 300 K.[10] Thus experimental studies of metal oxide surfaces in ambient air may be in situ experiments, depending on relative humidity, and the metal oxide surface may in fact be a metal hydroxide surface with a different structure and composition relative to the clean metal oxide surface, depending on the reactivity of the metal oxide surface with water. Very little is known about the structure and composition of metal oxide surfaces in air, and even less is known about such surfaces in contact with bulk aqueous solution.

This review is organized essentially from the simple to the complex, beginning with a consideration of the structure (both geometric and electronic) and properties of clean metal oxide surfaces (section 2). Important here are various types of defects on single-crystal surfaces which play a key role in surface reactivity. Metal oxide particles, colloids, and nanostructured materials are also considered briefly. Section 3 considers the interaction of water vapor with metal oxide surfaces. By performing adsorption experiments on well-characterized surfaces in a vacuum environment, a great deal can be learned about the nature of reactive sites on these surfaces. The largest section of the paper, section 4, addresses the interactions that occur when metal oxides are immersed in liquid water. It begins by considering the speciation and complexation of metal ions in solution, and then discusses processes that occur at the solid−solution interface, including some of the methods that are used to probe the interfacial region at atomic/molecular-scale resolution. Important properties and processes include the structure and composition of the electrical double layer at the interface; charge transfer and atom transport (i.e., dissolution) across the interface; the formation of passivating layers; chemical reactions, catalysis, and photocatalysis; and metal ion sorption. The dissolution and growth of metal oxides in aqueous solutions are addressed in section 5. Section 6 considers biotic processes involving bacterial utilization and production of metal oxides. The various theoretical approaches that are being used to interpret and predict the structure and properties of metal oxide−aqueous interfaces are described in section 7. Section 8 then considers the challenges that face this emerging field and the future directions in which research must go if answers to the important unanswered questions are to be obtained.

Table 1 lists the important metal oxides that will be considered here, together with a variety of structural and reactivity-determining parameters for each. Not listed in Table 1, nor covered in a detailed fashion in this paper, is γ-Al_2O_3, an important synthetic substrate used in heterogeneous catalysis and a model substrate commonly used as a surrogate for more complex aluminosilicate substrates important in interfacial geochemistry and soil chemistry. To the best of our knowledge, γ-Al_2O_3 has not been prepared in single-crystal form, and it does not occur naturally. Numerous papers have been published on the surface chemistry of γ-Al_2O_3 in high-surface area powdered forms, including, e.g., refs 11−14, and a number of studies of absorption of aqueous metal cations at the γ-Al_2O_3−water interface are discussed in this paper. In addition, the surface chemistry of α-SiO_2 (quartz) and α-FeOOH (goethite) is not examined to the same extent as that of the other metal oxides listed in

Table 1. Properties of Selected Metal Oxides at 298 K and 1 bar

oxide	mineral name	cation valence	cleavage	surfaces studied	ϵ^g	log K^h	pH_{PPZC}[i]	band gap[j] (eV)
MgO	periclase	II	(100)	(100)	9.83	21.36	12.4	7.7
CaO	lime	II	(100)	(100)	11.95	32.58	12.3	6.9
α-Al_2O_3	corundum	III	(0001)[c]	(0001) $(10\bar{1}2)$	10.43	19.05	9.1	9.5
α-TiO_2	rutile	IV[a]	(110)[d] (100)	(110) (100) (111)	120.9	−9.64	5.8	3.1
α-Fe_2O_3	hematite	III[2]	(0001)[c]	(0001) $(10\bar{1}2)$	25.0	0.11	8.5	≈2.2[k]
Fe_3O_4	magnetite	II, III	(111)[e]	(111) (100) (110)	20,000	10.47	6.6	metallic
α-FeO(OH)	goethite	III	(010) (100)	(110)	11.7	0.53	9.0−9.7	2−3[l]
α-SiO_2	quartz	IV	none[f]	$(10\bar{1}0)$ (0001) $(10\bar{1}1)$	4.58	−4.00	2.9	8.9

[a] Can be reduced to III or II at surface defect sites. [b] Can be reduced to II at surface defect sites. [c] Parting, not cleavage. There is also parting on $(10\bar{1}1)$ for α-Al_2O_3 and α-Fe_2O_3. [d] Although these "cleavages" are observed for natural rutile crystals, they are not observed in pure, synthetic TiO_2 (rutile). [e] Parting, not cleavage. [f] There is occasionally indistinct parting on $(10\bar{1}1)$, $(01\bar{1}1)$, $(10\bar{1}0)$, $(11\bar{2}0)$, and (0001). [g] Dielectric constants (ϵ) from compilation by Sverjensky (1994).[16] [h] Hydrolysis constants (log K) for reactions of the type $Al_2O_3 + 3H_2O = 2Al(OH)_3$. Values from ref 17. [i] Experimental values from compilation by Sverjensky (1994).[16] [j] Values from ref 18. [k] Cation d → d transitions complicate the determination of the charge-transfer band gap. [l] See ref 19.

Table 1 because there has been much less work on single-crystal surfaces of these materials. Since a large amount of the interest in aqueous solution−metal oxide interfaces comes from the geochemistry, soil science, and molecular environmental science communities, we will emphasize naturally occurring metal oxides; we do not include a large number of less common, yet technologically important, materials such as Sc oxides, high-temperature superconductors, SnO_2, ZnO, etc. Fundamental studies of these other materials are also of great use in understanding the behavior of the oxides listed.[15]

2. Characterization of Clean Metal Oxide Surfaces

This section will consider the structure and properties of several atomically clean metal oxide surfaces and some of the techniques that are used to determine them.

2.1. The Nature of Defects on Metal Oxide Surfaces

Single-crystal surfaces, unless prepared with extreme care, generally possess a wide variety of defects. For metal oxides and many other materials, these defects are often key to their chemical reactivity. A simple block model (Figure 2) shows that a real surface (which, in itself, is a two-dimensional defect in a bulk solid) will generally have one-dimensional defects in the form of steps and that the steps will in turn have point defects in the form of kink sites. Beyond this simple view, however, these two-, one-, and zero-dimensional defects can support a variety of different defect types.

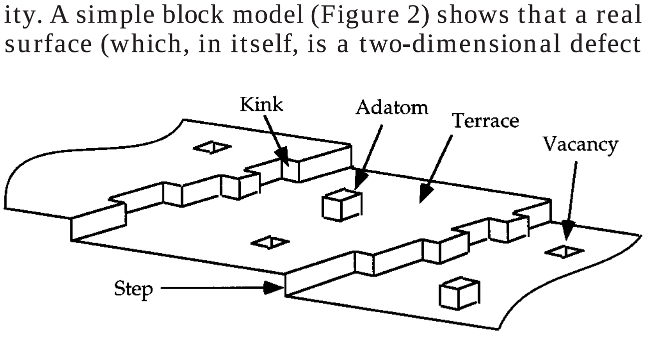

Figure 2. Simple block model of defects on a single-crystal surface.

Terraces may have a variety of different surface sites on an ordered surface (including those that are found on ordered surface reconstructions). Terraces may also exhibit vacancies, adatoms, and substitutional/interstitial point defects. Surface reconstructions may have several different equivalent orientations on terraces, leading to surface phase boundaries. Condon et al.[20] have observed what they call "biphase ordering" of an α-Fe_2O_3 (0001) that has been partially reduced in preparation, such that terraces show a highly ordered array of islands of α-Fe_2O_3 (0001) with islands of Fe_3O_4 (111). Several complicated surface reconstructions have also been observed on single-crystal surfaces of TiO_2.[21−27] Surface terraces may also intersect a variety of two-dimensional defects in the bulk solid, such as stacking faults or twin planes, that produce linear defects on surfaces.[28]

Steps can also occur with various types of defects segregated along them. Kink sites can have several different structures depending upon step orientation and kink location relative to the unit cell. Steps may also interact with each other under annealing (or aqueous) conditions, leading to (for example) formation of double-height steps in response to a difference in step structure from one layer to the next; the Si (001) (2 × 1) surface reconstruction is a famous non-oxide example.[29] There are indications that magnetite (Fe_3O_4) may behave in a related way.[30,31]

As this discussion implies, defects are important to the overall reactivity of metal oxide surfaces. A key question is: what kinds of defects are particularly important? One can create surface structures (reconstructions) and defects in vacuum that are unlikely to persist for very long in contact with an aqueous solution, but some defects will persist (albeit in altered form) and likely will affect subsequent reactivity.

2.2. Overview of UHV Surface Science Methods Used To Study Clean Metal Oxide Surfaces

Extremely detailed information on the geometric and electronic properties of solid surfaces can be obtained from electron, ion, atom, and X-ray spectroscopies and scattering performed in high vacuum.[32] Techniques that are extremely surface-sensitive, such as low-energy electron diffraction (LEED), ion-scattering spectroscopy (ISS), photoelectron (UPS, XPS, etc.) and inverse photoelectron (IPS) spectroscopies, electron energy loss (ELS and HREELS) and Auger spectroscopies, etc., were developed originally as a result of work on metals and semiconductors, but in recent years they have also been applied successfully to oxides[15] and other ionic compounds. The chemical properties of surfaces can also be determined by use of the above techniques, along with temperature-programmed desorption (TPD) and reaction (TPR) spectroscopies, etc. Over the last 5 years, the scanning probe microscopies (STM, AFM, etc.) have also begun to yield atomic-scale information on oxide surfaces.[33]

Most of the above techniques require a reasonable vacuum since they involve beams of incident or emitted particles, as well as perhaps photons. This puts inherent limits on their utility for the study of interfaces or surface chemistry under industrially or atmospherically relevant ambient conditions. The "pressure gap" between vacuum measurements and atmospheric pressure or high-pressure catalysis is very real, and it must always be kept in mind when extrapolating experimental results obtained at very low pressures. However, despite these limitations, a great deal of important information relevant to oxide surface chemistry and interfacial interactions has been, and will continue to be, obtained by surface science techniques.[15]

In considering the application of surface science methods to the study of aqueous solution−metal oxide interfaces, several caveats must be kept in mind:

- Surface chemical reactions, particularly on ionic compounds, are very often stronger on defects than on perfect terraces. Many of the experimental techniques sum over large areas of the surface ($>10^{12}$ unit cells). Thus, what a particular technique tells you may not be as important as what it misses.
- In natural systems, impurities may dominate surface chemistry. Small impurity concentrations can often be missed using techniques that average or sum over the surface.
- Since many UHV spectroscopies involve charged particles in either the incidence or emission step, surface charging on insulating samples can distort spectra unless methods are found to compensate for or eliminate it. The use of thin oxide films on conducting substrates discussed later in the article is one approach to that problem.[34,35]
- The most detailed atomic-scale information can be obtained on carefully prepared single-crystal surfaces. However, polycrystalline or particulate samples are often encountered in practical situations. Care must thus be taken to adequately model such surfaces if single crystals are used in experimental studies.
- The pressure gap discussed above must always be considered in interpreting surface chemical reaction or adsorption data.

Some of the most useful techniques for determining the positions of atoms on highly ordered single-crystal surfaces involve the elastic scattering of beams of electrons, ions, atoms, or X-rays off of the surface.[32] The diffraction patterns obtained give the reciprocal lattice of the surface and near-surface regions. If the entire surface has the same geometrical order, these techniques are extremely powerful. However, they sample large areas of the surface, and if the surface contains regions of different types of order, or if part of the surface is disordered due to defects, they can give incomplete or misleading information. Insulating surfaces can generally be studied by these particle scattering techniques without surface charging playing too large a role. The advent of scanning probe microscopies offers the possibility of obtaining complementary information that can help to overcome some of those difficulties. However, the scanning probe microscopy (SPM) method most likely to yield atomic resolution (i.e., scanning tunneling microscopy) cannot be applied to insulating solids. X-ray standing wave techniques are also useful for determining surface and adsorbate geometries on clean surfaces (see section 4.3.2.3).

LEED is a surface sensitive technique that has been extensively used to determine the surface structure of metals, semiconductors, and insulators in UHV (see refs 36 and 37 for a review). Surface sensitivity and selectivity result from the short mean free path of low-energy electrons. For a surface that is not reconstructed, the LEED pattern is that expected from the bulk crystal structure and is referred to as a "1×1" pattern, and the LEED spots are called "integer order" spots. For a reconstructed surface, the surface unit cell is larger than the bulk unit cell, and this gives rise to "fractional order" LEED spots [e.g., ($^1/_2{}^1/_2$) for a 2×2 pattern] in addition to the integer order spots. While the surface unit cell notation gives the surface symmetry and unit cell size, it does not provide the surface structure. To determine this, the intensity of the integer and fractional order LEED spots are measured as a function of electron voltage. These intensity−voltage, or $I(V)$, curves are then analyzed to determine the surface structure. Unlike X-ray diffraction (which is kinematical), a full multiple scattering (or dynamical) calculation is needed for this analysis, which requires much computation and the use of several nonstructural parameters.[38] As with most diffraction techniques, LEED requires long-range order (≥ 50 Å) and averages over the entire ordered part of the surface. However, in certain situations LEED can be used to study surface defects such as steps.[36,39−41]

While several hundred LEED determinations of metal and semiconductor surface structures have been reported,[42] there have been far fewer LEED determinations of metal oxide surface structures (in UHV).[15] This is partly due to the difficulty of surface preparation and partly due to the insulating nature of oxides, which limits the usable range of incident electron voltages. For example, LEED patterns for albite, a sodium aluminosilicate, have been observed, but $I(V)$ curves could not be obtained because the pattern disappeared rapidly due to either surface charging or damage.[43] LEED cannot be used for in situ measurements of solid−liquid interfaces because of the short mean free path of electrons. The same statement can be made for photoelectron diffraction, which also requires a UHV environment. In contrast, surface X-ray scattering offers the possibility of in situ measurements. Neither photoelectron diffraction nor surface X-ray scattering have been applied to any great extent in UHV studies of clean metal oxide surfaces, although this situation is beginning to change.[44,45]

Scanning probe microscopies (SPM) offer the most direct means of studying short-range order on the surface of materials since they can achieve (or nearly achieve) atomic resolution. SPM is an umbrella term for a number of different scanned probe techniques. Scanning tunneling microscopy (STM) was the first of these (see references in ref 46). The atomic force microscope (AFM), also known as the scanning force microscope (SFM), was invented in 1986. Since that time, many versions of these two techniques have appeared based on magnetic and electrostatic forces, heat flow, and frictional forces. More recently, cantilever oscillation modes have allowed noncontact, so-called “tapping”, and frequency or phase-shift imaging and force-modulation imaging. Many of these newer techniques are designed for “soft” biological samples or for semiconductor quality control applications and are not well-suited to high-resolution applications of SPM. Therefore, STM and AFM still dominate the high-resolution imaging of solid surfaces.

These SPM techniques rely upon the extremely local nature of the interaction between a sharp tip and a surface. This interaction varies with location on the surface, so that recording of the magnitude of interaction as a function of location can give a spatially resolved image of the interaction. In STM, a sharp metal tip (usually W or Pt/Ir) is raster-scanned over a conductor or semiconductor surface. A bias voltage sets up a tunneling current of electrons between tip and sample. This current is exponentially dependent on distance between tip and sample, so that by using a feedback loop to keep the tunneling current constant by adjusting the height of the tip, a topographic map of the surface with atomic resolution can be achieved. STM images can be taken at either polarity, with electrons tunneling from occupied states on the surface to the tip or tunneling from the tip to unoccupied states on the surface. STM has been used extensively since the mid-1980s to image metal and semiconductor surfaces both in UHV and under ambient conditions.[46] A particularly useful feature of STM and AFM for in situ work is the ability to control the electrochemical potential of the sample relative to some reference (often, in practice, a calibrated quasi-reference such as a silver wire).

In AFM, a tip (usually silicon nitride or silicon) is attached to a cantilever whose deflection can be used as a measure of the force acting on the tip. Cantilever deflection is usually measured with an optical lever consisting of a diode laser reflected off of the back of the cantilever into a photodiode detector; vertical deflections, as well as twisting deflections, of the cantilever can be measured in order to control or monitor both the contact and frictional forces between tip and sample. Topographic images with up to molecular-scale resolution are possible but are less often achieved than in STM. Many contact AFM images with periodicities characteristic of the sample under consideration have been obtained, but it cannot be assumed that they represent “true” high resolution. Usually, if tip−sample contact forces (after accounting for the nonlocal attractive forces that often act on the tip) are above about 1 nanonewton (nN), the tip−sample contact area must be larger than a typical unit cell. Periodic images are often an “artifact” of multiple tip−sample contact points, each of which may give a periodic signal; the image recorded is generally then a superposition of signals from a number of different tip−sample contacts. With multiple tip−sample contact points, point defects such as vacancies cannot be detected; for example, if one microtip encounters a vacancy, the tip will be supported by the other contacts so that no cantilever deflection is detected. Only rarely have point defects been detected by AFM; only if tip−sample contact forces are reduced to about 1 nN or below does one observe periodic lattice-scale surface with steps, vacancies and other defects.[46]

Another very common artifact with both STM and AFM is convolution of tip and sample shapes. Clearly, if a feature on the surface is “sharper” than the tip, an image of the tip rather than of the feature will be recorded locally. High-resolution (lattice-scale) imaging is usually only possible on very flat surfaces for which molecular-scale roughness and asperities on the tip can interact with the flat surface without interference from other parts of the tip which may come into contact with other parts of the surface. Other examples of tip−sample shape convolution are cases of vertical macrosteps for which SPM gives slopes related to tip shape (indeed, the radius of curvature of the tip can be measured from such images), pore openings (AFM may show a small dimple if the tip is small enough), overhangs (inaccessible to SPM), and narrow fractures.

Because of the above possible artifacts both at the unit cell and microtopographic scales, SPM cannot easily be used to image defective areas of a surface. Thus STM and AFM images of defective areas of a surface are difficult or impossible to interpret, and much published imaging reflects an inherent selectivity for areas of a surface in which relatively simple, well-ordered images can be obtained. This is not to say, however, that defective areas on surfaces are not reported in the literature, particularly for oxides, or that STM is not well-suited to detecting defects or to assessing the extent to which a surface is defective. The problems lie in understanding the precise atomic and electronic structure of defects that are often clearly evident in STM images.

In contrast to SPM methods, which provide a relatively poor statistical sampling of a surface, there are some techniques that sample large surface areas. For example, photoelectron diffraction[47] and surface X-ray absorption fine structure spectroscopy (SEXAFS)[48−50] sum over a large number of surface sites but give only short-range information. Surface X-ray diffraction[44,51] also sums over a large number of surface sites but provides information on long-range order.

2.3. Geometric and Electronic Structure of Clean, Well-Ordered Surfaces

There have been a large number of studies of the atomic geometry and electronic structure of single-crystal metal oxides under well-controlled UHV conditions.[15,34] Here we present a few examples of those studies.

2.3.1. Atomic Geometry

The most important geometric property of any surface is the coordinative unsaturation of its surface atoms and ions. An example of how this differs for different crystal faces is shown for rutile (TiO_2) in Figure 3. In the bulk rutile structure, all metal cations are in (slightly distorted) octahedral sites, coordinated by six oxygen anions. The thermodynamically most stable rutile face is (110), in which one-half of the surface cations retain their bulk O ion coordination, and the other half are 5-fold coordinated.[15] [Two O anions have been removed from the (110) face in Figure 3a to model point defects, which will be discussed later.] Less stable is the (100) face, in which all surface cations have 5-fold coordination (Figure 3b). The least stable low-index face of rutile is (001), in which all surface cations have only four oxygen ligands; experimentally this face on TiO_2 is found to facet easily into planes containing a higher ligand coordination of the cations (Figure 3c).[15] Much of the surface chemistry of oxides is driven by the coordinative unsaturation of surface ions.

Another example of an idealized single-crystal terrace is shown in Figure 4 for corundum (0001), a surface that has received a great deal of study on both α-Al_2O_3 and α-Fe_2O_3 (see refs 52 and 53 for a detailed discussion of this crystal structure). Here the surface cations are only 3-fold coordinated with oxygen ligands. This low coordination is not energetically preferred, and experimental measurements on both alumina (Al_2O_3) and hematite (α-Fe_2O_3) suggest that the surface cations partially relax into the underlying plane of oxygen ions in a vacuum environment (see sections 2.3.1.2 and 2.3.1.4).[54−57] Much of this relaxation would be expected to be removed, however, when the surfaces are placed in an aqueous environment, since water molecules, hydroxyls, etc., will replace some of the missing ligands. Figure 5 shows an STM image of the hematite (0001) surface taken in air; the image is consistent with the model of the surface as a simple truncation of the bulk structure,[58] although it is difficult to reliably determine small amounts of inward or outward relaxation of surface and near-surface atoms using the STM.

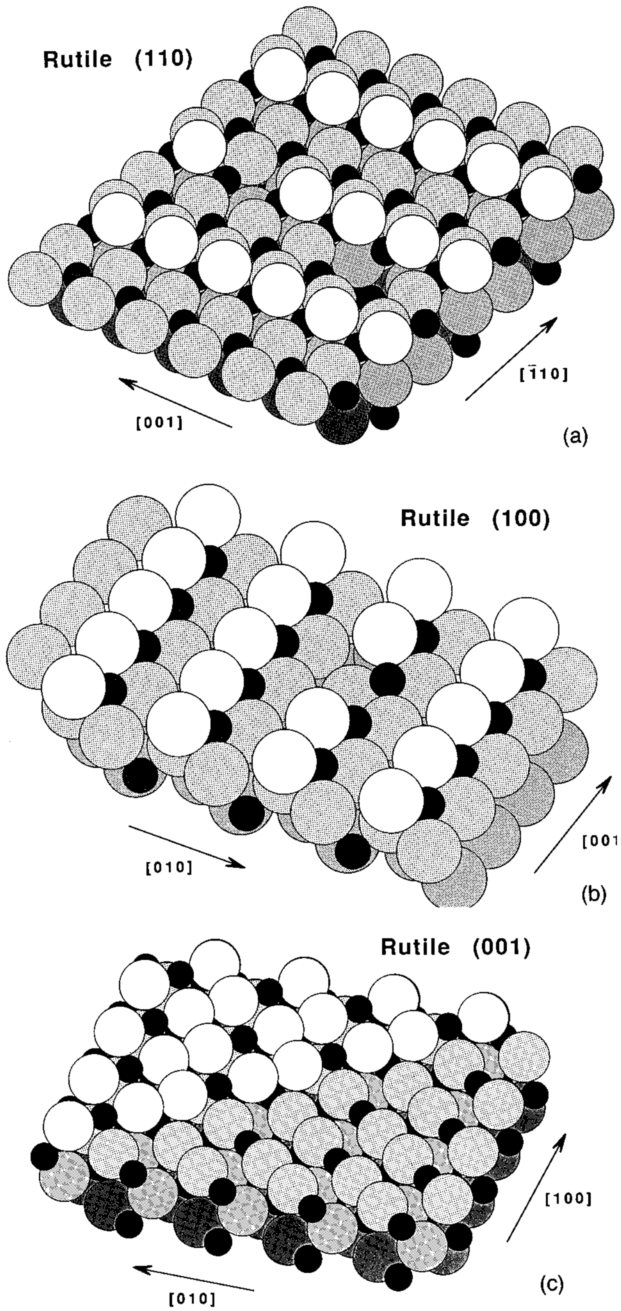

Figure 3. Models of the rutile (110), (100), and (001) surfaces. Small black circles are metal cations; large circles are oxygen anions. Two O vacancy point defects are included on the (110) surface (a) and one on the (100) surface (b), and an atomic height step is shown on the (001) surface (c).

Since surface ions are coordinatively unsaturated, they need not retain the positions that they have in the bulk structure. Such reconstruction of the surface plane, and often several subsurface planes, generally occurs on any single-crystal surface. The oxide surface that has been found to be closest to an ideal termination of the bulk crystal structure is rocksalt (100). For MgO and NiO, LEED measurements indicate less than 2% relaxation or rumpling on the (100) surface.[15] At the other extreme, the α-Al_2O_3 (0001) surface exhibits several extremely complex

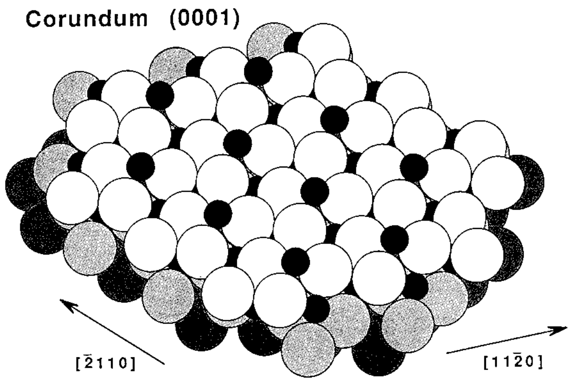

Figure 4. Model of the corundum (0001) surface, illustrating 3-fold oxygen coordination of metal cations (small dark circles) on the (0001) face.

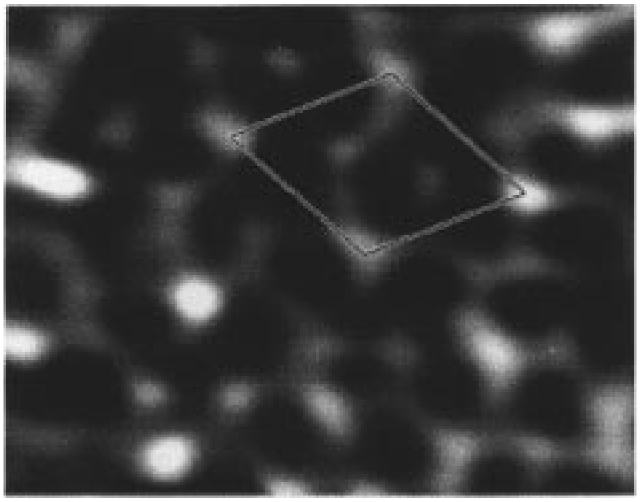

Figure 5. STM image of hematite, α-Fe_2O_3, under the following conditions: +1.1 V, 2.7 nA; edges of unit cell are 5.04 Å long; note higher and lower spots as expected for Fe locations at the hematite (0001) surface (see Figure 4).

reconstructions.[15] However, most determinations of surface reconstruction are performed in UHV; the situation in aqueous solution may be quite different and has yet to be explored.

Coordinatively unsaturated atomic sites at steps can be very important in chemisorption and catalysis. LEED and reflection high-energy electron diffraction (RHEED) are of some use in measuring regular arrays of steps on single-crystal surfaces; steps can also be observed by reflection electron microscopy. However, STM and AFM have proven far more useful and will likely be the primary methods of studying surface steps in the future. Point defects on oxide surfaces are particularly important in adsorption since their electronic structure is often very different than that on terraces (see sections 2.4.2. and 3.1.1).[15]

Another important property of surfaces is their electric dipole moment. If each atomic plane parallel to the surface in the crystal structure contains an equal amount of positive and negative ionic charge (i.e., if it is “charge neutral”), then there is no macroscopic dipole moment perpendicular to the surface, and the surface is referred to as “nonpolar”. An example of such a surface is rocksalt (100). However, even if each atomically flat plane of ions is not charge neutral, the surface may still be nonpolar if a crystal having opposite faces of the same orientation *and having no net charge* does not possess a net dipole moment. Examples of this are rutile (110) and corundum (0001). An example of a “polar” surface is rocksalt (111), where an uncharged crystal will have all cations exposed on one face and all anions on the other. Such a crystal would have a large macroscopic dipole moment perpendicular to the surface and would not be stable in the absence of some charge-compensating mechanism. Of course, one of the crystal habits of periclase, the mineral form of MgO, is an octahedron exposing primarily (111) faces. Those surfaces can be stabilized by nonstoichiometry or the presence of other charged species; this *must* be the case in nature in order for the crystals to grow as they do. From a theoretical standpoint it is difficult to treat polar surfaces, although new methods for handling them are currently being developed.[59]

2.3.1.1. MgO (100). The surface structure and properties of MgO (100) have received considerable attention because of its use as a substrate for the epitaxial growth of lattice-matched metals and metal oxides and as a support for finely dispersed catalysts.[60−62] This surface has also served as a simple model in quantum chemical and molecular dynamics simulations of chemical reactions on metal oxide surfaces.[63,64] Experimental and theoretical results on the atomic arrangement of the MgO (1 × 1) surface are summarized in several recent papers.[44,65,66] Reported relaxations of the topmost surface layer range from −17% to +2.5% based on LEED, RHEED, ICISS, and SEELFS measurements. However, recent X-ray standing wave measurements on a vacuum-cleaved MgO (100) surface[66] and grazing-incidence crystal truncation rod measurements on clean MgO (100) surfaces[44] indicate no detectable reconstruction or relaxation of the surface.

2.3.1.2. α-Al_2O_3 (0001). A recent grazing-incidence X-ray scattering study of the clean, unreconstructed (0001) surface of α-Al_2O_3 has provided a relatively detailed picture of this important model surface.[55] The surface was first annealed in air at 1773 K for 2 h, followed by heating for 20 min at 1173 K in a UHV chamber with an oxygen partial pressure of 10^{-5} Torr. Analyses of crystal truncation rods along (11*l*), (10*l*), (20*l*), and (21*l*) (Figure 6a) indicate that the (0001) surface is terminated by aluminum atoms rather than oxygens and that the most likely surface termination is a single, rather than a double, layer of aluminum atoms. The data fit is consistent with displacements of the top four layers of Al and O atoms by −51%, +16%, −29%, and +20% of the associated bulk values, respectively (Figure 6b). The top Al layer is displaced down toward the bulk, and the underlying oxygens are displaced radially toward the third-layer Al sites, resulting in an interlayer spacing between surface Al and next-layer oxygens that is 51% of the bulk spacing. Similar results were obtained in a time-of-flight scattering and recoiling spectrometry and LEED study.[67] These results contrast with the findings of a recent LEED study of the oxygen plasma cleaned and annealed α-Al_2O_3 (0001) surface, which suggest an outward relaxation of the top layer with some twisting and relief of buckling

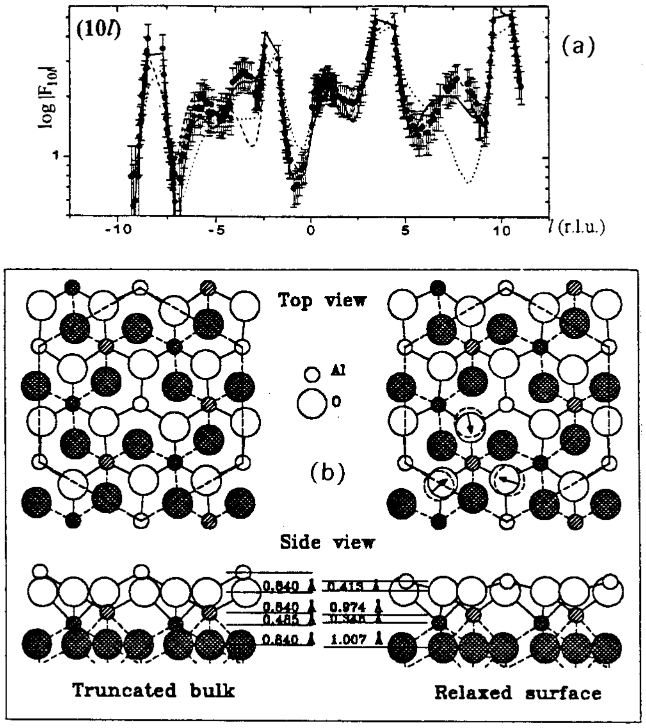

Figure 6. (a) Crystal truncation rod data (solid circles) along (10*l*) for α-Al_2O_3 (0001) and best fit models for surface terminations by a single Al layer (solid line), a double Al layer (dashed line), and oxygen (dotted line). (b) Structures of the α-Al_2O_3 (0001) surface showing the truncated bulk (left) and the best fit model (right) from crystal truncation rod measurements (adapted from ref 55).

in deeper layers.[68] However, the bulk of the experimental data to date support an inward relaxation of the outermost Al layer on the clean α-Al_2O_3 (0001) surface.

A recent theoretical study of the structure of the clean α-Al_2O_3 (0001) surface using a parameter-free molecular dynamics simulation based on density functional theory[69] predicts relaxations of the first four interlayer spacings of −82%, +7%, −52%, and +25%, respectively, relative to the bulk spacings, with a corresponding surface relaxation energy of 1.89 J/m^2. This prediction is similar to that of an ab initio Hartree−Fock "slab model" calculation of the surface structure of α-Al_2O_3 (0001), which finds an inward relaxation of the outermost Al atoms of 68% of the corresponding bulk lattice spacing (i.e., 0.57 Å).[70]

2.3.1.3. TiO_2 (110). Perhaps the most thoroughly studied metal oxide surface is TiO_2 (110), in large part because of interest in the photocatalytic dissociation of water on this surface.[15] A large number of STM studies conducted over the past few years have shown that even the thermodynamically stable (110) surface can be much more complicated than the simple truncation of the bulk structure shown in Figure 3a.

By careful surface preparation, a stoichiometric (110) (1 × 1) surface that is a good approximation of the bulk termination can be obtained. Figure 7 shows an STM image of such a surface, taken with the tip at negative bias with respect to the sample.[25] (110) terraces, monatomic height steps, point defects, and adatoms can all be seen. The bright lines along the [001] direction resemble the rows of bridging O ions in Figure 3a. However, electrons are tunneling *into* the sample with this bias, and most of the O^{2-} electronic levels are occupied and lie several electron volts below the vacuum level. It is now believed that the bright spots in STM images of TiO_2 under negative tip bias correspond to electrons tunneling into the empty 3d states of the surface Ti cations.[71] Recent surface X-ray diffraction results indicate that this surface is, however, relaxed, with a rumpling of the surface planes by as much as 0.27 Å.[72]

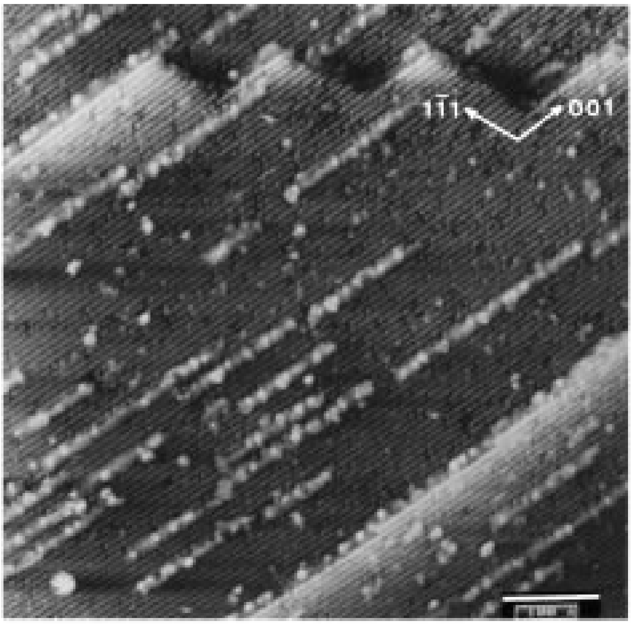

Figure 7. Atomically resolved STM image of the TiO_2 (110) surface annealed in UHV at 1070 K. Tip voltage = −1.70 V. (Reprinted with permission from ref 25. Copyright 1995 Elsevier.)

When the TiO_2 (110) surface is annealed in various ways, a wide variety of surface structures can be created; these are believed to result from different amounts of reduction of the surface and the subsequent ordering of surface defects. Commonly observed is a (1 × 2) reconstruction, which has been modeled in terms of missing rows of bridging O ions.[21−23,26,27] More complicated, longer period (1 × *n*) reconstructions have also been observed,[27] as have double-strand features, which have been modeled as rows of Ti_2O_3-like structures that contain the reduced surface Ti cations.[24] Even more complicated two-dimensional structures consisting of cross-linked rows are stable under a range of preparation procedures; one such structure is shown in the STM image in Figure 8.[21,23] These various reduced surface defect structures no doubt play a major role in the surface chemistry of TiO_2 (110), since the stoichiometric surface, which contains all Ti(IV) cations, is quite unreactive.[15]

2.3.1.4. α-Fe_2O_3 (0001). Condon et al.[20] used STM to study the (0001) surface of hematite, α-Fe_2O_3, after preparation by ion bombardment and annealing. They observed what they call "biphase ordering" of the partially reduced surface in which nanomole-scale domains of hematite (0001), consistent with Fe atoms at the hematite surface, alternate with domains

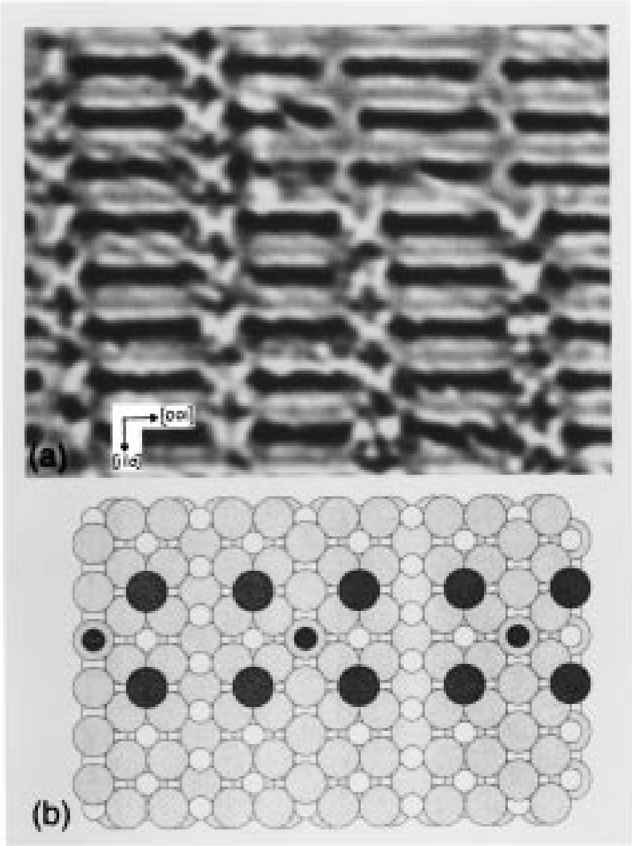

Figure 8. (a) Computer-enhanced image of the 1 × 2 phase on TiO_2 (110) with cross-linking. Tip voltage = −1.5 V. (b) Model of the 1 × 2 phase with cross-linking rows. The small and large circles represent Ti and O ions, respectively. The Ti and O in the cross-links are darkened to highlight them. (Reprinted with permission from ref 23. Copyright 1995 Elsevier.)

consistent with wustite FeO (111). Interestingly, there is no discernible difference between the STM images of the hematite (0001) domains in UHV and those taken in humid air. Certainly, however, there will be some relaxation differences between the UHV surface and surface Fe coordinated by water molecules which the STM did not detect. We are aware of no STM studies of hematite surfaces other than (0001).

A recent X-ray photoelectron diffraction study of the clean surface of α-Fe_2O_3 (0001) grown epitaxially (≈350 Å thick) on α-Al_2O_3 (0001) shows that this surface is Fe-terminated and that the first four layer spacings are −41%, +18%, −8%, and +47% of the associated bulk values, respectively.[45] The surface structure of α-Fe_2O_3 (0001) is similar to that of α-Al_2O_3 (0001) (1 × 1) (see section 2.3.1.2).

A recent theoretical study by Wang et al.[822] of the structure of the clean α-Fe_2O_3 (0001) surface using spin-density functional theory and the full-potential linearlized augmented plane wave method predicted that this surface could be terminated by both Fe and O, with the former relaxed inward by 57% of the bulk spacing and the latter relaxed inward by 79% of the bulk spacing. The inward relaxation of Fe on the Fe-terminated surface is consistent with the photoelectron diffraction results of Thevusathan et al.,[45] but the magnitude of the relaxation differs. Wang et al.[822] also report STM images of the α-Fe_2O_3 (0001) surface for a thin (10-nm) hematite film grown epitaxially on Pt (111) and interpret bright and dark regions in the STM image as being due to Fe-terminated and O-terminated regions, respectively. We are not aware of any other experimental results on hematite (0001) surfaces that provide evidence for oxygen termination.

2.3.1.5. Fe_3O_4 (100), (110), and (111). Magnetite, Fe_3O_4, is a mixed-valence inverse-spinel iron oxide that has received some surface science attention because of its importance in magnetic recording media and because of interest in magnetic properties of iron oxides more generally, particularly with regard to magnetic field sensors. It is also an important naturally occurring iron oxide that can reduce metal cations and dehalogenate halocarbon compounds (see section 4.4.3.4).

(100): Magnetite (100) was imaged with STM by Wiesendanger et al.[73] using a magnetic tip in order to achieve atomic resolution spin discrimination. On terraces, an apparently unreconstructed 1 × 1 surface structure was observed. Gaines et al.[74] grew magnetite epitaxially on MgO (100) to produce a (100) surface. These layers were exposed to air for a few minutes during transfer to an STM chamber, where they were cleaned using 500 eV Ar^+ ion bombardment followed by annealing at 873 K. Steps oriented in ⟨110⟩ directions were observed on magnetite (100) and were generally one atomic layer high. Parts of the surface were found to be reconstructed from a c(1 × 1) unit cell to a p(1 × 1) unit cell composed of elongated features (along ⟨110⟩ directions) whose origin remains somewhat unclear, but they are probably clusters of atoms with imaged states of Fe character. These findings are in general agreement with the earlier results of Tarrach et al.[75] In contrast to these findings, Chambers and Joyce[76] have suggested that the surface of Fe_3O_4 (100) grown epitaxially on MgO (100) undergoes a $(\sqrt{2}\times\sqrt{2})$R45° reconstruction based on LEED, RHEED, and STM measurements, and they found that the Fe_3O_4 (100) surface can be readily converted into γ-Fe_2O_3 (100) (1 × 1) by exposure to an oxygen plasma at room temperature. Annealing the oxidized magnetite (100) surface in vacuum at 523 K converts it back to the reconstructed magnetite surface.

(110): Jansen et al.[31] performed an STM study of an Ar^+ ion sputtered and annealed magnetite (110) surface and found a one-dimensional reconstruction with rows running in the [110] direction.

(111): Condon et al.[30] used STM to image a nominal α-Fe_2O_3 (0001) surface in UHV. The sputter-and-anneal preparation led to a reduced surface. The STM imaging and LEED patterns are consistent with an Fe_3O_4 (111) surface; the STM imaged only the locations of Fe atoms, in agreement with the conclusions of Tarrach et al.[75] for the (100) surface.

2.3.2. Electronic Structure

Much of what we know about the electronic structure of solid surfaces has been determined by UHV electron spectroscopic techniques.[32,36] Photoelectron spectroscopy, utilizing a wide range of photon ener-

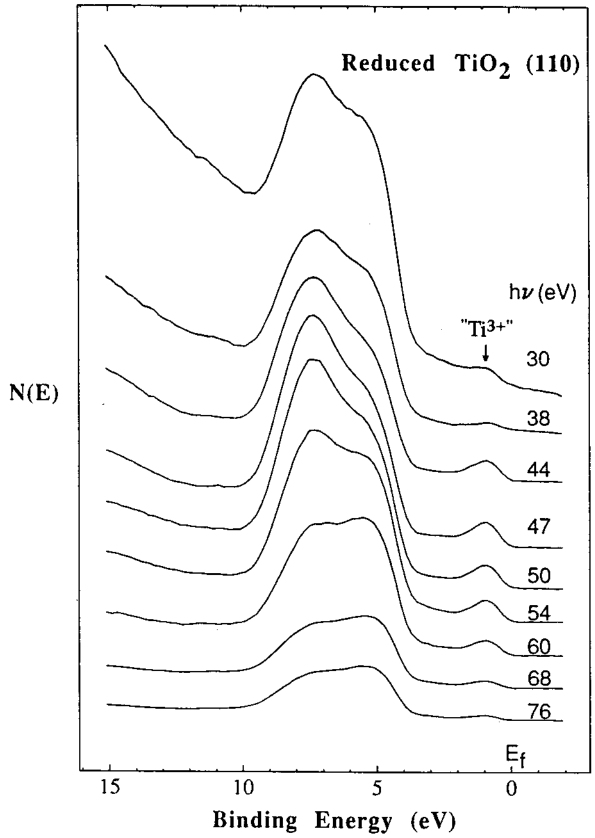

Figure 9. Series of angle-integrated UPS spectra from reduced TiO_2 (110) taken for photon energies between 30 and 76 eV. (Reprinted with permission from ref 77. Copyright 1991 American Institute of Physics.)

gies, is a powerful technique for determining surface and near-surface electronic structure. Information on initial and excited states of electrons on surface atoms and ions can be obtained fairly directly. (In highly correlated electron systems such as oxides, photoemission spectra often exhibit final-state effects that complicate interpretation of the data, but our theoretical understanding of those effects is at a fairly advanced stage.[15])

Resonant photoemission, in which the incident photon energy is varied through an atomic core → valence optical absorption transition, is an atom-specific technique that can be used to measure the type and degree of orbital hybridization in solids, as well as to separate the contributions of different ions to the overall electronic structure.[15] An example of this is shown in Figure 9 for a slightly reduced rutile TiO_2 (110) surface.[77] The different UPS spectra were taken at the incident photon energies indicated, which ranged from below to above the Ti 3p → 3d optical absorption threshold at about 48 eV. The small emission feature near 1 eV is from reduced surface Ti 3d cations; it is seen to exhibit a maximum in intensity near 48 eV photon energy, confirming its cation 3d character. However, significant changes in the shape of the valence band emission between 4 and 10 eV can also be seen. The valence band is primarily of O 2p character, but no purely O-derived features would resonate in this photon energy range. The changes in the relative intensities of different parts of the band arise because of the hybridization of Ti 3d (and 4s,p) wave functions with the O 2p orbitals in that band. Resonant photoemission can also be applied to the study of adsorbate–substrate interactions in adsorption.

Being a large-area technique, photoemission sums over the electronic structure of all types of surface sites. However, rather detailed information on point defects has been obtained on oxides by comparison of spectra from defective and stoichiometric surfaces.[15] Since the electronic states associated with point defects on ionic compounds often occur at significantly different energies than those of the perfect surface, they are easier to identify in photoemission spectra than is the case for metals or covalent semiconductors. Figure 10 shows an example of this for α-Fe_2O_3 (hematite). UPS spectra are shown for a stoichiometric α-Fe_2O_3 (0001) surface, where all cations are Fe(III). When the surface is partially reduced by ion bombardment, a new band of electronic states appears between 0 and 2 eV that corresponds to emission from reduced surface Fe(II) cations. The surface defect states seen in Figure 10 and on TiO_2 in Figure 9 are characteristic of most transition-metal oxides. Core-level photoemission (i.e., XPS) provides complementary information in that it identifies the valence state of surface ions.

Inverse photoelectron spectroscopy (IPS) is a very direct way to determine the energies of normally empty electronic surface states.[78] ELS spectra also contain information about empty states since they measure the joint density-of-states between the ground and excited states; however, since ELS spectra are a convolution of the two densities-of-states, the information is difficult to extract. The near-edge fine structure in SEXAFS (NEXAFS) gives a different type of joint density-of-states information, since the transitions are from core-level initial states to conduction-band final states. (See section 4.3.2.2 for a discussion of X-ray absorption spectroscopies.) All of these techniques sum over large areas of the surface.

There have been experimental surface science studies of the electronic structure of many metal oxide surfaces.[15] Measurements of the spectra of both occupied and normally empty electronic states have been performed on carefully prepared, nominally stoichiometric single-crystal surfaces. While it is often difficult to separate surface from bulk electronic states experimentally due to the finite sampling depth of the techniques, one general conclusion has been found for most of the oxide surfaces studied: despite the coordinative unsaturation of the surface ions, the electronic structure of the surface is surprisingly similar to that of the bulk oxide. There are exceptions—as, for example, the excitonic surface states on MgO (100)[15]—but in general there does not appear to be major redistribution of charge among the surface ions. This is not surprising in non-transition-metal oxides, where the cations can have only one valence state, but it need not be the case for transition-metal oxides where the energy barrier to changing the cation valence state may be quite small.

An example of the similarity of the surface electronic structure for different degrees of coordinative

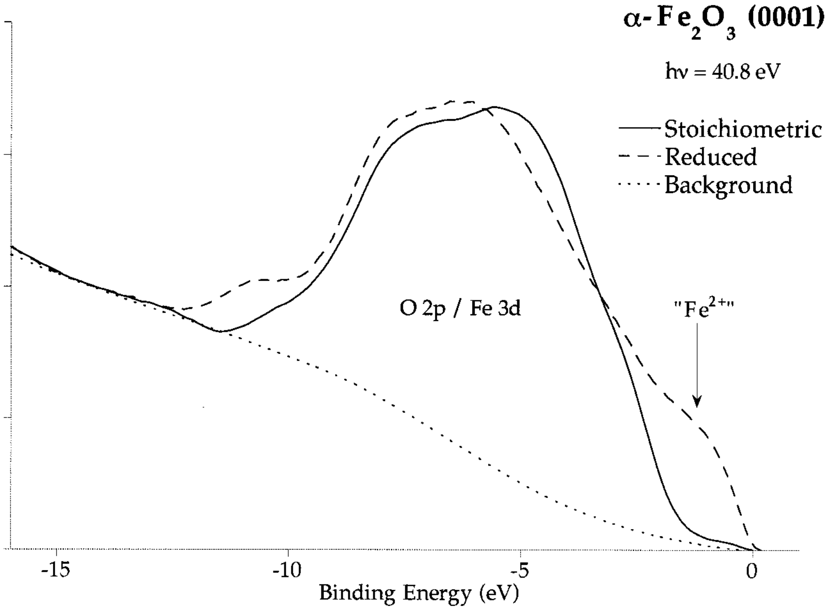

Figure 10. UPS spectra for stoichiometric (solid line) and reduced (dashed line) α-Fe_2O_3 (0001) surface. The dotted line is the secondary electron background.

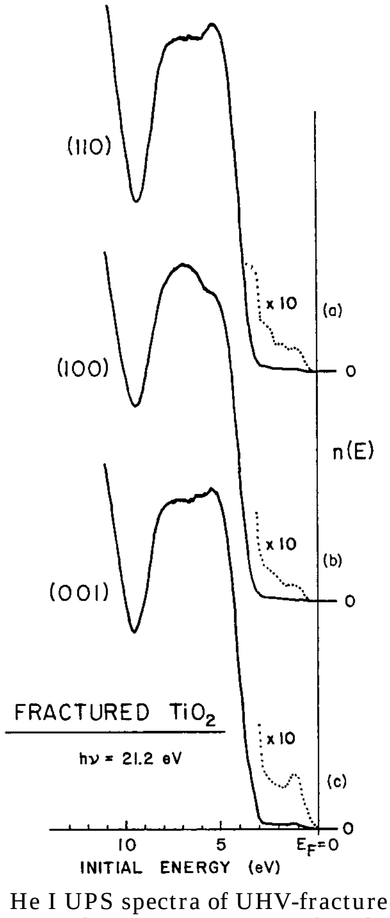

Figure 11. He I UPS spectra of UHV-fractured TiO_2: (a) (110), (b) (100), and (c) (001). (Reprinted with permission from ref 79. Copyright 1981 American Institute of Physics.)

unsaturation on TiO_2 surfaces is given in Figure 11.[79] UPS spectra for UHV-fractured (110), (100), and (001) surfaces are shown; these are the same surfaces for which models are shown in Figure 3. While the spectra are not identical (particularly in the relative amplitudes of the bonding and nonbonding O 2p components of the valence band), they are very similar. In particular, increasing the coordinative unsaturation of the surface Ti ions from six and five, as on the (110) surface, to four on the (001) surface does not produce significant emission in the bulk band gap region, which will be shown in section 3.1.3 to be characteristic of charge transfer to, and consequent reduction of, Ti cations. Presumably the stability of the closed-shell configuration on the O^{2-} anions retains the bulk ionicity into the surface plane. However, this situation changes dramatically in the presence of point defects and surface nonstoichiometry, which is discussed below.

2.4. Imperfections on Oxide Surfaces

Much of the important interfacial chemistry that takes place on oxide surfaces does so at surface defect sites. Such sites can consist of missing atoms or adatoms (point defects), steps, the surface termination of bulk dislocations or grain boundaries, or impurities. We consider here the properties of defects on atomically clean surfaces; the role of defects in adsorption and catalysis will be considered later. Since surface defects can originate from or diffuse into the bulk, we begin by discussing the properties of bulk defects in metal oxides.

2.4.1. Bulk Point Defects

Consider a metal oxide, such as α-Fe_2O_3 (hematite) or TiO_2 (rutile). Both materials are semiconductors, their band gaps being 2.2 and 3.1 eV, respectively, cf. Table 1. Point defects arise in the oxide as a consequence of lattice imperfections, e.g., the presence of interstitials and vacancies. Alternatively, they are formed by substitutional doping, i.e., the replacement of lattice ions by foreign constituents. The presence of point defects can exert a profound effect on the electronic properties as well as the chemical reactivity of the oxide. Some important cases are discussed below using hematite as an example. Kröger–Vinck notation[80] is employed to describe the defects.

Oxygen vacancies (V_O) are formed typically under anaerobic conditions as a result of loss of lattice oxygen to the environment:

$$O_O \rightleftharpoons V_O + {}^1/_2O_2 \tag{1}$$

Here, O_O denotes an oxygen dianion on its lattice site, while V_O is an oxygen vacancy filled with two electrons. The latter will ionize spontaneously at room temperature, producing two conduction-band electrons [e^-(cb)]:

$$V_O \rightleftharpoons V_O^{\bullet\bullet} + 2e^-(cb) \tag{2}$$

where the two dots in the superscript indicate that the vacancy has acquired two positive charges through the electron loss with respect to the rest of the lattice. From eqs 1 and 2 it is apparent that the formation of oxygen vacancies leads to n-type doping of the oxide. If n-doped α-Fe_2O_3 is placed in contact with water, the electrons will be trapped by surface Fe^{3+} ions, producing Fe^{2+}:

$$e^-(cb) + Fe^{3+}{}_S \rightleftharpoons Fe^{2+}{}_S \tag{3}$$

The likely result is the formation of a layer of magnetite (Fe_3O_4) on the surface of α-Fe_2O_3.[81] Films of this type are electronically conducting and act as recombination centers for electron−hole pairs. As a consequence, the quantum yields observed in photoelectrochemical experiments with polycrystalline α-Fe_2O_3 electrodes are notoriously low.[82] This example is instructive inasmuch as it shows how ambient conditions, i.e., low oxygen partial pressure, can lead to electronic doping and—ultimately—to structural transformations at the metal oxide−water interface which have important consequences for the chemical and electrochemical reactivity of the oxide.

Substitutional dopants may be introduced deliberately or inadvertently during the formation of a metal oxide. In the following example, we consider the effect of doping α-Fe_2O_3 with two impurities which are typical for natural environments: Si and Mg. The incorporation of the former into the hematite lattice follows eq 4:

$$2SiO_2 \rightleftharpoons 2Si_{Fe} + {}^1/_2O_2 + 3O_O \tag{4}$$

where Si_{Fe} denotes a trivalent silicon ion located on an Fe lattice site. Trivalent silicon is a strong reductant and converts spontaneously to the stable tetravalent state, generating conduction-band electrons:

$$Si_{Fe} \rightleftharpoons Si_{Fe}^{\bullet} + e^-(cb) \tag{5}$$

Thus, silicon ions act as n-type dopants for α-Fe_2O_3 and, by analogy to oxygen vacancies, are expected to induce magnetite formation at the hematite−water interface.

The incorporation of magnesium ions in the α-Fe_2O_3 lattice is described by eq 6:

$${}^1/_2O_2 + MgO \rightleftharpoons Mg_{Fe} + 3O_O \tag{6}$$

where Mg_{Fe} denotes a trivalent magnesium ion located on an Fe lattice site. Trivalent magnesium is a strong oxidant and therefore is able to abstract an electron from the valence band of the oxide, generating a hole.

$$Mg_{Fe} \rightleftharpoons Mg_{Fe}' + h^+(vb) \tag{7}$$

Thus, in contrast to silicon ions, magnesium acts as a p-type dopant for α-Fe_2O_3, thereby protecting the surface against magnetite formation.

2.4.2. Steps, Kinks, and Point Defects

No real crystal surface consists of only idealized terraces; steps, kinks, adatoms, point defects, etc., will always be present, as shown schematically in Figure 2. The structural differences at such sites will change—often drastically—the surface electronic structure and chemical behavior of the surfaces.

There have been very few studies of the properties of steps on metal oxides.[15] Their orientation can be determined by STM or AFM, but nothing is known about the relaxation of ions at step edges—which, according to theory, must occur. The ligand coordination of ions at the upper edges of steps is always lower than that on terraces, while that of ions at the bottom of steps is closer to the bulk value. A jog in a step, called a kink, further reduces the coordination of ions at its outside corner (see Figure 2). Such highly coordinatively unsaturated sites must play a major role in surface chemistry, even though there is no clear experimental evidence of large differences in their electronic structure from that of the bulk.

The largest effects on surface electronic structure are produced by point defects associated with surface nonstoichiometry. This is particularly important for transition-metal oxides, where the metal cations can have more than one valence state. The predominant type of surface defect that is found on transition-metal oxide surfaces is an O vacancy (although there may be exceptions to this, such as Cr_2O_3 and NiO). When an O^{2-} ion is removed from an oxide surface—as is shown for TiO_2 (110) in Figure 3a—it is necessary to leave a compensating negative charge associated with the defect site in order to maintain local charge neutrality. Since the O 2p orbitals are essentially filled, the extra electrons must partially populate the normally empty cation orbitals (3d for the fourth-row transition-metal oxides) adjacent to the vacancy, giving rise to totally new electronic states that do not exist on perfect terraces (or, to the best of our ability to measure, on steps). This is the origin of the emission between 2 and 3 eV above the top of the valence band in Figure 9. In addition to the change in electronic structure, the ions surrounding the O vacancy become more coordinatively unsaturated. (The role that these electronic and structural changes play in the dissociation of water on titanias is discussed in section 3.1.3.)

3. Water Vapor−Metal Oxide Interactions

A variety of surface science techniques have been applied to the study of the interaction of water vapor with metal oxide surfaces under high vacuum conditions; the data up to 1992 have been collected in tabular form in ref 15. For all oxides, both molecular and dissociative adsorption occur via acid−base (or donor−acceptor) interactions in which there is no change in the valence state of the adsorbate and little change in the population of substrate electronic states.

An essential step in determining how bulk water reacts with a metal oxide surface at the molecular level is to study the initial interaction of water molecules with a clean surface. This is best accomplished in a UHV environment in which a well-characterized clean, single-crystal metal oxide is exposed to water vapor at very low pressures, followed by photoemission spectroscopy or another UHV method that is sensitive to the electronic structure of the surface and the sorbed water. Here we will review recent studies of the sorption of water on clean surfaces of MgO, CaO, TiO_2 (rutile), TiO_2 (anatase), α-Al_2O_3, and α-Fe_2O_3. These studies illustrate the fact that water molecules react dissociatively with defect sites at very low water vapor pressures ($\leq 10^{-9}$ Torr) then with terrace sites at water vapor pressures that exceed a “threshold” pressure.

3.1. Experimental Studies on Single-Crystal Metal Oxides

Surface science techniques in a vacuum environment have been widely applied to the study of adsorption on metal oxides.[15] As discussed above, the most detailed information can be obtained on well-characterized single-crystal surfaces, although many of the techniques have also been applied to polycrystalline samples and supported catalysts. The limit here is one of pressure, and it is not possible to directly simulate high-pressure processes in the UHV environment. In some cases, high-vacuum surface analysis systems have been coupled to high-pressure or electrochemical cells, although the surface must be removed from the catalytic environment into vacuum before the surface spectroscopies can be applied.[83−86] Some useful information has been obtained in this way, but it is probably better to try to find techniques, such as X-ray or optical spectroscopies or magnetic resonance, that can be applied directly in situ.

The geometric arrangement of well-ordered monolayers of adsorbates can be determined by LEED (section 2.3.1), but all of the caveats above about disorder and different surface structures apply. STM and AFM (section 2.3.1) have exhibited some success in the study of adsorbates on oxides, but the techniques are potentially disruptive in that a mechanical tip and/or a large electric field are present and can displace adsorbed moieties. Surface X-ray scattering (section 4.3.2.1), surface XAFS (section 4.3.2.2), and X-ray standing wave methods (section 4.3.2.3) can also provide detailed structural information on adsorbates on metal oxide surfaces under ambient or UHV conditions, although such studies on metal oxide surfaces are quite limited (e.g., see refs 87−89). Much more work needs to be done in this area.

To determine the electronic structure of adsorbates on surfaces, all of the techniques discussed in section 2.3.2 for clean surfaces can be used. Photoemission difference spectroscopy[90] is a powerful method for measuring the occupied molecular orbital structure of adsorbates and for studying adsorbate−substrate interactions. Synchrotron-based near-edge X-ray absorption fine structure (NEXAFS) spectroscopy[50] and X-ray emission spectroscopy[91] can also provide detailed information on the structure and bonding of adsorbates on surfaces. Most of these techniques sum over the surface, so they do not give detailed information on a specific type of site, unless only a single type is present. On oxides, whose stoichiometric surfaces are often relatively chemically inert, it has been possible to study adsorption at defect sites in some detail.[15] High-resolution electron energy loss spectroscopies (HREELS) are a powerful technique for the determination of adsorbate species through their vibrational spectra.[32] The vibrational information obtained in vacuum can also be compared with infrared absorption/reflection data taken in situ, so that a partial bridge across the “pressure gap” is a possibility. Temperature-programmed desorption (TPD) and reduction (TPR) are particularly useful for following reaction pathways on surfaces. A great deal of work on adsorption on metal oxide surfaces has been done by using those methods in combination with XPS.[92]

3.1.1. MgO and CaO

The reaction of water vapor with the clean MgO (100) and CaO (100) surfaces at 300 K has been studied by Liu et al.[65,66,93,94] using synchrotron-based photoemission spectroscopy at an incident photon energy of 80 eV. Such surfaces are arguably the simplest metal oxide surfaces in terms of their geometric and electronic structures; thus they provide a good starting point in developing a mechanistic understanding of the interaction of water molecules with a metal oxide surface. Moreover, the greater reactivity of CaO with water relative to MgO permits the testing of hypotheses concerning surface reactivity. Surfaces were prepared by cleaving an MgO single crystal in a vacuum of $\approx 10^{-11}$ Torr, followed by collection of the combined valence band O 2s spectra and O 1s spectra, and then the collection of analogous spectra after successive 3-min exposures to water pressures from 5×10^{-9} to 10^{-3} Torr, using a water-dosing needle placed within a few centimeters of the surface. The surface was charge-neutralized during these photoemission experiments using 4−6 eV electrons from a flood gun. The combined valence band O 2s spectra for MgO (100) at different water exposure pressures are shown in Figure 12. The valence band O 2s photoemission spectrum of the clean MgO (100) surface is characterized by two main features, one centered at a kinetic energy of $\approx$66 eV [binding energy (BE) of $\approx$4 eV relative to the Fermi level] and one at $\approx$49 eV (BE $\approx$21 eV). A small shoulder is also observed at 63 eV kinetic energy. After exposure of this surface to 5×10^{-9} Torr water vapor pressure, a weak new feature at $\approx$10 eV BE is observed. This weak feature is attributed to the formation of OH^- groups, based on a comparison of the spectrum with that of clean $Mg(OH)_2$ (001) (Figure 12), which shows a strong feature at this

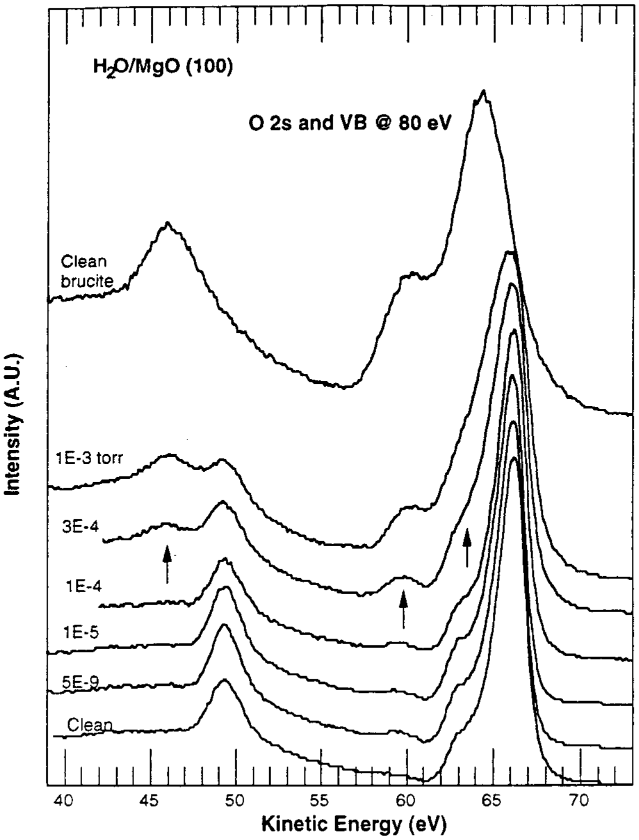

Figure 12. O 2s and valence band UPS spectra of clean and water-dosed MgO (100) and clean brucite [$Mg(OH)_2$] taken at a photon energy of 80 eV. The water dosing pressures are indicated (in Torr), and the dosing time at each pressure was 3 min. The three features indicated by arrows are due to hydroxyl groups on the MgO surface. (Reprinted with permission from ref 65. Copyright 1998 Elsevier.)

binding energy due to OH^- groups. The $MgO + H_2O$ spectrum is relatively unchanged from this initial water vapor pressure up to a pressure of 1×10^{-4} Torr. However, after exposure of the surface to a water vapor pressure of 3×10^{-4} Torr, the weak feature at ≈10 eV and the shoulder at ≈4 eV grow significantly, and a new feature at ≈24 eV binding energy is evident. These features, which are attributed to OH^- groups on the MgO (100) surface, grow significantly after exposure of the surface to a water vapor pressure of 1×10^{-3} Torr or greater.

The defect density on the vacuum-cleaved MgO (100) surface is estimated to be 5−10% of the available surface sites, based on relative changes in the valence band O 2s photoemission spectrum following exposure to Na and, in separate experiments, to Cs that were deposited on similarly prepared MgO (100) surfaces.[95] On the basis of this defect density measurement, Liu et al.[65] suggested that, at water exposure pressures of 5×10^{-9} to 1×10^{-4} Torr, water molecules react dissociatively primarily with defect sites on the MgO (100) surface. For MgO (100) surfaces prepared with higher defect densities (up to 35% of the surface sites) by Ar^+ ion bombardment, up to 0.35 monolayer of OH forms over the same range of water exposure pressures as in the low-defect density study, but no additional dissociation of water beyond this coverage was found with increasing exposure time, suggesting that dissociation is occurring primarily on defect sites.[94] At water exposure pressures > 3×10^{-4} Torr, these studies suggest that water dissociates on terrace sites, resulting in ≈0.6 monolayer of OH groups at an exposure pressure of 1×10^{-3} Torr.[65] These findings led Liu et al. to suggest a “threshold” pressure of water vapor, below which water reacts dissociatively, primarily with defect sites, and above which water reacts dissociatively with terrace sites. Increased exposure times above this threshold pressure resulted in additional hydroxylation of the surface, eventually leading to full monolayer OH coverage. However, increased exposure times below this threshold resulted in no change in OH surface coverage up to exposure times of several hours. This finding was interpreted as indicating that the reaction is thermodynamically rather than kinetically controlled.

A thermodynamic analysis of the reaction of water vapor with the MgO (100) surface[65] predicts a “threshold” water pressure of 4.5×10^{-4} Torr for the reaction $MgO + H_2O = Mg(OH)_2$, in which 1 mol of the MgO (100) surface is converted to 1 mol of $Mg(OH)_2$ at the surface. This prediction is consistent with the experimental results of Liu et al.[65] A similar photoemission study of the interaction of water vapor with CaO (100)[93] showed that the experimental threshold pressure for dissociative chemisorption of water is $\approx 10^{-9}$ Torr, whereas the predicted threshold pressure for dissociative chemisorption of water on terrace sites, based on a thermodynamic analysis of the reaction $CaO + H_2O = Ca(OH)_2$, is 2.2×10^{-9} Torr.[93]

These experimental results at very low water vapor pressures are consistent with the predictions of high-level quantum-chemical studies of the interaction of water molecules with MgO (100), which suggest that water chemisorbs dissociatively at corner (three-coordinated Mg) and edge (four-coordinated Mg) sites and shows almost no tendency to dissociatively chemisorb on terrace (five-coordinated Mg) sites.[96−99] However, these theoretical results are at variance with the photoemission results for water vapor pressures higher than the “threshold” pressure, where dissociative chemisorption on terrace sites was found to occur.[65] This variance may be due in part to the simplified models of the MgO (100)−H_2O interface and reaction mechanism used in the calculations. More recent ab initio correlation-corrected periodic Hartree−Fock calculations by McCarthy (see section 7.2.1) predict that protons and hydroxyl groups chemisorb in a cooperative fashion on the MgO (100) surface with a combined binding energy (≈−370 kcal/mol) that is similar to the dissociation energy of water (≈400 kcal/mol); these results appear to be consistent with the experimental findings of Liu et al.[65]

In addition, recent ab initio total energy calculations based on the gradient-corrected local density approximation[63] have shown that adjacent water molecules in the experimentally observed (3 × 2) water monolayer[100,101] interact, form hydrogen bonds, and strongly dimerize, which promotes the dissociation of two out of the six water molecules in the surface unit cell. To our knowledge, this is the first theoretical evidence for water dissociation on terrace sites on the MgO (100) surface and is consistent with the photoemission results described above,[65] which show that water dissociates on defect sites at low water coverage ($<5\%$ ML) and on terrace sites at higher coverage ($>5\%$ ML). These theoretical predictions and photoemission results contrast with predictions from a recent interaction−potential minimization and molecular dynamics simulation of water adsorption on MgO (100),[64] which found no evidence of hydrogen bonding between the (3×2) water layer and the substrate nor evidence for dissociation of water on terrace sites on MgO (100).

Other experimental studies of the interaction of water (or D_2O) with single-crystal MgO (100) have been performed by a number of groups.[100,102−105] The results of these studies, which were performed at temperatures ranging from 100 to 250 K, are consistent for the most part with dissociative chemisorption of water at defect sites and the nondissociative chemisorption of water molecules on terrace sites. These differences in low-temperature (theoretical) and room-temperature (photoemission) results indicate a need for caution in extrapolating the results of low-temperature studies of adsorbate interactions, particularly that of water (which forms an icelike structure on surfaces at low temperature), to room-temperature adsorbate interactions with metal oxide surfaces. Other studies at 300 K on powdered MgO[106−108] and on single-crystal MgO (100)[109] provide evidence for monolayer coverages of hydroxyl groups on MgO after high water exposures (>2 Torr for several minutes) or immersion in bulk water, in agreement with the results of Liu et al.[65] In contrast, an elastic recoil depth analysis (ERDA) of MgO (100) reacted with acidic aqueous solutions using a 7.5 MeV $^{16}O^{4+}$ beam was originally interpreted as indicating the formation of a 1000-Å thick coating of $Mg(OH)_2$ on MgO.[110] However, a more recent ERDA and SIMS study by Berry et al.[111] contradicts these earlier findings, concluding that the ERDA interpretation was incorrect and that a monolayer of hydroxyls is more consistent with SIMS results. This body of work raises an important point for understanding the geochemistry of oxide minerals: undercoordinated metal ions probably do not exist at the aqueous−oxide interface. These metal ions are likely to react immediately with water molecules to complete their coordination spheres.

3.1.2. α-Al_2O_3

The interaction of water vapor with the single-crystal α-Al_2O_3 (0001) surface has been studied using photoemission spectroscopy[112,113] and theoretical methods.[69,114] There have also been detailed laser-induced thermal desorption and temperature-programmed desorption studies of water on α-Al_2O_3 (0001) surfaces, which were interpreted as suggesting a variety of hydroxyl surface sites with different binding energies.[823,824] In addition, there have been a number of experimental studies of the interaction of water with powdered α-Al_2O_3 samples.[115] The experimental studies find evidence for dissociative chemisorption of water on this surface, with an observed "threshold" pressure of $\approx$1 Torr for the dissociative chemisorption of water vapor on terrace sites on this surface.[112] Diffuse reflectance infrared Fourier transform (DRIFT) spectroscopy studies of powdered α-Al_2O_3 washed in distilled water for over 1 h show that the surfaces of the alumina particles are converted into a mixture of α-$Al(OH)_3$ (bayerite) and γ-$Al(OH)_3$ (gibbsite).[115,825]

A recent molecular dynamics simulation of the interaction of water with α-Al_2O_3 (0001) using density functional theory by Hass et al. [69] predicts that water dissociatively chemisorbs on this surface. Furthermore, these theoretical results suggest three different behavior regimes for the interaction depending on surface coverage: a differential heat of adsorption (ΔH_{ads}) of >44 kcal/mol at coverages of <5 OH/nm^2, a ΔH_{ads} of ≈ 37 kcal/mol from 5 to 10 OH/nm^2, and a near-exponential decrease in ΔH_{ads} above 10 OH/nm^2. These changes were interpreted by Hass et al. as indicating that reaction in the low-coverage regime is dominated by surface defects, that the intermediate-coverage regime corresponds to "intrinsic" adsorption processes (which we interpret as consistent with dissociative chemisorption of water on terrace sites of α-alumina), and that the high-coverage regime involves a number of competing processes, including hydrogen bond formation and multiple H_2O adsorption on both first- and second-layer Al, which results in the straining or breaking of surface Al−O bonds and the exchange of adsorbed and surface oxygens. This regime is also suggested to correspond to the possible formation of $Al(OH)_3$ phases.

These theoretical predictions are consistent with the photoemission results of Liu et al.[112] discussed above, which indicate a threshold pressure of $\approx$1 Torr for the α-Al_2O_3 (0001) surface, below which dissociative chemisorption of water occurs primarily on defect sites and above which dissociative chemisorption occurs on terrace sites. At higher water vapor exposures, Liu et al. [113] suggest that bulk hydroxylation occurs, resulting in the formation of $Al(OH)_3$ phases, as was found by other[115,825] DRIFT studies of α- and γ-alumina powders exposed to bulk water. This agreement between experiment and theory is quite encouraging, although unusual in metal oxide−water systems that are this complicated. Additional photoemission and new X-ray crystal truncation rod experiments on different surfaces of α-alumina reacted with water vapor are needed in order to test the suggestions from the energy minimization calculations of Nygren et al.[114] that polar, oxygen-terminated surfaces of α-alumina undergo very small relaxations during hydroxylation, whereas the clean, nonpolar Al-terminated (0001) surface undergoes very large relaxations.

3.1.3. TiO_2 (Rutile)

A good example of the application of surface science techniques to the interaction of monolayer amounts of water with metal oxide surfaces is that for titanias.[15] There have been many experimental studies of water exposed to nominally stoichiometric single-crystal rutile (110) surfaces,[15] and there is still some controversy as to whether, and in what way, water interacts with that surface in a UHV environment. However, any interaction that may occur is weak,

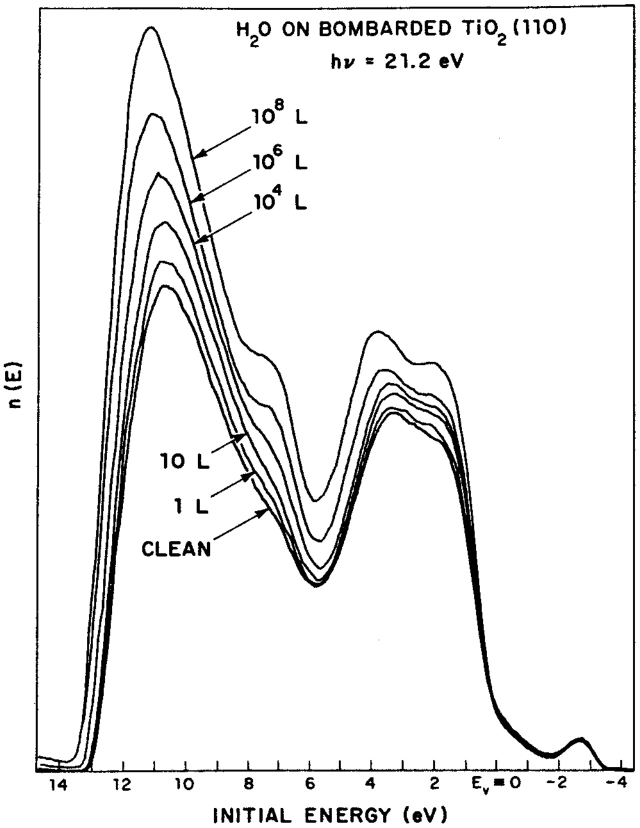

Figure 13. He I UPS spectra of Ar^+ ion-bombarded TiO_2 (110) after successive exposures to H_2O. (Reprinted with permission from ref 117. Copyright 1977 Elsevier.)

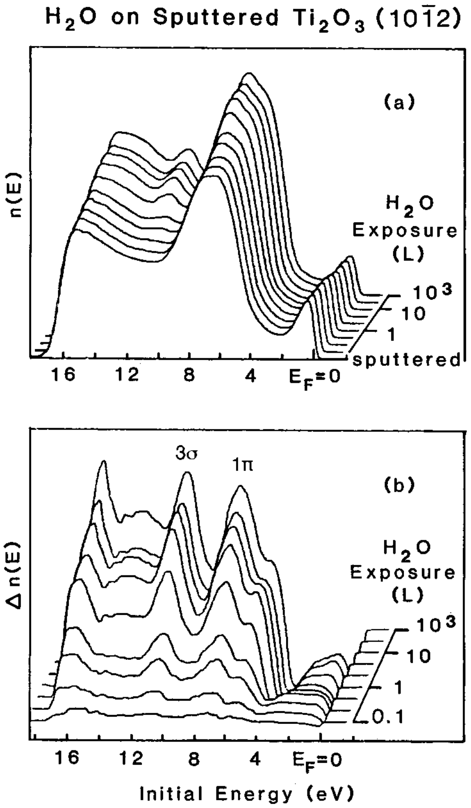

Figure 14. (a) UPS spectra for H_2O exposure of the reduced Ti_2O_3 (102) surface. (b) UPS difference spectra for the data in panel a. (Reprinted with permission from ref 118. Copyright 1982 Elsevier.)

and very little is adsorbed, whether in the form of water or in the form of OH^-. The problem here is that even the most carefully prepared single-crystal rutile surfaces are quite defective,[116] and no two groups have surfaces with the same defect structures. However, it is generally agreed that the reduced rutile (110) surface dissociates water at O vacancy defect sites (at least at low water vapor pressures), resulting in adsorbed OH^-. Figure 13 presents UPS spectra for partially reduced TiO_2 (110), both clean and after various exposures to H_2O.[117] The initial interpretation of this dissociation was that the Ti 3d electrons associated with the O vacancy defects were primarily responsible. However, in Figure 13 there is very little depopulation of the Ti 3d defect states (consistent with an acid–base interaction), suggesting that other factors might be important. To test this hypothesis, water adsorption experiments were performed on UHV-cleaved $(10\bar{1}2)$ surfaces of single-crystal corundum Ti_2O_3, where every Ti cation in the oxide has a $3d^1$ configuration. Ti_2O_3 cleaves extremely well, and the stoichiometric surface has a very low density of defects. The initial sticking coefficient for H_2O on the stoichiometric surface is quite large, although adsorption effectively ceases after 0.3 Langmuir exposure. Photoemission spectra indicate that the adsorbate is molecular water, with no indication of the formation of surface OH^- species. Thus the presence of Ti 3d electrons on the otherwise well-ordered Ti_2O_3 $(10\bar{1}2)$ surface is not, in itself, sufficient for the dissociation of water. However, when the Ti_2O_3 surface is ion-bombarded, it becomes slightly reduced as well as structurally disordered. UPS spectra of the defective surface exposed to H_2O are shown in Figure 14.[118] Figure 14a shows the spectrum for the clean surface (front spectrum) and for increasing H_2O exposures up to 10^3 Langmuir. Note that here also, as for reduced TiO_2, there is only a small depopulation of the Ti 3d electronic states. The spectra in Figure 14b are difference spectra, in which the clean surface UPS spectrum has been subtracted from each of the other spectra. (The apparent peak near 16 eV is an artifact that results from changes in the sample work function.) Photoemission difference spectra,[90] Figure 14b, are indicative of the molecular orbital emission from the adsorbate, and for low exposures here they exhibit the two-peaked structure indicative of the 3σ and 1π orbitals of OH^-. Thus the surface defect sites clearly dissociate H_2O, with molecular adsorption (characterized by the emission at about 14 eV) occurring for large exposures after the defect sites have been titrated with OH^-. These studies suggest that dissociative adsorption of water on titanias appears to require some type of structural defect in order to produce an active site.

In contrast with the above conclusion, a recent theoretical study by Lindan et al.[119] of the interaction of water with rutile (110), using first-principles density-functional methods and a symmetry-unconstrained adsorbate layer, found that water in both molecular and dissociated forms can coexist on this surface and that O defects are not required for the dissociation of water molecules. Single water molecules with no immediate water neighbors were found to dissociate, whereas adjacent hydrogen-bonded molecules may not, depending on the strength of hydrogen bonding, the spacing of water molecules, and bonding interactions of water with the surface. This study also revealed that these intermolecular interactions influence the geometry of the adsorbates and their vibrational spectra. These theoretical results appear to reconcile many of the contradictory conclusions published in a number of past experimental and theoretical studies of the interaction of water with rutile (110); however, they do not fully explain the observations from several O 1s photoemission studies of the interaction of water with this surface under UHV conditions,[113,120] which show that very high exposure pressures (>0.6 Torr for 3 min) are required for significant dissociation of water on these surfaces. If defects are not required for water dissociation on rutile (110) as suggested by Lindan et al., one might expect more significant OH coverages on this surface than found in these recent photoemission studies.

3.1.4. TiO_2 (Anatase)

The surface chemistry of anatase- and titania-supported catalysts has recently been reviewed,[121] and only the most important features concerning water adsorption will be summarized here. Widespread attention to this topic arises from the extensive use of TiO_2 as a pigment in paints and as a catalyst support. This interest is further enhanced by the intense current research on anatase for photocatalytic water cleavage and pollution abatement.[122] The interaction of water with the TiO_2 surface is of fundamental importance for all of these applications. Hence it has been closely scrutinized, with most results having been obtained by IR spectroscopy. The main cleavage planes exposed at the surface of anatase are (100) and (101); the latter also prevails in the case of nanocrystalline samples prepared via a hydrothermal sol−gel route.[123] Surprisingly, water is adsorbed on these crystal planes in a molecular fashion, the $\delta(H_2O)$ IR band being located at 1600 cm^{-1}.[124] Very recent first-principles molecular dynamics calculations[125] support this observation, indicating that water adsorption on the anatase (101) surface is nondissociative, with an adsorption energy of 77 kJ/mol.

Heating anatase to 573−673 K in vacuum results in dehydration. A small coverage of surface hydroxyl groups, i.e., about 0.5 surface hydroxyl group/nm^2, is left behind which can be readily identified by their IR absorption bands located at 3715 and 3675 cm^{-1}. Increasing the evacuation temperature results in dehydroxylation accompanied by IR spectral changes. Repetition of the hydroxylation−dehydroxylation cycle leads to decreasing concentration of surface sites for dissociative adsorption of water and hence lower hydroxyl group density, probably due to surface reconstruction.[126] Although the precise nature of the residual hydroxyl groups has not yet been identified, the groups are likely to be associated with Ti(III) ions situated on the edges of surface-exposed (100) planes.[121]

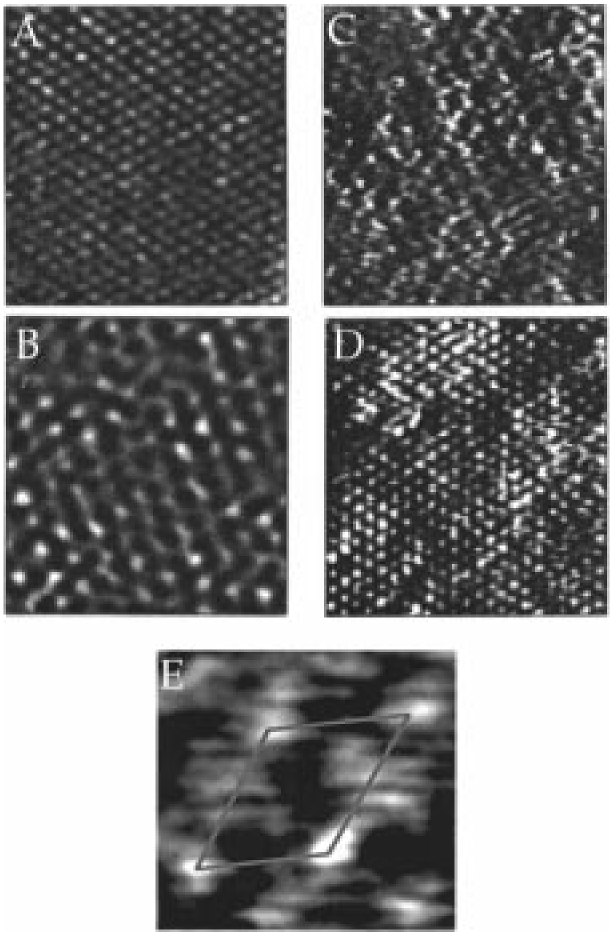

Figure 15. STM images of hematite (0001). Panels A and B were taken at −335.6 mV/1.03 nA and +900 mV/1.53 nA, respectively, and show occupied states (3- × 3-Å periodicity; A) and unoccupied states (5- × 5-Å periodicity, B). Panels C and D confirm a prediction from Becker et al.;[129] they go from imaging one second-layer Fe site with the tip far from the surface (C; +1.15V/4.8 nA) to imaging all Fe sites with the tip close to the surface (D; +1.15 V/19.69 nA, same area as C). An intermediate image (E; +1.15 V/10.1 nA) shows the expected structure of the Fe sublattice on a (0001) plane; 5- × 5-Å unit cell marked [this image is very similar to that of Condon et al.[20] for hematite (0001)].

3.1.5. α-Fe_2O_3

Although the α-Fe_2O_3 (0001) surface has been studied in UHV by STM, little high-resolution work has been done under ambient (air) conditions. Some examples include refs 56, 127, and 128.

Figure 15a shows a 6- × 6-nm STM image of hematite (0001) under negative bias conditions, in which electrons tunnel from the sample surface to the STM tip. The bright sites (corresponding to points of high current) are hexagonally arranged, with a periodicity of 2.9 Å; this is the pattern expected of the oxygen sublattice on the (0001) surface (see Figure 4). One would expect the Fe atoms to be at different altitudes with respect to the surface plane, and thus at first glance it seems unlikely that the Fe atoms could result in an image in which all Fe sites give the same STM current.[56]

Figure 15b shows a commonly observed STM image (6 × 6 nm) of unoccupied states (electrons tunneling from tip to surface). The hexagonal pattern has 5- ×

5-Å periodicity characteristic of the hematite unit cell on this termination and suggestive of imaging of the uppermost Fe atoms (Figure 4), with the caveats discussed below. Initial interpretations of images of the type seen in Figure 15a,b invoked imaging of the oxygen sublattice under occupied-states-imaging conditions and the uppermost Fe sublattice under unoccupied-states-imaging conditions.[20,56]

Becker et al.[129] have made a series of ab initio cluster and slab calculations of electronic structure, STM images, and tunneling spectra for hematite (0001). They conclude that high current should occur over Fe locations in STM imaging of both the hematite valence and conduction bands, although the calculated valence-band images involve oxygen states. Recognizing, however, that hematite is an n-type semiconductor (typically with poor charge carrier mobility;[130] hematite does not conduct if there are insufficient electron donor impurities such as Fe^{2+}),[81] the simplest assumption to make is that electrons being transported to or from the surface through the solid during STM imaging must be moving through the conduction band (which has mostly Fe character[129]). Therefore, a simple interpretation is that the STM tip should accept electrons from or donate electrons to surface Fe sites.

Figure 15c,d is consistent with this assumption. These images were taken under unoccupied-state-imaging conditions. When the tip is relatively far from the surface (Figure 15c), a 5- × 5-Å periodicity is seen. According to Becker *et al.*.,[129] the points of highest tunneling current here are not the uppermost Fe atoms (Figure 4), but the higher of the two Fe locations in the second layer of Fe under the top oxygen layer. Only when the tip is brought closer to the surface (Figure 15d), or the bias voltage is increased, are the uppermost Fe atoms "seen". Intermediate tip–distance images (Figure 15e) reveal the corrugated unit cell expected of the Fe sublattice. The overall implications are the following:

- Only Fe atoms are being imaged in STM of hematite, whether in vacuum or under ambient conditions (this conclusion was also reached for magnetite by Tarrach et al.[75]).
- The structure of the surface is entirely consistent with Figure 4, probably with only minor relaxations (see ref 129).
- The most easily reduced Fe site on the hematite (0001) surface is probably not the uppermost Fe, but Fe in the second layer. This may have implications for the lability of reduced Fe at the surface of hematite (e.g., with regard to reductive dissolution).
- The greater height of the uppermost Fe relative to a scanning STM tip is compensated by the better energetic accessibility of the second-layer Fe, giving misleading STM images under some conditions.

Another aspect of the ambient conditions STM imaging of hematite (0001) is the fact that uppermost Fe, in water or humid air, will be partially hydrated. On the basis of a comparison of the activation energy for electron hopping between Fe sites in the solid (~0.3 eV[131]) to that in aqueous solution (2.6 eV[132]), one might expect that the reorganization inhibition of electron transmission through Fe sites at the surface might be greater for uppermost Fe than for second-layer Fe. This is supported by Tao,[133] who showed that the STM electron current through Fe sites in protoporphyrins in a self-assembled monolayer on graphite can be related to reorganization energy.

In addition to these STM measurements and calculations on the wet α-Fe_2O_3 (0001) surface, the interaction of water vapor with vacuum-cleaned hematite (0001) surfaces has been studied recently by O 1s photoemission spectroscopy.[112,113] Water was found to dissociatively chemisorb on defect sites on this surface at water vapor pressures $< 10^{-4}$ Torr and on terrace sites at $\geq 10^{-4}$ Torr.

3.2. NMR Studies of Amorphous and Polycrystalline Samples under Ambient Conditions

Most UHV studies of adsorption on metal oxides have utilized single-crystal samples. However, a very interesting body of work on high-surface area powder or amorphous samples has been conducted using solid-state NMR spectroscopy, which has the advantage that it can be used on samples in air or in liquid environments.

3.2.1. NMR Methods

The study of chemical structure and dynamics of solid surfaces by nuclear magnetic resonance (NMR)[134,135] has a long history, much of it motivated by the need to understand heterogeneous catalysis and water adsorption. However, because of severe limitations of the NMR techniques available previously, it has been primarily during the last 20 years, with the development of modern solid-state NMR techniques,[134−137] that detailed information has been forthcoming.

The NMR signals of solid surfaces are typically dominated, in the absence of specific line-narrowing techniques, by the same anisotropic spin interactions [magnetic dipole–dipole, chemical shift (shielding), and nuclear electric quadrupole] as govern the NMR of solids in general.[135,136] Much of the recent history of solid-state NMR has been devoted to the development of techniques to eliminate the line-broadening effects of these interactions, while maintaining some aspect (typically via the isotropic averages) of their information content.[135−137]

The most common of these techniques is magic-angle spinning (MAS), which uses coherent rotational averaging to accomplish line narrowing of solid-state NMR signals. Figure 16 represents the line narrowing by MAS of a broad-line NMR pattern described by a second-rank tensor (e.g., the chemical shift anisotropy). Other resolution-enhancing techniques include (1) straightforward "decoupling" (rapid "stirring") of one set of spins (e.g., protons of OH groups) to average to zero their dipolar effects on a set of spins being observed (e.g., ^{29}Si or ^{27}Al in their respective oxides);[134−137] (2) multiple pulse decoupling,[138,139] e.g., in CRAMPS (combined rotation and multiple pulse spectroscopy),[137,140,141] of proton–proton dipolar interactions; (3) multiangle sample spinning [e.g., double rotation (DOR; simultaneous

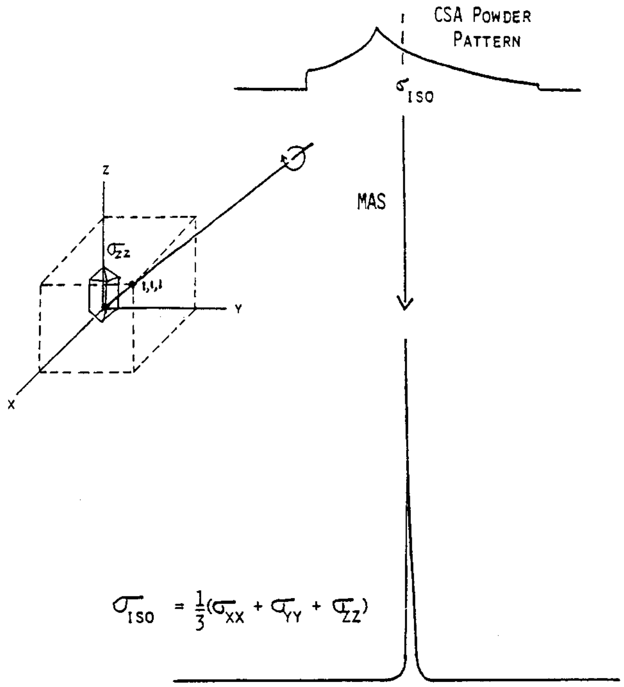

Figure 16. Line narrowing by magic-angle spinning (MAS). Left: a crystal-fixed coordinate system with the z axis parallel to the static magnetic field $\mathbf{B_0}$ at some instant (yielding an instantaneous chemical shift s_{zz}), showing a line drawn between the origin (0,0,0) and the 1,1,1 point as the axis for sample spinning. Top: the chemical shift anisotropy (CSA) pattern obtained for a powder, showing values of the chemical shift tensor for specific orientations (corresponding to the "principal values" of the tensor). Bottom: the narrowed peak obtained by MAS, at the isotropic average, s_{iso}.

sample rotation about two axes[142,143]) or dynamic angle spinning (DAS; sequential sample spinning about two axes[144,145]) for averaging the second-order quadrupolar effect in ^{27}Al NMR]; (4) a variety of two-dimensional techniques [e.g., heteronuclear correlation (HetCor) spectroscopy[146] for correlating a metal nuclide with nearby protons]; and (5) multiple quantum techniques (another way to simplify the spectra of quadrupolar nuclei[147,148] and a strategy for estimating the number of protons in a "cluster"[149,150]). Of course, all of these approaches have been limited largely to diamagnetic solids. The role of paramagnetic centers in solid-state NMR has not yet been broadly characterized, and ferromagnetic centers are assumed to be incompatible with conventional NMR techniques. The application of magnetic field gradients to measure diffusion, while a well-established approach,[151−153] has apparently not yet been applied to the study of metal oxide surfaces or interfaces, although among its many uses is an application to the study of water diffusion in a clay system.[154]

A priori, NMR would seem to be well-suited to study chemical structure and/or dynamics of interfaces between metal oxides and aqueous solutions, since in principle NMR spectra can be obtained on nuclei in both the liquid and solid phases, as well as in the interface region (although each "phase" may require a different NMR technique). Peak positions (resonance frequencies) typically reflect chemical structure (e.g., via the chemical shift), whereas line shapes and relaxation phenomena typically provide information on dynamics, spanning time constants ranging from perhaps 10^{-9} to 10 s. A variety of modern NMR techniques, based on the magnetic dipole−dipole interaction, can be used to extract internuclear distances (usually for isotopically labeled samples) in rigid or largely rigid systems.[155−159] Most NMR techniques can be implemented over a wide temperature range, which is useful for adjusting structural mobility, measuring activation energies, and manipulating the rates of chemical exchange.

The most serious limitation of NMR is its poor sensitivity. At the current or projected state of the art, NMR will typically not be capable of observing the small concentrations of solutes or defects that are often of interest on metal oxide surfaces or at metal oxide−aqueous solution interfaces. Hence, in the studies of these kinds of systems, NMR will be used in "modeling" chemical issues of interest at much higher levels of concentration, having typically about 10^{17}−10^{20} observation nuclei, depending on various details of the NMR experiment, including the magnetic field strength employed ($\mathbf{B}_0$), the nuclear magnetic moment (or magnetogyric ratio) of the nuclide to be observed, and the relevant relaxation behavior and line widths. Another important characteristic of NMR, which in some instances will be judged to be a limitation, is its inability to provide "snapshots" of the system on a short time frame. Thus, in a system undergoing rapid chemical exchange among different sites, NMR yields a weighted average spectrum. Hence, at room temperature one often does not expect to distinguish separate proton signals corresponding to different hydroxyl or water sites, because one expects that rapid proton exchange may be occurring. Similarly, a metal ion that rapidly shuttles among different structural arrangements at the interface will also yield a weighted average NMR signal (see below). While the ability of NMR to provide distinct signals in a specific dynamical system depends on relevant details, as a guideline we should not expect separate NMR peaks in a system for which the lifetimes of specific species are less than about 1 ms.

A variety of nuclides are available for study of metal oxide surfaces and interfaces. These include ^{1}H (I = 1/2, natural abundance = 99.9%), ^{2}H (I = 1, natural abundance = 0.015%), and ^{17}O (I = 5/2, natural abundance = 0.037%), which are relevant for characterizing the hydroxyl groups (in the latter case, O^{2-}, $-O^{-}$, or −O− moieties) that are commonly present on metal oxide surfaces, as well as dozens of nuclides of metallic elements. Some of the metal nuclides (e.g., ^{29}Si, ^{57}Fe, ^{89}Y, ^{103}Rh, ^{109}Ag, ^{113}Cd, ^{119}Sn, and ^{195}Pt) are spin 1/2 cases and hence have no nuclear electric quadrupole effects; others have $I >$ 1/2 (e.g., ^{11}B, ^{25}Mg, ^{27}Al, ^{47}Ti, ^{51}V, ^{55}Mn, ^{59}Co, and ^{67}Zn), and their NMR characteristics are often dominated by quadrupole effects. By far the largest numbers of NMR studies with metal nuclei have been based on ^{29}Si or ^{27}Al, partly because of convenience and partly driven by specific scientific and technical interests in silicas and aluminas, especially in catalysis and ceramics. In many cases, certain metal nuclides have been neglected in terms of NMR largely because of a lack of interest or commitment, rather than any fundamental NMR-based limitations. In general, one can expect that a serious motivation and commitment could yield useful NMR results with many, if not most, of the nuclides mentioned above, in some cases (e.g., ^{17}O) requiring isotopic enrichment. Surface studies by NMR are, for sensitivity reasons, typically limited to samples with rather large surface areas, say, >10 m^2/g, although some promising methods of spin polarization enhancement may be on the horizon to alleviate this restriction.

3.2.2. Cross-Polarization NMR as a Surface-Selective Technique

As with any experimental method for detecting metal atom (ion) centers in metal oxide systems, an NMR technique that does not provide a major detection advantage to nuclei at the surface, relative to nuclei in the interiors of particles, will generate signals that are dominated by resonances due to the latter. This situation can be avoided if a surface-selective mechanism is used for generating polarization in the spins to be observed. Most of the hydrogen atoms present in a metal oxide sample are on the surface (as either covalently bonded hydroxyls or as adsorbed water); hence, M spin polarization (e.g., M $= {}^{29}Si$, ^{27}Al, or ^{89}Y) can be generated by polarization transfer from protons via cross-polarization (CP),[136] which is a double-resonance technique in which spin polarization is transferred between two spin sets that are coupled together via (a static component of) magnetic dipole−dipole interactions. In the case of $^1H \rightarrow M$ CP, which is based on $^1H{-}M$ dipolar interactions (which fall off as the third power of $^1H{-}M$ internuclear distance), this approach discriminates dramatically in favor of M nuclei at or very near the surface.

3.2.3. NMR Applied to Metal Oxide Surfaces

NMR techniques that are designed explicitly for solid samples have proved useful for the characterization of metal oxides. To date, they have been applied primarily to aluminas and silicas, with substantially less attention directed to SnO_2, CdO, and a few others. Since hydrogen in such samples is usually limited to the surface region, it has often been possible to select strategies (e.g., cross-polarization) that focus on the surface. Often it is the nature and distribution of surface hydroxyl groups that are of primary interest, and combinations of NMR studies with metal nuclides (e.g., ^{27}Al), ^{17}O, and ^1H have proved useful in this regard.

A substantial body of work has been reported on the use of both low-resolution and high-resolution ^1H NMR techniques for characterizing the state(s) of water adsorbed on metal oxides (mainly SiO_2);[160−180] there have also been some reports on the use of NMR to study the adsorption of metal ions (primarily alkali metal ions)[181−190] on metal oxide surfaces. Little of this work, however, has focused on metal oxide−aqueous solution interfaces. Much of the metal ion−substrate work that has been reported has focused on zeolites or clays, at least partly because of the large surface areas and technological importance of those adsorbents.

The behaviors of organic adsorbates on alumina have been observed via ^{13}C and ^2H NMR; this work has included characterizing adsorbed surfactants[191] and chemical transformations (e.g., aldol-type condensations) of adsorbed acetone[192] by ^{13}C NMR and the study of motion of adsorbed organic species by ^2H NMR line shapes.[193] For the reasons indicated above, especially the relationship to catalysis, much more of this kind of work has been directed at species adsorbed on zeolites.[194−197] ^{13}C NMR studies of acetone adsorbed on silica provide convincing evidence for the formation of a hydrogen-bonded complex between silanol groups of the silica surface and the carbonyl group (oxygen site) of acetone, yielding values of the relevant equilibrium constants and activation energies.[198−202]

Amorphous forms of silica provide good examples (and the most well-developed case) of how NMR can or could be used to characterize important details of metal oxide surfaces. The use of $^1H \rightarrow {}^{29}Si$ CP−MAS techniques has made possible a wide range of studies of silica systems, including the changes that occur in $Q_2/Q_3/Q_4$ surface site distributions (where Q_2 refers to SiO_4 tetrahedra bonded to two other SiO_4 tetrahedra through oxo bridges and to two OH groups, Q_3 refers to SiO_4 tetrahedra bonded to three other SiO_4 tetrahedra and one OH group, etc.) that accompany dehydration/rehydration[203,204] or derivatization via silylation,[203,204] i.e., reactions of the type:

$$\mathit{Si}{-}O{-}H + X{-}Si(R)\!< \;\rightarrow\; \mathit{Si}{-}O{-}Si(R)\!< + HX \quad (8)$$

where Si represents a silicon atom of the surface framework.

Figure 17 shows the application of surface-selective $^1H \rightarrow {}^{29}Si$ CP experiments for amorphous silica, as well as for ^{113}Cd (CdO) and ^{27}Al (alumina). In the silica case, one can see three partially overlapping peaks, due to $(\equiv SiO)_2\mathit{Si}(OH)_2$ (Q_2) sites at about −89 ppm (relative to a liquid tetramethylsilane peak), $(\equiv SiO)_3\mathit{Si}OH$ (Q_3) sites at −100 ppm, and $\mathit{Si}(OSi\equiv)_4$ (Q_4) sites at −110 ppm. This spectrum also shows the dramatic difference between the narrow peak due to crystalline silica (quartz form) and the broad peaks due to amorphous forms of silica (silica gel and fumed silicas), caused by distributions of bond angles and/or lengths in the amorphous materials. One also sees the dominance of the Q_4 peak observed in ^{29}Si MAS spectra of silicas obtained *without* cross-polarization. For CdO, the comparison between ^{113}Cd MAS spectra obtained with and without cross-polarization shows that CP generates only the sharp peak due to surface sites, whereas intensity in the spectrum obtained without CP is dominated by a broad signal due to Cd sites in the interior of the CdO particles (the width due to a distribution of Knight shifts associated with varying degrees of semiconductor behavior among the various particles).[205] The $^1H \rightarrow {}^{27}Al$ CP−MAS spectra for alumina in Figure 17 show discrimination against tetrahedral Al sites (∼60 ppm) by the CP process, relative to the octahedral Al sites (∼0 ppm), which are much more dominant in the spectrum obtained with $^1H \rightarrow {}^{27}Al$ CP.[137] Analogous results (CP vs non-CP comparisons) have been shown in ^{17}O NMR spectra of silica.[206] Such $^1H \rightarrow M$ cross-

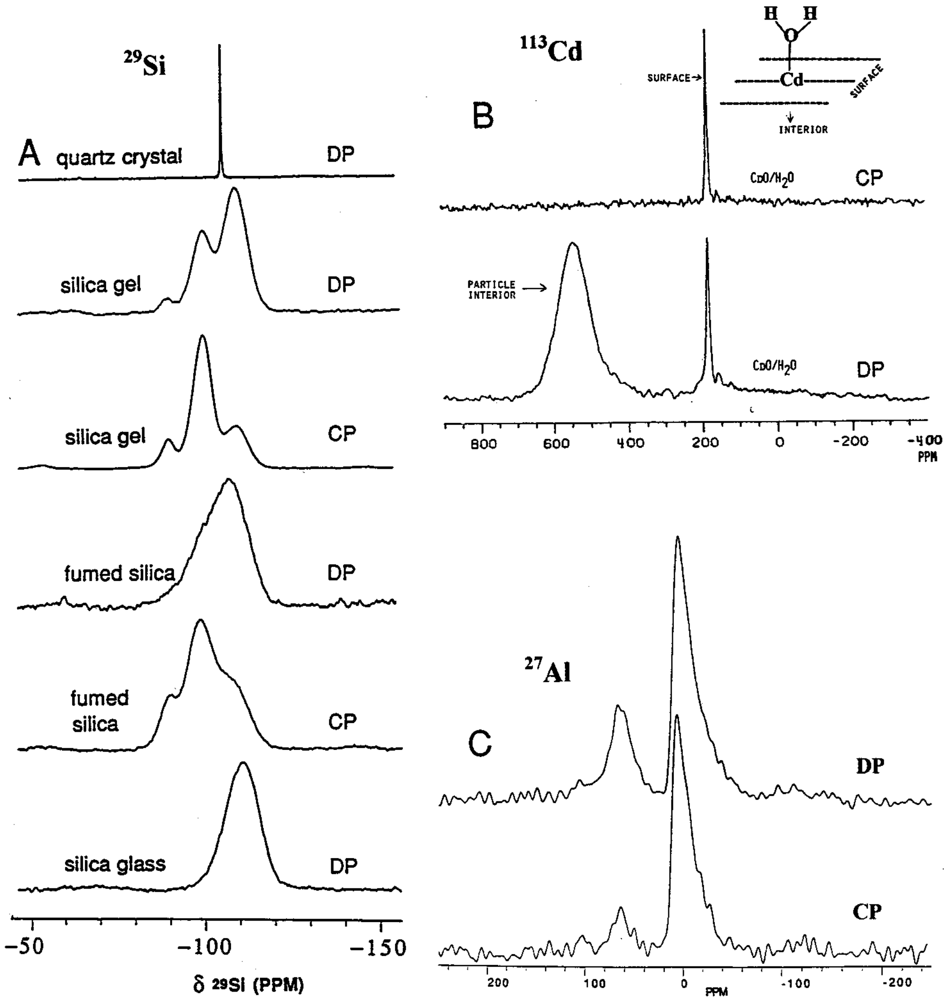

Figure 17. Magic-angle spinning (MAS) NMR spectra obtained with (CP) and without (DP) cross-polarization. (A) ^{29}Si MAS spectra of silica, obtained with and without ^{1}H → ^{29}Si CP. (B) ^{113}Cd MAS spectra of CdO, obtained with and without ^{1}H → ^{113}Cd CP. (C) ^{27}Al MAS spectra of γ-Al_2O_3, obtained with and without ^{1}H → ^{27}Al CP.

polarization studies could most likely be used for surface-selective measurements in a wide variety of metal oxides.

While ^{29}Si MAS NMR experiments are capable of elucidating the concentrations of Q_2, Q_3, and Q_4 sites on silica surfaces, ^{1}H MAS NMR, with or without multiple pulse line narrowing, is not directly able to make the distinction between Q_2 and Q_3 silanols but is capable of distinguishing between hydrogen-bonded and non-hydrogen-bonded ("isolated") hydroxyl groups on the silica surface.[207] Compelling evidence for this distinction in ^{1}H MAS NMR can be based on the rate at which transverse proton magnetization is *dephased* under the influence of ^{1}H$-$^{1}H dipolar interactions. Since the hydrogen−hydrogen distance within a hydrogen-bonded pair of hydroxyls is smaller than between a pair of isolated hydroxyls, this dephasing is much faster for the hydrogen-bonded case. The ^{1}H CRAMPS spectrum of silica gel given in Figure 18 shows the following three main contributions: a sharp peak at about 1.7 ppm due to isolated silanols (which remains even after evacuation at 773 K), a well-defined peak at about 3.5 ppm (which is easily removed by evacuation at moderate temperatures) due to physisorbed water, and a broad underlying peak with its maximum at about 3.0 ppm (removed by evacuation at 773 K) due to a distribution of hydrogen-bonded hydroxyl groups. ^{1}H CRAMPS studies of silicas as a function of water content have provided valuable information on the state of water in these systems.[204,207−210]

^{29}Si and ^{1}H NMR data of the type represented in Figures 18 and 17 are much more valuable when they can be correlated, i.e., when the fraction of each type of silanol (Q_2 or Q_3, as determined by ^{29}Si NMR) that is hydrogen-bonded (as determined by ^{1}H NMR) can be elucidated. While the most direct strategy for making such correlations by NMR would seem to be two-dimensional HETCOR spectroscopy, to date more definitive results have been obtained by systematically manipulating the ^{1}H spins (e.g., allowing them to dephase) in an appropriate segment of a ^{29}Si CP−MAS experiment. Figure 19 shows ^{29}Si CP−MAS spectra obtained on silica gel in experiments in which a variable ^{1}H$-$^{1}H dephasing period was inserted prior to the cross-polarization transfer of ^{1}H spin polarization to ^{29}Si.[207] These spectra, and analogous results obtained by a variety of related techniques, show that the Q_2 silanols are more extensively hydrogen-bonded than the Q_3 silanols in the sample represented in Figure 19. From results of this type in samples prepared with various water contents, it has been possible to develop a model of the silica gel (and probably fumed silica) surface in terms of

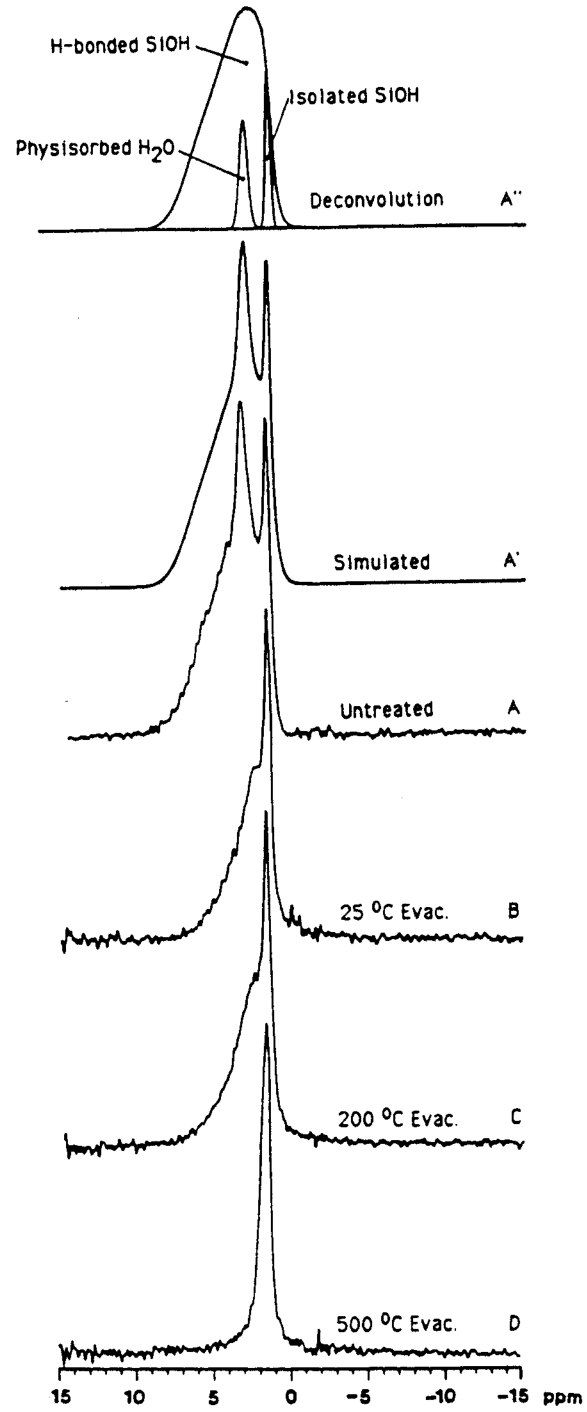

Figure 18. ^{1}H CRAMPS spectra, obtained by combined MAS and multiple-pulse line narrowing, of silica gel at various levels of water content. Top: deconvolution of the spectrum of untreated silica gel.[207-210]

surface segments that resemble specific surface faces of β-cristobalite.[211] This model is represented in Figure 20.

Although less extensive than the analogous studies on silica samples, there is significant literature on the application of solid-state NMR techniques to the characterization of alumina surfaces.[178-180,213-215] As discussed above, these studies have included the use of $^{1}H \rightarrow {}^{27}Al$ cross-polarization.[137,213,215] While easily distinguishing between tetrahedral and octahedral aluminum sites [with ^{27}Al chemical shifts of about 55–60 and about 0–6 ppm, respectively, relative to the resonance of $Al^{3+}(aq)$], ^{27}Al NMR is not quite as straightforward as ^{29}Si NMR because of the line broadening associated with the nuclear electric quadrupole effects of the ^{27}Al nucleus. These effects not only influence the detection of ^{27}Al resonances (with or without $^{1}H \rightarrow {}^{27}Al$ CP) but also broaden the resonances of ^{1}H NMR signals of nearby protons (by interfering with the MAS averaging of $^{1}H-{}^{27}Al$ magnetic dipolar effects). Nuclear electric quadrupole effects also complicate the use of ^{17}O NMR for the characterization of metal oxides, although such studies are still feasible. For example, Oldfield et al.[206,216] have employed ^{17}O NMR, with and without $^{1}H \rightarrow {}^{17}O$ CP or MAS, to study surface sites of ^{17}O-enriched silicas and aluminas. The ^{17}O NMR spectrum of

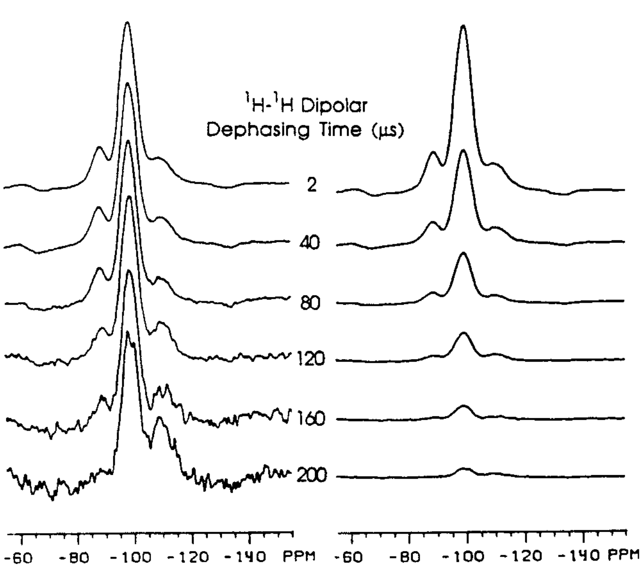

Figure 19. ^{29}Si MAS spectra, based on $^{1}H \rightarrow {}^{29}Si$ CP, of silica gel, obtained using various periods of $^{1}H-{}^{1}H$ dipolar dephasing prior to cross-polarization. Right: absolute intensities. Left: intensities arbitrarily scaled to the same maximum peak height.[207]

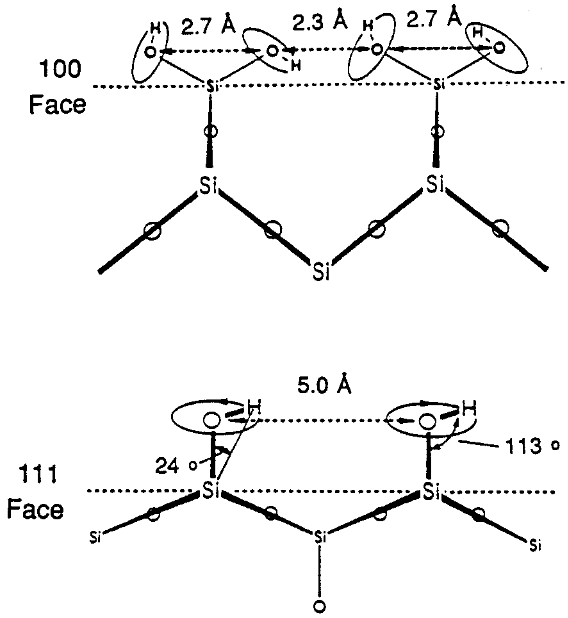

Figure 20. Side views of the (100) and (111) surface faces of β-cristobalite, showing surface hydroxyl arrangements.[211,212]

boehmite, AlO(OH), displays two peaks, assigned to OAl_4 and Al_2OH sites, with $^{1}H \rightarrow {}^{17}O$ CP selectively enhancing the weak Al_2OH peak.

Fitzgerald et al.[180] have carried out an extensive ^{1}H and ^{27}Al NMR study of the dehydration of a high-surface area alumina, covering a temperature range of 383–1373 K; samples were heated both in air and under vacuum. Three ^{1}H NMR peaks could be distinguished by CRAMPS techniques: a broad peak centered at about 4.0 ± 0.2 ppm attributed to the protons of physisorbed water and two peaks, at about 8.2 ± 0.3 and 3.0 ± 0.2 ppm, attributed to protons of structural AlOH groups. Dipolar dephasing experiments, in which the magnetization due to protons that are strongly coupled to other protons by magnetic dipole–dipole interactions (and, hence, probably involved in strong hydrogen bonding) is selectively attenuated by a dephasing period prior to detection, aided the assignment of the 8.2 ppm peak to "clustered" Al_2OH moieties and the 3.0 ppm peak to terminal, "isolated" AlOH groups. ^{1}H CRAMPS results show that, in experiments in which the alumina is heated to successively higher temperatures, the desorption of physisorbed water occurs over the 383–573 K temperature range, and condensation/dehydroxylation of aluminum-bound hydroxyl groups begins at about 623 K for the Al_2OH groups and at about 823 K for the "isolated" AlOH groups. ^{27}Al NMR results indicate that these dehydrations convert Al_2OH and AlOH moieties into distorted, hydrogen-bearing four-, five-, and six-coordinate aluminum centers.

Coster et al.[215] have reported a $^{1}H \rightarrow {}^{27}Al$ CP–MAS study of acidic sites on aluminas. They employed ammonia as a probe of acid sites at the surface, observing ^{27}Al NMR peaks corresponding to two types of Lewis acid sites, a four-coordinate site and a five-coordinate site. Analogous studies by Morris and Ellis[213] employed pyridine as the basic probe. These studies are specific examples of a fruitful class of NMR-based strategies for examining acidic sites on surfaces, including those of metal oxides, by examining the effects of adsorbed basic probe molecules. In many cases, the nucleus that is observed is part of the probe molecule; examples include ^{15}N (isotopically enriched) in amines such as pyridine and *n*-butylamine (both applied to aluminas),[178,179,217,218] and ^{31}P in phosphines and phosphine oxides. Figure 21 shows an example of results from a study in which trimethylphosphine, Me_3P, was used as a probe of surface sites on alumina.[219] The CP–MAS ^{31}P spectra (for samples with two different loading levels, as indicated) are seen to reveal the presence of complexes with Brønsted acid sites (−4 ppm) and Lewis acid sites (−48 ppm), as well as physisorbed trimethylphosphine (−58 ppm). With the short CP contact period employed in obtaining these CP–MAS spectra, these experiments discriminate strongly against the more mobile physisorbed species relative to the more tightly bound acid–base complexes. The intensity of the physisorbed Me_3P peak is larger if a longer CP contact period is used (not shown), but even then it does not achieve the relative intensity seen in the corresponding spectrum obtained via the direct polarization (DP–MAS) mode, which favors the less rigid species.

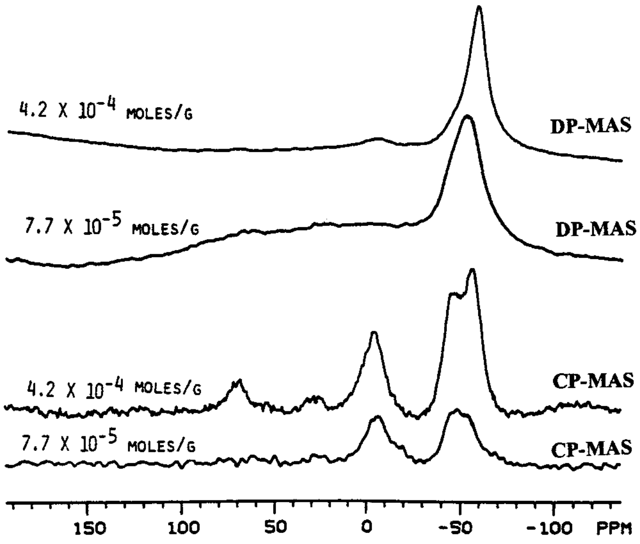

Figure 21. ^{31}P MAS NMR spectra of trimethylphosphine (Me_3P) adsorbed on γ-Al_2O_3 at two loading levels (as indicated), obtained by cross-polarization (CP–MAS) and by direct polarization (DP–MAS, with no cross-polarization) (adapted from ref 219).

4. Aqueous Solution–Metal Oxide Interfaces

This section examines chemical interactions that occur at metal oxide surfaces in aqueous environments, including the structure and chemical properties of the metal oxide surface. The properties of ions in bulk solution are considered before discussing experiments on adsorption and reaction at oxide–solute interfaces. Complexation in aqueous solution provides illustrative models of the types of aqueous species that will sorb at the metal oxide–water interface.

4.1. Metal Ions in Aqueous Solutions

The chemical behavior of any element in aqueous solution depends on the nature of the individual solution components [i.e., metal concentration, ligand concentration, pH, Eh (the reduction–oxidation potential relative to the standard hydrogen electrode), ionic strength, etc.]. To understand the factors that control the concentrations of metal ions in aqueous solution, their chemical reactivity and affinity for various ligands must be known. The identity of the chemical species in solution (*speciation*) is extremely important for understanding the ability of aqueous metal ions to adsorb to a metal oxide surface. The adsorption of cations or anions may be quite different when they occur as complexed rather than uncomplexed ions. For example, cationic uranium(VI) hydroxo complexes interact strongly with metal oxides or oxyhydroxides, whereas anionic U(VI) carbonato complexes interact only weakly with these same solids.[220] The adsorption behavior of U(VI), as with any metal ion, depends on its aqueous speciation, which is a function of pH, redox conditions, and ligands that form U(VI) complexes, because different metal complexes will have intrinsically different tendencies to interact with metal oxide surfaces.

The influence of chemical equilibrium and/or kinetics on the progress of chemical reactions often determines the abundance and distribution of chemical species in aqueous solution.[221,222] The tendency to form metal oxide−surface complexes is correlated with the tendency of metal ions to form inner-sphere coordination complexes in aqueous solution. Kinetics is important for determining whether a reaction is sufficiently fast and reversible that it can be considered as chemical equilibrium controlled. Equilibrium processes occur widely in aqueous systems, and the measurement of their equilibrium constants is an important step in describing and understanding the behavior of metal ions in aqueous solution.[222,223]

Bare metal ions do not exist in aqueous solution; the metal ions are always hydrated or coordinated by water molecules to form aquo ions, hydrolyzed (partially or completely) or coordinated by hydroxyl ions (see section 4.1.1.2) or coordinated by oxo ions. For example, large univalent metal ions [e.g., Na(I) and Rb(I)] are typically coordinated by water molecules; divalent, trivalent, and tetravalent metal ions [e.g., Mg(II), Al(III), and Si(IV)] are hydrolyzed to different extents, depending on pH; and small, highly charged metal ions [e.g., Cr(VI) and Mn(VI)] generally occur in aqueous solutions as oxoanions at moderate to high pH due to the repulsion of protons in the first coordination sphere by the cation.[224,225]

4.1.1. Complexation

4.1.1.1. Thermodynamics of Complex Formation in Aqueous Solution. Metal ions will form coordination compounds as a result of Lewis acid−base reactions, in which the metal ion is the acid (acceptor) and the ligand is the base (donor). The formation and dissociation of complex compounds often involve successive equilibria. The complexation strength is a measure of how effectively a ligand can compete with water in the coordination sphere of a metal ion. Equilibria involving ionic species are affected by the presence of all ions in solution, which together make up the ionic strength. Thermodynamic data are generally referenced to a standard state: for solution measurements, the standard state of 298 K and zero ionic strength is generally used. Detailed discussions of the measurement of thermodynamic formation constants and their extrapolation to different ionic strengths have been published by Connors,[223] Martell and Motekaitis,[226] Ciavatta,[227] and Grenthe.[228]

4.1.1.2. Hydrolysis of Metal Ions. The acidity of water molecules coordinated to a metal ion is much larger than that of uncomplexed water and generally increases with decreasing radius and increasing charge of the central metal ion. In aqueous solution, the loss of a proton from an aquo metal complex to form hydroxo complexes is particularly important; it has been discussed in detail by Baes and Mesmer.[224] For simple metal ions, the determination of hydrolysis constants is of fundamental importance, since the ions' behavior in various reactions as a function of pH is governed by the value of the hydrolysis constant. As the pH of a solution is varied, hydrolysis can proceed in a stepwise manner to form neutral, or even anionic, species. For example, the hydrolysis of Fe(III) can proceed from $Fe(OH_2)_6^{3+}$ through an entire series of ions of formulas $Fe(OH)(OH_2)_5^{2+}$, $Fe(OH)_2(OH_2)_4^{+}$, $Fe(OH)_3(OH_2)_3$, and even $Fe(OH)_4(OH_2)_2^{-}$. An additional complexity in hydrolyzed ions is their tendency to oligomerize to form polymeric ions, such as $(OH_2)_5Fe(\mu\text{-}OH)_2Fe(OH_2)_5^{4+}$, which can be considered as the dimer of $Fe(OH)(OH_2)_5^{2+}$.

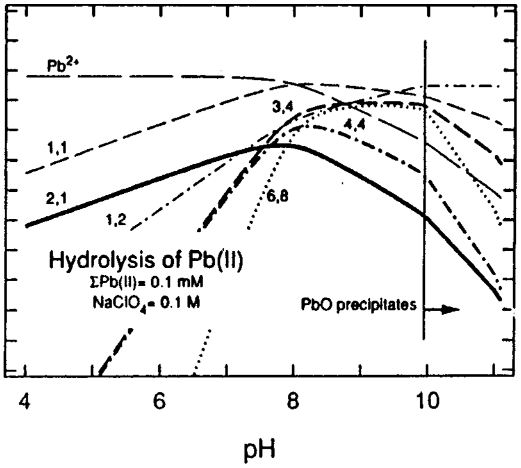

Figure 22. Predominance diagram (log molar concentration of Pb species vs pH) for Pb(II) for a total Pb(II) concentration of 0.1 mM and a background electrolyte ($NaClO_4$) concentration of 0.1 M.

Polymeric hydrolysis species are known for most metal cations, and the tendency to oligomerize is highly dependent on metal ion concentrations. During the sequence of successive hydrolysis steps, the overall charge of the metal complex is correspondingly reduced, and the resulting ions are very different in terms of chemical properties such as solubility, complexation, adsorption, etc. The study of the hydrolysis of highly charged ions poses perhaps one of the most formidable challenges to the solution chemist, due to the multiplicity of species that may form simultaneously and which are also a function of the other ions present in the solution. The distribution of metal ion species under a variety of conditions can be predicted if the hydrolysis constants and solubility product of the solubility-controlling phase are known.

An example that illustrates these various degrees of complexity is provided by aqueous Pb(II). At a total metal ion concentration of 0.1 mM, a background electrolyte concentration of 0.1 M $NaClO_4$, and pH values of 4 to ≈8, the predominant Pb(II) species is the aquo complex (Figure 22). Present at lower concentrations are $Pb(OH)(OH_2)_x^{+}$, $Pb(OH)_2(OH_2)_x^{0}$, $Pb_2(OH)(OH_2)_x^{3+}$, $Pb_3(OH)_4(OH_2)_x^{2+}$, $Pb_4(OH)_4(OH_2)_x^{4+}$, and $Pb_6(OH)_8(OH_2)_x^{4+}$ species, where x has a different value for each species listed. At pH values from 8 to ≈9.5, the $Pb(OH)(OH_2)_x^{+}$ species is dominant, and at pH from ≈9.5 to 10, the $Pb(OH)_2(OH_2)_x^{0}$ complex is dominant. At pH > 10 under these conditions, where one would predict $Pb(OH)_3^{-}$ to form, PbO precipitates. This example illustrates the importance of understanding the predominance of different aqueous metal ion species when considering the possible types of adsorption complexes that might bind to a metal oxide surface in contact with an aqueous solution. Species predominance diagrams such as that shown in Figure 22 can be calculated for specific solution conditions using a number of available computer codes such as EQ3/6,[17] or SPE.[226] However, care should be taken to ensure that the results of such calculations are consistent with the principles of coordination chemistry and that the thermodynamic database is self-consistent, up-to-date, and appropriate for the given solution conditions (i.e., T and ionic strength) (see section 4.1.2).

4.1.1.3. Redox Considerations. Many metal ions can undergo electron-transfer, or redox, reactions in aqueous solution. The solubility, thermodynamic stability, and kinetic lability of a metal ion can be dramatically altered through changes in oxidation state; this must be considered when studying metal ions in aqueous solution. For example, Cr(VI) occurs predominantly as the oxoanion CrO_4^{2-} in aqueous solutions at pH > 6 and as $HCrO_4^-$ below pH 6 and is highly soluble and relative toxic, whereas Cr(III) occurs predominantly as the species $Cr(OH)_2(OH_2)_4^+$, $Cr(OH)_3(OH_2)_3^0$, and $Cr(OH)_4(OH_2)_2^-$ at pH > 6, is relatively insoluble, and has low toxicity.

The stability field of water in terms of Eh and pH bounds the redox reactions that can take place in aqueous solution under most environmental conditions. The values of Eh in aqueous systems generally range from −0.8 to +1.2V.[221,222] It is often convenient to construct a stability field diagram to represent which species will predominate under any given condition of pH and Eh, and Eh−pH diagrams for many common metal ions are readily available in the literature.[221,222]

4.1.1.4. Kinetics of Ligand Exchange in Aqueous Solution. From a consideration of equilibrium constants, one can only decide whether a complex is thermodynamically stable or unstable. These thermodynamic considerations contain no information about the *rate* at which chemical equilibrium is attained. From a kinetic perspective, complexes can be either *labile* or *inert*; these distinctions are generally governed by the electronic structure of the central metal ion. Reaction rates between a metal ion and its ligands are often related to the rate at which a water molecule enters or leaves the coordination sphere of the central metal ion. For many metal ions, this rate is often fast and under diffusion control of 10^9−10^{10} s^{-1}, such as seen in $Na(OH_2)_6^+$. Hence Na^+(aq) is considered substitutionally labile. For most metal cations, for which there are few stereochemical or electronic effects due to metal−ligand bonding, these rates tend to decrease with increasing size of the ion and can be on the order of 10^7 s^{-1} for $Ca(OH_2)_6^{2+}$ or $La(OH_2)_9^{3+}$ ions. For transition metals, however, the rates can span up to 15 orders of magnitude; this dramatic spread in rates is related to the ion's electronic structure, especially its d^n electron configuration. For example, high-spin $Mn(OH_2)_6^{2+}$ has a ground-state electronic configuration t_{2g}^3 e_g^2 in an octahedral ligand field. With two d electrons in the metal−ligand antibonding e_g orbitals, metal−ligand σ-bonding is rather weak, water-exchange rates are fast at $k_{ex} = 10^7$ s^{-1}, and Mn(II) is considered substitutionally labile. By contrast, $Cr(OH_2)_6^{3+}$ has a t_{2g}^3 ground-state electronic configuration and, with no metal−ligand σ-antibonding orbitals occupied, Cr(III) is substitutionally inert, with $k_{ex} = 10^{-6}$ s^{-1}. The kinetics of ligand-exchange reactions for metal ions in aqueous solution has been discussed extensively.[229−231]

For polymeric or oligomeric ions, it has been found that the rates of ligand exchange can vary markedly, depending on whether the ligand is terminal or bridging. For example, μ_3-oxo groups (where μ_3 indicates that the ligand bridges three metal atoms) are less reactive than μ_2-oxo groups; μ_3-OH groups are less reactive than μ_2-OH groups; and terminal water ligands are the most reactive. These differences are profound: Richens et al.[232] found no evidence for exchange of the μ_2- or μ_3-oxo bridges in the $Mo_3(\mu_3\text{-}O)(\mu_2\text{-}O)_3(OH_2)_9^{4+}$(aq) complex shown below over a 2-year period. In contrast, the terminal water ligands exchange readily, yet the rates of exchange of the water molecules cis or trans to the μ-oxo bridges differ by a factor of 10^5!

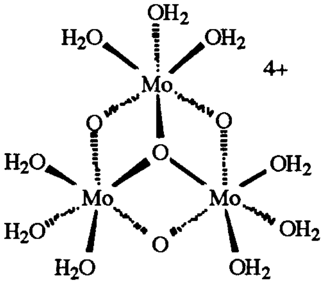

Substitution of a stable ligand into an oligomeric coordination complex can enhance or retard the depolymerization rates. The simplest such ligand-directed labilization is deprotonation of a terminal water to form a coordinated hydroxyl group. Such deprotonation proceeds to equilibrium, and the rates of a wide range of hydrolytic reactions (Table 2) increase with the number of stable hydroxyls in the oligomer.[233] Rates of dimerization of Cr(III), for example, increase by a factor of 60 for each extra hydroxyl group that is involved in the reaction. The rates of condensation of Fe(III) complexes into dimers increase by a factor of 10^{10} as the hydration water molecules deprotonate! Similar enhanced labilities are observed in metal chelates,[234] where the rates of oxygen exchange in a metal−(hydr)oxo complex increase dramatically, sometimes by orders of magnitude, with increased coordination of amino or carboxylate groups to the metal. The effects of these substitutions are also observed in metal−ligand complexes of geochemical importance. Substitution of one and two fluoride ligands for water ligands in $Al(H_2O)_6^{3+}$(aq) causes rates of exchange of the remaining water molecules to increase by factors of 10^2 and 10^4, respectively.[235]

In summary, the depolymerizations of metal oxo and hydroxo oligomers have acid-enhanced, base-enhanced, and pH-independent pathways for bridge cleavage, although in some metal dimers [e.g., Co(III)] the pH-dependent pathways are not apparent. The acid-enhanced path arises from attachment of a proton to a bridging hydroxide, converting it to a poorly bridging water molecule. These protonation and deprotonation reactions proceed to equilibrium

Table 2. Variation in the Rates of Hydrolytic Processes with the OH/Cr(III) Ratios in Monomers and Oligomers at 298 K and $I = 1.0$ M[a]

reactant	OH/Cr(III)	$10^5 \times$ rate (s^{-1})	comments
1. Exchange of Water from Inner Coordination Sphere to Bulk			
$Cr(OH_2)_6^{3+}$	0	0.24	fully hydrated monomer
$Cr(OH)^{2+}$	1.0	18	hydrolyzed monomer
$[Cr(\mu\text{-}OH)_2Cr]^{4+}$			
trans to μ-OH	1	36	doubly bridged dimer, fully hydrated
cis to μ-OH	1	6.6	doubly bridged dimer, fully hydrated
$[Cr(\mu\text{-}OH)_2CrOH]^{3+}$			
trans to μ-OH	1.5	1260	doubly bridged dimer, hydrolyzed
cis to μ-OH	1.5	490	doubly bridged dimer, hydrolyzed
2. Intramolecular Bridge Formation			
$[Cr(\mu\text{-}OH)Cr]^{5+} + H_2O$			
$^{-}$DBD + H^+	0.5	10	SBD^{-}DBD; fully hydrated reactant
$[Cr(\mu\text{-}OH)CrOH]^{4+} + H_2O$			
$^{-}$DBD + H^+	1.0	40	SBD^{-}DBD; singly hydrolyzed
$[HOCr(\mu\text{-}OH)CrOH]^{3+} + H_2O$			
$^{-}$DBD-H	1.5	1140	SBD^{-}DBD, doubly hydrolyzed $[Cr_4(OH)_6]^{6+-}$
closed tetramer	1.5	8700	
$[Cr_4(OH)_7]^{5+-}$			
closed tetramer	1.75	24000	
3. Sulfate Anation			
$Cr(OH_2)_6^{3+}$	0	1.1	hydrated monomer
$Cr(OH)^{2+}$	1.0	61	hydrolyzed monomer
$[Cr(\mu\text{-}OH)_2Cr]^{4+}$	1	35	hydrated DBD
$[Cr(\mu\text{-}OH)_2CrOH]^{3+}$	1.5	1700	hydrolyzed DBD

[a] From ref 233. The abbreviations SBD and DBD correspond to a singly bridged dimer and a doubly bridged dimer, respectively, e.g., $[Cr(\mu\text{-}OH)Cr]^{5+}$ and $[Cr(\mu\text{-}OH)_2Cr]^{4+}$.

long before metal−oxygen bond cleavage and introduce a pronounced pH dependence to an otherwise slow, pH-independent reaction. Electron transfer to a metal is also critically important to the depolymerization reaction and introduces a reductive pathway to the overall process. Such variations in exchange rates and reaction kinetics for different sites on oligomers indicate that the local structure has a dramatic effect on the reaction rates and imply that oxide surface sites should also have different rates for different sites.

4.1.2. Speciation

Speciation is an important factor influencing the behavior of metal ions in aqueous solution, as well as adsorbed on metal oxide surfaces. Speciation refers to the chemical form in which a molecule or ion exists in solution, whether it is a monomer or polymer, an aquo or hydroxo complex, etc. Depending on the nature of the problem under study, multiple levels of speciation information may be needed, including: (1) the identity of the element, (2) the oxidation state, (3) the molecular chemical formula, and (4) the detailed molecular structure.

4.1.2.1. Elemental Identification. In many cases, this primary level of chemical element identification may be all that is required in addressing a problem. For example, knowledge of the presence or absence of a toxic metal ion such as lead or chromium in an environmental sample may be the only chemical issue of interest, although, as discussed in section 4.1.1.3, differences in the oxidation state of an element and the structure of its molecular complex in aqueous solution can have a profound effect on its properties.

4.1.2.2. Oxidation State. The oxidation state of a metal ion can greatly influence its mobility, solubility, and reactivity (see section 4.1.1.3).

4.1.2.3. Molecular Formula. The identity of the molecular formula influences the size and charge of a solution species and thus exerts a dominant role on species transport. For example, the empirical formula for an Fe(III) hydroxo complex is $Fe(OH)(OH_2)_5^{2+}$. Under low iron concentrations, the monomer has this same formula; however, under more concentrated iron conditions it exists as the dimer of molecular formula $(OH_2)_5Fe(\mu\text{-}OH)_2Fe(OH_2)_5^{4+}$ (see section 4.1.1.2). The higher charge of the dimer results in very different solubility and complexation behavior than that of the monomer, although they have the same empirical formula.

4.1.2.4. Molecular Structure. Molecular structure represents the highest level of information about speciation. For example, from the molecular structure of the $(OH_2)_5Fe(\mu\text{-}OH)_2Fe(OH_2)_5^{4+}$ ion, we obtain the bond distances and angles of the discrete complex.

The majority of speciation studies have placed a tremendous effort on identification of the molecular formula and determination of the thermodynamic formation constant of a given species. Experimental methods for determination of formation constants can be classified as one-phase (homogeneous) or two-phase (heterogeneous) methods. One-phase methods include spectrophotometry or potentiometry; two-phase methods include solubility, liquid−liquid extraction, and chromatography. An alternative description is as equilibrium or nonequilibrium methods. A nonequilibrium method is one that perturbs the system when observing it, such as spectrophotometry. Spectrophotometry is considered a nonequilibrium method because there is always a possibility that the equilibrium can be perturbed through interaction of photons with the system. An equilibrium method is exemplified by solubility measurements, where the system is brought to equilibrium with respect to

Table 3. General Speciation Techniques

method	lower limit (M)	application[a]	state[b]
neutron activation analysis (NAA)	$>10^{-12}$	1	S
chemiluminescence	$>10^{-10}$	1, 3	S
mass spectrometry (ICP, TOF, FAB, etc.)	$>10^{-9}$	1	L
polarography	$>10^{-9}$	1, 3, 4	L
gas/liquid chromatographic techniques	$10^{-6}-10^{-9}$	1	G, L
radiochemical trace analysis	$10^{-8}-10^{-12}$	1, 2, 3	L
atomic absorption/emission (AA, AE)	$10^{-6}-10^{-10}$	1	L
electron spin resonance (ESR)	$10^{-5}-10^{-12}$	1, 3, 4, 5	S, L
photothermal spectroscopy (PAS, TLS)	$10^{-5}-10^{-9}$	3, 4	S, L
laser-induced fluorescence (LIF)	$10^{-5}-10^{-9}$	3, 4	S, L
EMF techniques (potentiometry)	$10^{-3}-10^{-8}$	4	L
electronic spectroscopy (UV−vis−NIR)	$10^{-3}-10^{-6}$	3, 4	L
X-ray photoelectron spectroscopy (XPS)	10^{-3}	1, 3	S
vibrational spectroscopy (Raman, FT-IR)	$10^{-1}-10^{-3}$	3, 4, 5	S, L
diffuse reflectance spectroscopy	$10^{-1}-10^{-3}$	3, 4, 5	S
nuclearagnetic resonance (NMR)	$10^{-1}-10^{-4}$	3, 4, 5	S, L, G
X-ray absorption spectroscopy (XANES, EXAFS)	$10^{-1}-10^{-4}$	3, 4, 5	S, L
X-ray and neutron diffraction (single crystal, powder)	10^{0}	5	S
X-ray fluorescence (XRF)		1, 3	S
energy dispersive X-ray analysis (EDX)			S
Mössbauer spectroscopy	10^{0}	1, 3	S
neutron and X-ray scattering (SANS, WAXS)	≥ 1	5	L

[a] (1) Elemental identification, (2) physical state, (3) oxidation state, (4) molecular formula, (5) molecular structure. [b] S, solid; L, liquid; G, gas.

solubility and complexation, the solution phase is physically separated from the excess solute, and further analysis is performed on the solute, without affecting any equilibrium.[223] Techniques such as solubility measurement,[236−240] potentiometry,[241−252] liquid−liquid partitioning, dialysis, chromatography, and optical spectroscopy[253,254] have been in use for some time and can be considered classical methods. Recently, a number of more modern spectroscopic techniques have been applied, including photoacoustic and thermal lensing,[255−262] laser-induced fluorescence,[263−273] magnetic resonance,[254,274−281] and X-ray absorption spectroscopies.[282−288]

Table 3 lists a number of commonly used techniques for determining speciation, along with their applicable concentration range, sensitivity, and required physical state for sample analysis. Modern speciation measurements are often made using a combination of these techniques. Each has its own particular sensitivity, specificity, cost, and benefit. Some methods can be applied only to solid samples, whereas others can be used for both solid and liquid systems. In general, spectroscopic techniques such as NMR and XAFS spectroscopy, which yield detailed molecular structural information, require relatively large concentrations of the target species ($10^{-3}-10^{-4}$ M), whereas techniques for obtaining only elemental composition, such as neutron activation analysis, can detect low concentrations (10^{-12} M).

There have been considerable advances over the last several decades in the characterization of selected elements in complex chemical systems by the application of species-sensitive techniques in combination with species-determining techniques. For example, advances in optical spectroscopy may provide unique spectral signatures for a given type of species, from which the existence and relative concentrations can be determined. The species-determining techniques (such as potentiometric titration) must identify the chemical species in such a way that its behavior can be understood and predicted.

Solution speciation processes are often labile, and some techniques that determine the speciation also perturb the system. Techniques that are neither physically nor chemically invasive are particularly valuable for examination of speciation. Solid-phase speciation investigations are generally much less susceptible to perturbation than are solution investigations.

Speciation is also often a function of analyte concentration. For example, in aqueous media at millimolar concentrations, hydrolytic metal ion oligomers may form in solution, whereas at submicromolar concentrations the systems are frequently monomeric. As an illustration of this point, in solutions containing less than 10^{-4} M uranium, the first hydrolytic species is monomeric $UO_2(OH)^+$, while at U concentrations above 10^{-4} M, it is generally agreed that the dimeric species $(UO_2)_2(OH)_2{}^{2+}$ predominates. Even where polymer formation is not a serious problem, experimental data can often be interpreted with a number of possible species, resulting in a great deal of uncertainty in proposed speciation models. In these situations, unequivocal clarification of species identity requires spectroscopic identification or confirmation of the species proposed. Within the time constraints of experimentation, speciation models developed and confirmed from a variety of techniques have the greatest scientific credibility and applicability to the fate and transport of contaminants in the environment.

During the last 10 years, the introduction of personal computers has revolutionized the calculation of formation constants from classical experimental data, so that extremely complex systems can be studied with relative ease. A large amount of equilibrium data has been produced, although there is a wide diversity in both the nature and quality of the results. There has thus been a large increase in the number of reported equilibrium parameters in the literature, with some of these having no real chemical meaning.[226] This proliferation of formation constant data underscores the need for investigators to understand the fundamental principles of coordination chemistry in order to avoid the postulation of unjustified or unrealistic species. Several recent books have been written on this subject, which outline methods for avoiding misinterpretation or overinterpretation of equilibrium data.[223,226] Quality standards for measuring and reporting such data have also been established.[228,289−295]

4.2. Solubility and Thermodynamics of Metal Oxide Surfaces in Contact with Aqueous Solutions

4.2.1. Metal Oxide Dissolution/Solubility

The bulk stability of metal oxide phases in water is the starting point for understanding equilibrium surface chemistry. This stability is dramatically affected by solution chemistry, temperature, ionic strength, and the experimental time frames of interest.[224]

4.2.1.1. Solubility of Metal Oxides in Water. Many of the metal oxides that have been used in UHV studies of surface chemistry are not stable in the presence of water. For example, periclase [MgO(s)] recrystallizes to the mineral brucite [$Mg(OH)_2(s)$] in water (see section 3.1.1), and the near-surface region of refractory minerals such as corundum [α-Al_2O_3(s)] hydrate to form more stable phases [e.g., bayerite, α-$Al(OH)_3$(s); gibbsite, γ-$Al(OH)_3$; and boehmite, γ-AlO(OH)(s)] at the near-surface region when wet. On the other hand, hematite (α-Fe_2O_3) appears structurally almost identical in UHV, air, and aqueous solution. The important conclusion is that some of the information derived from studies of metal oxide surfaces in the absence of water may not be representative of the oxide−water interface. Removal of a solid from water can also fundamentally change the surface chemistry, as salts precipitate, gases adsorb, and in some cases the surface reconstructs to reflect the new environment. Furthermore, many studies of metal oxide surface chemistry in aqueous media were conducted on slowly recrystallizing surfaces; such recrystallization may be common because many metal oxides are available in polymorphs of only slightly differing stabilities.

Most metal oxides used in studies of surface chemistry involve metal ions that are hard Lewis acids, such as Be(II), Mg(II), Al(III), Si(IV), Ti(IV), or Zr(IV). Some of these metal oxides are not thermodynamically or kinetically stable in water. The solubility of anhydrous oxides of these metals in water is related to the ionic potential of the metal ions *z*/*r*, where *z* is the formal charge of the ion and *r* is the ionic radius, reflecting the strength of bonds to oxygens.[224]

Oxides of divalent and trivalent hard metals have a wide range of hydrolysis species that reach appreciable concentrations in the pH ranges of most aqueous solutions (Figure 23). The concentrations of these hydrolysis species depend sensitively on the solution pH, reflecting the Brønsted reactions at the waters of hydration; these are amphoteric in that they can act as both proton donors and proton acceptors, depending upon the solution pH. Thus the total concentration of dissolved ferric iron in equilibrium with ferric oxyhydroxide decreases by 6 orders of magnitude as pH increases from 2 to 4 (Figure 23). These metal oxides exhibit a minimum in solubility as a function of pH, and this minimum is an expression of the amphoteric nature of the solutes and the solid surfaces. Note also in Figure 23 that the overall solubility of the metal oxide varies

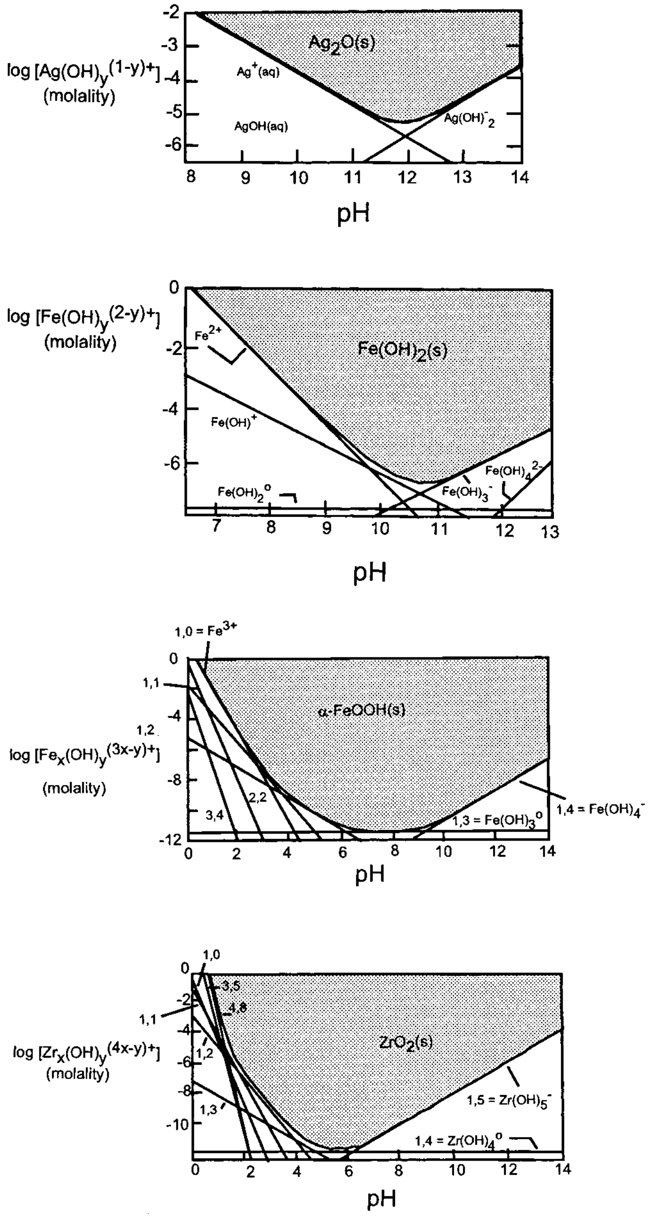

Figure 23. Speciation of metal hydrolysis products as a function of solution pH in equilibrium with the indicated solid. The formalism used to identify each dissolved species is as follows: *x* refers to the number of metals in the solute; *y* identifies the number of waters or hydroxo or oxo ligands in the inner coordination sphere. The diagrams are chosen for solids of increasing formal metal charge. (a) Ag(I) species are in equilibrium with $Ag_2O(s)$; (b) the Fe(II) species are in equilibrium with $Fe(OH)_2(s)$; (c) the Fe(III) species are in equilibrium with FeO(OH)(s); (d) the Zr(IV) species are in equilibrium with $ZrO_2(s)$ and a function of pH. (Adapted from ref 224.)

with the formal charge on the metal, so that $Ag_2O(s)$ is more soluble than $Fe(OH)_2$, which is in turn more soluble than α-FeOOH(s) and $ZrO_2(s)$.

Hydrolysis species link via hydroxyl bridges at high concentrations and precipitate the more stable hydroxide [e.g., $Fe(OH)_2$] or oxyhydroxide (e.g., α-FeOOH) phases (see section 4.1.1.2). Before the onset of precipitation, a wide range of oligomeric complexes form that have more than a single metal ion in the complex. These oligomers are useful models for surfaces because the oxygen coordination chemistry is intermediate between a dissolved monomer and the solid. Polymerization of dissolved monomers to form higher molecular weight complexes can take place at the surface of the dissolving metal oxide, leading to an epitaxial layer of the less soluble (i.e., more stable) phase on the surface of the metal oxide. There is a close connection between acidity of the metal and the structure of the resulting phase; Fe(III) in solution is considerably more acidic than Al(III), and correspondingly, the thermodynamically stable Fe(III) phase is an oxide, hematite, α-Fe_2O_3, while the stable Al(III) phase is a hydroxide, probably boehmite, γ-AlO(OH), or gibbsite, $Al(OH)_3$, depending upon differences in temperature and solution composition.

In general, tetravalent and pentavalent metals bind to oxygens so strongly that dissolved complexes are partly [e.g., $Si(OH)_4{}^0$] or fully [e.g., $PO_4{}^{3-}(aq)$] deprotonated in aqueous solutions. Correspondingly, titania (TiO_2 as rutile or anatase), hafnia (HfO_2), and zirconia (ZrO_2) are virtually insoluble in aqueous solution, and silica (SiO_2) has limited solubility in nearly neutral or acidic solutions. The kinetic stability of these bulk metal oxides, however, cannot be used as a criterion to indicate that the surfaces do not recrystallize when in contact with aqueous solutions.

The solubilities of metal oxides are strongly affected by other ligands and metals present in the solution. In simple solutions, amorphous silica can reach equilibrium with the aqueous solution and attain roughly millimolar concentrations in the absence of dissolved Al. If Al is present, one of several aluminosilicate phases, such as kaolinite, $Al_2Si_2O_5(OH)_4(s)$, can precipitate, and dissolved silica concentrations are depressed by many orders of magnitude. Periclase (MgO) converts to the stable hydroxide in the presence of pure water and to magnesite, $MgCO_3(s)$, or a hydromagnesite, $Mg(OH)_2(MgCO_3)_4(H_2O)_3(s)$, if $CO_2(aq)$ is present.

Likewise, strong ligands dramatically affect the solubility of metal oxides. The assessment of these effects requires the use of multicomponent chemical equilibrium programs. These programs are easy to use and provide a first estimate for the stable solids and solutes.[296]

4.2.1.2. Lattice Dislocations and Bulk Solubilities. It was long hypothesized that extended defect structures, such as dislocations and crystallographic shear planes, affected the solubility of metal oxide minerals near deformed rocks and in areas of high radiation fluxes. It is now clear that the equilibrium solubility of a metal oxide is virtually unaffected by large dislocation densities until extraordinarily high densities are achieved (on the order of 10^{11} cm^{-2}), and at such high concentrations the metal oxide lattice is almost completely destroyed.[297] Most naturally occurring metal oxides have been through sufficient heating/cooling cycles during rock formation to reduce high dislocation densities to densities on the order of 10^5-10^6 (see ref 297).

A much larger effect on solubilities can be attributed to the high surface energies associated with submicron particles. Submicron particles can have such a high surface area that the solubilities are appreciably higher than large, well-crystallized phases, giving rise to Ostwald ripening. The elevated surface energy is understandable when one realizes that 27% of the volume of a sphere of 100-nm diameter lies within 5 nm of the surface; for a sphere of diameter 50 nm, almost half of the volume lies within 5 nm of the surface. In fact, when particles of α-Al_2O_3 reach these dimensions, surface energy becomes a dominant contribution to the free energy and the structure rearranges to form γ-Al_2O_3.[298]

4.2.1.3. Retreat and Growth of Monoatomic Steps: Burton–Cabrera–Frank (BCF) Theory. Virtually all dissolution and growth reactions are initiated at defects on the surface, either at monatomic steps and kink sites or at the surface outcrop of dislocations. The factors affecting the rates of retreat or growth of the monatomic steps are well-established and, on a broad scale, are crystallographically controlled; that is, growth along one step direction is generally highly favored over another.[299,300] The general features of dissolution/growth by movement of these monatomic steps are consistent with BCF theory,[301] and the relative importance of growth directions can be tailored somewhat by addition of sorbate additives that poison growth sites by strong adsorption, e.g., Davey.[302] Phosphates and phosphonates are particularly strong poisons for dissolution but are largely indiscriminant.[303,304] Addition of such poisons to tailor growth is a major commercial endeavor because the crystals can be potentially engineered to make a strong composite solid.

Growth rates of metal oxide crystal surfaces vary considerably with the saturation state of the solution, as birth and spread of isolated nuclei on surfaces compete with the continuous growth of monatomic steps at outcrops of screw dislocations.[301,305] Nucleation on the surface proceeds only at high saturation states, whereas growth by the rotation of monatomic steps at screw dislocation outcrops does not require additional surface area to be created and can proceed at appreciable rates even at solution compositions that are close to equilibrium. The BCF model and its offspring have been very useful in explaining the dependence of growth rates on the bulk saturation state of the fluid, as well as resulting microtopographies. Indeed, the BCF theory is a remarkable early example of linking a microscopic surface structural model to macroscopic growth and dissolution data.

4.2.1.4. Lattice Defects and Excavation of Etch Pits. The excavation of dislocation outcrops by selective dissolution creates conspicuous etch pits on metal oxide surfaces, consistent with the general features of BCF theory (see ref 306), and these have been used to quantitatively estimate the defect densities of oxide minerals. Etch pits are pronounced in soil minerals, where extended crystallographic features, such as twin lamellae and exsolution lamellae, are excavated selectively by dissolution. Monte Carlo simulations of the excavation of etch pits on surfaces indicate that they are manifested on surfaces only when a critical degree of undersaturation is exceeded.[307,308] Near equilibrium, the nucleation of the pit is prevented by the activation energy needed to create new surface area.

Surprisingly, however, there is little experimental evidence that the concentration of extended lattice defects such as dislocations dramatically affects the flux of metal from the surface. Experiments have been conducted on shock-deformed materials[309,310] and the products of deformation in a piston−cylinder apparatus.[308,311] The etch pits are conspicuous features of the surface, but excavation of these etch pits apparently contributes a small fraction of the mass to solution compared to the mass contributed by the retreat of monatomic steps that are not associated with dislocation outcrops.

4.2.1.5. Point Defects and Bulk Dissolution Rates. High point defect concentrations have a dramatic effect on bulk metal oxide dissolution rates, as one expects from the relative reactivities of metals at different redox states, and a very strong effect on the photodissolution rates. Addition of Li^+ to NiO(s) (bunsenite), for example, creates a defective solid that is much more reactive than stoichiometric NiO(s).[312−314] Similar changes in bulk dissolution rates with point defect concentrations have been reported for a wide range of semiconducting oxides (see ref 315 for a review). The changes in reactivity can be interpreted in terms of the semiconducting properties of the metal oxide,[315] or in some cases they can be interpreted qualitatively in terms of ligand exchange and surface complexation at metal sites of different valence.

4.2.2. Thermodynamics of Surfaces in Contact with Aqueous Solution

The formation of a surface requires the input of energy (work). The thermodynamic expression for surface free energy is given by eq 9:

$$\gamma = (\delta G/\delta A)_{T,P,n} \tag{9}$$

where A represents surface area. The surface free energies of metal oxides are poorly known on a quantitative, crystal-face-specific basis. The problems inherent in estimating the surface energy of quartz are discussed by Parks,[316] who estimates a value of 351 ± 23 mJ/m^2 [except at high pH, where adsorption of counterions to the charged quartz (SiO_2) surface further reduces the surface free energy in an ionic-strength-dependent fashion[317]]. One of the methods used for this estimation typifies the problems with determining surface free energies of solids. The surface energy of quartz has been calculated on the basis of the increased thermodynamic solubility of small particles.[316] This method, while one of the few approaches available for surface area measurement for solids in aqueous solutions, is not crystal-face-specific. As pointed out by Stumm[7] and Parks,[316,317] estimates of surface free energies for oxides vary widely depending on the method used and a variety of other factors that are difficult to control.

The surface free energy of quartz has been examined by Brantley et al.[311] on the basis of etch pit formation. The thermodynamic expression for the energy barrier to etch pit formation includes a surface free energy factor. In the presence of dislocation outcrops, the expression implies a critical concentration of silica in solution, above which etch pits will not form. Extrapolation of etch pit density data as a function of saturation index gives an estimate of this critical concentration. The Brantley et al.[311] estimate of surface free energy on this basis is 280 ± 90 mJ/m^2. This 573 K value is consistent with, but perhaps lower than, the 298 K finding of Parks,[316] but the uncertainties are large. In particular, the key critical concentration depends on the strain energies of the dislocations involved.[308] These must be estimated, and they impose added uncertainty on measurements. However, this approach is promising because it gives information on the surface energy of the crystal faces exposed in the etch pits and thus may contain some crystal-face-specific information.

The overall surface energy of a solid must include contributions from local surface "defects" such as steps and kink sites. Some very intriguing work on Si (001) (2 × 1) reconstructed surfaces in vacuum has been done by Swartzentruber et al.,[29] but little work along these lines has been done for metal oxides. A recent thermochemical study of nanocrystalline alumina (Al_2O_3) shows that surface energy becomes an important contribution to the free energy when the surface area exceeds 125 m^2/g, at which point γ-Al_2O_3 becomes energetically favored over α-Al_2O_3.[298] A general expression for the overall surface energy of a particular crystal plane subject to varying number densities of steps as a function of angle θ from a low Miller index face, with step height a, is given by eq 10:[36]

$$\gamma(\theta) = \gamma(0) + (\beta/a)|\theta| \tag{10}$$

where β is the energy per step. The energy per step will vary with step length, which for a given crystal face varies with step "roughness", "meandering", or, more precisely, with the formation of kink sites along steps. There are also more complicated treatments of how steps interact with each other as they meander.[318,319] For example, from kink size and population data for Si (001) (2 × 1), Swartzentruber et al.[29] found that the expression in eq 11 for kink formation energy was adequate to describe their data:

$$E_k(n) = nE_k + C \tag{11}$$

where the energy of formation E_k of a kink site n units wide is simply n times the per-unit step energy of the step segment within the kink, plus a term C attributed to the formation of the inside and outside corners of the kink.

Similar work has not yet been done for metal oxides, mostly because of the difficulty of ensuring equilibrium for metal oxide surfaces in UHV without chemically altering the surface or inducing surface reconstruction; ensuring overall equilibration in situ takes a prohibitively long time. However, experiments similar to those of Swartzentruber et al.[29] are still possible. Kink site formation energies have been estimated for gypsum, $CaSO_4 \cdot 2H_2O$, on the basis of an early paper by Frenkel[320] (see also ref 301), whose expression for mean distance is given by eq 12:

$$x_0 = 1/2a[\exp(\epsilon/kT) + 2] \tag{12}$$

where x_0 is the mean distance between kink sites along a step, a is the length of a structural unit along the step, and ϵ is the kink formation energy. For gypsum in aqueous solution, $\epsilon = 4.1 \pm 0.7$ kJ/mol along [001] steps on (010) gypsum surfaces.[321]

Eggleston (unpublished data) used AFM to image calcite ($CaCO_3$) surfaces in equilibrium with aqueous solution (pH 9.9) with unit-cell-scale resolution and used eq 11 to calculate a kink formation energy of 2.4 kJ/mol per unit step segment, plus 1.8 kJ/mol for corner formation. Both of these numbers must be regarded as order-of-magnitude estimates because they are based on a statistically very small number of observations.

Metal oxides, oxyhydroxides, and hydroxides in natural environments are often porous, making capillary condensation phenomena important. The effect is described by the Kelvin equation, which relates the reduction in the equilibrium saturation pressure of water, expressed by the ratio $p(r)/p(r = \infty)$, to the pore radius r and the Laplace pressure π of the liquid water in the pore:

$$p(r)/p(r = \infty) = \exp[\pi v/(RT)] \tag{13}$$

where v is the molar volume of water and π is defined by eq 14:

$$\pi = -2\gamma \cos \phi/r \tag{14}$$

Here γ is the interfacial tension of water ($\gamma = 72$ g/s^2 at 298 K) and ϕ is the contact angle it forms with the oxide surface. Assuming complete wetting ($\phi = 0°$), the ratio $p(r)/p(r = \infty)$ varies between 0.9 and 0.34 for pore sizes ranging from 10 down to 1 nm. Thus in micro- or mesoporous solids of these pore dimensions, water condenses at room temperature at 34–90% relative humidity. Capillary condensation manifests itself by the appearance of hysteresis in water adsorption isotherms.[322]

4.3. Experimental Studies of the Electrical Double Layer

4.3.1. Experimental Issues Concerning the Aqueous Solution–Metal Oxide Interface

Tremendous strides have been made in recent years in experimentally determining the properties of solid surfaces in contact with aqueous solutions. This is largely due to the development and application of new in situ experimental techniques to such systems. These techniques include X-ray absorption fine structure (XAFS), X-ray standing waves (XSW), infrared methods, second-harmonic generation (SHG) methods, and surface X-ray diffraction (crystal truncation rod measurements) and reflectivity. In addition, a number of more conventional methods have been used to probe the aqueous solution–metal oxide interface, including NMR and EPR spectroscopies. These methods have been quite successful and are described in the following sections. However, some of the limitations of the techniques must be kept in mind when studying such complex systems. No single spectroscopic or scattering method can provide a complete description of sorption products at metal oxide–aqueous solution interfaces or a complete description about the surface structure of an (hydr)oxide in contact with an aqueous solution. For example, X-ray absorption fine structure (XAFS) analysis cannot detect hydrogen ions, cannot provide quantitative information about the size of extended surface complexes or surface precipitates, and is not as sensitive to well-ordered surface structures as are LEED, X-ray standing, wave and surface X-ray diffraction measurements. With the exception of LEED, these techniques are all photon-in/photon-out methods and hence can be used for in situ studies. UHV methods such as photoemission, which are photon-in/electron-out methods, require that the sample be dried and placed in a vacuum chamber, which could alter the surface complex, especially if it is weakly bound as a fully solvated, outer-sphere surface complex.

NMR spectroscopy has a fundamental limitation due to the number of NMR-active nuclei required for a detectable signal (see section 3.2.1). Thus, sorbed species at low coverages on a low-surface area metal oxide cannot be characterized currently using NMR spectroscopy. This concentration problem also precludes detailed NMR study of hydrolyzed species sorbed on metal oxide surfaces in the presence of bulk water. Because of this limitation and the low sensitivity of the applicable in situ methods to protons, it is not possible to determine the number of protons bonded to oxygen or other ligands around a sorbed metal ion. In contrast, it is possible to use proton NMR spectroscopy to provide this type of information for solution species at relatively high concentrations. The other problem commonly encountered in the sorption of aquated metal ions on hydroxylated metal oxide surfaces is that the protons released, as measured by potentiometric titrations, cannot be assigned to hydrolysis of the metal ion vs release from the metal (hydr)oxide surface.

FTIR methods such as attenuated total reflectance, (ATR)-IR, can provide information on the nature of sorbed water, oxoanions such as phosphate and sulfate, and simple organics at metal oxide–aqueous solution interfaces (see section 4.3.2.4). However, the dominant IR contribution from the bulk solution must be carefully subtracted from the relatively weak IR contribution from the sorbate. In addition, the resulting IR spectrum provides only indirect information about the structure of adsorbates and their mode of attachment to the metal (hydr)oxide surface. When an adsorbate species exhibits characteristic UV–vis absorption or luminescence, these methods can be sensitive to adsorbate species (e.g., ref 323).

However, most adsorbates are not luminescent, and the UV−vis absorption of the adsorbate species is overwhelmed by absorption from the bulk solid or solution.

AFM methods do not currently have the atomic resolution needed to provide structural information on individual sorbate species or the surface sites to which they are bound (see section 2.2). Second-harmonic generation (SHG) and sum-frequency generation (SFG) methods are just beginning to be used for studies of adsorbates (mostly organic) at metal oxide−aqueous solution interfaces (see sections 4.3.2.6 and 4.4.2.8).

It is essential that the time frame of a given spectroscopic effect be understood. This is true because ligand-exchange rates vary widely, depending on the metal ion (see section 4.1.1.4.). For example, Pb(II) has one of the highest ligand-exchange rates between water in its first coordination sphere and bulk water ($\approx 10^{10}\ s^{-1}$), whereas Cr(III) has a ligand-exchange rate ($\approx 10^{-7}\ s^{-1}$) that is 17 orders of magnitude lower! In photon or electron scattering or emission spectroscopies, the transition time for a single event is $10^{-15}-10^{-16}\ s^{-1}$. This is very fast on the time scale of any ligand exchange, so each event is a snapshot of the system in a particular state. However, obtaining a spectrum with a good signal-to-noise ratio takes from seconds to hours; the resulting spectra may thus sum over an enormous number of possible configurations. (For XAFS, for example, it may be surprising that a signal is observed at all for dilute sorbed species at metal oxide−aqueous solution interfaces. However, because of the regularity and relative rigidity of first coordination spheres of most metal ion sorption species, their XAFS signal is typically quite strong.) In NMR, spin relaxation times range from about 10^{-9} to 10 s, so ligand exchange with an atom may take place during the time of a single measurement. In SPM, the time to acquire an image is typically seconds to minutes (with perhaps milliseconds spent in the vicinity of each surface atom), so again ligand exchange with a particular atom may occur while it is being imaged or its electron energy spectrum is being obtained in STS. These considerations must be kept in mind in the interpretation of all experimental data.

4.3.2. Experimental Techniques

4.3.2.1. Surface X-ray Scattering. X-ray scattering methods of determining atomic structure at interfaces have been reviewed recently for surfaces[51,324,325] and with specific application to solid−liquid interfaces.[326−328] A recent review of the application of these methods to a number of clean metal oxide surfaces is also available.[44] Here we will only briefly describe the techniques that are used elsewhere in this paper or that are potentially useful for determining structure at metal oxide−aqueous solution interfaces. A much more thorough description of these methods and their limitations can be found in ref 44. Surface X-ray scattering is a relatively straightforward extension of conventional X-ray crystallography. Surface sensitivity is achieved through the use of intense synchrotron radiation.[329] Surface selectivity results in several ways. For reconstructed surfaces, the fractional-order diffraction peaks (or “spots” in LEED notation) are distinct from the bulk Bragg peaks and are easily measured. For unreconstructed surfaces and measurements of integer-order diffraction peaks, one relies on the fact that an interface at a single crystal creates X-ray scattering that is additional to the Bragg peaks of the crystal.[324,330,331] These “truncation rods” consist of ridges of intensity that run perpendicular to the interface and through Bragg peaks. For the specular truncation rod, the scattering vector $\mathbf{Q}$ (difference between incident and scattered X-rays) is normal to the interface, and the intensity depends on the structure of the interface in that direction. For nonspecular truncation rods (where $\mathbf{Q}$ has a component along the solid surface), the intensity only depends on the surface structure, since the solution is disordered parallel to the interface. From measurements of surface X-ray diffraction, structural models of the surface are developed and fit to the experimental data, as in conventional X-ray crystallography (see section 2.3.1).

Surface X-ray diffraction has several advantages compared with other surface structural methods. Importantly, the use of X-rays with energies $\geq$ 8 keV results in a large penetration depth in aqueous solutions and permits in situ studies of metal oxide−solution interfaces. X-ray scattering is kinematical (as opposed to LEED and XANES), so data interpretation is relatively simple. This results in accurate, quantitative determination of atomic positions at surfaces and interfaces. Under favorable circumstances, surface X-ray scattering can provide insight into the nature of surface defects such as steps and islands.[51,332,333]

Surface X-ray diffraction also has several disadvantages. It requires long-range order ($\approx$5 nm), although in the case of water−Ag (111) this limitation has been overcome (see section 4.3.3.5).[330,331] As with LEED, it is an averaging technique and can give unrepresentative results if much of the surface is disordered. The X-ray scattering cross section varies roughly as Z^2, and hence the scattering from low-Z elements is weak (hydrogen is effectively invisible). This can be a severe problem for in situ measurements, where the background scattering of the solution is often large. While smooth surfaces are not required, they are certainly beneficial.

4.3.2.2. X-ray Absorption Fine Structure (XAFS) Spectroscopy. Synchrotron-based XAFS spectroscopy in the fluorescence yield mode is capable of providing atomic- or molecular-scale structural information on metal ion sorption complexes at metal (hydr)oxide−aqueous solution interfaces at surface coverages ranging from very low (<0.1 monolayer of the sorbate ion) to greater than monolayer on both high-surface area powders and oriented single crystals for a variety of sorbate−sorbent systems.[334] XAFS has the ability to probe selected metal ions in disordered or ordered arrays on poorly or well-ordered surfaces, which is one of its major advantages relative to surface-sensitive structural methods such as X-ray standing wave and surface X-ray scattering measurements. These latter methods require the surface to be periodically ordered and the adsorbate to be arranged in a relatively ordered fashion at the surface.

XAFS can be divided conveniently into two spectral ranges: one beginning about 10 eV below an absorption edge of an element and extending to about 50 eV above the edge, which is referred to as the X-ray absorption near-edge structure (XANES) or near-edge X-ray absorption fine structure (NEXAFS) region, and one starting at about 50 eV above an absorption edge and extending to as much as 1000 eV above the edge, which is referred to as the extended XAFS (EXAFS) region. XANES or NEXAFS spectra are dominated by bound-state electronic transitions and multiple scattering of the photoelectron among atoms around the absorber. EXAFS spectra are best described in terms of single-photoelectron scattering involving interference between the outgoing and the backscattered photoelectron waves.

Recent reviews of NEXAFS (or XANES) spectroscopy can be found in refs 50 and 335. NEXAFS spectra provide quantitative information on oxidation state of the absorbing element and its coordination number when the edge energy is properly calibrated against standards with different oxidation states of the element, and the position and intensity of preedge features are calibrated against appropriate coordination number standards for the element. NEXAFS spectroscopy has been used extensively to study organic and simple inorganic adsorbates on metal surfaces under UHV conditions,[50] but it is not as widely used as EXAFS spectroscopy for studies of adsorbates on metal oxide surfaces because of the difficulty of extracting quantitative information about bond distances and the identity of backscattering atoms from a NEXAFS spectrum. Nonetheless, NEXAFS or XANES spectra can provide quantitative information on coordination numbers of metal ions in solids as well as on metal oxide surfaces. Because a NEXAFS spectrum for a dilute surface species is always more intense than the corresponding EXAFS spectrum, the NEXAFS spectrum is often all that can be measured accurately. Recent advances in multiple-scattering codes used to simulate NEXAFS spectra (e.g., refs 336 and 337) have made it possible to extract quantitative information on the local structural environment of cations.[338−340]

The information provided in an EXAFS spectrum includes the average distance to, and the number and identity of, atoms in the first and, in favorable cases, second and higher coordination shells (up to ≈6-Å radius) around a metal ion; it also includes a measure of the thermal and/or positional disorder of the environment around that ion. For sorbates on single-crystal surfaces, one can take advantage of the natural polarization of the synchrotron X-rays (the electric vector lies in the plane of the storage ring) to probe the orientation of the sorbate relative to different crystallographic orientations of the surface. This feature can be important, for example, in showing that a multinuclear surface complex is oriented parallel or perpendicular to the surface. Analysis of the second coordination shell around an adsorbate ion provides interatomic distances and identity of second neighbors, which is essential information for determining the mode of sorption (inner- vs outer-sphere; mono-, bi-, or tridentate surface bonding; mononuclear vs multinuclear surface complexes vs precipitate). Quantitative analysis of EXAFS spectra has benefited significantly from the availability of multiple-scattering codes such as FEFF,[336,337] which are capable of providing accurate phase-shift and amplitude functions for essentially any arrangement of first and more distant shells of atoms around an absorbing atom, including distances, coordination numbers, and atom identities from the second coordination shell.[341] Recent improvements in these codes (e.g., ref 337) have also made it possible to extract quantitative information on the local structural environment of cations from their XANES.[338−340]

Two of the basic requirements for fluorescence yield XAFS studies of low concentrations of metal ion sorbates are high X-ray flux and a sensitive, high-throughput detector. Past studies of sorbates at surface coverages as low as 0.05 monolayer and of contaminant ions in soils at the 10−20 ppm level have been successfully carried out using Stern−Heald-type ion chamber fluorescence detectors[342−344] and multielement solid-state detectors. Several additional technical considerations are important for XAFS measurements on surface adsorbates. If one wishes to study sorption processes at metal oxide−aqueous solution interfaces, measurements must be made in situ, i.e., in the presence of bulk water. This requirement places limitations on the sorbates that can be studied using XAFS methods. For example, experience has shown that dilute sorbates (≤ 0.1 monolayer coverage) with X-ray absorption edge energies less than about 4.5 keV cannot be studied in the presence of water in powder XAFS experiments with currently available synchrotron beam lines. This means that Cr, which has a K absorption edge energy of 5989 eV, and elements with higher atomic numbers than Cr can be studied under in situ conditions using XAFS spectroscopy. Requirements are more stringent for GI-XAFS experiments.[345] For example, Co sorbed on single-crystal α-Al_2O_3 and TiO_2 (rutile) surfaces cannot be studied by GI-XAFS in the presence of a significant bulk water layer present (>1-μm thickness) due to the very low incidence angle of the X-rays and the relatively long path of X-rays through the water, which results in essentially complete absorption of the Co X-rays (K edge = 7709 eV).[346] On the other hand, elements such as Pb (L_{III} edge = 13 055 eV) sorbed on single-crystal α-Al_2O_3 in the presence of a 1−2-μm layer of water on the surface can be studied using GI-XAFS methods. Even when XAFS studies are carried out under "dry" ex situ conditions at room temperature and pressure, multiple monolayers of water are present on oxide surfaces at relative humidities higher than 40%.[10] While low-temperature XAFS measurements can significantly improve the quality of data, particularly at high *k* values which enhance analysis of the second coordination shell around adsorbed metal ions, such measurements can also change the nature of the sorbate, relative to room-temperature measurements, for certain sorbates [e.g., Pb(II) on α-Fe_2O_3[347]]. Thus caution must be exercised in utilizing low-temperature XAFS in the study of adsorbates at metal oxide–aqueous solution interfaces.

4.3.2.3. X-ray Standing Wave Methods. X-ray standing wave (XSW) methods have recently emerged as an important and relatively simple tool for studying the geometry of adsorbed atoms or molecules on surfaces.[348–354] The XSW method is experimentally less demanding than surface EXAFS (SEXAFS), as one measures X-ray absorption of a specific element within a narrow range of photon energies (or angles) near the Bragg condition. Mathematical analysis of XSW data is also straightforward.

The theory underlying the XSW method is based on the dynamical description of X-ray diffraction from crystals.[355,356] In short, as the photon energy is swept through the Bragg condition, a standing wave is formed within and external to the substrate surface. The phase of the standing wave changes by π within the energy range of total reflection, which causes a shift in the position of the nodes and antinodes of the electric field intensity relative to the diffracting planes by one-half of a lattice spacing. Since photoelectric effects are proportional to the electric field intensity at the center of atoms (the dipole approximation), the presence of adions located above the substrate surface modulates the X-ray absorption (and the subsequent fluorescence) when the position of the XSW field intensity coincides with the center of the adion. Thus, absorption minima occur when the minimum of the E-field intensity (nodes) sweeps through the adion position; correspondingly, maxima occur when the maximum of the E-field (antinodes) coincides with adion positions. Analysis of the variation of X-ray absorption as a function of photon energy (or incidence angle of the X-ray beam) in the neighborhood of the Bragg condition allows determination of the position of adions relative to the substrate's atomic planes and the coherent fraction (i.e., fraction of adions occupying this position) (e.g., ref 350). As in the case of SEXAFS, fluorescent or Auger electron yields are used as a measure of X-ray absorption in XSW experiments. The distance between the adsorbed ions and the substrate planes is often obtained with an accuracy better than 2% of the lattice spacing. By using several different diffracting planes of a single substrate, full adsorption geometries can be determined by triangulation techniques.[351,357] The recent XSW study of adsorbed SeO_3^{2-} on the calcite $(10\bar{1}4)$ surface by Cheng et al.[358] used this approach to show that SeO_3^{2-} oxoanions replace CO_3^{2-} oxoanions in the near-surface region of calcite. Cheng et al.[359] have also used XSW combined with surface EXAFS methods to show that Zn^{2+} replaces Ca^{2+} in the $(10\bar{1}4)$ surface of calcite. One significant disadvantage of XSW experiments is that they require nearly perfect single-crystal substrates, which are often unavailable.

Despite its utility, XSW has only recently been used to study interfaces that are fabricated in vacuum.[66,350,352–354,360] For example, in studies of semiconductor interfaces, a variant of the technique was used in which the XSW signal is detected by varying the incident photon energy rather than the incident X-ray beam angle.[352,353,361] The angle-variation XSW method, which uses hard X-ray radiation ($\approx$10 keV), is currently more popular despite the rather complex apparatus required for the necessary high-precision angular motion. However, the soft X-ray back-reflection version of the XSW technique, which uses the lowest energy for each Bragg diffraction, is often better suited for UHV surface studies because the requirement for highly perfect surfaces is reduced. In addition to a simpler apparatus, this modification of the XSW method also reduces complexities or artifacts due to extinction or to the presence of hot electrons excited by the energetic beam (i.e., those of higher energy).

4.3.2.4. Vibrational Spectroscopy Methods. Infrared and Raman spectroscopic techniques can be used to study the nature of water and adsorbates on metal oxide surfaces and at metal oxide–aqueous solution interfaces (see refs 362–365). For example, a recent study by Koretsky et al.[366] used diffuse reflectance FTIR (sometimes referred to as DRIFT) to characterize chemisorbed water on powdered samples of quartz, γ-Al_2O_3, and various feldspar minerals, (K,Na)-$AlSi_3O_8$–$CaAl_2Si_2O_8$, before and after heating in air. A single IR band at $\approx$3745 cm^{-1} was found for quartz and the feldspar samples and was interpreted as being due to >SiOH surface groups. A single IR band at $\approx$3800 cm^{-1} for γ-Al_2O_3, characteristic of >AlOH surface groups, was not observed for the feldspar samples, which is somewhat surprising and indicative of how little is known about the molecular-scale nature of water on feldspar surfaces. Russell et al.[367] used infrared spectroscopy to identify three types of surface hydroxyl groups on hydroxylated goethite (α-FeOOH) surfaces, including type A groups [coordinated to one Fe(III) cation on the surface], type B groups [coordinated to three Fe(III) cations], and type C groups [coordinated to two Fe(III) cations], with the type A site being most reactive and the type B site being least reactive.

In general, IR methods are not surface-specific and hence integrate signals arising from the bulk solid, aqueous solution, and interface regions. Because IR contributions from bulk water are large and those from the interface region are small, detection of surface interactions is difficult using IR methods when a bulk aqueous phase is in contact with the metal oxide surface. This problem can be overcome to some extent by using attenuated-total-reflection infrared absorption (ATR-IR), which reduces the path length through the bulk solution and makes subtraction of the aqueous solution background absorption possible.[368–372] The ATR method, as recently modified by Hug and Sulzberger,[373] uses a horizontal ATR element coated with a layer of metal oxide particles that is placed in contact with an aqueous solution, allowing for quantitative in situ analysis of the metal oxide–water interface. The FTIR spectra obtained are analyzed using singular-value decomposition and global fitting routines, yielding information on the structural characteristics of adsorbates. For example, the surface complexation of oxalate on TiO_2 (anatase) has been studied in this fashion (see section 4.4.2.7).[373]

4.3.2.5. Laser Methods. Laser spectroscopy has been employed as a diagnostic tool in two different areas. Pulsed lasers have been used to measure the dynamics of charge carrier reactions at the oxide surfaces.[374] A recent highlight of this is the observation of sensitized electron injection from dyes into the conduction band of TiO_2, which was found to occur on a femtosecond time scale, exceeding the rate of photosynthetic charge separation by a factor of 100.[375] Second-harmonic generation (SHG) and other laser-based nonlinear optical techniques are also beginning to be used to study adsorbates on metal oxide surfaces, as discussed in the following section.

4.3.2.6. Second-Harmonic Generation (SHG) Methods. SHG is a nonlinear optical process in which two input photons of frequency ω in a noncentrosymmetric medium give one output photon of frequency 2ω. The application of SHG to the study of surfaces has been reviewed in refs 376−378. An interface, whether solid−liquid, solid−gas, liquid−gas, etc., represents a break in the bulk symmetry and thus a noncentrosymmetric boundary. Within the electric dipole approximation, centrosymmetric media (e.g., bulk aqueous solutions) do not give rise to primary SHG (higher order magnetic dipole and quadrupole interactions remain allowed but are usually negligible), making SHG inherently surface-sensitive for centrosymmetric bulk phases.

SHG can arise from a number of sources: (1) the bulk of a noncentrosymmetric material [e.g., quartz, potassium dihydrogen phosphate (KDP)]; (2) the inherent surface nonlinear susceptibility; (3) surface adsorbates with substantial second-order nonlinear susceptibilities; (4) changes in the nonlinear susceptibility due to surface−adsorbate interactions; and (5) static electric fields present at the interface. The overall SHG intensity $I(2\omega)$ can be represented by the following expression:

$$I(2\omega) \propto |\mathbf{e}(2\omega)\cdot\chi^{(2)}\cdot\mathbf{e}(\omega)\ \mathbf{e}(\omega)|^2 I^2(\omega) \qquad (15)$$

where $I(\omega)$ is the input light power, $\mathbf{e}(\omega)$ and $\mathbf{e}(2\omega)$ are the polarization vectors describing the input and output light fields, and $\chi^{(2)}$ is the complex second-order nonlinear susceptibility tensor of the system. Because $\chi^{(2)}$ relates the two input light vectors to the second-harmonic output vector, it is a third-rank tensor and can possess up to 18 *distinct* nonzero elements χ_{ijk}, where i, j, and k refer to the Cartesian axes defined by Z as the surface normal. In most systems, surface symmetry greatly reduces the number of nonzero elements of χ.

Because the apparent χ is the complex sum of nonzero χ_{ijk} elements, the rotational anisotropy (about the azimuth) of the SHG intensity for a fixed input−output configuration (e.g., p-polarized fundamental input, s-polarized second-harmonic output) can be used to probe a reduced number of nonzero elements χ_{ijk} of χ. This method is particularly valuable for determining changes in surface symmetry as a result of adsorption. The angular resolved SHG signal reflects the combined substrate−adsorbate surface symmetry.

SHG can be used to probe the orientation of adsorbed organic molecules. While rotationally mobile single adsorbed molecules will probably not have a fixed orientation at room temperature, in ordered overlayers this may change, and SHG may provide information about molecular interactions. The molecular nonlinear polarizability tensor, β, defined in terms of molecular coordinates (x,y,z), is related to the observed surface nonlinear susceptibility $\chi^{(2)}$, defined in terms of laboratory coordinates (X,Y,Z). If organic chelates adsorb as inner-sphere complexes, they might be expected to display a preferred orientation on a well-ordered oxide surface, as determined by the geometry of the surface complex. The measured surface nonlinear susceptibility $\chi^{(2)}$ and β are related by a transformation matrix describing the absolute molecular orientation on the surface. Determination of contributing elements of χ_A can be obtained by observing the input polarization dependence of the SHG response. The procedure for determining molecular orientation has been fully described[379] and applied to adsorbate−surface systems.[380] The application of SHG to an organic adsorbate on α-Al_2O_3 is discussed in section 4.4.2.8.

4.3.2.7. Low-Angle X-ray and Neutron Reflectivity. Low-angle X-ray reflectivity[381] is related to diffraction, but it is used to measure electron density profiles normal to an interface on length scales of 1−100 nm. In a typical reflectivity experiment, the incident X-rays impinge on a flat interface at a small angle θ, and the intensity of the specularly reflected X-rays is detected at 2θ. Data are collected as a function of θ or $\mathbf{Q} = (4\pi/\lambda)\sin\theta$, where λ is the X-ray wavelength and $\mathbf{Q}$ is normal to the interface. Specular low-angle X-ray reflectivity is analogous to optical reflectivity, and the Fresnel formulas are used to calculate reflectivities.[381] Since the refractive index at X-ray energies is closely related to the electron density, analysis of a reflectivity profile yields the electron density normal to an interface. From this one can determine the thickness, density, and roughness (or interfacial width) of thin films adsorbed on substrates. One disadvantage of this technique is that it requires relatively smooth surfaces (e.g., rms roughness < 1 nm).

4.3.3. The Electrical Double Layer

Metal oxide surfaces in contact with water generally develop surface charge for several reasons, including permanent structural charge, protonation−deprotonation reactions, and specific adsorption of other ions that determine the surface potential (these may include the constituent ions of the solid). The useful and well-developed models derived to account for many electrochemical phenomena, including sorption, i.e., the family of “electrical double-layer” (EDL) models (refs 2, 3, 222, and 382−385), are hypotheses based on simplifying assumptions. These assumptions, such as “outer-sphere binding” or “contact adsorption” of a significant fraction of the counterions adsorbed to achieve interfacial electroneutrality near charged surfaces,[382] need to be tested by direct measurements of the spatial distribution of ions in the EDL as a function of pH, ionic strength, solution metal ion concentration, and other variables for a given sorbent and sorbate.

According to the models proposed for the EDL, ions bound in either inner- or outer-sphere complexes with surface sites should be limited to a single layer close to the surface (the Helmholtz model), while ions accumulated Coulombically should appear in a diffuse cloud that decays approximately exponentially with distance from the surface (the Gouy–Chapman–Stern model); see Figures 1 and 52.[386] The difference between these two models is important because it reflects the binding mechanism and affects the way the sorbed ions influence sorption equilibria and interfacial reaction kinetics.

Indirect evidence for the Gouy–Chapman–Stern model of the EDL has been provided by measurements of the force between two charged surfaces in an electrolyte, which should depend on the ion distribution in the diffuse layer (plus the van der Waals attraction).[387] These experiments are described elsewhere[387] and will not be reviewed here. We note only that in general there is reasonable quantitative agreement with the theory, even at small surface–surface separations (e.g., less than the Debye length).

Structural hypotheses concerning the EDL are just beginning to be tested directly for metal oxide–aqueous solution interfaces now that appropriate measurement tools are becoming available. In this section, we focus on theoretical simulations and direct probes of the structure and properties of the EDL.

4.3.3.1. Theoretical Simulations of the Structure and Properties of the Electrical Double Layer. The arrangement of water molecules at charged metal oxide–aqueous solution interfaces plays an important role in determining the chemical interactions of solution species, such as metal cations, oxyanions, and organic molecules, with the interface. This importance has stimulated extensive theoretical investigations of the orientation and spatial distribution of water molecules at charged interfaces using statistical models and computer simulations (see also section 7.1.1).[388−398] Due to the complexity of the problem, nearly all work has been conducted on metal–water interfaces. In these systems, it is generally predicted that water is ordered in layers extending several molecular diameters from an interface, and the areal density (or coverage) in the innermost layer is about the same as that expected from the bulk water density. In addition, there have been suggestions that, driven by hydrogen bonding, the inner layer adopts a solidlike structure similar to ice–I, where the oxygen atoms form puckered hexagons linked by hydrogen bonds.[389,390,394,395,397,399] For charged electrodes, electrostatic considerations suggest that, as the electrode charge (or potential) changes from negative to positive, the average molecular orientation of inner-layer water molecules changes from oxygen-up (e.g., away from the electrode) to oxygen-down.[388,396,397] As shown in Figure 24, this results in a decrease in the oxygen–electrode spacing with increasing positive potential. Some simulations suggest that with an increasing magnitude of the applied potential there is an increase in the inner-layer density (i.e., ≈20%),[397] although others indicate either no change or a drop in density.[390,396] In the following sections we describe experimental studies of the distribution of solute and solvent molecules near metal oxide–aqueous solution interfaces: specifically, the distribution of ions in the diffuse layer and the layering, structure, and properties of water at the interface.

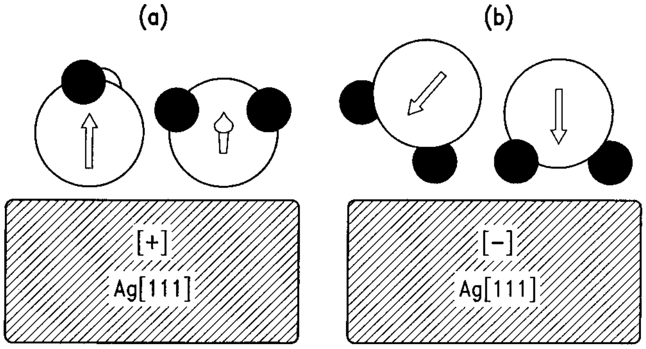

Figure 24. Possible orientations for water near a surface, showing the orientations that provide the most favorable electrostatic interactions. The arrows show the directions of the dipole moments. (a) Positively charged surface. The arrow on the right molecule is pointed partially out of the plane of the page. (b) Negatively charged surface. Note that the oxygen atoms are farther from the electrode surface in panel b. (Reprinted by permission of *Nature* (ref 330) copyright (1994) Macmillan Magazines, Ltd.)

4.3.3.2. AFM Studies of the Electrical Double Layer. Although scanning probe microscopy (SPM) is perhaps most famous for high-resolution in situ imaging, atomic force microscopes (AFM) can also be used as sensitive force measurement devices. The tip, which may be chemically tailored for suitability to a particular system, can be thought of as a large molecule or small particle attached to a spring (the cantilever) that allows measurement of the forces acting on the tip “particles”. AFM has therefore been used in a number of cases to examine the forces acting on a tip as a function of separation of the tip from the sample surface (see section 2.2). For an oxide–electrolyte interface, this means that the EDL repulsion between a tip and sample of like properties can be probed.

AFM has been used to study the forces that are present in the EDL.[400−403] The exponential dependence of forces on distance, or the “thickness” of the EDL as a function of ionic strength, and the variation of surface charge with pH were investigated and found to agree relatively well with Derjaguin–Landau–Verwey–Overbeek (DLVO) theory. Hillier et al.[403] have measured the potential of zero charge for a silica tip interacting, at pH 5.5, with a variable potential gold electrode.

Figure 25 shows that the EDL repulsion forces between tip and sample agree quite well with DLVO theory (which accounts for both the repulsion of overlapping double layers and the van der Waals attraction) for large tip–sample separations but that agreement is not so good when the tip and sample are nearly in contact (within about 1 nm). The “thickness” of the diffuse layer of the EDL decreases with increasing ionic strength, as predicted by theory. Also, the EDL repulsion decreases systematically as the pH_{PZC} (pH at the point of zero charge) of the oxide surface is approached, because the surface charge that gives rise to the EDL is at a minimum at the

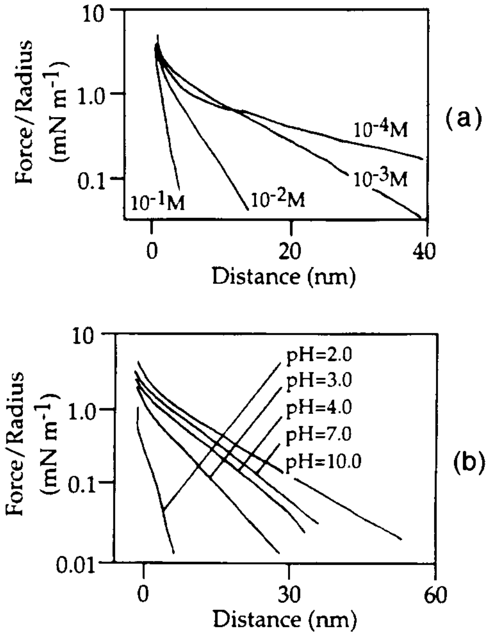

Figure 25. Some data on repulsive forces (as measured by AFM) as a function of (a) ionic strength and (b) pH for a silica tip positioned over a silica surface in situ. (Reprinted from ref 402. Copyright 1992 American Chemical Society.)

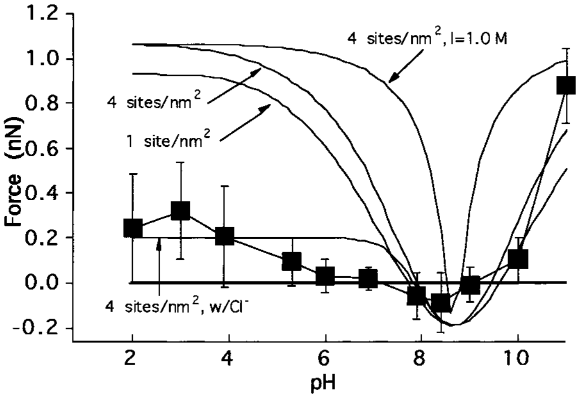

Figure 26. Interaction forces (repulsion or attraction) between a hematite (α-Fe_2O_3) tip over a hematite (0001) surface in 0.01 M NaCl, measured as a function of pH using an AFM. Labeled curves are calculations of EDL repulsion forces from DLVO theory, for which pK_{a1} and pK_{a2} for surface deprotonation reactions were taken from ref 405. Disagreement between calculation and experiment at low pH can be accounted for by assuming that Cl^- from HCl adsorbs specifically to the surface, limiting the buildup of positive charge: $>FeOH_2^+ + Cl^- = >FeOH_2Cl$, log K = 2.45. Typical tip–sample approach rates were 6 or 12 nm s^{-1}; faster rates can lead to hydrodynamic damping and artifactual curvature.[400] Ionic strength is 0.01 M except where noted.[404]

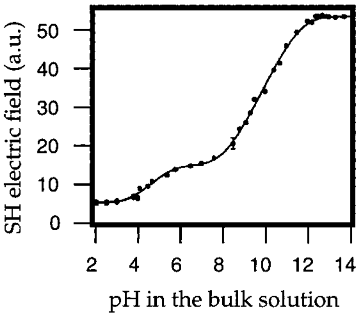

Figure 27. Electric field strength (from the square root of the SHG signal) at the amorphous silica-aqueous solution interface as a function of pH. This signal stems from an "electric field-induced second harmonic" (EFISH). As the pH rises, surface silanol sites deprotonate to produce negative surface charge; the resulting electric field near the interface gives rise to an increasing EFISH signal with rising pH. The results suggest two different surface sites and are consistent with a pH of zero net proton charge of pH = 2–3 (adapted from ref 407).

pH_{PZC}. This fact suggests a novel method for measurement of pH_{PZC}; namely, measurement of repulsive forces as a function of pH by AFM. This has been done for metal electrodes[403] but has only recently been attempted for metal oxides (see Figure 26); the technique used in this measurement is discussed in ref 404.

Marti et al.[406] used changes in frictional forces between a silicon nitride tip and an SiO_2 sample as a function of pH to relate surface charge and the EDL to pH. Frictional forces were greatest when tip and sample were of opposite charge and decreased in pH regions where tip and sample had like charge.

4.3.3.3. SHG Study of the Electrical Double Layer. Ong et al.[407] showed pH-dependent SHG response directly related to the surface protonation of two distinct sites on amorphous SiO_2 possessing different surface acidity (e.g., two distinct pK_a values, see Figure 5 from ref 407, reproduced here as Figure 27). This is highly promising for the use of SHG to probe crystal-face-specific proton adsorption. Du et al.[408] used a technique related to SHG—sum-frequency generation (SFG)[377,409]—to study the vibrational spectra of water at a quartz–water interface, showing that the structure of water near the quartz surface changes as a function of pH and thus of surface charge (it is not clear in this study whether "quartz" refers to fused silica or crystalline quartz).

4.3.3.4. X-ray Standing Wave Studies of the Electrical Double Layer. Bedzyk et al.[410] have successfully used X-ray standing waves, employing long period multilayers and a total external reflection condition, to study the distribution of Zn(II) ions in a dilute $ZnCl_2$ solution above a Langmuir–Blodgett phospholipid film deposited on the multilayer substrate. The method they employed is a straightforward extension of Bragg diffraction but used a synthetic multilayer consisting of low-Z (Si) and high-Z (W) metals to set up standing waves with periods of tens of Ångstroms. Alternatively, the standing wave may be formed at the metal surface by interference between the primary beam at grazing incidence and a secondary beam undergoing total external reflection (see section 4.3.2.3). Bedzyk et al.[410] were able to show that the distribution of Zn(II) cations near the negatively charged, polymerized phospholipid membrane is consistent with a Gouy–Chapman–Stern model and not with the Helmholtz model and that the Debye length increases with increasing pH. Experiments by Abruna et al.[411] examined iodine adsorption on Pt using X-ray standing waves generated from C/Pt multilayers. Although their results were not quantified in terms of the adsorption profile, they did show that this method can be used to probe ion distributions in the diffuse layer without the use of phospholipid films. The most important results of these XSW studies is that they show that this approach can be used to directly measure the diffuse layer structure.

Although these examples are of a limited value for metal oxide−water interfaces, it is clear that a similar application of the XSW method to metal ion distributions at metal oxide−aqueous solution interfaces should produce critically needed information about the nature of the aqueous metal ion distribution in the electrical double layer. Such work is now underway on the distribution of Zn(II) ions in the interfacial region of the α-Al_2O_3 (0001)−aqueous solution interface.[412]

4.3.3.5. Structure and Properties of Interfacial Water. Evidence for molecular layering of water at surfaces has been obtained from mica/electrolyte/mica surface force experiments.[413−415] Damped, oscillatory force-separation curves were observed in KCl (0.001 M) and NaCl (0.1−1.0 M) for mica−mica separations of $\leq$15 Å. The average periodicity for the oscillatory force was 2.5 ± 0.3 and 3.0 ± 0.5 Å in KCl and NaCl, respectively. Since this spacing is about the hard-sphere diameter of water, these data were interpreted as due to the ordered layering of water near the mica surface. Implicit in this interpretation is a model in which the water layers pack like hard spheres near the surface. Since the mica surface has a large negative charge density, the water near the surface (that sensed by the experiment) contains a large cation concentration (e.g., $\approx$10 M).[416] The importance of these ions in the observation is unclear. Like AFM, this method is actually measuring the structure of water *between* two interfaces, not at a single interface, and thus may not be representative of a single oxide−water interface.

The properties of water near metal oxide and clay mineral surfaces have been examined using measurements of the dielectric constant (ratio of static permittivity to the permittivity of a vacuum), dielectric relaxation (dipole response to an alternating external field), and dielectric loss (heat loss from relaxation).[5,417] As in heat of immersion studies, dielectric measurements are usually conducted on high-surface area powders exposed to variable amounts of water vapor. Surface coverage is often expressed as a function of a monolayer(s) of adsorbed water using the BET method and assuming a cross-sectional area for the water molecule (usually in the range of 10−12 Å^2). The dielectric measurements show, in general, that water molecules near a metal oxide surface are less able to reorient their dipoles in the presence of an electric field than they are in bulk water, similar to the dielectric response of ice. These results are similar to those for water near metal electrode surfaces discussed later in this section. This behavior has been attributed to stronger hydrogen bonding of the adsorbed water and an increase in molecular orientation or ordering relative to that of liquid water.[418] Despite a number of investigations (see summaries in refs 417, 419, and 420), there is little agreement on the values of the static dielectric constant of water, ϵ_s, near a metal oxide surface due, in part, to the difficulty of distinguishing between electrical effects from the surface and from the aqueous solution and to differences in experimental technique.[5] For water near insulating metal oxide surfaces that have been studied, ϵ_s is significantly lower than its value in liquid water (78.2 at 298 K), perhaps as low as 2−10 for the first monolayer of adsorbed water, and increases with adsorption of multiple layers of water. A reduction in solvent permittivity would favor the formation of metal adsorption complexes of low charge density (e.g., neutral or polar species) near a surface (see, e.g., refs 421 and 422). The low permittivity would also favor ion pairing.

To date, there have been very few direct structure-sensitive, in situ experiments to probe the arrangement of water molecules at the inner layer in metal oxide−aqueous solution interfaces. One such experiment by Fenter et al.[423] used crystal truncation rod measurements to probe the calcite $(10\bar{1}4)$−water interface at near-neutral solution pH. The CTR data are consistent with relaxation of the outermost layer of calcite, involving a rotation of carbonate groups such that they are nearly coplanar with the $(10\bar{1}4)$ cleavage surface. Perhaps more significant, in the context of the diffuse layer, is the finding that the CTR data are consistent with a monolayer of water located about 2.4 Å above the first-layer Ca atoms. This experimental result is in good agreement with the predictions of a recent MD simulation of the calcite−water interface.[424] In addition, a few such experiments have been conducted at metal−electrolyte interfaces, and it is valuable to consider the results and conclusions of those. Before doing this, however, we note that much work has been done using differential capacitance measurements at metal−electrolyte interfaces to infer the distribution of water molecules in the inner water layer.[425] The conclusions of such experiments are based on many assumptions, and a discussion of these experiments falls outside the scope of this review.

Porter and Zinn[416,426] measured some of the interfacial properties of water using a novel tunnel junction device made by immersing two Hg electrodes in an aqueous nitrate solution. As the Hg surfaces were brought together in the solution (at zero bias), discrete changes in the tunnel junction conductance were observed. These data were interpreted as indicating time-averaged structuring, or layering, of water extending about 0.8 nm from the metal surface. Although convincing, the method required a number of assumptions about the tunnel junction, which are difficult to verify independently. Furthermore, as in surface force experiments, this method measures the structure of water between two interfaces.

Recently, X-ray scattering has been used to probe the water distribution at charged Ag (111)−electrolyte interfaces.[330,331] The intensities of the nonspecular and specular truncation rods (see section 4.3.2.1.) were measured. Recall that the former is dependent only on the Ag (111) surface structure, while the latter depends on both the Ag (111) surface and the water distribution near the interface. Thus, measurement of both permits an independent determination of the electrode surface structure and the water

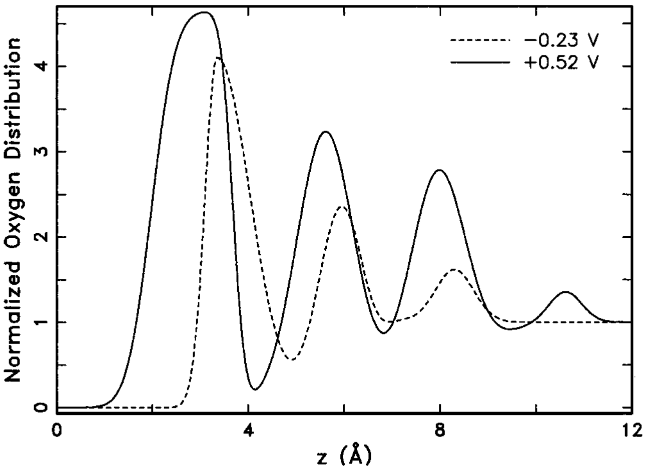

Figure 28. Best fit models of the normalized oxygen distributions for water near Ag (111) at -0.23 V (dashed) and $+0.52$ V (solid) of the pH_{PZC}. Here **z** is distance above the top Ag (111) atomic plane (e.g., distance from the ion cores). These distribution functions are normalized to their value far from the interface (e.g., 3.34×10^{22} cm^{-3}). Note that X-ray experiments are insensitive to the hydrogen atoms and measure only the oxygen spatial distribution. (Reprinted by permission from *Nature* (ref 330) copyright (1994) Macmillan Magazines, Ltd.)

distribution. It is important to note that the sensitivity of this method depends on the atomic number of the substrate: more sensitivity to the water distribution is achieved with a lower *Z* electrode. Furthermore, smooth surfaces are required.

These X-ray experiments[330,331] were conducted at the Ag (111) surface in contact with 0.1 M NaF at two potentials: $+0.52$ V from the potential of zero charge (PZC) and -0.23 V from the pH_{PZC}, corresponding to surface charge densities of about $+25$ and -10 mC/cm^2, respectively. The results are summarized in Figure 28, which shows the normalized oxygen distributions for water, where **z** is the distance from the top Ag (111) atomic plane. This distribution is proportional to the probability of finding an oxygen nucleus at a distance **z** from the electrode. Figure 28 illustrates several important features of the water structure. First, the water is ordered in layers extending about three molecular diameters from the electrode. This is qualitatively consistent with the layering predicted by computer simulations[389−397] and observed in the mica/electrolyte/mica surface force experiments[413−415] and tunnel junction conductance measurements.[416,426] Second, Figure 28 shows that the spacing between the electrode and inner-layer oxygen atoms is larger at -0.23 V than at $+0.52$ V, specifically 3.7 and 2.7 Å, respectively. This change provides definitive evidence for water reorientation from oxygen-up to oxygen-down as the electrode charge changes from negative to positive (see Figure 24). The most remarkable result of the distribution profiles in Figure 28 is that the areal densities (e.g., the coverage or the number of inner-layer water molecules per unit area) in the inner layer are larger than expected from the bulk density of water and from previous work. The expected areal density based on the bulk water density is 1.2×10^{15} cm^{-2}, while densities of 1.6×10^{15} and 2.6×10^{15} cm^{-2} at -0.23 and $+0.52$ V, respectively, were deduced. This large density is qualitatively explained as resulting from the large electric field ($\approx 10^7$ V/cm) at the charged electrode;[331] this field orients the dipoles of the inner-layer molecules, creating a force that pulls water molecules from the bulk electrolyte into the inner layer or electrical double layer (where the free energy is lower).

The results of the experiments on Ag show that the structure of water at charged interfaces is determined by more complicated factors than simple steric packing. This points out the significant limitations of models of solid−aqueous solution interfaces that treat water molecules as hard spheres and ignore the effect that the electric field can have in increasing the inner-layer density. The results also show that, for the potentials investigated, the inner layer cannot exist as an "icelike" structure, since the areal density of this is much smaller than observed. These points must be born in mind when modeling metal oxide−aqueous solution interfaces.

4.3.3.6. NMR Studies of Water in the Interfacial Region. There is a rich literature on the study of proton NMR relaxation in water on high-surface area substrates of the metal oxide type.[160−177] Most of this work has been carried out in a "low-resolution" mode (i.e., no chemical shift information) and on either silica[160−168] or clay systems.[171−177] Detailed and often elegant treatments of apparent multicomponent relaxation behavior have led to models for the various states or "phases" of water in these systems and their degrees of mobility. The common features of most of the models used to interpret low-resolution relaxation data involve the following three types of contributions to the proton NMR signals: (1) hydroxyl groups of the metal oxide surface, (2) surface-bound water, and (3) "free" (or unbound) water. Experimentally, a distinction between the two categories of water has been made on the basis of freezing behavior: surface-bonded water experiences a very strong freezing point depression, while "free" water freezes such as bulk water. Spin exchange among the three types of protons has been characterized (presumably via cross-relaxation) between metal oxide surface hydroxyl groups and surface-bonded water and via chemical exchange between surface-bonded and "free" water. This "three-phase" proton relaxation behavior has been related quantitatively to pore size and volume in silicas. The diffusion of water in clay has been characterized by magnetic field gradient techniques.[154] Other aspects of water adsorbed on metal oxide surfaces have been studied by high-resolution NMR techniques.

4.3.4. Geometric Structure of Metal Oxide Surfaces in Contact with Bulk Water

The only metal oxide whose surface structure has been studied to date in an aqueous environment using AFM is α-Fe_2O_3 (0001).[427,428] This surface consistently gives a 5- × 5-Å hexagonal AFM pattern, as expected for the uppermost Fe atoms in Figure 4. This is not surprising because it agrees with the unit-cell-scale periodicity of the hematite (0001) surface. However, because these uppermost Fe atoms should be coordinated by water molecules, a 3- × 3-Å hexagonal pattern much like that calculated for STM images of α-Fe_2O_3 (0001)[129] is also a strong possibility. The fact that such a pattern is not observed suggests that the AFM is probably not capable of true atomic-scale resolution given the contact force and tip-size limitations of the imaging conditions used.[46]

4.4. Chemical Reactions at Aqueous Solution–Metal Oxide Interfaces

4.4.1. Conceptual Models of Sorption of Aqueous Inorganic and Organic Species at Metal Oxide Surfaces

This section considers conceptual models of sorption of inorganic and organic species at the metal oxide−aqueous solution interface, followed by a review of selected experimental studies of sorption processes at those interfaces.

4.4.1.1. Sorption of Aqueous Inorganic Species. When aqueous metal cation and anion species partition from aqueous solution to a solid surface, this process is termed *sorption*, and the added cation or anion is referred to as an *adsorbate* or an *adion*. The solid phase involved in sorption reactions is referred to as the *adsorbent*. Sorption reactions on a metal oxide surface may result in the loss of one or more waters of hydration from the adsorbate ion and the formation of a relatively strong chemical bond(s) between adsorbate and adsorbent. This process is known as *specific adsorption* or *chemisorption*, and the adsorbed species is referred to as an *inner-sphere adsorption complex*. In general, strongly coordinated surface species are relatively immobile and are much less likely to detach or desorb from metal oxide surfaces as solution conditions change, such as an increase in ionic strength and change in pH. A weaker interaction may occur between a hydrated ion and a metal oxide surface in which waters of hydration are retained. In this case, the adsorbate is not bonded directly to the surface, and the attraction is due mainly to longer range electrostatic forces and hydrogen bonding. Adsorption of this type is termed *nonspecific*, and the adsorbed species is referred to as an *outer-sphere adsorption complex*. These more weakly sorbed species are much more likely to desorb under changing solution conditions.

The chemical/physical processes responsible for sorption on a nondissolving metal oxide surface can be described as follows. First, the reactant species must diffuse through the aqueous solution to the surface where it can be elastically or inelastically scattered back into solution or sorb onto the surface. Assuming that specific sorption of a monomeric species occurs, the adsorbed species will diffuse on the surface until an energetically favorable surface site is found. The most reactive sites on a metal oxide surface are often defect sites (see sections 2.1 and 4.2.1), although little is known about the nature of defect sites on a wet metal oxide surface. Other monomeric species may diffuse to the location of another monomeric surface species, resulting in the formation of hydroxo-bridged dimers and more complex cation−hydroxide oligomers. As the surface loading of a cation increases, this process of oligomerization should continue, resulting in the formation of larger three-dimensional clusters. Sorption may also involve formation of a precipitate on the metal oxide surface, which is characterized by a three-dimensional structure that may or may not be crystalline. Precipitates may coat the host oxide surface, entirely masking its properties. The precipitate-coated surface comprises a new sorption host and may be more or less reactive than the original, depending on physical form and surface area, the concentrations and types of defects, and the Lewis acid or base properties of the resulting surface sites. Species sorbed onto the original surface may be buried by the precipitate or incorporated into it, thus becoming less likely or slower to desorb when solution conditions change. Surface precipitates can be quite complex. Two distinct solids may precipitate together, or *coprecipitate*, in such an intimate mixture that they cannot be distinguished easily, resulting in a mixed-cation precipitate which may or may not be specifically associated with the metal oxide surface. Alternatively, several anions and cations of similar size and charge may coprecipitate or codeposit into a single structure forming a true *solid solution*. The term *<u>ab</u>sorption* refers to sorption processes through which the adsorbate becomes incorporated into the structure of the adsorbent, including sorption followed by solid-state diffusion and coprecipitation during dynamic recrystallization of the adsorbent itself. Another common process involves dissolution of the metal oxide followed by reprecipitation, which may incorporate the sorbate ion and result in the growth of a mixed-cation hydroxide or oxyhydroxide on the nanometer or larger scale. It is also possible in mixed-component systems (e.g., when the aqueous solution in contact with a metal oxide surface contains dissolved CO_2, PO_4^{3-}, or SO_4^{2-}) that more complex solid phases may form. The metal oxide−solution interface is a very dynamic region characterized by sorption, desorption, growth, and dissolution processes.

The amount of time that a species spends sorbed to the surface of the solid prior to desorption (or reaction) is fundamentally important to modeling transport of aqueous solute species. These chemical and physical interfacial processes have geochemical significance because the propensity of a natural metal oxide, oxyhydroxide, or hydroxide to sorb contaminants determines the mobility of waste products in the subsurface. In particular, the uptake and retention of contaminants by minerals in soils are directly reflected in measurements of contaminant plume shapes and concentrations in soil water or groundwater. Sorbates can subsequently participate in chemical reactions at the surface, producing products that eventually desorb back into the original phase and are transported away from the surface. In an alternate pathway, reactants can dissociate “immediately” upon contact with the solid surface, diffuse on the surface to some new location, recombine with some other moiety, and subsequently desorb. Information about the energetics of these different pathways and the reactant and product states can be derived from quantum mechanical calculations. The goal of atomic-level studies is to investigate the processes that drive these elementary reactions.

Further complications may arise if the adsorbate ion or molecule can be oxidized or reduced. For example, in some solutions the toxic, mobile Cr(VI) species is reduced to less toxic and much less mobile Cr(III) when sorbed onto Fe_3O_4 (magnetite) and other minerals that contain elements capable of donating electrons to Cr(VI). In this and similar cases, the adsorbent plays an active chemical role in the redox process (see section 4.4.3.4). Redox reactions can also be mediated by some redox-insensitive adsorbents when two species, each capable of existing in more than one oxidation state, cosorb. For example, reduction of Fe(III) by organic acids is enhanced in the presence of some inorganic oxides and clay minerals. Redox reactions at metal oxide surfaces may be *photosensitive*, i.e., catalyzed by light. Little is known about precisely how these reactions occur, e.g., whether the solid plays a direct role in electron transfer, alters the electronic structure of the sorbed species to facilitate transfer, or simply binds the reactants in close proximity.

Sorption alone does not dictate the fate of adsorbed species. Very small (nanometer- to micron-sized or colloidal) adsorbent particles may interact with each other and *coagulate* or *agglomerate* (bind together) forming aggregates. Small particles formed by homogeneous precipitation may agglomerate or *heterocoagulate* with other small particles in the system, or adhere to the surface of larger particles. Agglomeration and heterocoagulation may reduce the apparent mobility of adsorbed species carried by their constituent solid particles. Agglomeration is sensitive to solution composition, however, and under some conditions colloidal particles may remain dispersed and move with local groundwater or surface water, thus enhancing mobility of sorbed species.

4.4.1.2. Factors Affecting Sorption of Inorganic Species on Metal Oxide Surfaces. How strongly an aqueous metal ion binds to a metal oxide surface depends on a number of factors, including:

- the intrinsic nature of the surface, i.e., the surface charge as a function of pH, the double-layer properties, and the number and nature of reactive surface sites, including defects;
- the presence of organic and/or inorganic coatings on particle surfaces (e.g., fulvic and humic substances or oxyhydroxides of Al, Fe, or Mn), how these coatings affect the intrinsic properties of the particle surface, and the surface properties and reactive sites of the coatings;
- the pH and ionic strength of the solution, the total concentration of the aqueous metal ion of interest, and the metal ion-to-solid ratio;
- the coordination chemistry of the aqueous metal ion and possible changes in coordination chemistry during sorption, including cation coordination number, valence state, and hydrolysis;
- the mode of adsorbate bonding to the surface, e.g., inner-sphere, outer-sphere, or as a surface precipitate;
- the possibility that the adsorbent can act as a reductant or oxidant for aqueous metal ions that exist in different oxidation states;
- the effect of other complexants in solution such as organic species and CO_3^{2-}, which can cause either desorption of the metal ion or enhanced adsorption;
- the presence and reactivity of other adsorbates (e.g., PO_4^{3-} or SO_4^{2-}), which can compete with a metal ion for reactive surface sites; and
- the presence of microorganisms, which can affect the mechanisms and rates of surface species transformations.

Another important, but little explored, variable in this context is time; possible changes in the nature of the adsorbate or the surface with time can result in an increase or decrease in ease of desorption. Sorption processes are quite complicated because of these and other factors. To assess and understand their effects on metal ion sorption, the problem must be broken down into small, well-defined pieces that can be studied at a fundamental level.

4.4.1.3. Sorption of Organic Species on Metal Oxide Surfaces. Dissolved organic compounds and ions such as hydrocarbons, pesticides, and detergents also sorb onto metal oxide surfaces. Like inorganic species, organics can sorb onto metal oxide surfaces by various mechanisms, weakly or strongly, with correspondingly little or great retention by the metal oxide. They can also be transformed into different species during sorption reactions, such as dehalogenation of trichloroethylene on Fe_3O_4. Organic molecules such as the simple hydrocarbons (e.g., octane from gasoline) or halocarbons (e.g., carbon tetrachloride), for example, are not thought to form complexes with specific reactive sites on metal oxide surfaces as readily as do metal ions, but they do sorb through *hydrophobic bonding*. Hydrophobic bonding arises from changes in the structure of water near the organic molecule and the surface when the two are in close proximity.[387] The effect is widely observed in the natural environment but is poorly understood because little is known about the structure and properties of water near uncharged molecules or metal oxide surfaces. Better understanding of water structure and hydrophobic bonding could possibly lead to predictive methods and techniques for controlling sorption of nonpolar organic contaminants.

In contrast to the nonionic, nonpolar hydrocarbons, many environmentally significant organic molecules contain polar, ionizable parts or *functional groups*. For example, alcohols contain the hydroxyl functional group, soaps and some detergents contain the carboxylate group, and some personal care products and animal wastes contain the amine group. Through reaction of functional groups with reactive sites on metal oxide surfaces, organic molecules and ions can sorb relatively strongly. The strength of sorption depends strongly on the shape of the particular organic molecule and the location of the functional group relative to other parts of the molecule. However, it also depends on the polarity and ease of ionization of the group itself and its affinity for the sorbing site. Thus the members of a closely related family of organic compounds are likely to behave quite differently in terms of their adsorption behavior at metal oxide−aqueous solution interfaces. Some may form strong, inner-sphere complexes with the surface, while others are prevented from doing so by interference of other parts of the molecule and can form only weaker bonds, such as hydrogen bonds or van der Waals interactions. Finally, sorption of organic ions can be hindered or enhanced by the presence of dissolved inorganic compounds or other organic compounds, here termed *modifiers*. Sorption inhibition occurs when the interaction of the modifier with the potential sorbing organic forms a new, nonsorbing but soluble species. Enhancement can occur when the modifiers, the organic molecule or ion, and the surface form a ternary surface complex. Conceptual models have been developed to explain which types of interaction inhibit and which enhance sorption,[429,430] but more detailed understanding of the composition and structure of ternary complexes, and the factors that influence bond strength and configuration, is needed before quantitative use can be made of these models.

Finally, organic molecules that are *heteropolar*, i.e., that possess both polar (or ionic) and nonpolar portions, are often unusually *surface-active*. They sorb at air−water and metal oxide−water interfaces strongly. At the metal oxide−water interface it is thought that the polar functional group binds specifically to surface sites, while the nonpolar, hydrophobic portion of the molecule extends into the solution side of the interface. As the concentration of the surfactant on the surface increases, the nonpolar portions of adjacent sorbed molecules interact, forming clusters (*hemimicelles*) or bilayers (*admicelles*). These phenomena alter the relative wetability of the surface by hydrocarbons and water and the relative affinity of the solid for sorption of other organics, and thus the efficiency of petroleum recovery methods and/or environmental remediation technologies.

There have been a few in situ studies (i.e., with bulk water or another solvent such as methanol present) of the structure and growth of organic films on substrates such as octadecylphosphonic acid on mica using AFM methods[431] and stearic acid on calcite using X-ray reflectivity methods.[432] In addition, there have been a number of ex situ studies of the structure and interaction of organic molecules with metal oxide substrates. For example, Chambers et al. [433] determined the structure and bonding of formic acid on TiO_2 (110) using photoelectron diffraction.

4.4.1.4. Sorption of Metal−Organic Complexes on Metal Oxide Surfaces. In many environmental settings, the presence of organic ligands that form stable complexes with metal cations can strongly influence their sorption behavior to metal oxides, including those of Al and Fe. For example, Co(II) forms strong complexes with ligands such as ethylenediaminetetraacetic acid (EDTA) and nitrilotriacetic acid (NTA), and complexes of this type sorb to oxide surfaces in a fashion analogous to that of the bare ligand (e.g., EDTA, NTA) rather than the metal cation.[434,435] The sorption of these complexes increases with decreasing pH, until a pH is reached where the proton-promoted dissolution of the solid releases sufficient structural metal to induce competitive complex dissociation. Fe and Al oxide surfaces show high affinity for natural organic molecules containing carboxylate functional groups,[436] and these surfaces may be coated with a veneer of sorbed organic molecules in surface soils and aquatic sediments. Co(II) adsorption to both γ-Al$(OH)_3$ (gibbsite) and α-FeOOH (goethite), as well as natural materials containing these oxides, is enhanced by the presence of sorbed organic matter, which appears to function as a cocomplexant along with the oxide surface.[437]

A recent study by Cheah et al.[438] illustrates the significant effect that some organic ligands can have on metal adsorption at metal oxide−water interfaces. Cu(II) sorbs on γ-Al_2O_3 more strongly at low pH ($\approx$4) than on amorphous silica.[439,440] However, pyridine enhances Cu(II) sorption on am-SiO_2,[441] but inhibits uptake of Cu(II) on γ-Al_2O_3 relative to the bipyridine-free system.[438] Based on Cu(II) K-edge XAFS spectra, EPR, and UV−vis spectra, Cheah et al.[438] concluded that Cu(II) sorbs predominantly as dimeric complexes on the am-SiO_2 surface and as monomeric complexes on the γ-Al_2O_3 surface. In addition, the solution Cu(II)$(bipy)_2$ complex loses one of the bipy groups when it sorbs on the γ-Al_2O_3 surface but retains both bipy molecules when it sorbs on the am-SiO_2 surface. Hydrophobic bonding and the energy required to cleave the Cu(II)−bipy bonds are among the factors thought to be responsible for the enhanced uptake of Cu(II)$(bipy)_2$ on am-SiO_2 relative to γ-Al_2O_3. There are numerous examples where organic ligands can inhibit or enhance metal ion sorption, usually resulting in the formation of ternary complexes, but very little is known about the reasons for these effects at the molecular level or how the metal−organic complex bonds to an oxide surface.

An excellent summary of the interaction of selected organic molecules with oxide surfaces is given by Barteau,[442] with an emphasis on surface acid−base, redox, and adsorbate reactions on clean, well-defined oxide surfaces.

4.4.2. Experimental Studies of Metal Cation and Oxoanion Sorption at Metal Oxide–Aqueous Solution Interfaces

4.4.2.1. Macroscopic Approach to the Adsorption of Cations and Anions on Metal Oxides. A macroscopic approach commonly used to study how strongly an aqueous metal ion binds to a particle surface is the wet chemical measurement of adsorption isotherms as a function of pH, ionic strength, and total metal ion concentration, in the presence or absence of other metal ions, oxyanions, or organic coadsorbents. For example, it is often assumed that significant inhibition of adsorption with increasing ionic strength at a given pH indicates that the sorption complexes are dominantly of the weakly bound, outer-sphere type.[443] In contrast, when there is little or no dependence of metal ion sorption on ionic strength, the sorption complex is assumed to be more strongly bound as an inner-sphere type complex. Even when there is little ionic strength dependence of metal ion sorption, the pH_{ads} relative to the pH_{PZC} of the oxide can be used to infer differences in relative strength of binding as a function of pH (pH_{ads} is defined as the pH value at 50% uptake of the metal ion). Below, we present

Table 4. Uptake Data for Aqueous Co(II) on Selected Oxides

oxide	pH$_{PZC}$	surface area (m^2/L)	ΣCo (M)	ΣCo/Σ sites	ionic strength (M)	ref
α-SiO$_2$	2−3	75	1.2×10^{-4}	0.001_9	0.001	444
TiO$_2$ (rutile)	5.5	115	1.1×10^{-5}	0.004_7	0.001	444
α-Fe$_2$O$_3$	7.9	26.6	1.0×10^{-6}	0.003_8	0.1	445
γ-Al$_2$O$_3$	8.5	1170	1.0×10^{-4}	0.006_5	0.1	446

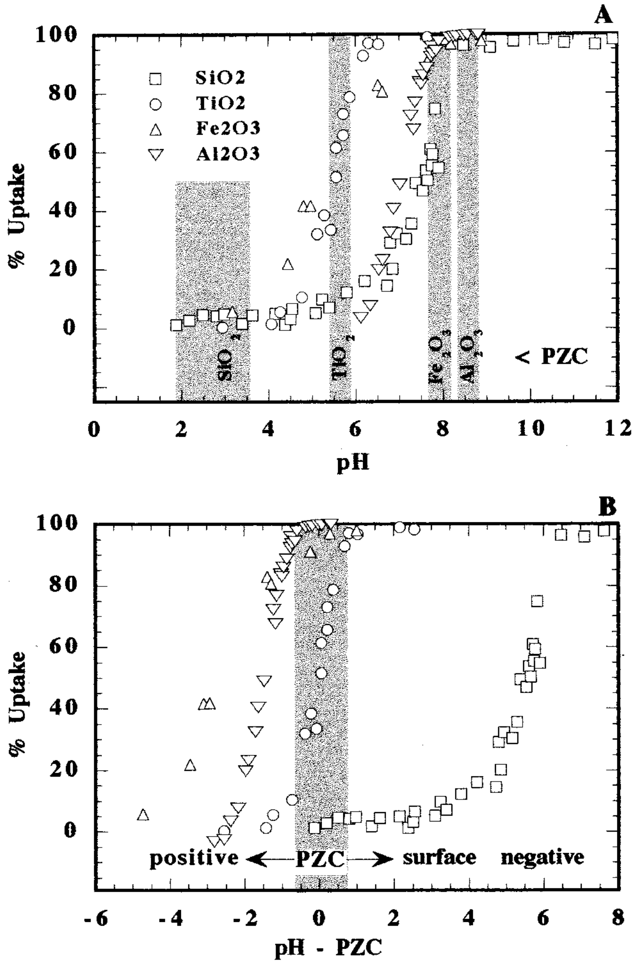

Figure 29. Sorption of Co(II) on four oxides, α-SiO$_2$, TiO$_2$ (rutile), α-Fe$_2$O$_3$, and γ-Al$_2$O$_3$, showing (A) pH dependence and (B) relative influence of the pH$_{PZC}$.

macroscopic wet chemical uptake data for Co(II) sorption on several metal oxides whose pH$_{PZC}$ values, surface areas, and solution conditions are given in Table 4.

Figure 29a shows the uptake of aqueous Co(II) onto α-SiO$_2$, TiO$_2$ (rutile), α-Fe$_2$O$_3$, and γ-Al$_2$O$_3$ for a relatively constant ionic strength. The trend shown (increasing uptake with increasing pH until a plateau is reached) is typical of cation adsorption on metal oxides. The opposite trend is typical of anions, including oxoanions. The vertical bands, representing pH$_{PZC}$ values for the four oxides, show the range of pH$_{PZC}$ values reported in the literature. The uptake data have been corrected for differences in surface area and estimated number of reactive surface sites of the respective solids, resulting in a relatively constant ratio of ΣCo(II):Σsites of 0.002−0.006. The pH$_{PZC}$ values of these surfaces differ significantly, ranging from about pH 2−3 for α-SiO$_2$ to pH 8.5 for γ-Al$_2$O$_3$.[447] Below the pH$_{PZC}$ of the solid, the surface is positively charged, indicating an excess of surface protons, whereas above the pH$_{PZC}$ the surface is negatively charged, indicating a proton deficiency. Aqueous Co(II) does not sorb significantly on the α-SiO$_2$ surface until well above the pH$_{PZC}$ of α-SiO$_2$, where the surface is negatively charged. In contrast, uptake of Co(II) on γ-Al$_2$O$_3$ and α-Fe$_2$O$_3$ is essentially complete below their respective pH$_{PZC}$ values, where the surfaces are positively charged. These differences can be more clearly seen in Figure 29b, which plots pH$_{ads}$ − pH$_{PZC}$ vs percent uptake for Co(II) on these solids. They suggest that Co(II) binds more strongly to the γ-Al$_2$O$_3$ and α-Fe$_2$O$_3$ surfaces than to the α-SiO$_2$ surface. The uptake behavior of Co(II) on TiO$_2$ (rutile) is intermediate between these two cases, with uptake beginning below the pH$_{PZC}$ and reaching 100% above pH$_{PZC}$. A more thorough understanding of adsorbate binding at oxide−water interfaces as a function of pH requires that the different contributions to the free energy of sorption be defined.

The free energy of sorption comprises several contributions, including: (1) the bond energy of sorption (short-range covalent and ionic bonding and hydrogen bonding); (2) long-range electrostatic attraction to charged surfaces (responsible for the accumulation of the diffuse ion layer in the electrical double layer); (3) hydrophobic bonding and the energy contributions due to changes in the extent and/or structure of hydration of both the surface and adion; and (4) the energy involved in protonation/deprotonation of the sorption sites and hydrolysis of the adion (either before or during sorption or precipitation). Cations that sorb predominantly through long-range electrostatic attraction should react primarily with negative surfaces ($pH > pH_{PZC}$). Cations that sorb at $pH < pH_{PZC}$ are sorbing even though long-range electrostatic forces are repulsive. In this case, sorption should be hindered. This suggests that free energy contributions from (1), (3), and (4) must be significantly stronger or more negative than that from long-range repulsive forces. The sorption of Co(II) on γ-Al$_2$O$_3$ and α-Fe$_2$O$_3$ should be of this type. If uptake begins just below pH$_{PZC}$, as for Co(II) sorption on TiO$_2$ (rutile), we might infer that (2) plays a significant role. If cation sorption is delayed to $pH \gg pH_{PZC}$, we might infer that free energy contributions (3) and/or (4) are positive, thus hindering cation sorption. Differences in the location of the adsorption edge of a single adion relative to the pH$_{PZC}$ reflect differences in the relative contributions of the different bonding forces. The properties of both the solid and the adsorbate contribute to the magnitude of these bonding forces, but for a given adsorbate which does not show significant changes in coordination chemistry in the aqueous solution as a function of pH, the solid must be primarily responsible for the differences.

4.4.2.2. XAFS Spectroscopic Studies of Aqueous Co(II) and Pb(II) Sorption onto Metal Oxide Surfaces. Adsorption isotherm measurements are usually performed on high-surface area powdered adsorbents, which expose a variety of crystallographic planes containing multiple types of reactive surface sites. While such measurements produce very useful and necessary information on uptake and can lead to interpretations of the type suggested above, they cannot provide direct information on the composition or structure of the sorbate, the stoichiometry and pathways of sorption reactions, or the types of surface sites to which the metal ion binds.[448,449] Such information is best obtained using direct spectroscopic probes that are sensitive to the local structural environment and valence state of the metal ion. X-ray absorption fine structure (XAFS) spectroscopy is one of the methods of choice for providing this type of information in a variety of aqueous metal ion−solid systems.[1,334,450−452] It is often desirable to conduct such studies at 298 K and 1 atm pressure in the presence of bulk water to mimic conditions at the earth's surface.

During the past few years, a growing number of groups have used XAFS spectroscopy, in combination with macroscopic uptake measurements and other molecular-scale probes such as XPS, FTIR, UV−vis, and EPR spectroscopies and transmission electron microscopy, to study surface complexation reactions of various metal ions on model oxide, oxyhydroxide, and silicate surfaces.[346,347,443,452−472] Such studies are typically done using fluorescence yield XAFS methods[342−344] as a function of surface metal ion loading and pH on high-surface area solids, with less than monolayer coverages of the adsorbate. The resulting information includes (1) the mode of sorption (inner- or outer-sphere complexes or precipitates: mono-, bi-, or tridentate binding); (2) the structure of the surface complex or precipitate (monomers, dimers, and/or more complex hydroxo-bridged metal ion oligomers); and (3) the composition of the surface complex or precipitate. Here we will focus on the results of (1) XAFS studies of Co(II) sorption on high-surface area α-SiO_2,[459] TiO_2 (rutile),[459] and γ-Al_2O_3;[473] (2) Pb(II) sorption on high-surface area α-Al_2O_3 and α-Fe_2O_3;[347,464] and (3) GI-XAFS studies of Co(II) and Pb(II) on oriented, single-crystal samples of α-Al_2O_3.[346,463,474] These studies have revealed differences in the molecular mode of sorption that help explain the observed differences in macroscopic uptake behavior discussed in section 4.4.2.1.

In situ powder XAFS studies of Co(II) sorption on α-SiO_2, TiO_2 (rutile), and γ-Al_2O_3 have revealed differences in the mode of sorption on the different oxides at similar surface coverages of Co.[454,459,473] On α-SiO_2, for example, aqueous Co(II) forms $Co(OH)_2$-like precipitates at low Co surface coverage. The abundance of second-neighbor Co and the very limited number of second-neighbor Si derived from the XAFS spectra suggest that octahedrally coordinated Co(II) adsorbs primarily in a bidentate fashion on other $Co(O,OH)_6$ octahedra rather than on SiO_4 tetrahedra. This observation can be explained by noting that the reactivity of the quartz surface should be limited by the presence of oxygens bridging between two silicon tetrahedra, which have a Pauling bond-valence sum of about 2.0 (where Pauling bond valence is defined as the charge on the ion divided by its coordination number and bond-valence sum is defined as the sum of bond valences of all bonds to an atom).[475] This surface bonding model predicts that this type of oxygen should be relatively unreactive, which helps explain why pH_{ads} for Co(II) is much higher than pH_{PZC} (Figure 29). In contrast, the surface of a growing $Co(OH)_2$-like structure should be more reactive, with the surface oxygens bonded to three six-coordinated Co(II), $^{[VI]}$Co(II), and most likely one H at the pH of the experiments. Another factor that may also play a role is the fact that the edge of a $Co(O,OH)_6$ octahedron is significantly longer than that of an SiO_4 tetrahedron. This difference should favor edge sharing between $Co(O,OH)_6$ octahedra over edge sharing between a $Co(O,OH)_6$ octahedron and an SiO_4 tetrahedron, although the latter type of polyhedral edge sharing is relatively common in silicate minerals. XAFS analysis of aqueous Co(II) sorption on TiO_2 (rutile) showed that the sorbed Co(II) ions occupy positions that are similar to those in the rutile or anatase structure, i.e., the sorbed complexes are simple extensions of the bulk structure. It was also found that the size of these surface complexes is smaller than those on quartz. The bond-valence model is consistent with this type of shared-edge structural arrangement locally, with sorbed protons present on oxygens requiring additional bond valence. A bond-valence sum of 2 on the surface oxygens to which Co(II) bonds cannot be maintained if this structure is propagated, which is consistent with the limited size of Co multinuclear complexes on rutile. Finally, sorption of Co(II) on γ-Al_2O_3, even at low sorption density, leads to relatively large multinuclear surface complexes, as indicated by the number of second-neighbor Co atoms.[454] There is also a clear indication of Co−Al pair correlations in the XAFS spectra, indicating that inner-sphere, bidentate bonding occurs, i.e., edge sharing between $Co(O,OH)_6$ and $Al(O,OH)_6$ octahedra. A recent solution uptake and XAFS study of Cu(II) sorption on high-surface area amorphous SiO_2 and γ-Al_2O_3 as a function of pH and Cu(II) solution concentration shows that the sorption products of Cu(II) on these surfaces are very similar to those formed by Co(II).[438]

One important result derived from several XAFS studies of the sorption of aqueous adsorbate ions, such as Co(II) and Ni(II), onto metal oxide surfaces is that a precipitate phase forms even when the solution concentration of the aqueous cation is less than that required to supersaturate the solution with respect to the cation hydroxide.[462,470,476] Sufficient amounts of the metal oxide substrate dissolve during the reaction period to result in the formation of a mixed-cation hydroxide (e.g., Co−Al hydroxide or Ni−Al hydroxide) that is less soluble than either end member cation hydroxide. This finding has important implications for the formation of unanticipated nanoscale precipitate phases in systems of geochemical and catalytic interest, resulting in the sequestering of contaminant ions in relatively insoluble solids and the production of new surfaces on which chemical reactions can occur.

Recent GI-XAFS studies of Co(II) and Pb(II) sorbed on α-Al_2O_3 (0001) and $(1\bar{1}02)$ surfaces[346,463,474,477] have found that Co(II) sorbs from aqueous solution as inner-sphere complexes on both the (0001) and (1$\bar{1}$02) surfaces, bonding in a dominantly tridentate fashion above tetrahedral interstices to surface OH^- groups at pH values near 8. Pb(II) was also found to bond in an inner-sphere fashion to the (1$\bar{1}$02) surface but formed a more weakly bonded outer-sphere complex on the (0001) surface at pH 7 (Figure 30).

These results can be rationalized using a simple short-range electrostatic surface bonding model[346] based on well-known crystal chemical principles. When one considers the different types of oxygens on the two perfectly terminated surfaces [oxygens are bonded to one or to three six-coordinated Al atoms, Al(VI), on the (1$\bar{1}$02) surface, whereas all oxygens on the (0001) surface are bonded to two Al(VI), Figure 31] and the differences in coordination chemistry of Co(II) and Pb(II) in aqueous solutions at pH 7 and 8, respectively, the formation of an outer-sphere Pb(II) complex on (0001) and an inner-sphere Pb(II) complex on (1$\bar{1}$02) is predicted. Also, Co(II) is predicted to form inner-sphere complexes on both surfaces, in agreement with observation. These predictions are based on the idea that the bond-valence sum to an oxygen should not deviate from 2.0 valence units (vu) by more than ±0.05 vu.[475] If the sum is lower than 2.0 vu for surface oxygens, the surface should react with ions in solution, including hydronium ions, until bond-valence saturation is achieved. If the sum is greater than 2.0 vu, desorption of ions from the surface should occur. This empirical model was adopted because there are no quantitative data on changes in the molecular-level contributions to the enthalpy and entropy of aqueous sorption systems (i.e., changes in bond energies, longer range electrostatic and hydrophobic forces, and hydrogen bonding and in vibrational and configurational contributions to entropy) as an aqueous metal ion approaches a charged or neutral interface through the diffuse swarm of ions and transforms from a solvated aqueous species to a solvated outer-sphere complex or partially solvated inner-sphere complex at an oxide–water interface. Using this model, predictions for Co(II) and Pb(II) bonding geometries are consistent with XAFS results.[346]

One key assumption made in the above XAFS and surface bonding analysis is that the α-Al_2O_3 (0001) and (1$\bar{1}$02) surfaces, after brief exposure to the Co- and Pb-containing aqueous solutions, are perfect terminations of the bulk. This assumption is supported by LEED studies of the samples prior to solution exposure, which show 1 × 1 LEED patterns consistent with little if any relaxation or reconstruction relative to the bulk structure, and by X-ray reflectivity studies, which give rms surface roughnesses of 1 and 3 Å, respectively, for the two surfaces. It is also supported by the GI-XAFS-derived Co–Al and Pb–Al distances and number of second Al neighbors,[347,464] which are consistent with the atomic arrangements on the α-Al_2O_3 (0001) and (1$\bar{1}$02) surfaces being the same as those in the bulk.

The studies discussed above have led to several new insights about metal ion sorption at oxide–water interfaces. First, different structural arrangements on crystallographically different surfaces of a given solid or on different solids may induce significant differences in mode of sorption of a given metal ion. This idea is implicit in the well-known MUSIC model[478,479] and more recent CD-MUSIC model of Hiemstra and Van Riemsdijk (see section 7.1.1),[480] but to our knowledge the GI-XAFS study of Pb(II) on different surfaces of α-Al_2O_3 is the first experimental verification of the idea for metal ion sorption at oxide–water interfaces. Second, the coordination chemistry of aqueous metal ions can be important in determining their mode of sorption and the reactive sites to which they can bind. For example, the difference in coordination chemistry of aqueous Pb(II) and Co(II) is largely responsible for their differences in sorption behavior on α-Al_2O_3. Third, the simple short-range electrostatic surface bonding model,[346] which is based on the bond-valence principle of Pauling[475] and the bond-valence–bond-length relationship of Brown and Shannon,[481] as revised by Brown and Altermatt,[482] can be used to predict the relative bonding affinities of different cations to different surface functional groups, including defective sites on hydrous oxide surfaces. Application of this surface bonding model to Pb(II) sorption on hydrous α-Al_2O_3 and α-Fe_2O_3 leads to the prediction that certain types of reactive sites do not lose their protons upon sorption of Pb(II).[347,464] This surface bonding model, which shares some characteristics with the one proposed by Ziolkowski,[483] but differs in several important ways, provides a framework for developing hypotheses about the relative bond strengths of different aqueous cations on oxide surfaces.

4.4.2.3. X-ray Scattering and XSW Studies of Precipitation and Pb(II) Sorption. Because of mineral oversaturation in natural waters, most minerals form by heterogeneous nucleation and growth. To better understand this process with the goal of developing accurate dissolution/precipitation rate laws, the growth of otavite ($CdCO_3$) on calcite (10$\bar{1}$4) was studied with surface X-ray scattering and low-angle specular reflectivity.[89] The experiments were conducted as a function of time after a small amount of otavite-saturated solution was introduced and was allowed to become oversaturated (through diffusion of CO_2 out of the solution). Low-angle reflectivity data were taken during the initial 900 min of otavite growth. These showed that (1) the growth rate was 15 Å/h; (2) the calcite–otavite interface roughness (≈15 Å) did not change with time and was equal to the initial calcite/fluid roughness; (3) the otavite–fluid roughness increased with time (from <5 to >15 Å); and (4) the otavite density was approximately 80% of the bulk density (which was unexplained but could result from alloying of the calcite and otavite). The scattering data showed that the otavite growth was well-oriented with the calcite. Furthermore, the otavite was initially compressed normal to the growth direction (by 2.2%) and became less compressed with time; in the substrate plane, the otavite was unstrained. The first observation is reasonable, since any epitaxial strain must be relieved as the otavite thickens, although one expects that there should also be in-

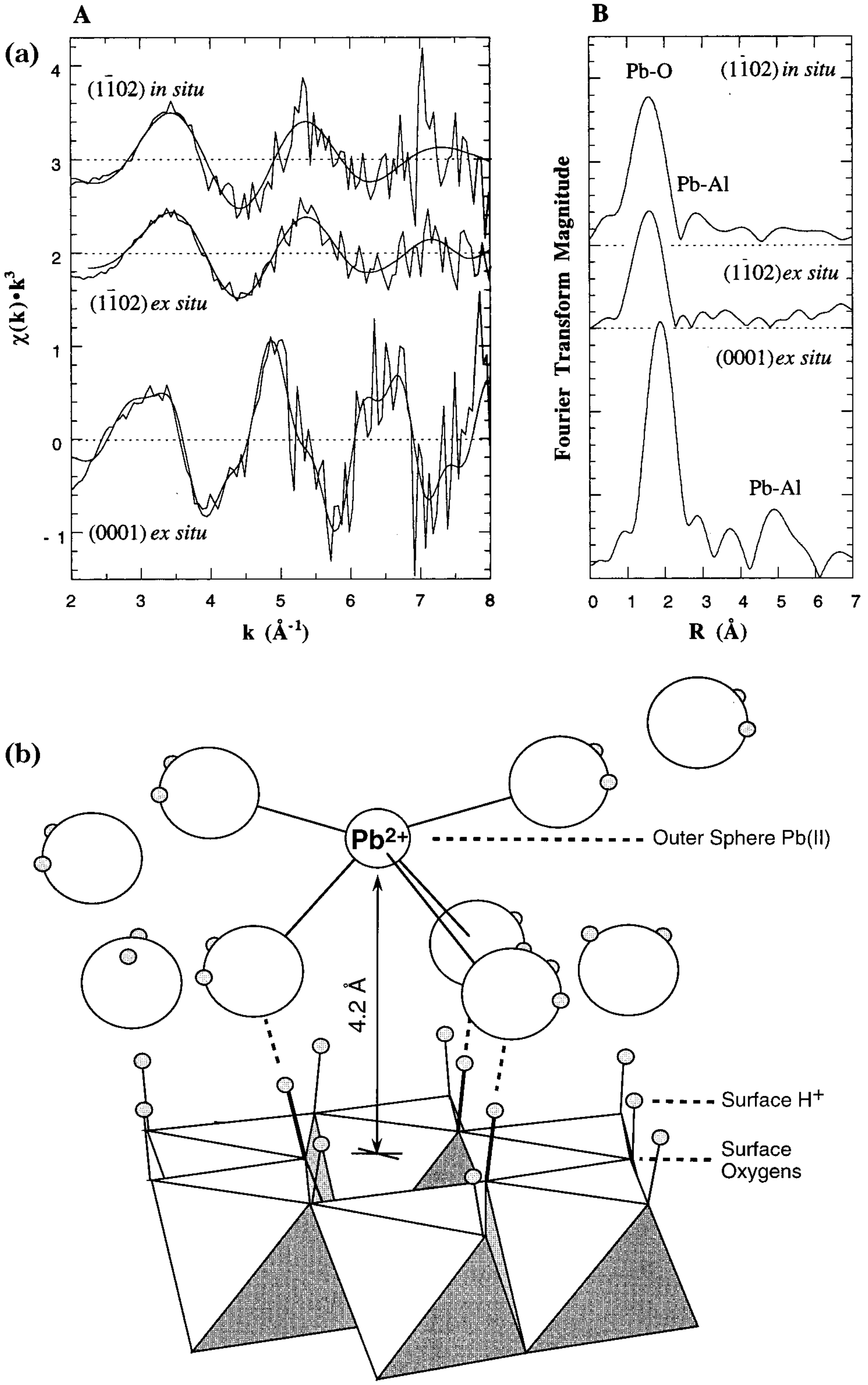

Figure 30. (a) (A) Normalized, k^3-weighted Pb L_{III}-EXAFS spectra of Pb(II)/α-Al_2O_3 single-crystal samples with fits to spectra overlaid (smooth lines). The fit to the in situ (102) sample spectrum contains no Al backscatterers. (B) Fourier transforms of EXAFS data in panel A uncorrected for phase shift. The large peak at 4.9 Å (corresponding to the fit value of 5.78 Å after correction for phase shift) in the (0001) sample Fourier transform indicates the presence of Al second neighbors. The peak at 3.8 Å in the (0001) spectrum is a Fourier ripple (artifact) from the Pb–O peak. (b) Schematic illustration of the specific adsorption of a solvated Pb(II) ion to an octahedral interstical site on the α-Al_2O_3 (0001) surface, represented by six AlO_6 octahedra. Hydrogen bonds are denoted by dashed lines. The Pb(II) adion is depicted as having at least five oxygen first neighbors in order to be consistent with the coordination chemistry of Pb(II) in crystalline hydrates and hydroxides, in which Pb(II) sites are often highly distorted. EXAFS studies of such compounds show that, due to the distortion of the Pb(II) first-neighbor shell, only the closest first-neighbor oxygens contribute to the EXAFS [three oxygens at ~2.5 Å in the case of Pb(II)/α-Al_2O_3 (0001)] and that an EXAFS-derived Pb–O bond length of ~2.5 Å is characteristic of coordination numbers = 5. (Panels a and b: Reprinted with permission from ref 463. Copyright 1996 Elsevier.)

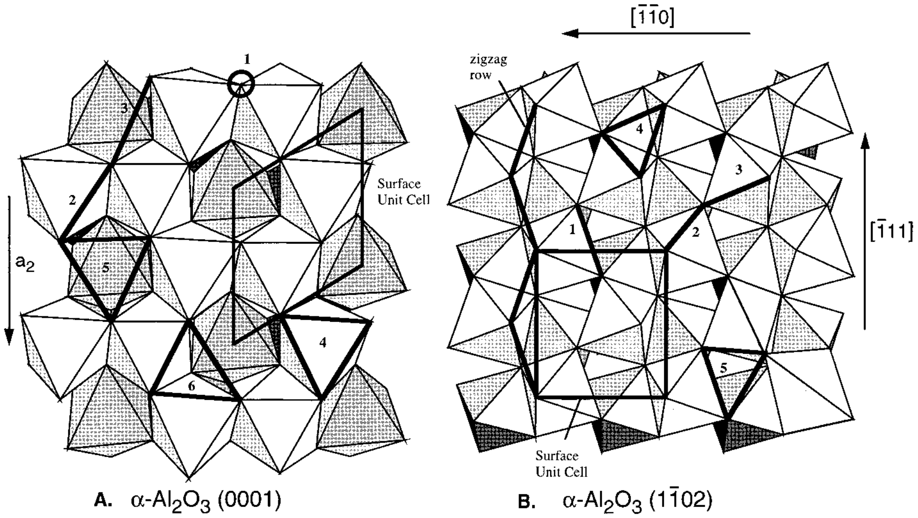

Figure 31. (A) Polyhedral representation of the oxygen-terminated α-Al_2O_3 (0001) surface. Unit cell edge length is 4.754 Å. (B) Polyhedral representation of the oxygen-terminated α-Al_2O_3 (102) surface. Surface unit cell edge lengths are 4.754 Å for the edge parallel to [0] and 5.127 Å for the edge parallel to [11], which is the projection of the *c*-axis. Some of the structural elements and possible binding sites (numbered) for metal ions are depicted with heavy black lines. (Reprinted with permission from ref 346. Copyright 1997 Academic Press.)

plane strain (which also decreases with growth thickness).

Lead is one of the most important toxic environmental contaminants and is also a strong X-ray scatterer (high *Z*). These considerations motivated a combined XSW and specular truncation rod study[87] to determine the position of submonolayer amounts of Pb(II) (≈0.05−0.10 monolayer) adsorbed onto calcite (10$\bar{1}$4). This example nicely illustrates how combined methods can be advantageously used for a clear structure determination. The Pb(II) was adsorbed from calcite-saturated aqueous solutions containing $CaCl_2$, $NaHCO_3$, and either HNO_3 or NH_4OH (final solution pH's of 8.0 or 9.0), which were mixed with a solution containing Pb nitrate and disodium EDTA (ethylenediaminetetraacetic acid). The EDTA was used to ensure understaturation of Pb-containing solid phases, so that only an adsorbed layer of Pb(II) formed. Note that the speciation of this solution is rather complex, with many species forming in addition to Pb(II). The XSW study used the triangulation method (see section 4.3.2.3) to determine that 60% (the coherent fraction) of the Pb(II) was adsorbed at the Ca sites in the calcite lattice and the remaining 40% was not well-ordered. However, the XSW measurements cannot determine the specific calcite layer where the ordered Pb(II) is adsorbed (e.g., at the surface or below the surface). Due to a rapid exchange between the calcite surface and ions in solution, it is not unreasonable to expect that Pb(II) is adsorbed below, or above, the oxide−solution interface. To resolve this question, specular truncation rod measurements were performed. These data showed that, to within experimental error, all of the ordered Pb(II) is adsorbed in the surface layer. Furthermore, to adequately fit these data, there must be significant relaxation of the oxygen atoms in the uppermost calcite layers (although these could not be specified with the present data set) and, possibly, the partially filled calcite layers. It is, at first glance, rather surprising that Pb(II) adsorbs at Ca(II) surface sites, because of the significantly larger size of Pb(II) relative to Ca(II) (1.20 vs 0.99 Å). However, this behavior can be rationalized on thermodynamic grounds.[87] We only note here that this microscopic information explains the unexpectedly strong adsorption of Pb onto calcite. The 40% disordered, adsorbed Pb(II) is speculated to be due to the weak physisorption of hydrated Pb(II) ions or Pb(II) complexes (e.g., Pb−EDTA).

These initial XSW and X-ray scattering and reflectivity studies show that these methods can provide useful microscopic information on the geometric structure and morphology at aqueous solution−metal oxide interfaces and that they hold much promise to further our understanding of these interfaces.

4.4.2.4. STM Study of Cr(III) Adsorbed on α-Fe_2O_3 from Aqueous Solution. There have been very few studies of adsorbates on metal oxide surfaces using SPM. This is in part because of the difficulties of doing so. For example, AFM is capable of true molecular or atomic resolution only under exceptional conditions (see section 2.2), so that we are aware of no studies of individual (monomeric) adsorbates on oxide surfaces by AFM. The scan rates used in SPM imaging are very slow (seconds) relative to adsorbate lifetimes and mobilities at the solid−solution interface. One of the few cases in which adsorbates are sufficiently immobile is that of Cr(III) adsorbed to hematite, α-Fe_2O_3, surfaces. Cr(III)(aq) has an extremely slow water exchange rate of $\approx 10^{-7}$ s^{-1}.[231,484] Indeed, to a first approximation, any aqueous adsorbate whose characteristic ligand-exchange rate (a property which is generally unknown for metals at oxide surfaces, though see section 4.1.1.4 for progress in this direction) is lower than that of the surface metal centers should have a surface lifetime and mobility that are limited by the surface rather than by the (slower) ligand-exchange properties of the sorbate.

Cr(III) adsorbed to α-Fe_2O_3 (0001) surfaces has been studied.[127,128] From image sequences lasting up

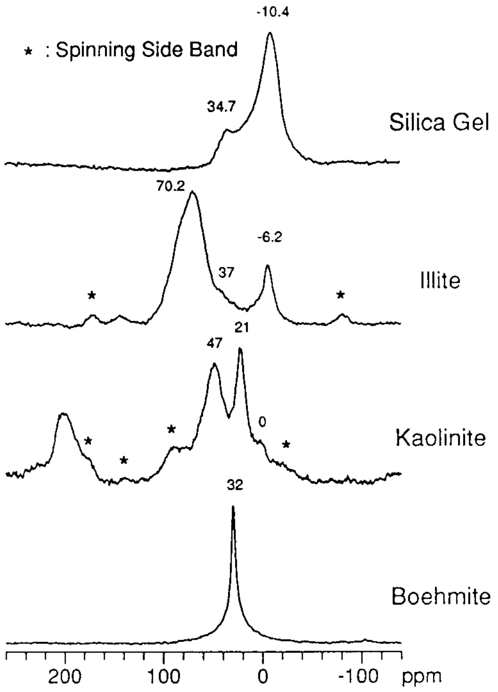

Figure 32. ^{133}Cs MAS NMR spectra of samples obtained by adsorption of 0.1 M CsCl(aq) on the indicated solids for 5 days.[182]

to 9 min, the lifetimes of adsorbates in single-surface sites were measured. From reasonable estimates of attempt frequency, an activation energy for desorption of about 45−50 kJ/mol was estimated.

Eggleston and Stumm,[128] as part of the STM imaging of adsorbed Cr(III) on α-Fe_2O_3 (0001), noted the presence of oligomeric surface clusters. In one case, they were able to observe a dimerization event. The Cr(III)-containing clusters were immobile in the time frame of the STM experiment.

4.4.2.5. NMR Studies of Cs and Other Ions Sorbed on Metal Oxides. There have been few published reports on the use of modern NMR techniques directed specifically at studying interfaces between binary metal oxides and aqueous electrolyte solutions. Perhaps the most extensive and promising studies are described in a recent publication by Kim et al.,[182] in which ^{133}Cs NMR was employed to study the state of Cs^+ in samples of Cs-exchanged silica gel (SiO_2) and boehmite, γ-AlO(OH), as well as the aluminosilicates illite and kaolinite. ^{133}Cs ($I = 7/2$) is especially attractive for such studies[181−185] because of its 100% natural isotopic abundance and its small nuclear electric quadrupole moment. These studies are also highly relevant to soil contamination by radioactive ^{137}Cs in connection with past production of nuclear weapons.

Figure 32 shows the ^{133}Cs NMR spectra reported by Kim et al.[182] on filtered samples prepared by adsorbing 0.1 M CsCl(aq) on the indicated adsorbates. The dependence of these kinds of spectra on variations in the concentration of the solution adsorbed, the humidity over the sample prior to loading in the magic-angle spinning (MAS) rotor, the manner or extent to which the sample was washed prior to loading in the rotor, and the temperature of the NMR measurements led the authors to identify various peaks as Cs^+ ions that are (a) bonded to the surface in the first coordination sphere, (b) interacting with the interface in only the second coordination sphere, (c) hydrated ions of the diffuse layer, or (d) CsCl(s) precipitated on the surface or, alternatively, exchange-averaged resonances resulting from site exchange between two or more sites. Confirming some of these tentative assignments is rendered difficult by the complexity of the systems, by the chemical exchange processes, and by the low signal-to-noise ratios often obtained in these kinds of spectra to date. Despite these difficulties, the reported studies clearly demonstrate a substantial promise for examining metal ions at the interface, as well as a need for improved NMR techniques to permit more definitive and quantitative interpretations.

Much more extensive than NMR studies of interfaces between binary metal oxides and aqueous electrolyte solutions have been analogous NMR studies involving various aluminosilicate minerals, especially clays. These studies have been based on a variety of NMR-active metal ions that are adsorbed and/or present in the aqueous electrolyte interface. These include, as above, ^{133}Cs,[181−185] as well as other alkali metal nuclides, including ^{7}Li,[186], ^{23}Na,[185−187] and ^{39}K,[188] and ^{111}Cd, and ^{113}Cd.[184,185,189,190] Much of this work has been hindered by some combination of broad and uncertain spectral patterns, compromised by low signal-to-noise characteristics and the complexities associated with chemical exchange effects. Although some of these studies have benefited from reducing chemical exchange rates by lowering the measurement temperature, most of these reports either have seemed to overinterpret marginally useful NMR data or have used NMR results that would be largely ambiguous on a stand-alone basis to provide support for prevailing views based on prior, non-NMR data. Probably the most convincing exception to this pattern is the variable-temperature ^{133}Cs NMR study of hectorite reported by Weiss et al.[183] This detailed study of both slurry and dried−humidified samples of CsCl(aq)−hectorite samples has shown that there are a number of different Cs^+ environments on the Cs-exchanged hectorite, their identities and dynamics depending on the hydration state and details of sample preparation. Chemical exchange between sites was observed in slurry and hydrated samples above about 203 K. The experimental strategies employed in this study, especially the extensive use of variable-temperature measurements, should prove useful for future NMR studies of interfaces between binary metal oxides and aqueous electrolytes.

4.4.2.6. EPR Studies of Adsorbates at the Metal Oxide−Aqueous Solution Interface. There have been a number of informative EPR studies of adsorbates of various types on metal oxide surfaces in contact with water and other solvents. An excellent review of some of this work with applications to heterogeneous catalysis can be found in ref 485. In addition, EPR spectroscopy has been used extensively in studies relevant to soils and aqueous surface chemistry. EPR studies relevant to adsorption phenomena in soils, for example, include the work of McBride and co-workers on the sorption of Cu(II), V(IV), Mn(II), and organic anions to various clays, metal oxyhydroxides, and natural organics[486−499] and the work of Bleam and co-workers on Cu(II) sorption on silica and boehmite.[500−502] Magnetic resonance studies relevant to aqueous surface chemistry include the EPR and ENDOR studies of Cu(II) sorption on aluminas, titanias, and silicas by Motschi and co-workers.[503−506]

4.4.2.7. Infrared Studies of Phosphate, Sulfate, and Organic Sorbates on Metal Oxides. Phosphate and sulfate are common oxoanions in soils and sorb strongly to many metal (hydr)oxide surfaces, interfering with the sorption of other species and affecting ligand-promoted dissolution and overall reactivity (see section 5.3). Uptake measurements for these oxoanions as a function of pH and ionic strength have been fit equally well using various surface complexation models and different assumptions about the types of surface complexes formed, including both inner-sphere and outer-sphere surface species (see citations in refs 507 and 508). Spectroscopic measurements sensitive to the mode of sorption of phosphate and sulfate groups are required to distinguish among these possible types of surface complexes. IR spectroscopy is well-suited for this purpose because it can provide in situ information on the surface complexes at metal (hydr)oxide−aqueous solution interfaces. However, as will be shown in the discussion below, some controversy still exists about the mode of sorption of both oxoanions on iron oxides.

IR measurements provided evidence for the formation of a bridging $(\mathit{Fe}O)_2POOH$ surface complex on goethite (α-FeOOH) (where *Fe* indicates a surface Fe site).[509,510] This bidentate mode of attachment is consistent with the slow rate of exchange of ^{32}P on phosphated goethite,[511] the strong adsorption of phosphate on goethite,[512,513] and the observation that phosphate could not be desorbed from goethite by washing at low pH.[514] A more recent study of orthophosphate adsorption on α-FeOOH using DRIFT methods (see section 4.3.2.4)[515] found evidence for monodentate, inner-sphere PO_4 surface complexes rather than bidentate complexes, as suggested by the earlier studies. In contrast, Persson et al.[515] found strong IR evidence for the formation of a three-dimensional phosphate precipitate on α-Fe_2O_3 (hematite) using a somewhat different sample preparation procedure than used in preparing the PO_4/goethite sorption samples.

The sorption of sulfate groups on goethite surfaces has also been studied by DRIFT methods[507,516] and on hematite surfaces by ATR-FTIR and STM methods.[508,517] The study of sulfate sorption on goethite by Persson and Lovgren[507] found evidence for outer-sphere complexation, based on both the DRIFT and the adsorption isotherm measurements as a function of ionic strength. This interpretation contradicts earlier IR studies of sulfate sorption on goethite,[516,518−521] which were interpreted as indicating inner-sphere, monodentate and/or bidentate sorption complexes. All of these studies were carried out on sorption samples that were dried after sulfate uptake. Hug[508] carried out in situ ATR-IR measurements of sulfate sorbed on hematite and concluded that sulfate is bonded in an inner-sphere, monodentate fashion, in agreement with the older studies and the more recent ATR-FTIR and STM study,[517] but in contradiction with the study by Persson and Lovgren.[507] These conflicting interpretations serve to emphasize the difficulty of comparing IR results on different samples prepared in different ways, only one of which was studied under in situ conditions. They also emphasize the difficulty of extracting structural information for sorbates at relatively low surface concentrations using IR spectroscopy.

There have also been FTIR studies of organic sorbents on metal (hydr)oxides, including in situ ATR-FTIR measurements of salicylate on δ-Al_2O_3, α-Al_2O_3, α-Fe_2O_3, and γ-FeOOH,[522] oxalate on TiO_2,[373] and *o*-phthalate on boehmite (γ-AlOOH)[523] and ex situ DRIFT measurements of phenyl phosphonate on γ-Al_2O_3 and γ-AlOOH.[524] These data were interpreted as consistent with inner-sphere complexation of the organic species on the (hydr)oxide surfaces. A variation on the ATR method known as cylindrical internal reflection (CIR)-FTIR, which uses cylindrical optics rather than the flat ATR optics, was developed by Tejedor-Tejedor et al.[525] and used to characterize benzoic, phenolic, and salicylic complexes at the goethite−aqueous solution interface in situ.[526,527]

In addition, a recent in situ ATR-FTIR, DRIFT, and EXAFS study of the interaction of Pb(II)−EDTA with goethite (α-FeOOH) surfaces found evidence for outer-sphere complexation of this ternary complex.[528] This finding contrasts with that of Nowack and Sigg,[529] who suggested that Pb(II)−EDTA forms inner-sphere complexes on the goethite surface based on adsorption isotherm measurements.

4.4.2.8. SHG Study of the Adsorption of 5,6-Carboxy-X-rhodamine on Al_2O_3. Higgins and Eggleston[530] used SHG to investigate the adsorption of 5,6-carboxy-X-rhodamine (5,6-ROX) to a polycrystalline corundum window. The adsorption behavior observed through SHG (increasing sorption as pH decreases, with an adsorption maximum between the pK_a values of the two carboxyl groups) is identical to that from wet chemical experiments for 5,6-ROX adsorption on corundum particles in suspension. Unlike wet chemical (stoichiometric) sorption studies with metal powders, this approach will, in the future, allow sorption studies on well-defined single-crystal surfaces. An overall goal is to develop better constrained structure−reactivity relations for mineral surfaces on the basis of crystal-face-specific investigations.

4.4.2.9. Kinetics of Phosphate Adsorption on Metal Oxide Surfaces. The geochemistry of the interaction of phosphates with metal hydroxide and clay particle surfaces in soils has been of considerable interest for many decades.[531] A detailed understanding of the uptake of phosphates by metal oxides and hydroxides such as hematite (α-Fe_2O_3), goethite (α-FeOOH), gibbsite [γ-$Al(OH)_3$], silica (SiO_2), and rutile (TiO_2) is not only relevant to the study of soils but is also key to other important technologies such as corrosion and biomimetic materials. Phosphate reactions with iron and aluminum oxides and hydroxides have been extensively studied by soil chemists because these soil components are the most abundant of the naturally occurring metal oxides[531,532] and are the inorganic soil constituents primarily responsible for phosphate reactions in soils.[533,534] Phosphate reactions with titania have been investigated to promote bone growth on titanium implants.[535]

There have been only a limited number of surface science studies of phosphate uptake from solution by aluminum and titanium oxide surfaces. One study using angle-resolved X-ray photoelectron spectroscopy (XPS) concluded that phosphate accumulated at the surface of gibbsite and was not incorporated into the bulk structure.[536] However, it is not at all clear that phosphate reactions are independent of particle size. For example, an investigation using ^{31}P MAS NMR has shown that, for larger particle sizes, phosphate was limited to surface reactions and was not incorporated into the bulk structure. However, for smaller particle sizes, phosphate reacted to form aluminum phosphate crystallites.[537]

Researchers in heterogeneous catalysis have examined alumina and titania after reaction with phosphoric acid[538] and found that POH groups at the surfaces of both oxides act as Brønsted acids. These investigators concluded that upon activation of the catalysts by heating in vacuum, the incorporated phosphate loses a proton, which then combines with an OH^- at the oxide surface to form H_2O; that is, an ionic bond is formed between the phosphate and the oxide surface.

Previous kinetic studies with iron oxides have defined two regimes of phosphate reaction:[539] an initially rapid first-layer chemisorption and a second regime characterized by the slower uptake kinetics thought to arise from solid-state diffusion, diffusion through surface pores, migration from within aggregated particles to surface sites, or precipitation of insoluble phosphates at the surface.[540] Most of the studies have focused upon the initial chemisorption reaction, particularly of phosphate with goethite, α-FeOOH. The models developed from studies of iron oxide have served as a prototype for phosphate reactions with other oxides.

A key early investigation into phosphate reactions with iron oxides postulated that ionic solution phosphate species reacted with OH^- groups at the surface by donating a proton to form $-OH_2$ and then exchanging with this species to form bonds to structural iron.[541] Subsequent investigations using ex situ transmission IR spectroscopy demonstrated that the hydroxyl groups involved in phosphate ligand-exchange reactions were those singly coordinated to iron.[367] From these investigations, phosphate is thought to bind to two OH^- groups to form a binuclear structure. More recent in situ ATR-FTIR studies, in which an aqueous solution remained in contact with the iron oxide particles during the IR measurements,[508] are consistent with this earlier interpretation (see section 4.4.2.7).

Calculations of hydroxyl packing densities for various faces have been performed for hematite.[367] The faces considered theoretically suitable for binuclear bridging complexes of phosphate were the $(11\bar{2}0)$, $(10\bar{1}0)$, and $(22\bar{4}3)$ planes. Calculations which assumed phosphate bonded in a binuclear complex predicted that phosphate uptake for these faces would be 4.2, 4.8, and 3.6 μmol/m^2 of P, respectively. Reported values from adsorption studies[532,534] range from 0.31 to 3.3 μmol/m^2 of P. A reason for the difference between the measured and calculated phosphate concentrations is that hematite can vary widely in crystal morphology, and the planes amenable to phosphate adsorption may not be the most dominant faces.[532]

Surface science techniques have not been fully exploited by investigators interested in phosphate adsorption at iron oxide and hydroxide surfaces. However, in one surface science study, the surface composition of phosphated synthetic goethite was examined by XPS. From estimates of sampling depth and atomic composition, phosphate adsorbed in a binuclear complex was considered plausible.[542] A later study, examining phosphate reactions with naturally occurring goethite, investigated both the initially rapid first-layer chemisorption reaction and the reactions characterized by slower uptake kinetics.[543] Findings indicated that phosphate in the first layer was bound as $H_2PO_4^-$ and comprised ~1.3 atom % of the surface. Phosphate present at the surface after long reaction times (90 days) existed in crystallites ranging in size from 0.1 to 4 μm on the goethite surface. Thus, after long reaction times, phosphate precipitation at the surface was considered likely, with the composition of the bulk phase phosphate dependent upon solution composition.

Recently the kinetics of phosphate uptake by hematite, titania, and alumina has been examined[544] by exposing freshly prepared thin films to phosphate solutions at incremental times and subsequently analyzing the surfaces by Auger electron spectroscopy (AES), temperature-programmed desorption (TPD), XPS, and AFM. The experiments were carried out in a combined UHV chamber and liquid adsorption cell.[545,546] These results show that, for thin-film hematite exposed to a sodium phosphate solution, initially rapid uptake occurs during the first 10 min of solution exposure, in which phosphate completes first-layer adsorption (Figure 33a). A short induction period ensues, lasting 10 min, which corresponds to a saturation of surface sites that comprise a TPD desorption feature at 1380 K (Figure 34). After this induction period, phosphate species precipitate as islands. The rate of uptake of calcium and potassium phosphate on alumina and titania surfaces can be directly compared from their respective adsorption isotherms shown in Figure 35. The onset of rapid uptake characterized by three-dimensional island growth is between 200 and 250 min for the titania surface and between 1500 and 2000 min for the alumina surface. This is comparable to in situ studies, where the onset of rapid growth is 160 min for titania powders and 1800 min for alumina powders. AFM images (Figure 36) show that large terraces and islands form on the metal oxide surfaces on the order of hundreds of nanometers in diameter.

A comparison of the adsorption isotherms for phosphate adsorption from the ex situ surface science studies on titania thin films and traditional in situ experiments on titania powders is shown in Figure

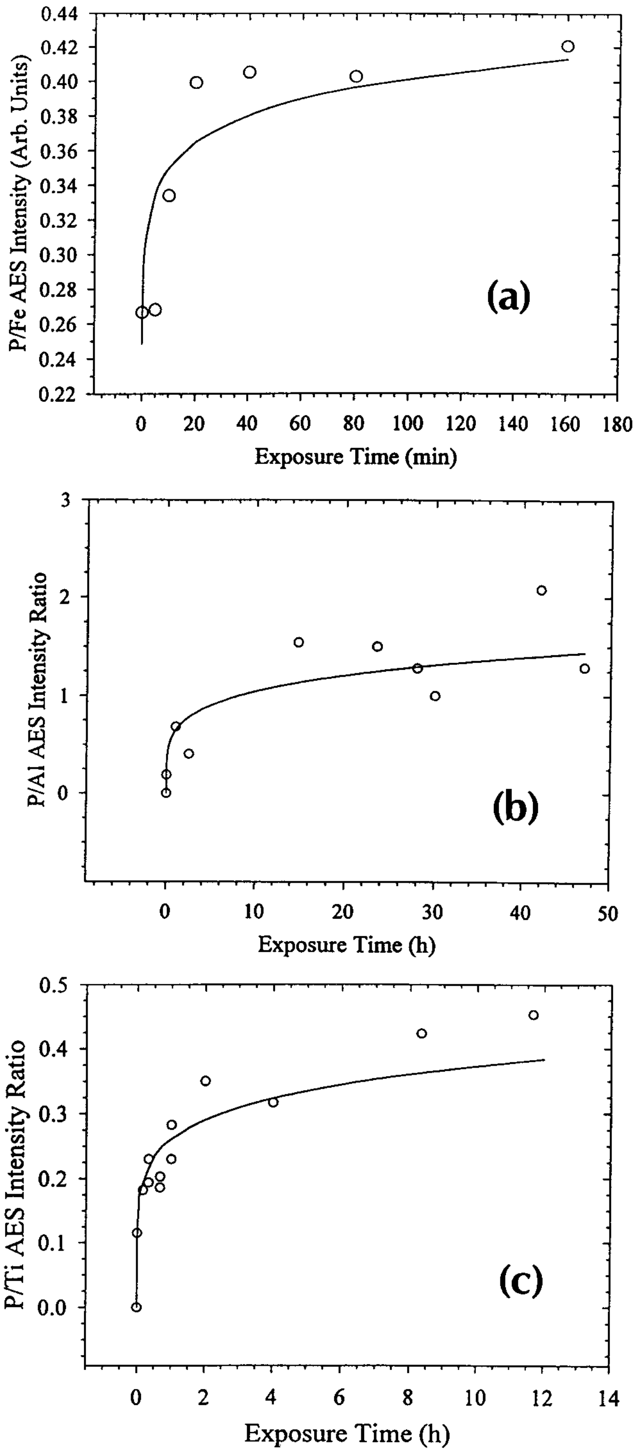

Figure 33. Phosphorus-to-metal AES peak ratios as a function of exposure to a phosphate-containing solution for the phosphate 110-eV peak to (a) the iron 651-eV peak, (b) the aluminum 60-eV peak, and (c) the titanium 387-eV peak. The iron oxide surface was exposed to a solution containing 3 μg/mL P, and the titania and alumina surfaces were exposed to a solution containing 119 μg/mL P.

37. The close correlation between the in situ and ex situ measurements validates the ex situ methodology for making kinetic measurements of phosphate adsorption on thin metal oxide films that have been exposed to solution and returned to vacuum.

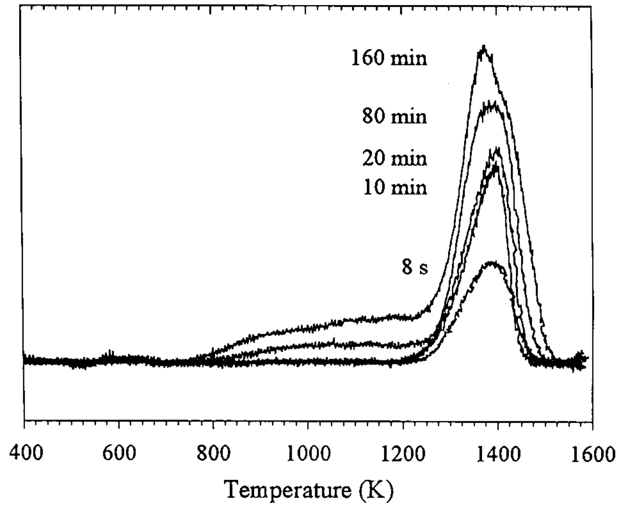

Figure 34. TPD spectra corresponding to the desorption of phosphate as mass 47 (PO) as a function of exposure of an Fe_2O_3 surface to a solution containing 3 μg/mL P, pH 6.7, and 0.01 M NaCl.

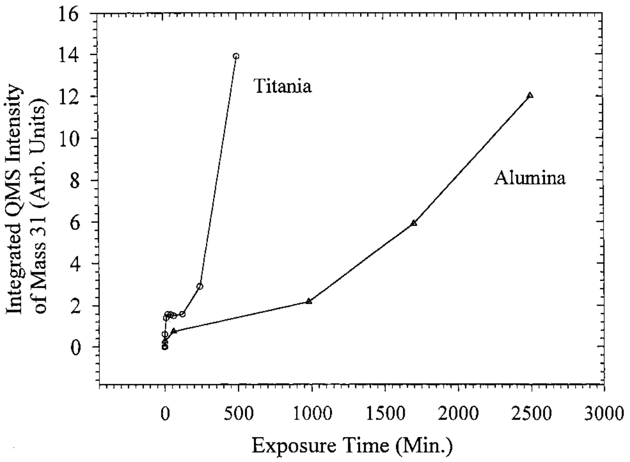

Figure 35. Integrated TPD spectra for mass 31 (P) from titania and alumina surfaces as a function of exposure to a calcium phosphate solution containing 119 μg/mL P.

Model studies of the kind described above using the full complement of surface science techniques offer exciting new opportunities to address the fundamental issues of chemical interactions at the metal oxide–aqueous solution interface. Although many of these techniques require ex situ examination, several important ones do not. For example, ATR-FTIR spectroscopy (see section 4.3.2.4) can be used in conjunction with a thin aqueous film cell. In addition, XAFS spectroscopy can provide direct structural and compositonal information on adsorbates in situ as well as information about reactive sites on oxide surfaces (see sections 4.3.2.2 and 4.4.2.2). Sum frequency generation (SFG) is also well-suited for such studies, since the technique is intrinsically sensitive only to the aqueous–solid interface (see section 4.3.2.6).

4.4.3. Heterogeneous Redox Reactions at Metal Oxide–Aqueous Solution Interfaces

Electron transfer reactions at oxide surfaces may be broadly characterized as occurring (1) from the solid to the adsorbate, (2) between sorbates, and (3) from the adsorbate to the solid. Examples of each of these classes of electron-transfer reactions are discussed below.

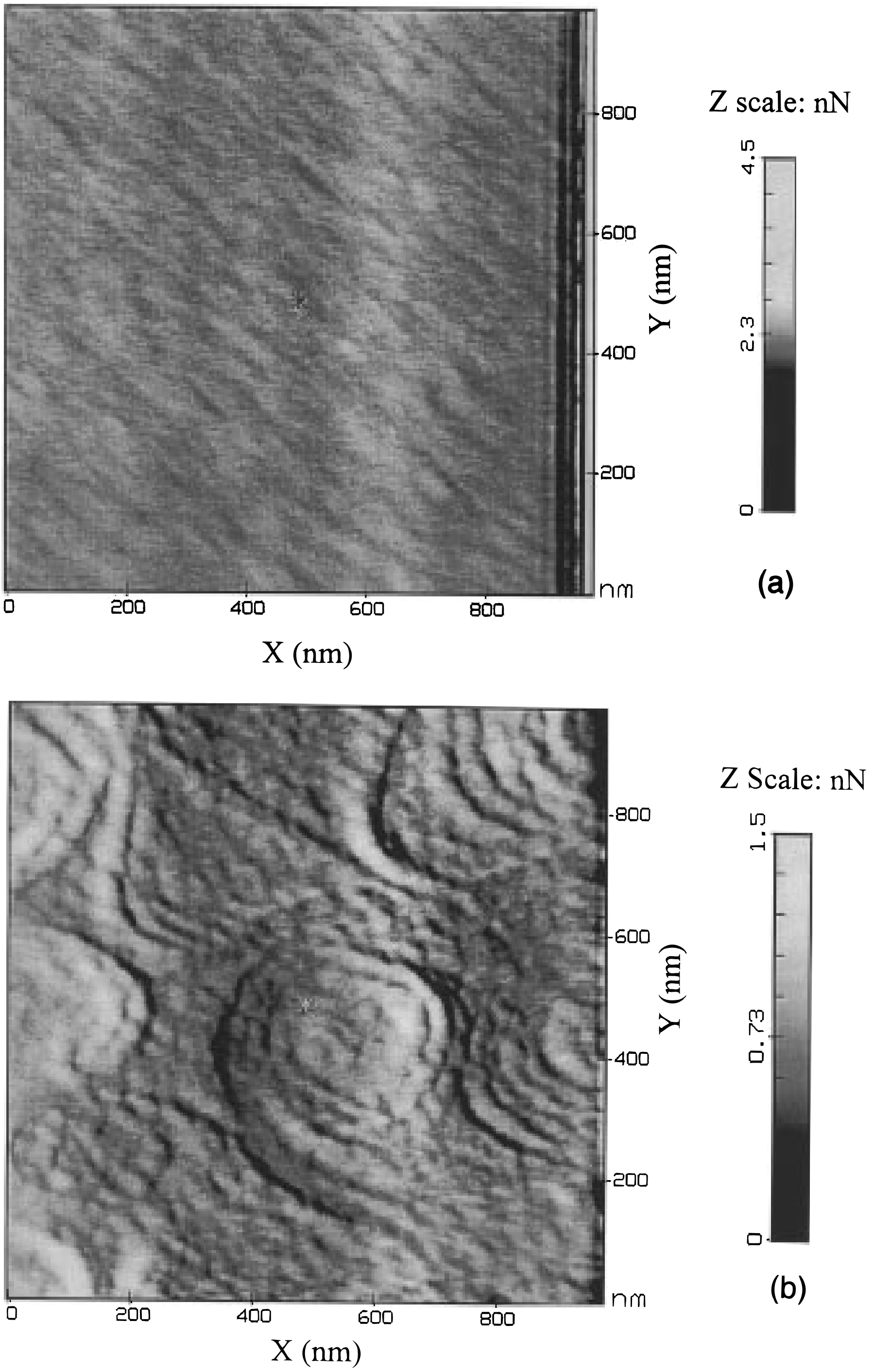

Figure 36. AFM image of a clean alumina film approximately 100 Å thick grown on a Mo foil substrate (a) can be compared to a similar surface exposed to a solution containing 119 μg/mL P for 90 h (b).

4.4.3.1. Electron Transfer from the Solid to the Adsorbate. Oxides with ferrous iron [e.g., magnetite (Fe_3O_4) and wustite (FeO)] and others with reduced component defects [e.g., Ti(III) in TiO_2] have the potential for solid-state electron transfer to adsorbates. Solid-state redox reactions are strongly influenced by surface charge and its compensation in the electrical double layer. The Fermi levels in the solid are fixed, in part, by the electrochemical potential at the solid–liquid interface, which in turn is influenced by the pH and electrolyte composition of the aqueous phase. Electron transfer from a reductive solid to an adsorbate occurs via an inner- or outer-sphere mechanism, as described by the heterogeneous electron-transfer theory of Marcus (see section 4.4.3.5).[547] Thus the rate and extent of electron transfer is controlled by the nature of the adsorbate surface complex (e.g., denticity, bond distances) and other dissolved ions impacting surface speciation and potential.

Magnetite is an effective reductant for $Cr(VI)O_4^{2-}$ and $Tc(VII)O_4^{-}$, leading to formation of insoluble Cr(III) and Tc(IV) on the surface.[461,548,549] The effective half-cell potential (E_H^0) for the solid-state electron-transfer reaction $Fe(III)_s + e^- = Fe(II)_s$ ranges between 0.34 and 0.65 V,[549] making structural Fe(II)

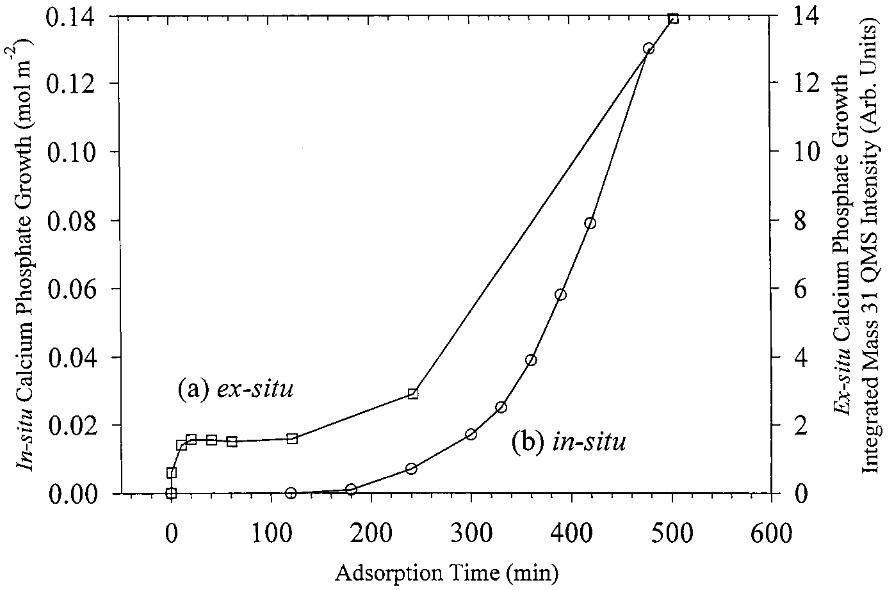

Figure 37. Comparison of the adsorption isotherms for phosphate on titania generated from (a) ex situ and (b) in situ adsorption experiments.

a stronger reductant than Fe(II)(aq) ($E_H{}^0 = 0.77$ V). Pertechnetate ($TcO_4{}^-$) is rapidly reduced by, but weakly sorbed by, the magnetite surface, implying an outer-sphere electron-transfer mechanism. Reductive electron transfer also occurs between the magnetite surface and V(V)$O_2{}^+$, which is reduced to V(IV)O^{2+}. [549,550] This reaction underscores the complexity of such interfacial processes, as its rate is strongly dependent on pH and related factors controlling the solubility of V(IV) solids [e.g., $VO(OH)_2$], surface charge, and the relative sorptivity of $VO_2{}^+$ compared to VO^{2+}, the latter forming stronger inner-sphere surface complexes. The topotactic surface conversion of magnetite to maghemite can accompany these heterogeneous electron reactions, leading to surface passivation (see section 4.4.3.4).[461,551,552] Magnetites that are exposed to oxic groundwaters (i.e., weathered) lose their reductive potential, possibly for this very same reason.

4.4.3.2. Electron Transfer between Sorbates. Electron transfer reactions that are known to be slow or thermodynamically unfeasible in the aqueous phase can be promoted by an oxide that adsorbs one or more of the reactants. For example, Mn(II)(aq) is slowly oxidized by dissolved O_2 in aqueous solution but is rapidly oxidized under the same O_2 partial pressure if an Fe(III) oxide is present. Surface complex formation (i.e., ligand substitution for H_2O) alters the electron density of Mn(II) and its water exchange rate, allowing for more rapid electron transfer with dissolved molecular oxygen in the interfacial region[553] (Figure 38). The structure of the surface complex is critical to heterogeneous oxygenation, as a surface complex with a proton stoichiometry of 2 [e.g., a bidentate $(SO)_2$–Mn(II) or hydrolyzed monodentate SO–MnOH complex, where SO denotes a surface metal site terminated by an oxygen] appears to promote oxidation. Spectroscopic studies on the structural nature of the Mn surface complex that promotes oxidation would be insightful. Both silica and alumina also promote the heterogeneous oxidation of Mn(II).

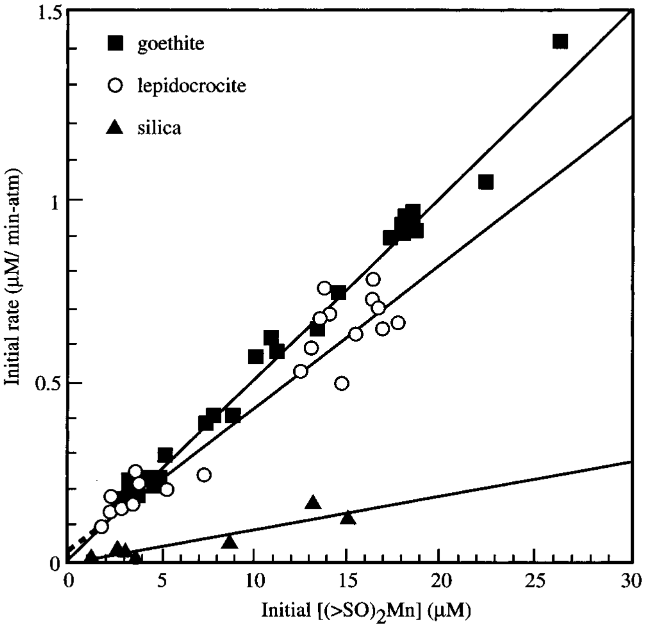

Figure 38. Initial rate of Mn(II) surface oxidation as a function of the computed initial equilibrium concentration of bidentate surface species for three oxides at 298 K, 0.1 M $NaClO_4$, and 1 atm P_{O_2} at pH 6. Surface complexation enhances the oxidation rate, and the effect is greater for Fe(III) oxides than for SiO_2 (adapted from ref 553).

Conversely, heterogeneous oxygenation at the oxide–water interface may also be slower than that observed in bulk solvent. The oxygenation rate of VO^{2+} in water increases with increasing pH, as the hydroxo complex $[VO(OH)^+]$ acts as a precursor to the oxidation step. The vanadyl ion (VO^{2+}) is strongly sorbed by metal oxides such as TiO_2 and Al_2O_3 through formation of a bidentate inner-sphere surface complex.[554] Adsorption (e.g., bidentate surface complex formation) enhances the oxidation rate of VO^{2+} to $VO_2{}^+$ at lower pH (Figure 39) but slows the rate at higher pH[555] because the bidentate surface complex resists hydrolysis. Surface coordinated OH^- groups are able, like aqueous hydroxo complexes, to

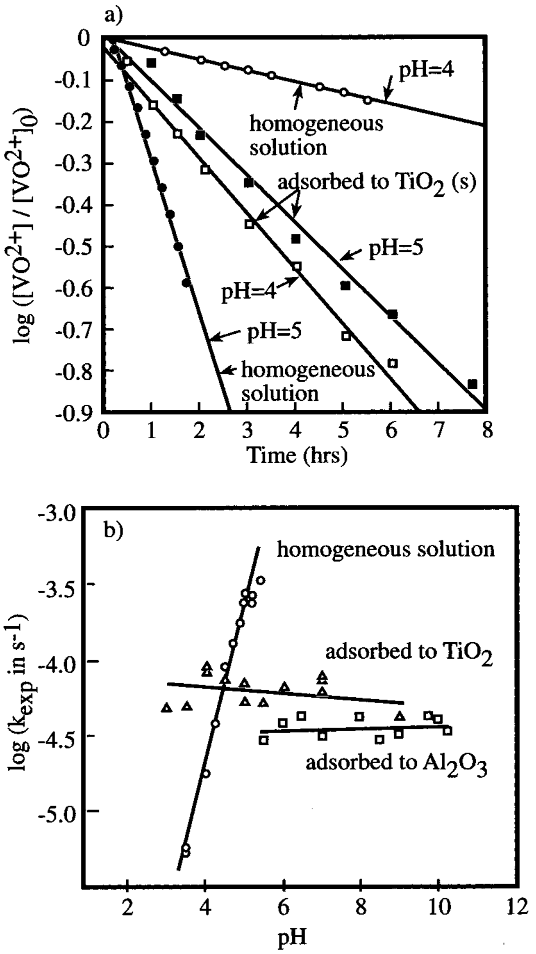

Figure 39. Vanadyl oxygenation. (a) First-order plots for the oxidation of vanadyl, VO^{2+}, by dissolved O_2 ($P_{O_2} = 0.2$ atm) in a homogeneous solution and in the presence of TiO_2. The oxygenation rate, $-d[V(IV)]dt$, in homogeneous solution is proportional to $[VO(OH)(aq)^+]$ and in the heterogeneous system (presence of TiO_2) to the concentration of adsorbed vanadyl. (b) pH dependence of vanadyl oxygenation kinetics. Adsorption enhances the oxygenation rate below pH 4 and reduces it above pH 4 (adapted from ref 555).

mediate the electron transfer from O_2 to metal ions. However, the rate enhancement of surface hydroxyls seems to be less than that of the aqueous ligand.

Many abiotic environmental redox reactions are mediated by Fe(II) as a reductant. The adsorption of Fe(II) as an inner-sphere complex on metal oxides enhances its electron-transfer rates and its reactivity with contaminants. This enhancement is greatest on Fe(III) oxides, where the Fe(III)−O−Fe(II) bond linkage imparts great stability and reactivity to the surface Fe(II) complex. The effective redox potential of adsorbed Fe(II) has been estimated, with the assumption of a bidentate surface complex:[556,557] $(Fe(III)O)_2{-}Fe(III)^+ + e^- = (Fe(III)O)_2{-}Fe(II)$; $E_H{}^0 = 0.36$ V. This couple compares favorably with that of the aqueous hydrolyzed analogues: $Fe(III)OH^{2+}(aq) + e^- = Fe(II)OH^+(aq)$; $E_H{}^0 = 0.36$ V. The kinetic reactivity of adsorbed Fe(II) exceeds that of unhydrolyzed Fe(II)(aq), allowing reduction of nitroaromatics, chlorinated hydrocarbons, $CrO_4{}^{2-}$, $UO_2{}^{2+}$, and $TcO_4{}^-$, to name just a few. The influence of factors such as the Fe(II) sorption density and binding strength, surface distribution, and substrate oxide (e.g., Al, Fe, or Ti) on the effective half-cell potential of the Fe(II)/Fe(III) couple and its reaction kinetics are unknown. The molecular mechanisms of these intersorbate, heterogeneous electron-transfer reactions have not been well-explored.

4.4.3.3. Electron Transfer from the Adsorbate to the Solid. Electron transfer to the solid phase is mediated by surface complexes. Mn(III,IV) oxides are strong oxidants and mediate heterogeneous electron-transfer reactions from a wide range of sorbates, including phenols, quinones, humic substances, and polyvalent metals [Cr(III), U(IV), Fe(II), and Co(II)]. Electron-transfer rates (reduction rates) for substituted phenols to Mn(III,IV) oxides correlate with the compound half-wave potentials.[558] Manganese(II) and -(III) result from such electron-transfer reactions. These may sorb to the Mn(IV) surface and passivate the electron-transfer reaction unless dissolved O_2 is present for surface regeneration. Manganese oxides are facile oxidants, and electron transfer between the surface and sorbates can apparently proceed by both inner- and outer-sphere mechanisms. Heterogeneous electron transfer may occur between the adsorbate and the Mn oxide surface even when sorption is weak. For example, the anion $Co(II)EDTA^{2-}$ is rapidly oxidized to $Co(III)EDTA^-$ by Mn(IV) oxides, despite there being limited potential for surface complexation.[435]

Organic ligands adsorbed by inner-sphere complexation can shift electron density toward surface metal ion centers and facilitate electron transfer to Fe(III) oxides.[559] Oxalate and EDTA form strong bridging surface complexes that allow electron transfer from Fe(II)(aq) to Fe(III) at the oxide surface.[560,561] Such reactions are strongly dependent on the surface concentration of the adsorbed organic ligand and the structural nature of the surface complex; both of these are pH-dependent. Ligand-exchanged surface complexes of organic chromophores such as oxalate, citrate, and humic substances on polyvalent metal oxides (Mn, Fe, and Ti) may be electronically excited by light, inducing electron transfer to the surface metal ion centers and oxide dissolution (Figure 40; refs 467, and 562−565). Such photochemical dissolution depends on the chromophore concentration and pH, which controls the sorption of the chromophore and the reduced metal product, e.g., Fe(II) or Mn(II). These photoassisted reactions induce diurnal solubilization and cycling of Fe and Mn in surface waters, and such a mechanism has been proposed as a means of supplying trace metal nutrients to plants and aquatic organisms.

4.4.3.4. Formation of Passivating Layers on Metal Oxides. Oxidation−reduction reactions can result in the formation of passivating layers on a metal oxide surface that stops further electron transfer. This can occur when a metal oxide containing a metal ion that can be oxidized or reduced comes in contact with an aqueous solution containing an oxidant or reductant. A good example of this effect is when a solution containing $CrO_4{}^{2-}$ comes in contact with an Fe^{2+}-containing oxide such as Fe_3O_4 (magnetite).[461] A combined XAFS spectroscopy and transmission elec-

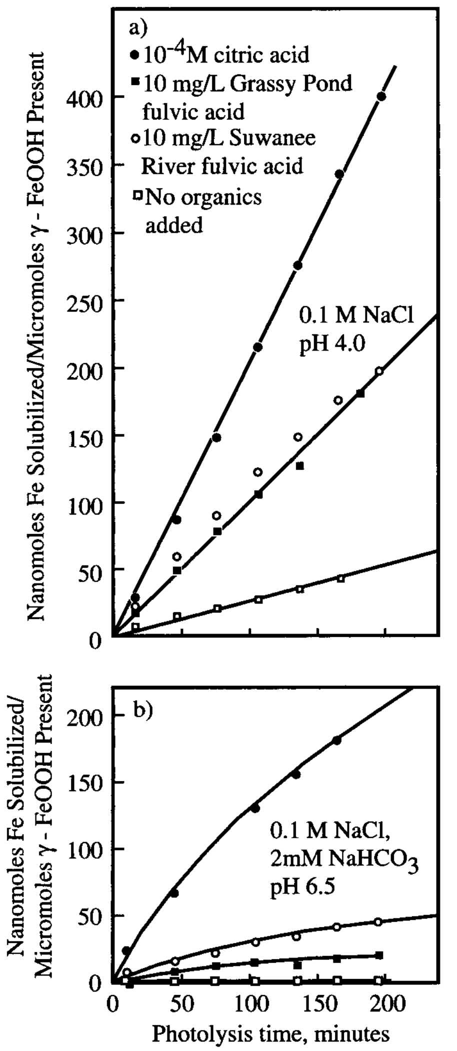

Figure 40. Dissolution of 5 μM γ-FeOOH on photolysis of (a) pH 4.0 and (b) pH 6.5 solutions containing either 10^{-4} M citrate, 10 mg/L aquatic fulvic acids, or no added organic agent (symbols the same as in panel a) (adapted from ref 562).

tron microscopy study of the reduction of CrO_4^{2-} on magnetite[552] showed that Cr(VI) is rapidly reduced to Cr(III) on the magnetite surface. This reduction reaction involves the transfer of three electrons from three Fe(II) to one Cr(VI) at the surface and results in the formation of γ-Fe_2O_3 (maghemite) or a mixed Fe(III)−Cr(III)$(OH)_3$ phase,[566] or both on the magnetite surface and adsorbed Cr(III) species. Chromium K-edge XAFS spectroscopy (see section 4.3.2.2) combined with high-resolution TEM on the reacted magnetite grains indicated that the redox reaction had ceased in the laboratory timeframe after a 15-Å rind of maghemite or a mixed Fe(III)−Cr(III) hydroxide had formed on each grain. Apparently, electron transfer through this layer does not occur on a time scale that results in further reduction of Cr(VI) to Cr(III) during the experiments. Such passivating layers can dramatically affect redox reactions on metal oxide surfaces.

In order for electron transfer to occur across metal oxide−aqueous solution interfaces in laboratory time scales, it is necessary for the physical separation between the oxidant and reductant to be only a few to tens of Ångstroms, depending on the electrical conductivity of the interface region. Furthermore, if a solution species that can undergo oxidation or reduction sorbs as an outer-sphere surface complex on a metal oxide that can serve as an electron source or sink, the intervening layer of water may inhibit electron transfer (see section 4.4.3.5).

4.4.3.5. Technological Applications of Charge-Transfer Processes as Solute−Substrate Interfaces. Interfacial charge-transfer processes at metal oxide surfaces are presently under intensive investigation. Initially, attention has focused on conductive metal oxides such as RuO_2 and IrO_2. Detailed electrochemical studies of these materials were motivated by their use as dimensionally stable anodes in chlorine production and as oxygen electrodes in water electrolyzers.[567] More recently, research interest has turned to other conducting oxides displaying a high overvoltage for water oxidation, such as SnO_2 or PbO_2. These have found diverse industrial applications, e.g., as anodes in the selective oxidation of aromatics and the oxidative destruction of pollutants in water.[568] An interesting example is the ozone generator developed by Brown Bovery Corp. to produce ozone by direct oxidation of water on a lead dioxide anode. The ozone reacts rapidly with any organic impurities under CO_2 formation. In his way ultrapure water is obtained which is suited for electronic applications.

Apart from these traditional electrochemical applications of conducting metal oxides, new developments have taken place over the last 2 decades which are linked to interfacial charge-transfer phenomena at the oxide surface. In particular, the advent of nanocrystalline films and their recent successful use in dye-sensitized solar cells has produced a wealth of information on the fundamentals of charge-transfer reactions on metal oxide semiconductor surfaces.[569−580] Dye sensitization forms the basis for applications in the fields of photography, photochromic devices, and photolithography.[581,582] Hence there has been a long-standing interest in the study of this phenomenon, particularly on semiconductor electrodes.[583−586] The primary goal of these investigations has been to unravel the factors governing the dynamics of electron injection from the electronically excited state of the dye into the conduction band of TiO_2. One important property to consider is the redox potential of the dye in the excited state, $E(S^+/S^*)$. In cases where the entropy energy for the formation of excited dye is small (as is often the case with Ru−polypyridine complexes), $E(S^+/S^*)$ is obtained by adding the 0−0 excitation energy of the sensitizer to the ground-state redox potential. There have been attempts to describe the charge injection kinetics by the same Marcus-type formalisms used for electron-transfer reactions of solution redox species, particularly for the rate dependence on the driving force associated with respective electron-transfer steps.[586] However, the ultrafast nature of electron injection processes occurring on a femtosecond time scale[375] and most likely involving vibrationally excited states poses a new challenge for theoreticians.

To obtain such high rates, which may be the fastest chemical processes known to date, one must ascertain

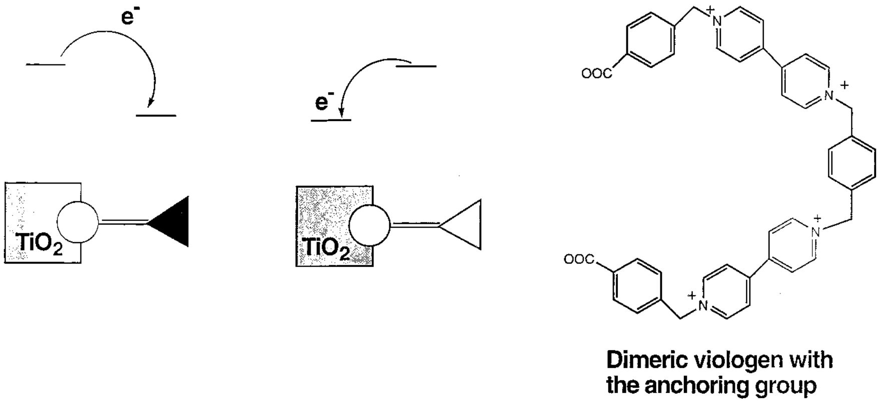

Figure 41. Electrochromic device based on a nanocrystalline oxide semiconductor, surface derivatized with a viologen electron relay. Under forward bias, conduction-band electrons are transferred from the conduction band of the oxide to the viologen. The reduced state of the viologen has a blue color, while the oxidized form is colorless. Thus, by electron injection, the film is switched from a colorless to a deep blue state.

that there is intimate contact (physical and electronic) between the dye and the semiconductor. This can be achieved via introduction of suitable anchoring groups, such as carboxyl or phosphonato functions, on the polypyridine ligand. 4,4′-Dicarboxy-2,2′-bipyridine (dcbpy) and 6-phosphonatoterpyridine are typical examples where the substituents play an important role in ensuring efficient adsorption of the dye on the surface of the amphoteric oxide TiO_2, while preserving or promoting electronic coupling between the donor levels of the excited dye (a molecular orbital which is largely π^* of the ligand in character) and the acceptor levels of the semiconductor, i.e., the 3d wave function of the conduction band of TiO_2.

On the basis of a comparison of FTIR and resonance Raman spectral data of ester and carboxylate anion derivatives of the photosensitizer with that observed for dyes adsorbed onto TiO_2 surface, metal oxide surface complexation has been inferred.[587,588] There are a number of literature precedents suggesting that carboxylic acid and hydroxylic groups form chelates or coordinative bonds with the metal ion at the oxide surface, as shown below:[587−590]

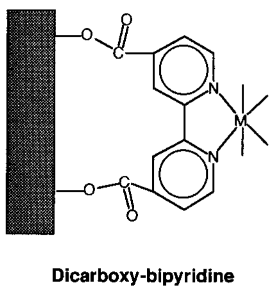

Dicarboxy-bipyridine

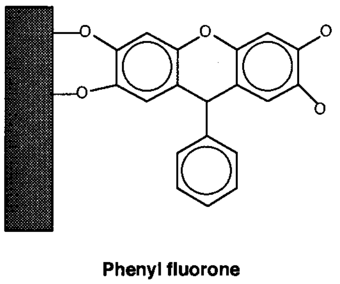

Phenyl fluorone

The adsorption of aryl and aliphatic carboxylic acids on TiO_2, for example, has been shown to follow the Langmuir isotherm. Complexation of these acids by the TiO_2 surface dramatically accelerates the rates of interfacial electron transfer to acceptors present in the solution.[587] In favorable cases, derivatization of the ligands to the metal oxide surface leads to distinct spectral changes and/or the appearance of new absorption bands corresponding to charge-transfer interactions. Typical examples of this category are 8-hydroxyquinoline,[588] $Fe(CN)_6^{4-}$,[589] and phenyl fluorene.[590]

Interfacial charge transfer is also the basis for the design of several types of sensors. One type involves the use of colloidal metal oxide particles, where injected electrons move through the network of particles by charge carrier percolation and arrive at the conducting glass collector electrode. An ideal description of the film would be as a collection of a large number of particles interconnected with large pores in between; electrons injected onto any of the constituent particles can travel through the network and reach the collector/back electrode. Electrons are majority carriers in n-type semiconducting oxides, and hence injection of electrons from outside into the junction drives the metal oxide film into the accumulation region. Accumulation of conduction band electrons in the metal oxide leads to an electrochromic effect, i.e., development of a broad absorption band in the visible and near-IR region. Electrochromic switching of mesoscopic films occurs rapidly due to ready compensation of the injected space charge by ion movement in the electrolyte present in the pores.[591]

Viologens form a group of redox indicators that undergo drastic color changes upon oxidation/reduction. The reduced form of methyl viologen, for example, is deep blue, while the oxidized form is colorless. Efficient reduction of anchored viologen compounds by conduction band electrons of TiO_2 can be used for the amplification of an optical signal, as shown schematically in Figure 41. The amplification is due to the extremely large molecular extinction coefficients of these relays. Upon electroreduction, transparent nanocrystalline films of TiO_2 containing viologen develop strong color; the film can be bleached by reversing the potential. By varying the chemical structure and redox potentials of the viologens, it is possible to tune the color and hence build a series of electrochromic display devices.[592,593] Such surface-derivatized oxides have achieved a performance which, in terms of figure of merit (i.e., the number of charges required to achieve an optical density change of 1), is already competitive with conventional electrochromic systems and hence shows great promise for practical applications.

Also relevant to the transfer of charge across oxide−solute interfaces is the relation between energy levels and redox activity. The Fermi level E_F of a semiconducting oxide, such as α-Fe_2O_3 or TiO_2, depends on the concentration of electrons and hence is sensitive to the presence of lattice defects of the type discussed in section 2.4.1. E_F is given by:

$$E_F = (E_{cb} - E_{vb})/2 + (RT/2F)\ln[e^-(cb)]/[h^+(vb)] + (3RT/4F)\ln[m(e^-)]/[m(h^+)] \quad (16)$$

where E_{cb} and E_{vb} are the energy levels of the bottom of the conduction band and of the top of the valence band, respectively; $m(e^-)$ and $m(h^+)$ are the effective masses of the conduction band electrons and valence band holes, respectively; and F is Faraday's constant.[594] If the effective mass of the electron and that of the hole do not differ greatly, the last term in eq 16 can be neglected. Hence, for intrinsic semiconductors in which the concentration of electrons and holes is equal, the Fermi level is located in the middle of the band gap. n-Type doping shifts E_F toward the conduction band edge, while p-type doping moves it toward the valence band.

The position of the Fermi level controls the thermodynamics of redox reactions involving oxides. For example, the reductive dissolution of α-Fe_2O_3 by anaerobic bacteria (see section 6.2) in soil and groundwaters requires the electron transfer from a donor D present in the bacteria (e.g., heme center in the active cytochrome) to the conduction band of the iron oxide. The driving force of the reaction is given by:

$$\Delta G = E(D/D^+) - E_F \quad (17)$$

where $E(D/D^+)$ is the redox potential of the electron donor (both terms on the right side of eq 17 should be expressed with regards to the same reference state, e.g., the standard hydrogen potential or the vacuum level of the electron). The Fermi level is related to the electrochemical potential μ of the electron in the oxide by:

$$E_F = \mu - F_\Phi \quad (18)$$

where μ is the chemical potential of the electron, F is Faraday's constant, and Φ is the Galvani potential of the oxide. The contribution of doping to the position of the Fermi level is contained in μ, while that of the space charge carried by the oxide is reflected in Φ. In the absence of a space charge layer in the solid, Φ is equal to the surface potential Φ_S of the oxide. The latter contains mainly ionic and solvent dipole contributions arising from the electrolytic double layer present at the oxide−water interface. For many metal oxides, the surface potential exhibits a Nernstian dependence on the pH:[595]

$$\Phi_S = \Phi_S(pH = 0) - (RT/F)\ln(pH) \quad (19)$$

This dependence is responsible for the effect of the pH value of the aqueous phase on the driving force of heterogeneous electron-transfer reactions involving metal oxides, which is treated in sections 4.4.3 and 6.2.2.

An electron-transfer event takes place much faster than atomic motion. Therefore, the donor and acceptor states must be at the same energy; otherwise photons must be generated or absorbed by the electron. Because the donor and acceptor are not at the same energy except in cases of self-exchange (i.e., when there is a free energy of reaction), significant distortion of the solvent structure must occur as part of the electron transfer (the "solvent" in this case may include the solid around a donor or acceptor at a surface[596]). As an example, because Fe(II)−O bond lengths are significantly longer (0.14 Å) than Fe(III)−O bond lengths, it takes significant energy to reorganize the solvent in response to an electron transfer to or from aqueous Fe ions.

The ΔG of activation is expressed in Marcus theory as:

$$\Delta G^{act} = [\Delta G^o_{et} + \lambda]^2/4\lambda \quad (20)$$

The reorganization energy λ is written: $\lambda = \lambda_i + \lambda_o$, where λ_i and λ_o are the "inner" and "outer" reorganization energies, respectively. "Inner" pertains to the first coordination sphere, and its value depends on the frequencies of atomic vibration in this sphere (e.g., see ref 132). "Outer" pertains to the reorganization of the solvent around the aquated aqueous ion (or at or near a metal oxide−solution interface). The simplest expression for λ_o is:

$$\lambda_o = (\Delta e)^2[1/2a_1 + 1/2a_2 - 1/r][1/D_{op} + 1/D_s] \quad (21)$$

where Δe is the charge transferred (this is usually a single electron; indeed, λ_o becomes quite large for multiple electron transfers in aqueous solution), a_1 and a_2 are the radii of the donor and acceptor, respectively, r is the distance between donor and acceptor, and D_{op} and D_s are the optical and static dielectric constants of the solvent medium (D_{op} is the square of the refractive index). Assuming that a_1, a_2, and r are on average constant for a given electron-transfer reaction, the expression for λ_o can be simplified to:

$$\lambda_o = B[1/D_{op} + 1/D_s] \quad (22)$$

where B is a solvent-independent factor; that is, a plot of ln k_{rate} should vary linearly with $(1/D_{op} + 1/D_s)$ for a given electron-transfer couple in different solvents. This brings up the intriguing possibility that a given metal oxide surface−solution redox couple could show an electron-transfer rate dependence on the solid dielectric constant.

Equations 21 and 22 are valid for aqueous donor and acceptor species, or more generally for dissolved species (not necessarily aqueous). The expressions for solids for which the dielectric constant is not infinite (i.e., nonconductors) are more complicated, involving dielectric constants for both phases, but the functional form is similar and reduces to the form above for conductors.

It is important to comment on the λ value relevant to Fe centers within solids versus that pertaining to aqueous solutes. The movement of electrons in the hematite conduction band is equivalent to self-exchange among aqueous Fe(II) and Fe(III) ions, but the activation energies (which for self-exchange only depend on λ) are about 2.6 eV for aqueous Fe (e.g., ref 594) and about 0.3 eV for electron hopping in the solid.[131] Thus, Fe(II) in a solid (and its contribution to overall activation energy) should have a somewhat smaller activation barrier for reduction of a given solute, but only if it is near enough to a surface for donor and acceptor states to overlap. Fe(II) that undergoes oxidation near a surface will cause reorganization of the solvent in contact with the surface, so its λ_o will not be as low as the activation energy of electron hopping within the solid; it will be intermediate between the aqueous and solid cases. As an example, for aqueous Fe(II)−Fe(III) self-exchange, $\lambda_i \approx 1.5$ eV and $\lambda_o \approx 1.1$ eV, making the total $\lambda \approx 2.6$ eV (e.g., refs 132 and 594).

4.4.3.6. Charge-Transfer Processes and STM Imaging. Interfacial charge transfer must also be considered in detail in order to interpret STM images meaningfully. Marcus' theory of electron-transfer kinetics is useful for the qualitative, and perhaps eventually quantitative, interpretation of the STM images of hematite. Marcus' theory is reviewed in ref 132 and discussed in section 4.4.3.5. It has recently been used to describe the role of surface ferric oxide layers in controlling electron-transfer pathways operating during pyrite oxidation.[597]

There is recent evidence that reorganization energy effects can have a profound influence on STM imaging of redox centers in a solvent.[133,598,599] Luttrull et al.[600] and Tao et al.[601] used STM to study protoporphyrins (PP) and their metal complexes adsorbed onto graphite surfaces. These molecules are the basis of biomolecules that are crucial to biological electron transfer, and they and their relatives may also be important in geomicrobiological electron transfer. The protoporphyrins form a self-assembled monolayer on graphite. Tao[133] extended this work by using electrochemical STM to measure the $E°$, and a value related to λ, of Fe-containing protoporphyrin (Fe−PP) molecules adsorbed onto graphite. As the potential of the graphite electrode was raised toward the $E°$ of the empty Fe 3d states of the Fe−PP molecules, electrons began to transfer from the graphite onto the Fe sites in the protoporphyrin molecules before tunneling to the STM tip. The Fe site thus acts as an intermediary between graphite and the STM tip; i.e., electrons resonate with the Fe(III) acceptor state. Thus the Fe sites were readily identifiable.

Also, the current of electrons through the Fe sites has a peak width as a function of potential that compares well with estimates of the molecule reorganization energy. The reorganization energy was less than that of an aqueous complex, as expected for Fe(III) four-coordinated by the PP molecule and lying on graphite (i.e., shielded from all but a hemisphere of "outer" solvent reorganization).

The Tao[133] study is interesting from the point of view of determining the thermodynamic and kinetic parameters needed to characterize specific redox sites at surfaces. For example, if the uppermost Fe atoms of hematite (Figures 4 and 5) are half-aquated (i.e., three water ligands), then it is possible that the ability of these sites to transmit electrons between the STM tip and the hematite conduction band could be reduced by a greater activation barrier, in direct analogy to the Tao study.

One caveat[133] is that there are two possible peak-broadening effects, only one of which is directly related to the reorganization energy. Another possible effect could be bonding interactions between the redox center and the graphite.

4.4.4. Precipitation Reactions in the Interfacial Region

The interfacial region of oxides is conducive to precipitation reactions because the formation of surface complexes concentrates adsorbates in the interfacial region. The two-dimensional array of reactive surface functional groups and resulting surface complexes and the proximity of reactive sites in regions of structural defects such as steps and dislocations allow for lateral interactions between sorbates. Structural control on surface site distribution and intersite dimensions can promote nucleation and directed growth of epitaxy or registry with structurally similar solids.

For hydrolyzable metals such as Co(II) and Pb(II), the general consensus is that adsorbate−surface reactions proceed from surface coordination (inner-/outer-sphere) at low surface densities, through hydroxy-cluster formation at intermediate surface densities, to surface precipitation as surface sites become saturated.[602] This model, while intuitively appealing, is an oversimplification. Convincing EXAFS data (section 4.4.2.2) have recently shown that the structure and geometry of multinuclear hydrolysis complexes and the nature and extent of surface precipitation products are strongly dependent on the surface structure of the sorbent.[459,469,474] Such structure is important in that the surface may either promote or retard the formation of an adsorbate solid phase depending on the extent of structural registry or coordinative registry. Registry or epitaxy, however, is not required for surface precipitation.

True surface precipitation occurs when the bulk aqueous phase is undersaturated with respect to the precipitating solid. Various accounts of this phenomena have been reported.[603] The most plausible explanation for these observations is the formation of surface sorbate phases with nonunit activity, such as solid solutions, that reduce the solubility of the sorbate below that of discrete, homogeneous solid phases. This concept was advanced as the surface precipitation model of Farley et al.[602] Towle et al.[462] have recently shown that Co(II) forms a surface precipitate on the surface of Al_2O_3 from solutions that are high in Co(II) but undersaturated with respect to known/plausible Co(II) solid phases. These authors document that the surface phase is a Co(II)−Al(III) hydroxy coprecipitate, with Al being a dissolution product of the sorbent surface. Similar observations were also reported for Ni(II) by Scheidegger et al.[476] and for Co(II) and Ni(II) by d'Espinose de la Caillerie et al.[470] While such phases are important in the environment, their formation is encouraged in the laboratory when thermodynamically unstable oxide phases are subject to large pH variation in attempts

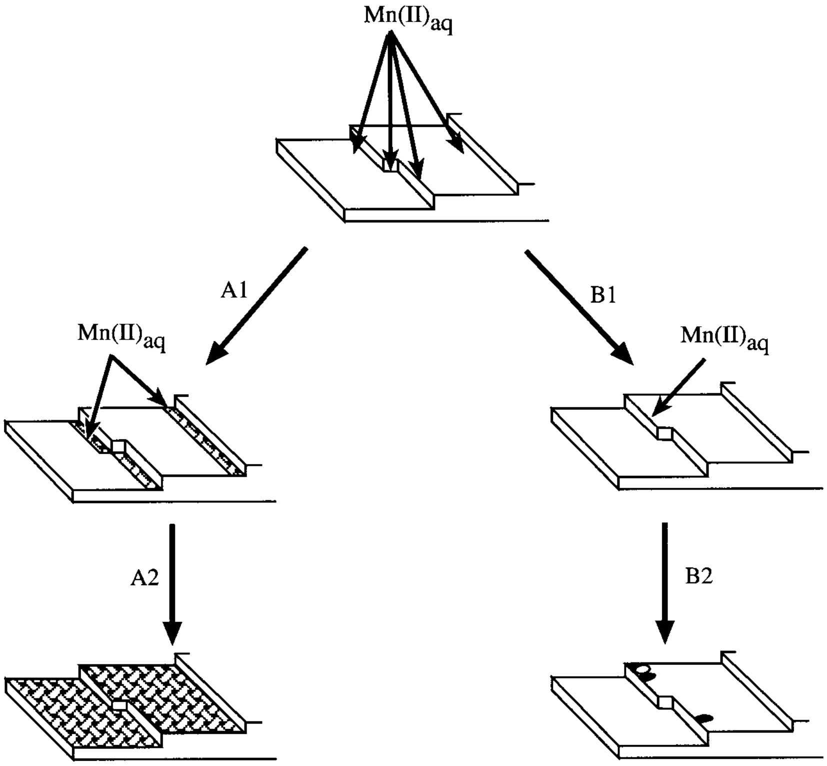

Figure 42. Schematic of two pathways for Mn precipitation on mineral substrates proposed by Junta and Hochella.[607] The reaction begins with adsorption of Mn(II) to sites along steps. Pathway A represent the growth found on surfaces which act as a template for Mn adsorption−oxidation (substrate-controlled growth). Pathway B represents the growth found on surfaces which cannot template adsorption−oxidation (precipitate-controlled growth). Active adsorption−oxidation sites are indicated by arrows in the first two steps of the schematic (adapted from ref 608).

to characterize pH-dependent surface reactions. Certain oxide phases, notably the Al oxides, show significant solubility at both high and low pH. Oxides that are equilibrated at these pH extremes will precipitate more stable oxide polymorphs if the pH is changed toward neutrality.

Heterogeneous nucleation promoted by the surface complexation of both constituents of an ionic solid by an oxide surface has been reported. Heterogeneous nucleation occurs when the aqueous phase is supersaturated with respect to the precipitating solid. The nucleated phase generally has the same crystalline structure and lattice distances as the substrate. The oxides CeO_2, TiO_2, and γ-Al_2O_3 have been shown to nucleate CaF_2, MgF_2, and $CaCO_3$, respectively, from aqueous solution.[604] In all cases, nucleation is promoted by the formation of surface complexes and the partial dehydration of the adion, as occurs in a inner-sphere complex. The heterogeneous nucleation occurs over a narrow pH range where the adsorbed concentrations of both ions in the solid are greatest. The heterogeneous nucleation of $CaCO_3$ by oxides and other solid-phase complexants, including microbiologic surfaces, is an important environmental process.

The refinement of UHV surface analytical techniques (e.g., scanning XPS and AES) and the development of scanning probe microscopies have allowed direct observations of surface precipitates on oxides and provided insights on their formation. These new developments hold great promise, as past understanding of the surface precipitation/nucleation process was based to a large degree on indirect measurements. Surface precipitation often follows the heterogeneous redox reactions described in the preceding section, since the lower valence reaction products often form solid phases with low solubility. Eary and Rai[605] proposed that surface precipitates of $Cr(OH)_3$ or Fe(III)−$Cr(OH)_3$ are formed after the homogeneous reduction of Cr(VI) in hematite and biotite suspensions, and $TcO_2{\cdot}nH_2O$ is suspected to be the reaction byproduct of the heterogeneous reduction of TcO_4^- by magnetite.[548] Neither of the solid phases has been spectroscopically confirmed. Recent XAFS studies of Cr(VI) reduction by magnetite suggest that the Cr(III) reaction product is more complex than a $Cr(OH)_3$ precipitate.[461,566,606] Junta and Hochella[607] identified the reaction products of the heterogeneous oxidation of Mn(II) by iron oxides (hematite and goethite) using modern surface methods. They found that oxidation of Mn(II) and precipitation of Mn(III) (as β-MnOOH) occurred initially at distinct surface sites associated with structural defects (steps) (Figure 42). It was speculated that these surface sites promoted the surface complexes (either the bidentate or monodentate hydrolyzed species) that are necessary precursors to oxidation.[553] Subsequent surface precipitation was substrate-controlled but originated from these defect locations.

4.4.5. Catalysis and Photocatalysis

Metal oxide surfaces play important roles in heterogeneous catalysis and photocatalysis. In heterogeneous catalysis, metal oxides of one type deposited on metal oxides of a second type ($M_IO/M_{II}O$) or metal oxide-supporting metals comprise two classes of catalytic materials used in the chemical industry to produce billions of dollars worth of chemicals each year and to remove harmful compounds from emissions.[609,610] Examples of important $M_IO/M_{II}O$ catalysts include V_2O_5/TiO_2 (used in ammoxidation of alkyl aromatics, selective catalytic reduction of NO_x emissions, and oxidation of dioxin and PCB emissions), TiO_2/SiO_2 (used in epoxidation of propylene by hydrogen peroxide), MoO_3/Al_2O_3 (used in hydrodesulfurization of crude oil and higher *n*-alkane dehydrogenation), and Re_2O_7/Al_2O_3 (used in olefin metathesis). Examples of oxide-supported metal catalysts include Pd/V_2O_5 (Wacker oxidation of ethylene), Rh/SiO_2 (olefin hydrogenation), and Cr/SiO_2 (polymerization of olefins). Though some correlations between catalytic activity and macroscopic properties of the host oxides ($M_{II}O$) or oxide substrates have been suggested (e.g., ref 611), there is limited fundamental understanding of how these oxide systems realize their unique catalytic properties or how metal on metal oxide support catalysts may be optimally prepared (see, e.g., ref 612). In the case of V_2O_5 on various $M_{II}O$ supports, for example, Wachs and Weckhuysen[611] have suggested a correlation between the turnover frequency in MeOH oxidation and the Sanderson electronegativity of the cation in $M_{II}O$ support oxides in the following order: $CeO_2 > ZrO_2 > TiO_2 > Al_2O_3 > SiO_2$. A fundamental understanding of this type of correlation will require detailed spectroscopic and microscopic studies of these types of catalysts.

In the area of photocatalysis, a new research front emerged in the late 1970s concerning the photoelectrochemical behavior of large-band gap metal oxide semiconductors, stimulated by the report of Fujishima and Honda[613] of photoinduced water cleavage using TiO_2 (rutile) electrodes; well over 1000 papers were published within only a few years.[614] Despite this large effort, the solar-to-hydrogen conversion efficiency obtained with this system remained well below 1% due to the poor harvesting of sunlight by TiO_2, whose fundamental absorption edge is in the UV region. In the mid-1980s, interest shifted to other photocatalytic applications of metal oxide semiconductors, the main research thrust being placed on the photocatalytic destruction of pollutants in water in the presence of TiO_2 particles.[615–618]

Figure 43 presents schematically the charge separation processes that occur in nanocrystalline oxide films following excitation of the semiconductor with light of energy equal to or greater than the band gap energy. There have been a number of studies devoted to the mechanism of charge separation in nanosized semiconductor films; their results have been reviewed elsewhere.[374] Here we cite only some key points. In mesoporous oxide films, the electrolyte penetrates the whole colloidal film up to the surface of the back contact, and a semiconductor–electrolyte junction thus occurs at each nanocrystal, much as in a normal colloidal system. During illumination, light absorption in any individual colloidal particle will generate an electron–hole pair. Assuming that the kinetics of charge transfer to the electrolyte is much faster for one of the charges (holes for TiO_2) than for the recombination processes, the other charge (electrons) can create a gradient in the electrochemical potential between the particle and the back contact. In this gradient, the electrons (for TiO_2) can be transported through the interconnected colloidal particles to the back contact, where they are withdrawn as a current.

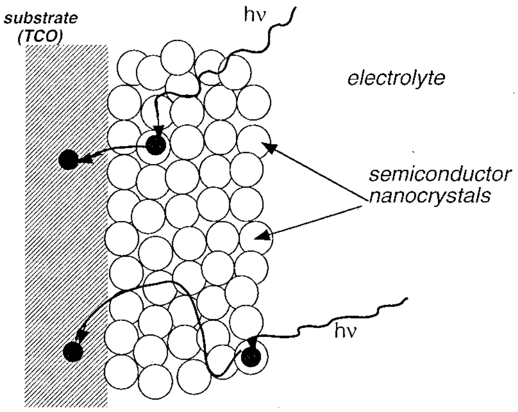

Figure 43. Schematic representation of the charge separation processes that occur in nanocrystalline oxide films following excitation of the semiconductor with light of energy equal to or greater than the band gap energy.

The charge separation in a nanocrystalline semiconductor therefore does not depend on a built-in electric field, i.e., a Schottky barrier, but is mainly determined by kinetics at the semiconductor–electrolyte interface. The creation of a light-induced electrochemical potential for the electrons in TiO_2 also explains the building up of a photovoltage. There will be an increased probability of recombination with increased film thickness, as the electron has, on average, to be transported across an increasing number of colloidal particles and grain boundaries. This indeed has been observed experimentally. Thus there exists an optimal thickness to obtain maximum photocurrent. Another loss mechanism due to increasing film thickness is a resistance loss, leading to a decrease in photovoltage and fill factor.

In the area of environmental remediation, TiO_2 particles have been used to photocatalytically oxidize organic contaminants and reduce heavy metals in industrial waste streams (see e.g., refs 619 and 620). The higher photocatalytic activity of TiO_2 nanoparticles, relative to bulk TiO_2, is well-known; however, the fundamental chemical basis for this phenomenon is not completely clear. To help provide this fundamental understanding, Chen et al.[621] used XAFS methods to study the photocatalytic reduction of the heavy metals Cu^{2+} and Hg^{2+} on nanoparticulate TiO_2. They concluded that the coordination number of Ti in TiO_2 nanoparticles as small as 30 Å in diameter remained 6-fold and that the increased catalytic activity was due to the increase number of Ti sites and the possible corner defect sites in these small particles.

Another example of the photocatalytic effect of TiO_2 (anatase) is provided by an XAFS spectroscopy study of the oxidation of arsenite [$As(III)O_3^{3-}$] to arsenate [$As(V)O_4^{3-}$] on natural kaolinites containing ≈1.8 wt % TiO_2 in the form of anatase inclusions.[622] Such reactions in surface soils can convert the more mobile and toxic form of arsenic [As(III)] into a less mobile and less toxic form.

4.4.6. Photocatalytic Effects of Oxides in the Atmosphere

Metal oxides such as Fe_2O_3, ZnO, Pb_2O_3, WO_3, and Cu_2O are semiconductors which, due to their electronic structure, can act as sensitizers. When a photon with energy greater than the charge-transfer band gap strikes such a material, it generates an electron−hole pair by promoting an electron from the valence band into the conduction band of the semiconductor. These charge carriers will recombine rapidly[615] unless they are trapped in the solid or scavenged by reagents present at the surface that can undergo redox reactions. The valence-band holes of most metal oxides are powerful oxidants ($E° = 2.0-4.0$ V vs NHE) and therefore are able to oxidize most organic materials, i.e., alkanes, alkenes, aliphatic alcohols, carboxylic acids, dyes, PCBs, simple aromatics, and halogenated compounds, as well as surfactants and pesticides. In general, the concomitant conduction band process is the reduction of oxygen to water or hydrogen peroxide. Other oxidants such as nitrogen oxides or Ag^+ and chromate and persulfate can also act as scavengers for conduction-band electrons.

Interest in photocatalysis by semiconductors has been growing very rapidly during the past decade due to the possibility of removing contaminants from water and air by such processes;[616] at present the rate of publications exceeds 200/year. A recent important example is the degradation of nitrophenols by a catalytic cycle involving copper oxides.[617] The rate is greatly enhanced by light due to the assistance of charge-carrier-induced redox reactions in the mineralization of this xenobiotic pollutant.

With regard to the importance of photocatalytic effects of oxides on atmospheric processes, we draw attention to the important role played by iron oxides, which has recently been reviewed.[618] Significant concentrations of Fe species (up to 0.2 mM) are present in atmospheric water, i.e., fog, where they mediate the oxidation of organic compounds by oxygen, producing H_2O_2. They also enhance the oxidation rate of SO_2 or sulfite. Thus, photoredox reactions involving iron oxides are important in the cycling of iron, carbon, and sulfur in atmospheric and surface waters.

5. Dissolution and Growth of Metal (Hydr)oxides

No reaction is more fundamental to our understanding of the metal (hydr)oxide surface than dissolution and growth, since most reactions at such surfaces either add or remove mass. These reactions proceed at monatomic steps on the surface, as discussed in section 2.1. The surface complexes that form on these monatomic steps generally consist of one or more metals linked to one another and to the surface via oxo or hydroxo bridges. These structural units immediately suggest a comparison to dissolved aqueous metal (hydr)oxide oligomers, which allows us to rank the reactivities of different sites in the surface metal (hydr)oxide complexes, to assign protons to reasonable sites, and to estimate rate coefficients for ligand exchange at the surface. Quantitative comparison may be possible in ideal cases where there is strong structural similarity between sites in the dissolved aqueous oligomer and sites at the metal oxide surface.

5.1. Reactivities of Metal (Hydr)oxide Oligomers: Models for Surface Complexes

Metal sites at the metal oxide surface in contact with water are coordinatively saturated; therefore, they exchange ligands via pathways with a considerable dissociative character, and proton-assisted depolymerization rates largely reflect the metal−oxygen bond strength. Reactivities are predictable from the metal position in the periodic table and electronic structure (e.g., ref 229).

5.2. Structural Similarities between Aqueous Oxo and Hydroxo Oligomers and Simple Surfaces

The oxygen coordination chemistry at surfaces is distinctly different than for most dissolved complexes, while the metal coordination chemistry commonly remains the same. For example, Ni(II) is hexacoordinated to oxygens in the $Ni(H_2O)_6^{2+}$(aq) species, the $Ni_2(OH)^{3+}$(aq) dimer, and NiO(s). In contrast, however, oxygen atoms exist in several distinct coordination environments at the surface of a metal oxide, and the variety of oxo bridges tends to increase with decreasing structural symmetry.

Oxygen atoms are coordinated to between one and six Mg(II) metal atoms at a kink site on a monatomic step on MgO(s) (Figure 44). These highly coordinated oxygen atoms have no analogue in dissolved oligomers, so that direct comparison between well-chosen dissolved oxo and hydroxo oligomers and metal oxide surfaces complexes is inexact; however, it is still useful because it potentially provides estimates of rate coefficients and reactivity trends. Compare, for example, the structure of the $Al_{13}O_4(OH)_{24}(H_2O)_{12}^{7+}$(aq) oligomer (Figure 45a) with the (0001) surface of α-Al_2O_3(s) (Figure 45b). Both the dissolved oligomer and the α-Al_2O_3(s) surface are dominated by six-membered rings of shared AlO_6^{9-} octahedra. The

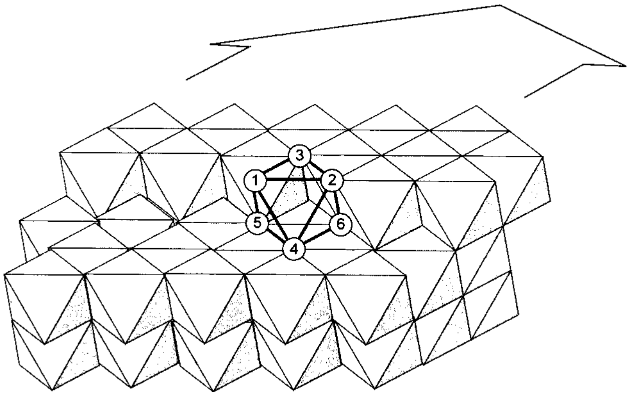

Figure 44. A kink site on the surface of a monomolecular step on an M(II) oxide mineral with the rocksalt structure [e.g., MgO(s)]. Oxygen atoms are coordinated to between one and six metal atoms at the kink site. The coordination number of oxygens to the metal is identified as a number in the wireframe diagram. As a monomer [e.g., $Mg(H_2O)_6^{2+}$] detaches from the migrating kink site, the coordination spheres of newly uncovered metals are satisfied by movement and dissociation of water molecules at the surface.

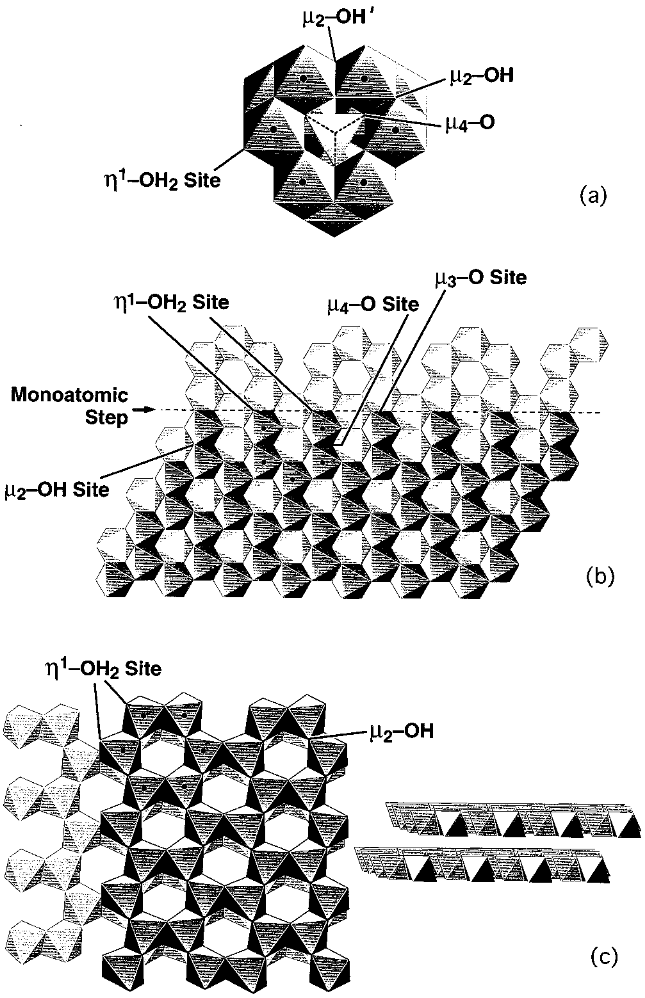

Figure 45. (a) $AlO_4Al_{12}(OH)_{24}(H_2O)_{12}^{7+}$(aq) tridecamer consists of AlO_6 octahedra that share edges and a single, central AlO_4 (or GaO_4) tetrahedron in a Keggin structure. At the apexes of the AlO_6 octahedra are 12 $-OH_2$ sites (η^1-OH_2) that can undergo Brønsted acid−base reactions with the aqueous phase. There are two types of μ_2-OH sites and one type of μ_4-O site; dots indicate a six-membered ring of linked AlO_6 octahedra. (b) Monomolecular step on the (0001) surface of α-Al_2O_3(s) with solid dots added to six-membered rings of AlO_6 octahedra that surround an unoccupied octahedral site. The octahedra are linked to one another via faces and edges and expose sets of coordinatively distinct oxygen sites, some of which are in common with those in the $AlO_4Al_{12}(OH)_{24}(H_2O)_{12}^{7+}$(aq) complex. (c) Monomolecular step on bayerite [β-Al$(OH)_3$], which consists of AlO_6 octahedra that share edges. Truncation of the surface without repolymerization exposes μ_2-OH groups and η^1-OH_2 groups to the aqueous phase. Solid dots are added to six-membered rings of AlO_6 octahedra to compare with the $AlO_4Al_{12}(OH)_{24}(H_2O)_{12}^{7+}$(aq) tridecamer. Also shown is a side view of the structure to emphasize that the layers are linked via van der Waals forces.

oligomer has only edge-shared octahedra that are each bound to an AlO_4^{5-} tetrahedron, while the α-Al_2O_3 structure includes shared octahedral faces perpendicular to (0001) as well as edge-shared octahedra. The reactive surface sites on α-Al_2O_3 are at monatomic steps, so there exist terminal water ligands on the kink octahedra as well as at oxo or hydroxo bridges.

Likewise, the (001) surface of bayerite, α-Al$(OH)_3$ (Figure 45c), a common soil mineral, is terminated by water molecules and doubly bridging hydroxyls, which are directly analogous to the $Al_{13}O_4(OH)_{24}(H_2O)_{12}^{7+}$(aq) oligomer. Quantitative similarity between the dissolved oligomers and metal (hydr)oxide surfaces will be better for low-symmetry oxyhydroxide minerals, such as the alumina phases, boehmite, gibbsite, and bayerite, than for high-symmetry phases. The high-symmetry phases commonly have highly coordinated oxygens that have no analogue in solution.

5.3. Dissolution Rates of Metal (Hydr)oxides and Depolymerization of Surface (Hydr)oxide Polymers

The surface chemistry of insulating oxides has received much recent attention because the materials are so common at the earth's surface. Dissolution of electrically insulating oxides is interpreted in terms of surface complexes and familiar ligand-exchange pathways. Pathways for dissolution of (hydr)oxide minerals are distinguished depending upon whether adsorbed protons, ligands, deprotonations, or electron exchanges control the reactivities (see refs 7 and 623). Dissolution rates of insulating oxides increase with the equilibrium concentration of key adsorbates (protons, hydroxyls, ligands) on the surface, and these adsorbed concentrations are expressed in the rate laws. Although direct evidence is missing, dissolution appears to proceed by detachment of monomeric surface complexes from retreating monomolecular steps; there is yet no evidence for detachment of oligomer units. Most experimental evidence also suggests that the ligands and protons that coordinate to the surface metal and enhance the rates of dissolution are consumed by detachment of a monomer from the dissolving surface. In other words, fluoride adsorbed onto the surface of AlOOH(s), which enhances the dissolution rate, is subsequently released to the aqueous solution as an $AlF_x(H_2O)_{6-x}^{3-x}$(aq) complex.

Rates of dissolution increase with both negative and positive charge, reflecting the amphoteric surface, but the actual sites of these protonations/deprotonations are unclear. By analogy with oligomer dissociation, protonation of hydroxyl bridges, such as those identified in Figure 45b as a μ_2-OH site, probably induces slow dissociation and accounts for the proton-assisted reaction pathways. This protonation is not catalytic if the resulting water molecule remains stably in the inner coordination sphere of the departing metal, as it would if a fully hydrated metal, such as $Al(H_2O)_6^{3+}$(aq), were released. In contrast, if the monomers are stronger acids than the protonated bridge, the protons dissociate and the reaction is proton catalyzed.

Likewise, by analogy with dissolved complexes, deprotonation of a water molecule coordinated to a monatomic step (e.g., Figure 45b):

$$\eta^1\text{-OH}_2 = \eta^1\text{-OH}^- + \text{H}^+(\text{aq})$$

probably also enhances the lability of the adjacent metal−oxygen bonds by a factor of 10^2−10^4.[231,234] These effects are progressive; that is, they increase as each hydroxyl coordinates. Hydroxylation by deprotonation of coordinated water molecules undoubtedly accounts for the correlation of dissolution rates with negative surface charge. Because deprotonation is so rapid, this reaction is essentially a ligand exchange of hydroxyl for a coordinated water molecule.

Likewise, exchange of this water molecule for an anion, such as fluoride, reduces the charge of the site and labilizes adjacent metal–oxygen bonds:[235]

$$\eta^1\text{-OH}_2 + \text{F}^-(\text{aq}) = \eta^1\text{-F}^- + \text{H}_2\text{O(aq)}$$

as can exchange of surface functional groups for charge-donating ligands such as carboxylates and amines (Table 2). These nonleaving ligands enhance reactivity by transferring charge to the surface metal center, thereby weakening bonds to structural oxygens, but addition of anions to the surface also reduces the electrostatic repulsion to proton adsorption at oxygen bridges. These protonations themselves accelerate dissolution so that ligand- and proton-assisted reaction pathways are coupled.

Detachment of a metal–ligand complex from the surface must proceed simultaneously with movement and dissociation of water molecules to maintain a steady-state surface, and this hydration is thought to control the overall rate of reaction. For similar concentrations of rate-enhancing adsorbates, and when it can be isolated from side reactions, metal release from a metal oxide surface proceeds with reactivity trends that resemble those for exchange of solvation water molecules around the corresponding dissolved, hydrated metal ions. This familiar reactivity trend is not accidental, but indicates that detachment of the metal ion from the surface is via a largely dissociative pathway with some mechanistic similarities to a ligand-exchange reaction. The simple oxide MnO(s), for example, dissolves at a faster rate via the proton-promoted pathway than does bunsenite (NiO) at otherwise similar conditions, as one expects from the electronic structure of the two metals and from the relative rates of exchange of solvation waters around the Mn(II) (10^7 s^{-1}) and Ni(II) (10^4 s^{-1})[229] hydrated metals (Figure 46). A similar reactivity trend is found for simple adsorption of divalent metals onto γ-Al_2O_3,[625] where a water molecule is displaced by adsorption.

The results are more complicated for minerals that have extensively polymerized silicate anions in their structure. For these minerals, the near-surface region commonly has a different bulk composition than the interior as more reactive sites are leached away. The leached zone can extend to hundreds of nanometers, and the extent of reaction depends sensitively on the solution pH, that is, the extent of protonation of surface sites.

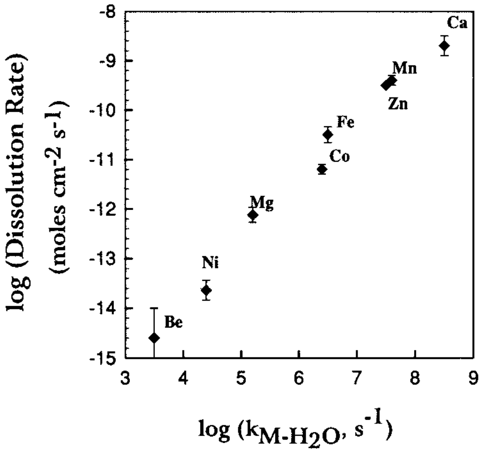

Figure 46. Dissolution rates at pH 2 of orthosilicate minerals plotted against the rate of exchange of water from the bulk aqueous phase into the inner coordination sphere of the corresponding hydrated metal in solution. The symbol Mg, for example, stands for both the dissolution rate of forsterite [Mg_2SiO_4(s)] at pH 2 and the rate of exchange of waters from the hydration sphere of $\text{Mg(H}_2\text{O)}_6^{2+}$(aq) and the bulk solution. The orthosilicate minerals do not have a polymerized silicate anion.[624]

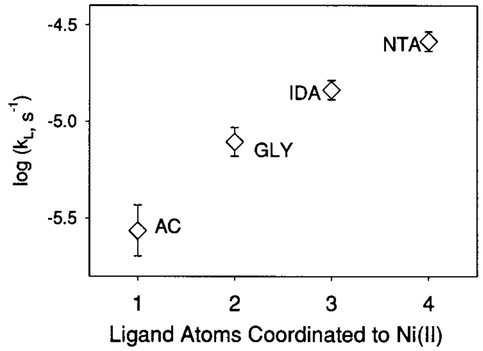

Figure 47. Rate coefficients (k_L) for ligand-induced dissolution of bunsenite, NiO(s), for a set of ligands differing in the number of ligand atoms coordinated to the metal center at the mineral surface. The rates increase as increased numbers of amino and carboxylate functional groups coordinate to a single metal center, which in this case is assumed to be at a retreating monatomic step on the NiO surface. The trend in reactivities of increased oxygen reactivity with increased ligand coordination is well established for dissolved Ni(II)–ligand–H_2O complexes.[234,626,627] The ligand abbreviations are AC, acetate; GLY, glycine; IDA, iminodiacetate; and NTA, nitrilotriacetate.

There is some consistency between the labilizing influence of nonleaving ligands in the inner coordination sphere of dissolved metal–ligand complexes and in metal–ligand complexes at the metal oxide surface.[626,627] For example, the flux of Ni(II) from dissolving NiO(s) increases with the number of carboxyl and amino functional groups from a ligand coordinated to a surface metal atom (Figure 47), although the actual conformation of the ligands about the surface metal atom is unknown.[239,626,627] These nonleaving ligands are well known to enhance rates of metal–oxygen bond dissociation in dissolved nickel complexes. Because so much information is available about labilization of μ-hydroxo and μ-oxo sites in Cr(III) or Co(III) oligomers (e.g., ref 628), similar experiments could profitably be conducted on Cr(OH)_3 or Co(OH)_3 to match the surface chemistry to the existing work on dissolved species.

Many industrial metals are unstable in water and quickly form passivating oxide layers (see section 4.4.3.4), some of which can become hazards. BeO(s), for example, is more toxic than beryllium metal; the accumulation of copper oxides on turbine blades dramatically shortens the serviceable life of a power plant; and considerable research is conducted by the nuclear power industry to eliminate oxides that accumulate fission products (e.g., ^{60}Co) in the cooling circuit. Chemical strategies for eliminating these corrosion products involve the addition of carboxylates, aminocarboxylates, or mercaptocarboxylates to the aqueous fluid; these ligands enhance the dissolution rates.[315] Some industrial oxides are conducting or semiconducting (e.g., ZnO, Fe_3O_4, NiO, UO_2), so that corrosion can also be eliminated by controlling the potential or by inducing photoreaction.[315] These reactions are usually interpreted in terms of electrode properties and not surface complexes (see sections 4.4.3.3, 4.4.5, and 4.4.6), and the pathways are commonly, but not exclusively, reductive. A counterexample is provided by NiO(s) dissolution,[315] where hole injection causes changes in bulk stoichiometry via the reaction (see section 2.4.2) and dissolution by oxidation is rapid:

$$>\mathrm{Ni(II)} + \mathrm{h}^+(\mathrm{vb}) = >\mathrm{Ni(III)}$$

Dissolution rates are separable into two parts: (i) rates of formation of redox-active defects and (ii) the rates of ligand exchange of the resulting surface metal [Ni(III) in this example]. If rates of forming the surface states by hole or electron injection are slow, the dissolution pathways reduce to those of the simple ionic oxides. If surface states form rapidly, and if the resulting defect exchanges ligands relatively rapidly, dissolution is accelerated. In the above example, Ni(III) exchanges ligands much more rapidly than Ni(II), so defective NiO(s) dissolves at a rapid rate relative to defect free NiO(s). The surface >Ni(III) can reduce after hydration and detachment from the lattice.

Much research into the corrosion of metals concerns the microscopic permeability of the passivating oxide layer, since an oxide product must be physically impermeable as well as chemically relatively inert in order to form an effective corrosion barrier. Aluminum metal is kinetically stable in air because oxide products form a passivation layer rapidly at the surface. If aluminum metal is first wetted with Hg^0, however, the metal oxidizes rapidly and completely.

6. Biotic Processes in Metal Oxide Surface Chemistry

The role of microbiota in the interfacial chemistry of metal oxides can be viewed from several perspectives, three of which are discussed here. The first involves the physical attachment of organisms to solid substrata and the formation of biofilm communities—a kind of behavioral microbiology as it relates to microbes and surfaces. The latter two arenas are more process-related in the sense that they deal with metabolism, either directly or via metabolic byproducts, and the relationship of these activities to metal dissolution or precipitation. These include (1) reductive dissolution via direct or indirect processes and (2) precipitation and deposition of metal oxides as a result of direct or indirect metabolic activities. In all of these cases, while some of the generalities and a few details can be identified, there is no data set that is sufficient to allow the specification with certainty of the role(s) of the microbes and their participation in the chemical processes alluded to in this review. These three areas, and many more that are relevant to the emerging field of geobiology, are reviewed in a recent publication.[629]

6.1. Surface Attachment and Biofilm Formation

In general, biofilms may be an important and overlooked aspect of the metal dissolution process. It is well-known through many studies[630] that biofilms are key ways that bacteria can isolate a surface environment from the overlying water, thus affecting the stagnant boundary layer, making microzones of anoxic or altered pH conditions, and optimizing conditions for growth of certain species of bacteria.[631] In addition, such biofilms have strong, and often specific, chelating or binding properties, often leading to the adsorption of cations, anions, organics, etc., depending upon the nature of the biofilm produced (e.g., extracellular polymers, etc.).[630]

Just a few years ago, biofilms were regarded as rather simple, two-dimensional structures in which organisms attached to substrates for particular metabolic reasons; little was known of any detailed three-dimensional community structure. With the advent of confocal laser scanning microscopy,[632,633] NMR, microelectrodes,[634] and other techniques, a variety of chemical gradients can be seen.[631,635,636] The complex biofilms have been modeled as three conceptually different types: (1) heterogeneous mosaic biofilms, (2) penetrated water-channel biofilms, and (3) dense confluent biofilms. As discussed by Wimpenny and Colasanti,[631] probably all three types are proper descriptions, depending on the nature of the substrate of attachment and the levels and types of dissolved growth substrates available to the bacteria.

The processes that occur within the biofilm can be imagined to be very complex and a function of the substratum (metal oxide type, etc.), the overlying water (marine, freshwater, etc.), and the type(s) of organisms within the biofilm community. Figure 48 shows the various types of reactions that might be expected to occur within the biofilm environment. A series of oxidative reactions may occur due to oxygen diffusion into the community, while another series of reductive reactions may occur, depending on what electron acceptors are available in the environment and on the metal oxide surface.

In terms of relating this to surface chemistry, it is notable that the double layer of interest to chemists for modeling metal oxide—aqueous solution interfaces is of the order of 4 Å and the overlying solvent region of interest may extend to 20—30 Å, while a single microbial cell layer is approximately 5000 Å, 100—200 times thicker! A biofilm of 50 cells becomes an almost infinite distance in terms of modeling complexity. This, coupled with the fact that single cells on the surface may extend from 10 000 to 20 000 Å in length, demands that bacterial layers and biofilms be seriously considered in terms of interfacial chemistry.

With regard to metal oxide surfaces and dissolution chemistry, biofilms can be imagined to exert two

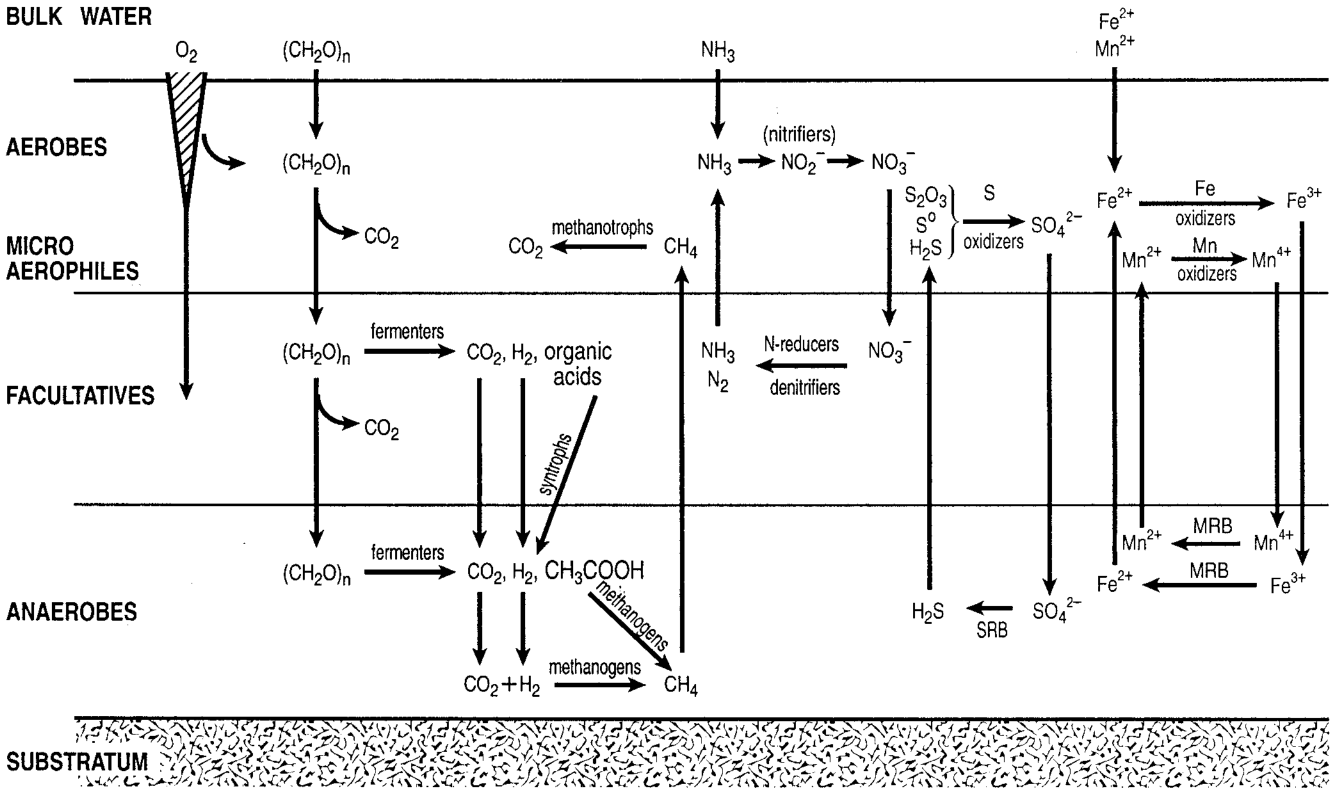

Figure 48. Depiction of potential chemical reactions catalyzed by members of a generalized biofilm community. The diagram seeks to identify the kinds of biogeochemical cycling that might be set up on any given substratum; the actual reactions that will occur will depend on the nature of the substratum, the overlying water, and the resulting microbial communities, which may range from single layers to multiple layers several micrometers, or more, in thickness.

distinctly different types of effects. First, biofilm formation can occur by cells that are growing on dissolved metabolites in the liquid phase and thus interfere with the chemistry of dissolution by interference with the double layer and overlying water. Second, biofilms can be composed of bacteria that interact chemically with the metal oxide surface, as discussed below for both indirect and direct reactions. An example of such a microbial layer (biofilm) is shown in Figure 49 for *Shewanella putrefaciens* in the process of growing on the manganese oxide manganite (Figure 49a). As shown by the environmental scanning microscope (Figure 49b), a polymeric coating is observed, which disappears upon dehydration and imaging via standard scanning electron microscopy. In marked contrast, when the same cells are grown on iron oxides, a similar monolayer of cells is formed, but no polymeric layer is formed.[637] In these cases, the microbial biofilm is intimately involved in the reductive dissolution of the surface, and a combination of imaging techniques is needed to eliminate the artifacts often encountered when standard SEM surface analyses are employed.[638]

A further complication of biofilms involves understanding the organisms and the regulation of their metabolism within the biofilm community. Modern molecular biology techniques (molecular probes that are specific for genes of given microbial groups) have recently been brought to bear on such problems, so that it is now possible to identify organisms on solid surfaces in situ without the need for culturing the bacteria.[639,640] The issue of gene (and metabolic) regulation in biofilm communities is only now beginning to be addressed, with several different approaches being used, all suggesting that metabolic activities can be diverse and complex and quite variable temporally and spatially. A recent example is the demonstration that some bacterial species are able to “communicate” with each other chemically, inducing certain activities only when the cell concentration reaches critical levels. This is done via a mechanism called autoinduction or quorum sensing.[641]

6.2. Metal Oxide Dissolution (Reductive and Nonreductive)

Both nonreductive and reductive dissolution of metal oxides in water can be enhanced by microbial activities, although studies of the former case are not abundant, and in general the role of microbes in nonreductive dissolution remains poorly documented.

6.2.1. Nonreductive Dissolution of Metal Oxides

Nonreductive dissolution by bacteria is an area in which the abiotic mechanisms are reasonably well-understood but for which little information is available concerning biotic contributions. The nonreductive dissolution of metal oxides presumably occurs via the protonation, deprotonation (local pH changes), and/or ligand binding of minerals, thus leading to destabilization or labilization as described in section 5 for abiotic processes. Such reactions may constitute precursors (perhaps necessary precursors) to metal reduction, if transport of the metal is needed to an active site in or on the involved microbes. Given that

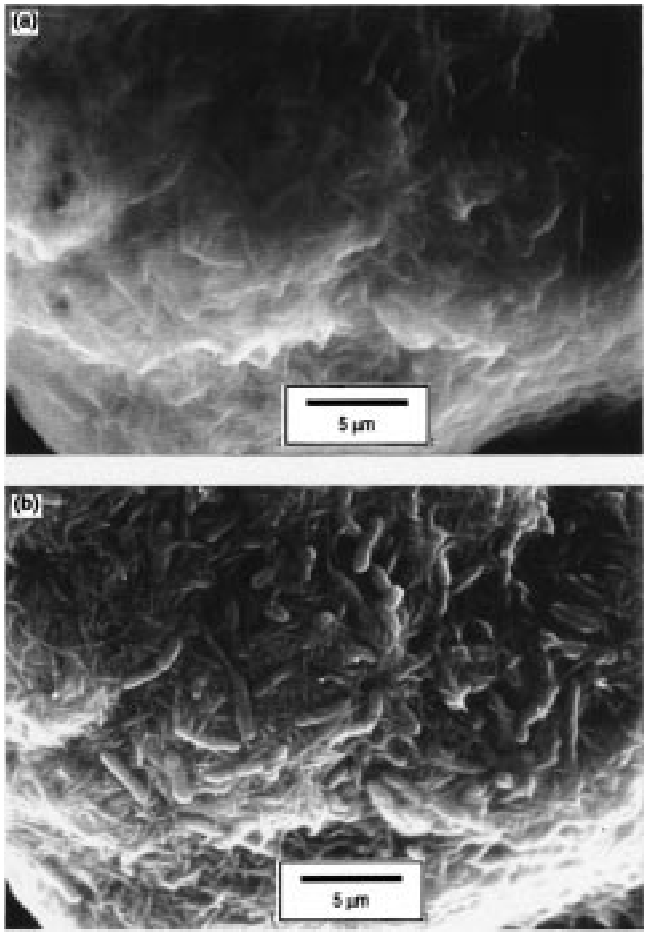

Figure 49. Manganese oxide particle with associated cells of metal-reducing bacteria. This figure shows a view of a MnO_2 particle in the process of reduction by cells of *S. putrefaciens* MR-4 as seen in the environmental scanning electron microscope (ESEM). In the top panel (a) the cells are barely visible because of the presence of a layer of extracellular polymer that obscures the attached cells. In the lower panel (b) the same field has been dehydrated, revealing the underlying cells closely associated with the manganese oxide substratum.

bacteria are well-known for the alteration of pH (via proton production, acid production, etc.) and that one of the things they do best is pumping protons,[642] it is not unreasonable to assume that proton donation or elimination could be a major part of metal oxide dissolution processes; however, there is little quantitative data to back up this hypothesis. Similarly, for iron, bacteria are well-known to produce specific ligands of high affinity.[643] Such compounds could be used independently, or in combination with pH changes, to destabilize and dissolve iron oxides. Similar high-affinity chelators for other metals (Mn, Si, Al, etc.) are not known and so cannot be invoked for nonreductive dissolution. General ligands (hydroxamates and other compounds) may have importance in this regard, but there is little information available. In terms of some oxides, like Mn(III) and Mn(IV) oxyhydroxides, local pH changes may be sufficient for dissolution, leading to mobile oxidized metals—again, there is only limited information concerning microbial contributions to such reactions.

Table 5. Microbially Reduced Metal-Containing Minerals and Compounds

mineral	compd	ref
	Manganese	
Mn(III)	manganite	644
	soluble chelates	645
Mn(IV)	colloidal MnO_2	Nealson et al., unpublished
	MnO_2	646, 647
	Iron	
Fe(III)	soluble chelates	648
ferrihydrite	$Fe(OH)_3$	649, 650
goethite	FeOOH	649, 650
hematite	Fe_2O_3	649, 650
magnetite	Fe_3O_4	651
clay minerals	smectite	652, 653
	Others	
Cr(VI)		654
U(VI)		655
I(VI)		656
Se		657
As		658

Table 6. Metal Reduction by Bacteria: Direct and Indirect Reduction

type of products	indirect reduction	direct reduction
inorganics[224]	hydrogen sulfide hydrogen peroxide	
organic acids[659]	formate acetate succinate	
other organics	cysteine quinones[660] humic acid analogues[661]	
proteins	cytochromes[662]	reductases[663] cytochromes[664,665]

6.2.2. Reductive Dissolution of Metal Oxides

As shown in Table 5, many different forms of oxidized Mn and Fe compounds are now known to be reduced by bacteria; in addition, Table 5 shows other metals that are known to be susceptible to microbial reduction.

For the purpose of this review, the focus will be on the dissolution of iron- and manganese-containing (hydr)oxides, but it is assumed that many of the general features that apply to (hydr)oxides containing these metals may apply to (hydr)oxides containing other metals listed in Table 5.

6.2.2.1. Direct and Indirect Reduction of Metal Oxides. Any consideration of bacterial interactions at metal oxide interfaces must begin with the distinction between those reactions that are directly mediated by bacterial enzymes or cell-bound catalysts and those that are the result of excreted products. Such considerations are particularly important with manganese and iron oxides, the dissolution of which can be catalyzed by a number of indirect reactions, as shown in Table 6. When these reactions occur, while the production and excretion of reductants may well be microbial, the processes and mechanisms involved are appropriately the realm of surface chemists and not microbiologists. In contrast, when cell-mediated (direct) dissolution occurs, it is the realm of the microbiologist, and many factors, most of which are still only minimally understood, come into play. Table

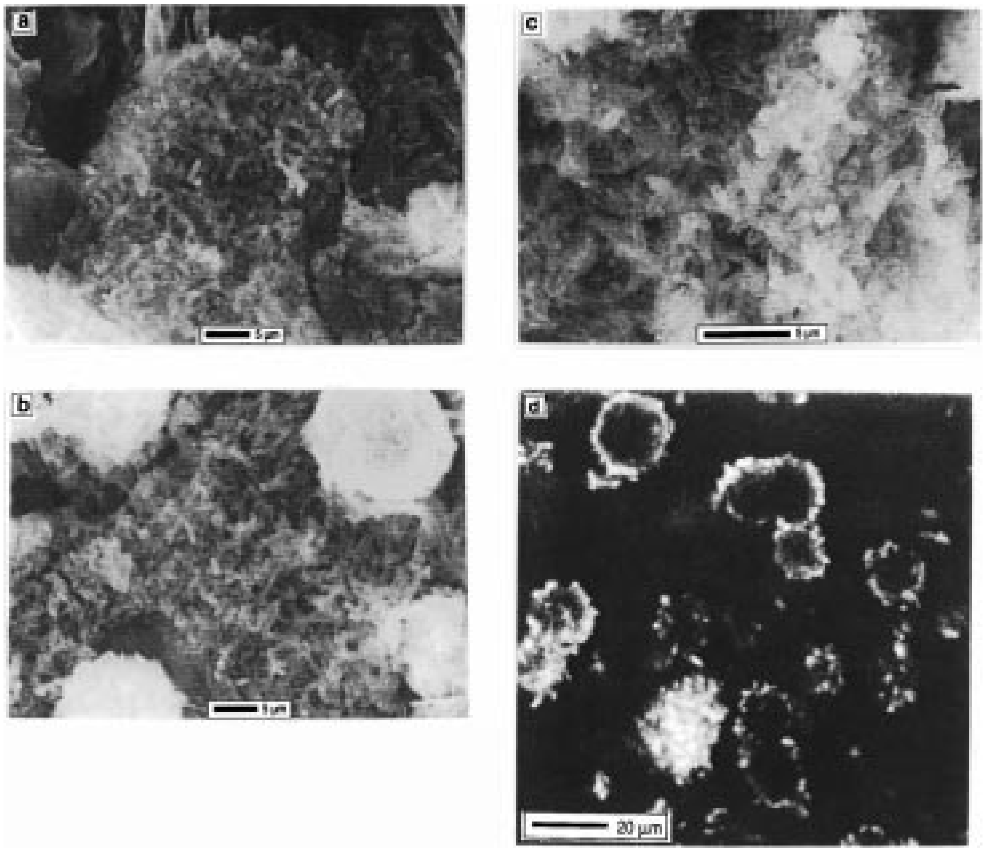

Figure 50. ESEM images of cells of *S. putrefaciens* growing on goethite, α-FeOOH, are shown in panels a−c, while a laser confocal image is shown in panel d. In the case of iron, no extracellular polymeric material is produced, and the bacteria are clearly seen on the oxide surfaces.

6 is not meant to be inclusive but to demonstrate that a large variety of possible bacterial reactants are available, and when these are released into the environment, either as a direct result of bacterial metabolism or inadvertently via cell death, metal reduction can be stimulated. From the mechanistic point of view, it is very important to know which type of reaction is occurring, as the indirect reactions are best studied using the approaches of surface chemistry, while the direct reactions lead one into the areas of bacterial physiology, biochemistry, and molecular biology.

Indirect reductive reactions are those in which dissolution of Mn oxides is not dependent on cell−metal oxide contact. In this case, metal oxides, in either liquid medium or suspended in an agar matrix, can be reduced at considerable distance from the bacteria as a result of reductants secreted by the cells. (Soft agar is a nonmetabolizable hydrated polymer through which bacteria are able to swim; zones of reduction can be visualized in three dimensions as the metal oxides are reduced.) This is a common occurrence when complex media are used for cell growth and when a fermentable carbon source like glucose is included in the growth medium. In such cases the advantage to the cells is subtle, if any. Small increases in cell yields are sometimes seen; this is thought to be due to the use of the metal oxides as external sinks for intracellular reductants that are excreted under anaerobic growth conditions.

Direct reactions require cell−mineral contact, so that on agar media no colonies are visible, although discrete zones of clearing of oxides are seen. Upon closer examination, using either fluorescence microscopy (Figure 50d) or environmental scanning electron microscopy (ESEM; Figure 50a−c), it can be seen that, while few or no cells are in the cleared zones, the particles around the edges of the cleared zones are coated with bacteria in various stages of particle reduction. The requirement for direct cell contact with the metal oxide is a characteristic of all direct reducers so far isolated. In general, separation of the cells from the oxides using a dialysis membrane is sufficient to completely inhibit metal dissolution.

Two exciting recent observations suggest that the situation may not be as simple as presented above. Lovley et al.[661] have noted that artificial humic acids can be reduced by iron-reducing bacteria and that these reduced humic analogues can act as electron shuttles to insoluble iron oxides, greatly increasing the rate of reduction. If such mechanisms operate in nature, it could lead to substantial amounts of indirect iron reduction, something that is in conflict with previous estimates, in which it is stated that virtually all iron reduction in nature is enzymatic and direct.[666] A second finding by Seeliger et al.[662] has shown that *Geobacter sulfurreducens* produces a small *c*-type cytochrome that is found extracellularly and can act as an electron shuttle for the reduction of iron and several other metals. Again, if this occurs in nature, it will be viewed as indirect reduction, supplying a mechanism whereby intracellular reduction is connected to extracellular oxidants via an indirect coupling mechanism. Given these findings,

Table 7. Cytochromes of *S. putrefaciens*[a]

cyt type	pure	aa sequence	cloned	gene sequence	MW (kD)	redox pot.	no. of hemes	ref
c	−	+	+	+/−	?	?	12	Saffarini, unpublished
c_3	+	+	+	+	12	−233	4	665
c_4	+	N-term	−	−	20	343	2	Nealson et al., unpublished
c	−	+	+	+	21	?	4	676
c_5	+	N-term	−	−	9	315	1	Nealson et al., unpublished
CCP	+	N-term	−	−	46	+230 −250	2	Nealson et al., unpublished
c'	+	+	+	+	32	+125	1	Nealson et al., unpublished
FC	+	+	+	+	62	−230	4	Nealson et al., unpublished, 677
FD	+	+	−	−	7.6	?	NA	Nealson et al., unpublished
c-mem	+	N-term	−	−	−	?	?	Nealson et al., unpublished

[a] *c*, *c* cytochromes; *c*-mem, membrane-bound *c*-type cytochrome; FC, flavocytochrome; FD, ferredoxin; N-term, first few amino acids of the N-terminal end have been sequenced; +/−, partially done; NA, not applicable; ?, not known.

it may well be that such biologically catalyzed indirect mechanisms are more common than has been appreciated. In fact, the use of such extracellular electron shuttles mechanistically would make it difficult to distinguish from abiotic dissolution of iron or manganese oxides as described by LaKind and Stone[660] and Stone and Morgan.[659]

6.2.2.2. Criteria for Direct (Dissimilatory) Reduction of Metal Oxides. In addition to a requirement for cell contact, a number of other criteria should be applied to metal oxide dissolution to validate the concept of direct (respiratory) reduction, including:

- temperature, the reaction should occur over ranges consistent with living organisms;
- pH, the reaction should occur only over ranges of pH consistent with living organisms;
- surface area dependence, while some effect of cell density is expected, these reactions are expected to be surface-limited reactions and thus not directly proportional to cell density;
- energy source, the dissolution should depend on the availability of an energy source; and
- inhibitors, the dissolution should be inhibited by inhibitors of electron transport and/or respiration.

If such criteria are not rigorously applied, it may well be that the dissolution could be occurring via an indirect process, especially for Mn oxides, which are easily reduced indirectly.[667,668]

The usual way of studying the dissolution of metal oxides by bacteria has been to monitor the appearance of the reduced (solubilized) metal in the liquid phase. While there are many traps involved in such methods, such as the adsorption of the reduced metals onto the solid metal oxides and the formation of insoluble reduced forms (siderite, rhodochrosite, vivianite, iron sulfides), if one accounts for such possibilities and keeps a good budget, this method is acceptable. Such studies have been performed to study the relationship between metal oxide reduction and the physiological state of the cells.[648,655,669,670]

6.2.2.3. Metal Reducers. The fact that bacteria reduce metals of many sorts has been known for many years, although it has only recently been proven that these reactions could be linked to cellular metabolism, using oxidized metals as electron acceptors for respiration (see Nealson and Saffarini[671] for discussion). This mode of respiratory metal reduction has been the object of much activity during the past decade and is of particular relevance to the subjects discussed in this article. Since the major mode of microbial metabolism involves electron transport and the pumping of protons, it should be expected that organisms gaining energy on the surfaces of metal oxides will have major impacts on the surface chemistry by extracting or adding one or the other of these components.

Two major groups of metal reducers have been identified:[672] (1) obligate anaerobes in the so-called *Geobacter* group and (2) facultative anaerobes in the *Shewanella* group. In neither group has the actual mechanism by which the reductive dissolution of metal oxides occurs been specified. The latter group has been more heavily studied because of the ease of manipulation under aerobic conditions, and several groups have reported mutants incapable of iron and/or manganese reduction.[671,673,674] However, the characterization of these mutants has not yet yielded insights into specific mechanisms.

6.2.2.4. Mechanisms of Metal Oxide Dissolution. Myers and Myers[663,675] have reported that some cytochromes (heme-containing electron-transfer components) as well as the ferric reductase of *Shewanella putrefaciens* MR-1 are located on the outer membranes of the bacteria, suggesting that the enzymatic machinery should be available for direct reduction of the extracellular metals, but no studies actually demonstrating the processes (e.g., electron or proton transfer) have been presented.

Other approaches have involved the purification of cytochromes that might be involved with reduction of the metals substrates. Lovley et al.[664] have partially purified a low-potential cytochrome c_3 from *Desulfobibrio vulgaris* that is capable of cell-free reduction of iron, chromium, and uranium, while a cytochrome c_3 has been isolated, purified, partially sequenced, and cloned from *S. putrefaciens*[665] and shown to reduce iron in cell-free extracts. Seeliger et al.[662] have recently shown that *G. sulfurreducens* produces a similar small cytochrome c_3 which can be found both in the periplasm (space between the cell membrane and the cell wall) and extracellularly. It appears that this cytochrome c_3 is capable of indirect reduction of several different metals by coupling cellular metabolism to extracellular insoluble metal oxides. In addition, a wide range of *S. putrefaciens* cytochromes are now in the stage of purification, sequencing, characterization, and cloning (Table 7). This organism has a wide array of *c*-type cytochromes induced under anoxic conditions, with a range of redox potentials spanning nearly 600 mV; whether one or more of these is the metal reductase is not known at this time. It is a reasonable supposition that a one-electron transfer occurs to stimulate reduction of the metal oxides, and the cytochromes are intimately involved, but no direct evidence is available to confirm this.

The purification of proteins with known redox potentials and the ability to directly reduce metal oxides offers the possibility of studying cell-free metal dissolution, although the relationship between these cytochromes, which almost certainly reside in the periplasmic space of the bacteria, will not be clear until detailed enzyme location studies are used to identify the cellular location of the cytochromes.

6.3. Metal Oxide Formation

Many metal ions change their solubility upon alteration of their redox state: Mn(II) and Fe(II) become insoluble upon oxidation, while U(VI) and Cr(VI) become insoluble upon reduction. In all of these cases there is thus the ability to form biologically mediated metal oxides, and several such examples are known. In most cases there is little mechanistic information, but the examples that follow serve to illustrate that the biota are intimately involved in catalyzing the formation of a variety of metal oxides.

6.3.1. Manganese Oxide Formation

Under normal conditions of seawater, lake water, or sediments (i.e., pH 6.5−8.5), Mn(IV) is the favored state, so that oxidation of Mn(II) should proceed. However, the activation energy of this reaction is sufficiently high that catalysis is needed below pH values of 9. Thus, many organisms are capable of precipitating Mn oxides by virtue of Mn-binding proteins or polysaccharides, and a wide variety of different microbial types are known that accumulate oxidized Mn in the form of MnO_2.[668,678] The biological function of this metal oxidation remains unspecified, and in no case has it been shown to be utilized as a cellular energy source. The oxidizing organisms often become encased in the metal oxide, taking on an entirely new morphology (Figure 51).

Mn(II) oxidizing proteins have been isolated and studied by several laboratories, and several genes coding for putative Mn oxidases have been identified.[680−682] In the case of a marine *Bacillus* strain SG-1, one of the genes codes for a protein whose amino acid sequence is similar to that of the family of multicopper oxidases.[680] This material has recently been reviewed by Tebo et al.[683]

Although little is known of the actual mechanism by which the metal oxides are precipitated, it is known that when the same organism is used to catalyze Mn oxidation, a variety of end products can be achieved, depending on the external conditions (temperature, Mn concentration, salinity of the growth medium, etc.).[684]

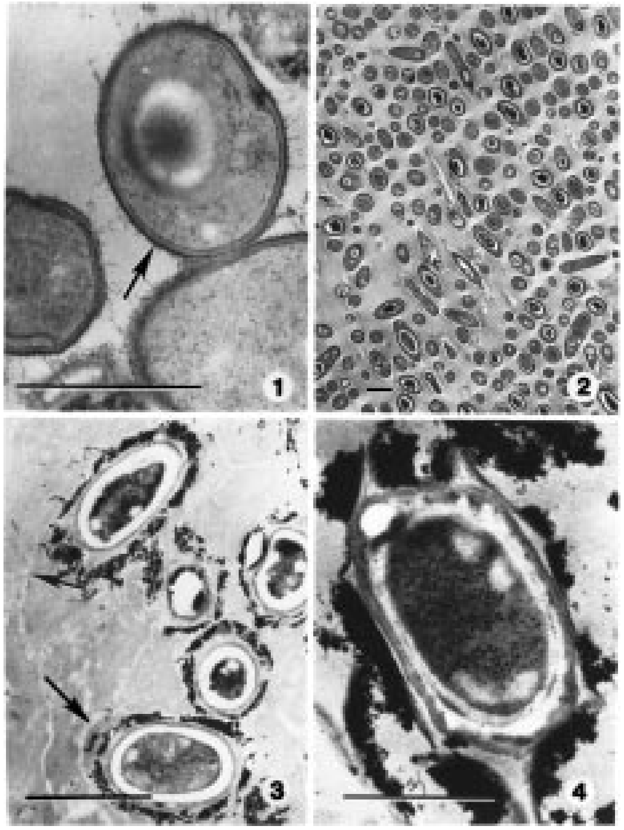

Figure 51. Stages of SG-1, a manganese oxidizing *Bacillus* species, as seen by transmission electron microscopy: (1) cells of SG-1 stained with ruthenium red, revealing a polyanionic-rich outer layer (arrow) apposed to the Gram-positive cell wall (bar = 0.5 μm); (2) vegetative cells of SG-1 just beginning to sporulate, as indicated by spore bodies inside some cells (bar = 1 μm); SG-1 cell and spores imaged without staining. Manganese, which is just beginning to be precipitated, is accumulating on the spores but not the vegetative cells. The outlines of the vegetative cell walls can be faintly seen in the background of the thin section (arrows) (bar = 1 μm). (4) Developing SG-1 spore with manganese precipitated on its surface. The outer structure of the spore is characterized by ridges that appear to be formed by the outer spore coat or exosporium. (Reprinted with permission from ref 679. Copyright 1988 Academic Press.)

6.3.2. Anaerobic Iron Oxide Formation

Many bacteria, algae, and fungi also accumulate iron oxides, but in this case they almost certainly bind the oxidized metals that have already oxidized due to the environmental pH and Eh. Recently, two different microbial reactions have been shown to be responsible for the oxidation of Fe(II) to Fe(III) under anoxic conditions, with the resultant formation of insoluble iron oxides. The first involves anaerobic photosynthetic bacteria, which utilize Fe(II) as the electron donor for photosynthesis,[685] while the second involves a group of iron oxidizing bacteria that utilize Fe(II) as their source of energy, using nitrate as an electron acceptor and growing autotrophically, e.g., with CO_2 as the source of carbon for growth.[686] In both these cases, reddish-brown iron oxides are formed during bacterial growth, but in neither case have these oxides been characterized.

6.3.3. Magnetite Formation

Perhaps the best known example of all bacterial metal oxides is that of the formation of intracellular magnetite by the magnetotactic bacteria (see articles in Frankel and Blakemore[687]). In this case, highly ordered crystals of magnetite are synthesized within the cell and utilized by the bacteria for orientation, allowing the organism to orient relative to the earth's magnetic field.[688] Upon cellular death, these highly ordered magnetite grains are released and are often found in abundance in anaerobic sediments. Recently it has also been shown that bacteria can use other ferromagnetic minerals, including the iron sulfides pyrrhotite and greigite.[688]

Similarly, iron reducing bacteria are capable of magnetite production under some conditions (see articles in Frankel and Blakemore[687]), converting environmental ferric oxides to mixed valence state magnetite, although little is known of the conditions that control magnetite formation. Recent detailed studies of such iron reducing bacteria have revealed critical factors that control the formation of magnetite and other minerals.[689−691] This work has demonstrated that a given strain of bacteria (in this case *S. putrefaciens*) can form a wide variety of different mineral forms (including magnetite or siderite) in different ratios depending on a variety of different conditions such as the type of buffer, the presence of quinones, and the amount of phosphorus in the medium. These results represent the first extensive studies of the factors that lead to different extracellular mineralogical end products with seemingly similar metabolic reactions driving the processes.

7. Theory

7.1. Background

Theoretical models of charged surface−water interfaces were first introduced with the pioneering work of Gouy,[692] Chapman,[693] Stern,[694] and others in the early 1900s. Much of the early work in this area focused on understanding metal−solution interfaces; an excellent discussion of these early studies is presented in a review article by Parsons.[695] The fundamental insight developed by these studies on the electrical double layer has been utilized in the development of models for the oxide−water interface using combined thermodynamic (i.e., site binding formulations) and electrostatic models of the electric double layer (see Westall and Hohl[385] for a summary and comparison of such models). Recent breakthroughs in computational technologies have facilitated the development of molecular-based theoretical approaches of oxide−water interactions in addition to advances in the macroscopic thermodynamic modeling methods. The molecular-based approaches include methods from ab initio quantum mechanical theories and classical mechanics simulations techniques. The integration of molecular-based and thermodynamic theoretical approaches with ongoing and new experimental efforts has greatly enhanced the understanding of oxide−water interfaces. This section presents a brief review of the thermodynamic and molecular-based theoretical methods, and some results relevant to the metal oxide−water interface.

7.1.1. Thermodynamic Approaches

Much is known about the macroscopic adsorptive properties of metal oxide powders in electrolyte solutions determined experimentally. To account for these experimental results, a wide variety of thermodynamic models describing the adsorption of chemical species to oxide surfaces have been developed, including the constant capacitance model (CCM), the diffuse-double-layer model (DDLM), the triple-layer model (TLM) (for a review of these models see Westall and Hohl[385]), the four-layer model,[696] the multisite complexation (MUSIC) model,[478,479,697] the charge distribution (CD) model,[698] and the heterogeneous model.[699] The thermodynamic models developed to describe experimental determinations of surface charge in electrolyte solutions can be divided into two groups. The first group (CCM, DDLM, and TLM), also termed two-p*K* models, treat the surfaces of metal oxides on a single-site basis (see Figure 52). Of these, the TLM is the most general because it specifically accounts for adsorption of electrolyte ions. A schematic visualization of the electrical double layer for the TLM is shown in Figure 53. It can be seen that the metal oxide surface consists of metal ions and oxygen ions partially or fully coordinated to the bulk structure. These surface species are thought to bond directly to ions or molecules adsorbed from the aqueous phase. For example, surface protonation of oxides in aqueous solutions is represented by equilibria involving the surface species represented by $>$SOH, $>\mathrm{SOH_2}^+$, and $>\mathrm{SO}^-$. These species permit representation of proton adsorption and desorption by equilibria described in eqs 23 and 24:

$$>\mathrm{SOH} + \mathrm{H}^+(\mathrm{aq}) \rightleftharpoons\ >\mathrm{SOH_2}^+ \qquad (23)$$

$$>\mathrm{SO}^- + \mathrm{H}^+(\mathrm{aq}) \rightleftharpoons\ >\mathrm{SOH} \qquad (24)$$

As a consequence, in the TLM these species contribute to the development of a proton surface charge (σ_o) on metal oxides.[700] Corresponding to the equilibria in eqs 23 and 24 are expressions of the law of mass action in systems subject to an electric field, which can be written:

$$K_1 = (\mathbf{a}_{>\mathrm{SOH2+}}/\mathbf{a}_{>\mathrm{SOH}}\mathrm{a}_{\mathrm{H+(aq)}})10^{(F\psi_0/2.303RT)} \qquad (25)$$

$$K_2 = (\mathbf{a}_{>\mathrm{SOH}}/\mathbf{a}_{>\mathrm{SO-}}\mathbf{a}_{\mathrm{H+(aq)}})10^{(F\psi_0/2.303RT)} \qquad (26)$$

In eqs 25 and 26, K_1 and K_2 represent intrinsic equilibrium constants, F is Faraday's constant, and ψ_0 represents the mean potential at the oxide surface in an electrolyte solution (Figure 53). Note that the potential ψ_0 in Figure 53 is represented by a plane, the 0-plane, but that this does not require that the surface is atomically planar.

A distinctive feature of the TLM is that electrolyte cations and anions are thought to adsorb by complexing with the protonated and deprotonated surface species. For example, in the case of a 1:1 electrolyte (ML) the adsorption reactions can be written (see Figure 53):

$$>\mathrm{SO}^- + \mathrm{M}^+(\mathrm{aq}) \rightleftharpoons\ >\mathrm{SO}^-\mathrm{M}^+ \qquad (27)$$

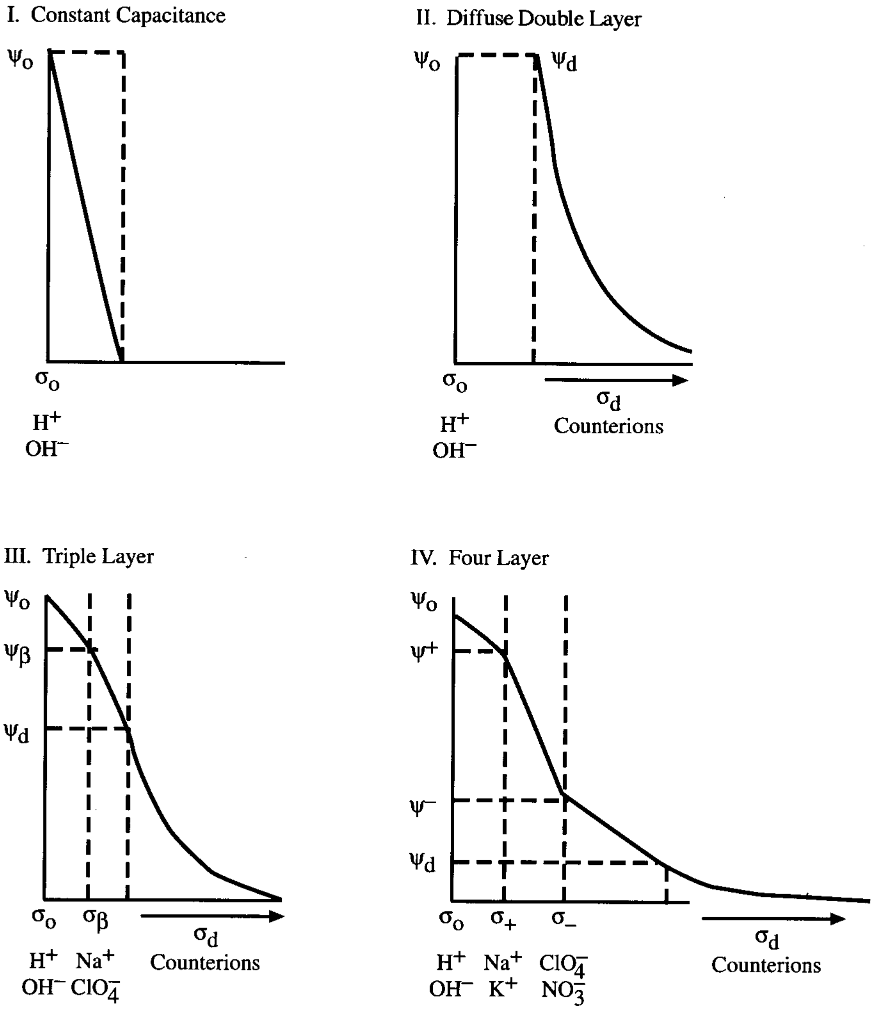

Figure 52. Idealized schematic drawing illustrating the decay of electrical potential with distance from the surface for the constant-capacitance, diffuse-double-layer, triple-layer, and four-layer models. Diagram assumes conditions typical of an oxide surface bathed in a simple electrolyte (e.g., NaCl) at a pH value different than the pH$_{\mathrm{PPZC}}$.

$$>\mathrm{SOH_2}^+ + \mathrm{L}^-(\mathrm{aq}) \rightleftharpoons >\mathrm{SOH_2}^+\mathrm{L}^- \qquad (28)$$

The cation M^+ and the anion L^- are placed on a plane at a distance β from the 0-plane in Figure 55. The charge and potential on this β-plane are represented by σ_β and ψ_β, respectively. However, it should be noted that because of the complexing of the electrolyte cation and anion with species on the 0-plane (Figure 53), the adsorption of the electrolyte cation and anion also contributes to the proton surface charge (σ_0) on metal oxides in electrolyte solutions. Expressions of the law of mass action corresponding to the electrolyte adsorption equilibria can be written:

$$K_{\mathrm{M}^+} = (\mathbf{a}_{>\mathrm{SO}^-\mathrm{M}^+}/\mathbf{a}_{>\mathrm{SO}^-}\mathbf{a}_{\mathrm{M}^+(\mathrm{aq})})10^{(F\psi_\beta/2.303RT)} \qquad (29)$$

$$K_{\mathrm{L}^-} = (\mathbf{a}_{>\mathrm{SOH}_2^+\mathrm{L}^-}/\mathbf{a}_{>\mathrm{SOH}_2^+}\mathbf{a}_{\mathrm{L}^-(\mathrm{aq})})10^{(-F\psi_\beta/2.303RT)} \qquad (30)$$

Extending outward from a third plane in Figures 52 and 53 (the d-plane) is the diffuse part of the electric double layer. This layer contains counterions balancing the surface charge represented by σ_0 plus σ_β. The total charge in the diffuse layer (σ_d) is evaluated from the Gouy−Chapman−Stern solution to the Poisson−Boltzmann equation.[701,702] Finally, an analogy with a parallel-plate capacitor is used to relate the charges and potentials described in Figure 53 to capacitances. The capacitance between the 0-plane and the β-plane is given by eq 31:

$$C_1 = \sigma_0/(\psi_0 - \psi_\beta) \qquad (31)$$

where C_1 for a given metal oxide and electrolyte has typically been obtained by fitting experimentally derived surface charges as a function of pH over a range of ionic strengths. The capacitance between the β-plane and the d-plane is given by eq 32:

$$C_2 = \sigma_\beta/(\psi_\beta - \psi_d) \qquad (32)$$

where C_2 for a given metal oxide and electrolyte has typically been set to a constant value of 0.2 F/m^2 in applications of the TLM.[2]

The TLM and related models constitute a group of models that make no allowance for variations in site-binding preferences due to coordination environment. This deficiency has been addressed to some extent in the second group of models to be addressed here, termed multisite models (e.g., MUSIC and CD). These models use arguments based on Pauling bond strengths at surface oxide ions to differentiate the binding at different surface sites. However, this framework is still relatively simple because it is

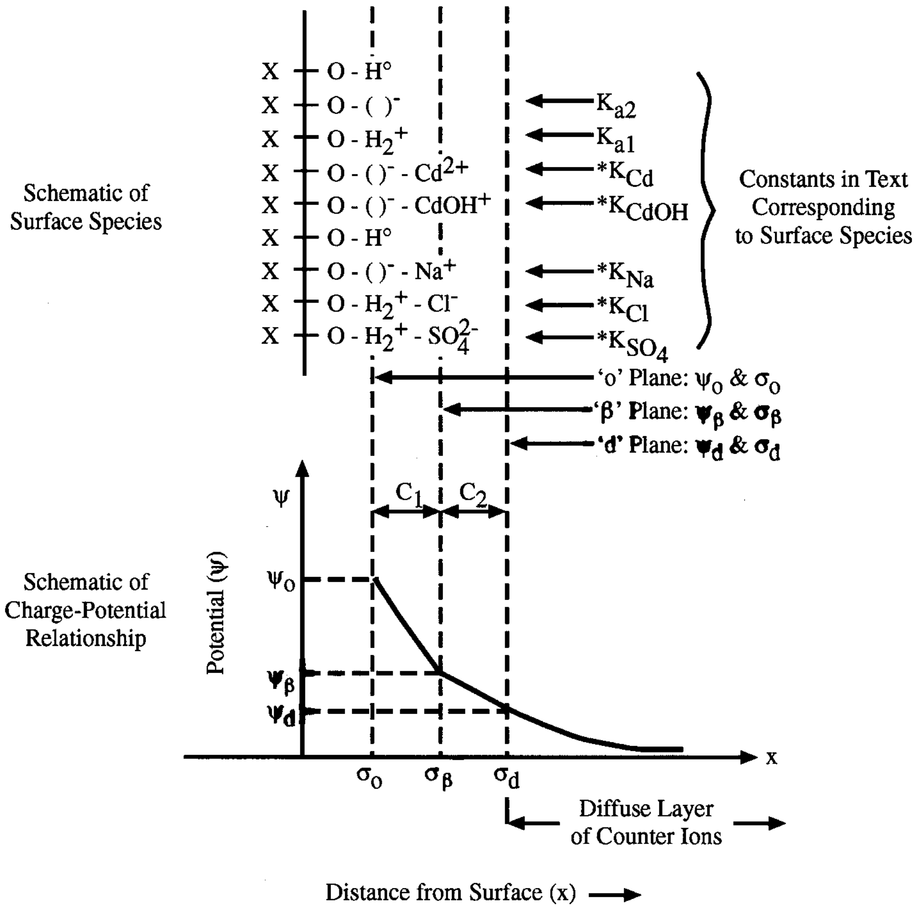

Figure 53. Schematic representation of surface species and surface charge–potential relationship of the triple-layer model. The subscripts 0, β, and d refer to the surface 0-plane, the β-plane, and the diffuse plane, respectively. Brackets in the 0-plane indicate deprotonated surface sites.

based primarily on electrostatic considerations and also does not explicitly take account of solvation (see section 7.2.3.1). Neither group of models has addressed the effects of increasing temperature beyond about 363 K.[405,703–711] A single pioneering study of rutile surface protonation to 523 K has been published.[712] Calorimetric studies of the oxide–water interface have been made to derive enthalpies of surface protonation during titrations and from heats of immersion, but all of these were conducted at 298 K.[699,708,713–720] As a consequence, few enthalpies and entropies of surface protonation are known, and the only reported heat capacity of surface protonation comes from the study by Machesky et al.[712]

Although many experimental and thermodynamic studies of the surface protonation of oxides in electrolyte solutions have been carried out, few attempts have been made to place the experimental measurements and derived thermodynamic equilibrium constants (e.g., in eqs 25, 26, 29, and 30 above) into a coherent framework that permits prediction for systems that have yet to be studied experimentally. In short, there is a large amount of experimental data and experimentally derived equilibrium constants and nothing theoretical to relate them. Given the enormous range of different natural and synthetic metal oxides of interest and the correspondingly large range of electrolyte types and concentrations of relevance to industrial and natural processes, there is clearly a need for a predictive thermodynamic theory of surface protonation. Such a theory should enable predictions of surface charge for specific metal oxides and electrolytes over a wide range of solution chemical conditions and temperatures. This would greatly facilitate the analysis of experimentally determined surface charge versus pH, as well as the interpretation of experimental studies of dissolution rates. In addition, it would aid the development of predictive models of adsorption for metals, ligands, and organic species in laboratory and natural systems.

7.1.2. Molecular-Based Approaches

The development and application of molecular-based theoretical methods for studying aqueous solution–metal oxide interfaces are very recent compared to the vast literature on thermodynamic modeling approaches. Technological breakthroughs in computer architectures (both hardware and software) have allowed researchers to use theoretical methods based on ab initio quantum mechanics, classical mechanics, and hybrid methods to probe the underlying chemistry of these interfaces. Mathematical and computational developments have allowed researchers to begin to utilize molecular-level simulations to give insight into macroscopic processes and to develop better thermodynamic models of metal oxide surface chemistry.[721–737] The goal of these methods is to gain an understanding of the atomic-scale chemistry and

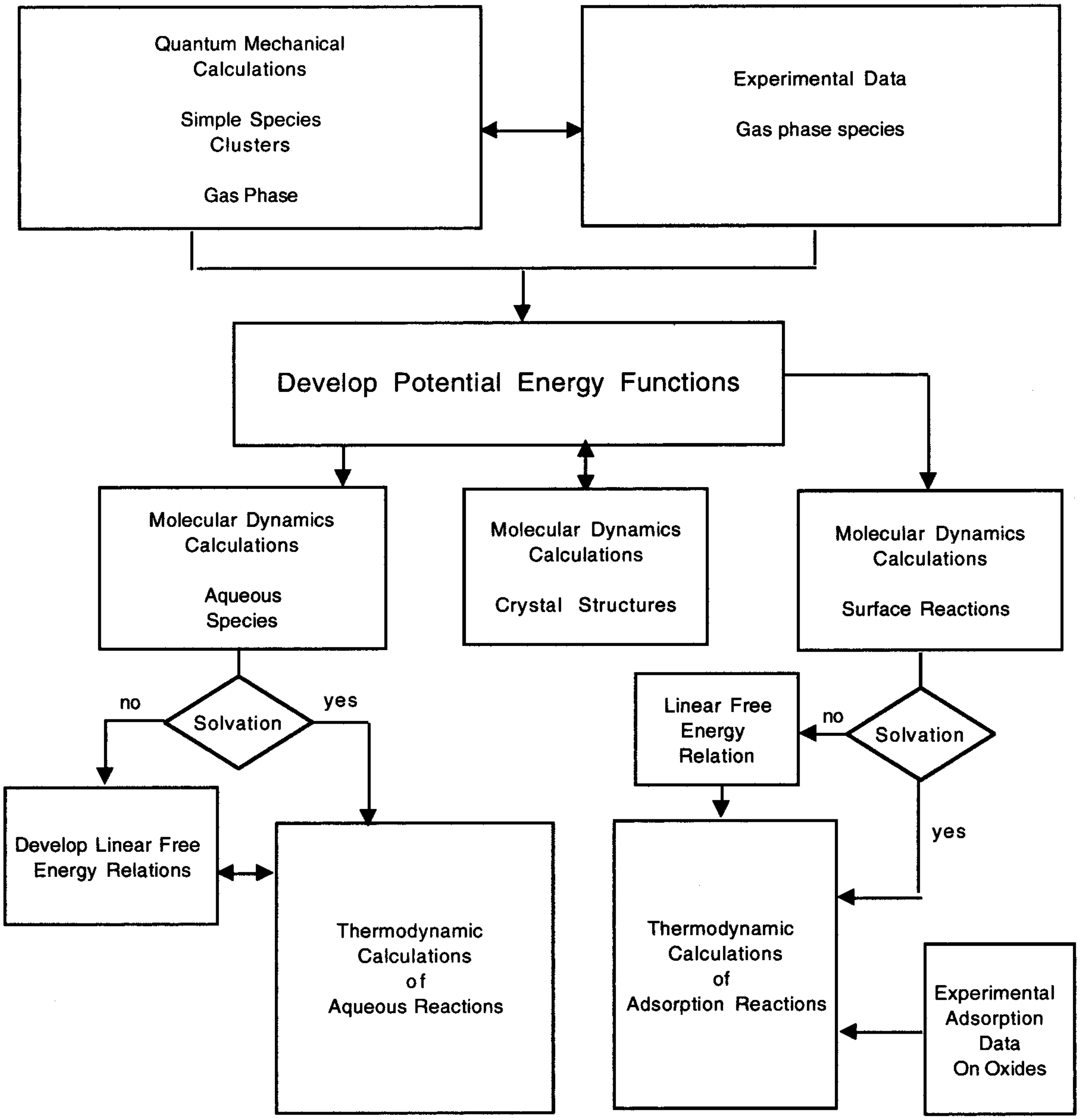

Figure 54. Schematic outline of the molecular modeling approach for defining the reactivity of oxide surface functional groups.

physics that determine the macroscopic properties of an aqueous solution−metal oxide interface.

The molecular-scale structure, reactivity, and electronic properties of metal oxides and metal oxide interfaces can be examined using ab initio electronic structure methods, molecular simulations techniques, and hybrid quantum/classical mechanics methods. The ab initio methods are based on either wave function solutions to the Schrödinger equation [e.g., self-consistent field (SCF) or Hartree−Fock (HF) and high levels of theory that treat electron correlation more exactly][738−741] density-functional theory,[742−753] or a tight-binding formalism.[754] These methods can be further divided into two classes: (1) methods that use finite clusters of atoms to represent chemically and physically important regions of an oxide material ("cluster methods") and (2) methods that treat the solid as an infinite (periodic) system possessing translational symmetry ("extended methods").

Dynamical and structural properties of metal oxide surfaces and interfaces have been studied using molecular (or atomistic) simulation methods based on classical mechanics, e.g., molecular dynamics (MD) and/or Monte Carlo (MC).[755−762] Hybrid methods that combine quantum and classical mechanical approaches include Car−Parinello methods[748] and quantum mechanical/molecular mechanical (QM/MM) methods.[753,763−767]

The inherent complexity of these systems requires the integration of many of these methods. One approach to developing such models (shown schematically in Figure 54) uses a combination of quantum mechanical calculations, molecular statics and dynamics calculations, and thermodynamic modeling. Utilizing a combined approach allows a great deal of theoretical and experimental data to be integrated into a description of site-specific binding to oxide surfaces which can, in turn, be used to develop better thermodynamic models for adsorption. One method begins by using quantum mechanical calculations and classical simulations on aqueous-ion clusters to parametrize potential energy interaction potentials.

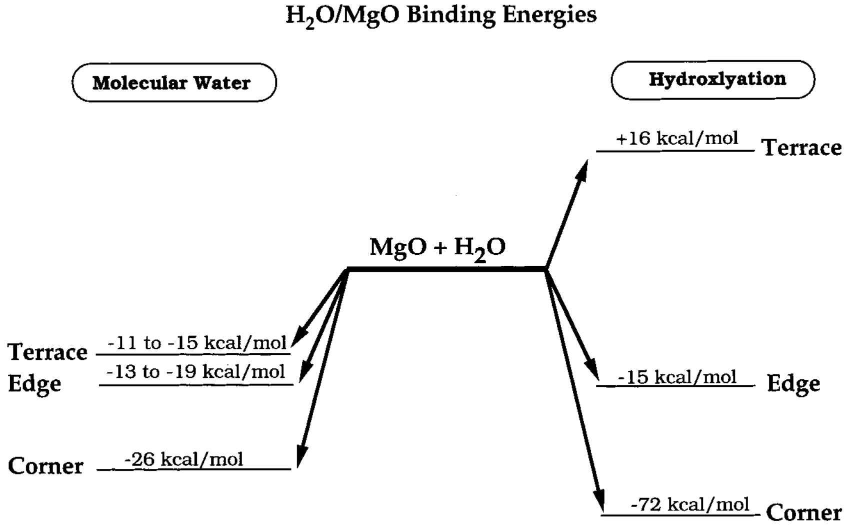

Figure 55. Correlation-corrected periodic Hartree–Fock binding energies and hydroxylation energies for water on MgO (100) terrace, edge, and corner sites. Negative numbers indicate exothermic (bound) configurations.

These potential energy functions are then used in molecular dynamics simulations of larger (many molecule) systems to investigate the effects of hydration, differences in metal oxide structures, and estimation of the relative binding energies to hydroxylated sites on metal oxide surfaces. These relative binding energies are then used to parametrize thermodynamic models of adsorption that can account for individual site reactivity.

7.2. Example Applications

7.2.1. Hydroxylation of MgO (100) and CaO (100)

The "structure sensitivity" of metal oxide surfaces complicates experimental observations of the water–solid interface. Experiments performed under UHV conditions often measure significantly different properties than those conducted "in situ" (i.e., at the liquid water–metal oxide interface). In many cases, molecular adsorption dominates in the low-coverage, low-temperature, and low-pressure regimes, but as the concentration of water is increased, chemidissociation becomes more prevalent. With many metal oxides, the end product of exposure to water at room temperature is conversion to a fully hydroxylated bulk material, as discussed in section 3.1. An example of this is MgO, which tends to be converted to the hydroxylated mineral brucite, $Mg(OH)_2$, at ambient temperatures. In contrast, many experimental studies performed under UHV conditions with low concentrations of water at the interface show little or no indication of surface hydroxylation.[15]

The extensive number of experimental[15,65,100,102–105,107–110,768–779] and theoretical studies[96–98,106,748,754,763,775,780–793] that probed the structure and reactivity of MgO (100) and the chemistry of water on MgO illustrates the complexity of this "simple" system. Empirical observations of molecular adsorption and chemidissociation vary depending on the experimental method used, sample preparation, and measurement conditions. The accuracy of theoretical studies depends on the inherent assumptions and accuracy of the ab initio or simulation approach used and on the model chosen to describe the "real" water/MgO system. The disparity in the results among the experimental and theoretical studies illustrates the difficulty in resolving the fundamental question, "What is the structure of water on MgO (100)?"

Several experimental studies performed on clean cleaved MgO (100) at low water concentrations indicate that water is weakly molecularly adsorbed on the flat surface and that hydroxylation occurs on step sites.[15,100,102–106,108,774,775] Surface hydroxylation was found to be more prevalent on thin-film MgO (100) grown on a variety of substrates[102,774,777,778] and on powdered MgO samples.[108,109,769] However, recent UHV photoemission studies have shown that as the pressure of water in the vacuum chamber is increased (from 10^{-8} to 10^{-4} Torr), the adsorbed water on MgO surfaces changes from molecular water to hydroxyl groups.[65] The defect concentration is assumed to remain constant during these experiments; hence hydroxylation of the terrace sites must be occurring when the pressure is increased. Similar experiments on the isostructural material CaO (100) indicated that surface hydroxylation of the undefected terrace sites occurs even at low (10^{-9} Torr) pressures of water in the vacuum chamber.[93]

The energetics of molecular adsorption and chemidissociation of water on clean and defective MgO (100) have been probed using ab initio correlation-corrected periodic Hartree–Fock (PHF) theory;[96,781,789,791] the results of these studies are summarized in Figure 55. At monolayer or submonolayer concentrations, molecular adsorption is the energetically favored channel on clean, defect-free MgO (100). Chemidissociation becomes the dominant pathway on defects, i.e., step edge and corner sites.

The molecular adsorption and surface hydroxylation energetics were computed relative to the asymptote of an isolated water molecule and the clean MgO (100) slab according to eq 33:

$$E = [E^{\infty}(\mathrm{MgO}) + E^{\infty}(\mathrm{H_2O})] - E^{\mathrm{eq}}(\mathrm{MgO/H_2O}) \quad (33)$$

This process, which requires dissociating molecular waters on the surface to form surface OH^- groups at both the cation and anion sites, is endothermic; hence molecular adsorption is the energetic minimum on the flat surface. The chemidissociation channel becomes nearly isoenergetic with molecular adsorption on step edges and energetically favored on step corners (kinks). The change in surface site coordination from 5-fold on the flat surface to 4- and 3-fold on the step edge and corner sites, respectively, increased the surface reactivity, thus making the chemidissociation channel energetically accessible. Similar results have been reported for water dissociation on small MgO clusters.[780,794] The study by Anchell and Hess[780] reported that water dissociates directly (no energetic barrier) on three-coordinated sites.

In real aqueous environments, hydroxylation of the surface can occur via reactions with hydronium ions or hydroxide−water ions in solution. Some empirical measurements indicate that metal oxide surface hydroxylation proceeds preferentially at anion sites (proton adsorption to oxygen) and much less favorably at cation sites (hydroxide adsorption).[7,15] At the liquid water−metal oxide interface, solvation by the surrounding bulk water is expected to stabilize the hydroxylated surface. The binding energies of a proton to a surface anion site (eq 34) and a hydroxide group (eq 35) to a surface cation site were computed using the 24-atom cluster $(MgO)_{12}$ shown in Figure 56 in order to probe the reactivity of surface anion and cation sites.

$$H^+ + (MgO)_{12} \rightarrow H^+/(MgO)_{12} \qquad (34)$$

$$OH^- + (MgO)_{12} \rightarrow OH^-/(MgO)_{12} \qquad (35)$$

These energies and computed energies of formation of hydronium and hydroxide−water complexes were used to model reactions that may occur at the aqueous solution−metal oxide interface according to the reactions shown in eqs 36 and 37:

$$H_3O^+ + (MgO)_{12} \rightarrow H^+/(MgO)_{12} + H_2O \qquad (36)$$

$$OH^-(H_2O) + (MgO)_{12} \rightarrow OH^-/(MgO)_{12} + H_2O \qquad (37)$$

The proton and hydroxide binding energies were also computed for a 24-atom CaO (100) cluster, $(CaO)_{12}$.

These data are summarized in Table 8. They show that, for both materials, the proton binding energy is 1−2 orders of magnitude greater than the hydroxide binding energy; hence the chemical reactivity of the anion sites is predicted to be significantly greater than that of the cation sites. The binding energy of a proton to the surface anion sites was also found to be significantly greater than the formation energy of hydronium, making the process represented by eq 36 exothermic (−58 kcal/mol for MgO and −91 kcal/mol for CaO). This implies that the presence of hydronium ions in solution will enhance the hydroxylation of the surface. In contrast, the binding energy of the hydroxide−water complex is greater than the binding energy of hydroxide to the surface cation site, making eq 37 endothermic (+33 kcal/mol for MgO and +12 kcal/mol for CaO). Although a significant energetic stabilization accompanies the hydroxylation of adjacent sites, the net energy for the dissociation of a single water molecule to form adjacent hydroxyl groups is still endothermic (+65 kcal/mol for MgO and +39 kcal/mol for CaO).

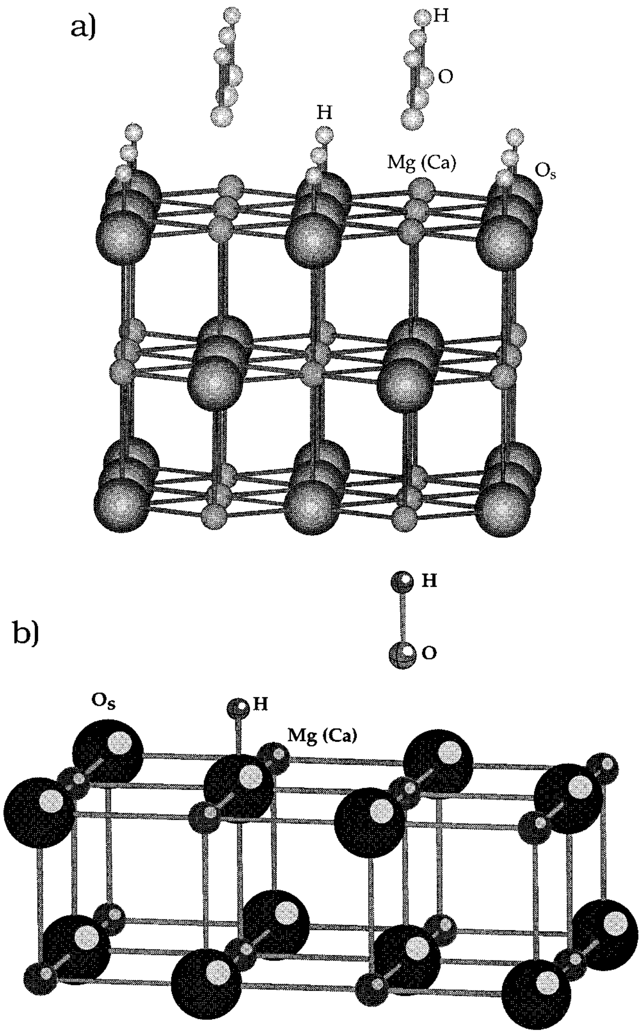

Figure 56. Hydroxylation of MgO (100). (a) Fully hydroxylated three-layer slab of MgO (100) or CaO (100). Hydrogen adsorption is to the anion sites (O_s) and hydroxyl adsorption is on the cation sites (Mg or Ca). Bond distance are $R(O_s{-}H) = 1.01$ Å and $R(OH) = 0.93$ Å for both materials, $R(Mg{-}O) = 1.76$ Å, and $R(Ca{-}O) = 2.14$ Å. (b) Proton and hydroxide binding sites on 24-atom cluster $(MgO)_{12}$ or $(CaO)_{12}$. Geometry of cluster is fixed at bulk distances ($a = 4.205$ Å for MgO and $a = 4.811$ Å for CaO). Bond distance are $R(O_s{-}H) = 1.01$ Å and $R(OH) = 0.93$ Å for both materials, $R(Mg{-}O) = 1.76$ Å, and $R(Ca{-}O) = 2.14$ Å.

The first ab initio molecular modeling study to provide clear theoretical evidence for the chemidissociation of water molecules on terrace sites on MgO(100) is that of Giordano et al.[63] They used an ab initio total energy method based on the gradient-corrected local density approximation to show that water molecules arranged in a (3 × 2) ordered fashion on this surface dissociate on terrace sites due, in part, to interactions between adjacent water molecules. These results, coupled with the recent theoretical

Table 8. Binding Energies for Water Clusters, Water/MgO, and Water/CaO[a]

	cluster binding energy (kcal/mol)
H_2O Clusters	
$OH^-(H_2O)$	−36
H_3O^+	−168
On $(MgO)_{12}$ Clusters	
$H^+/(MgO)_{12}$	−226
$OH^-/(MgO)_{12}$	−3
$H^+/OH^-/(MgO)_{12}$	−367
On $(CaO)_{12}$ Clusters	
$H^+/(CaO)_{12}$	−259
$OH^-/(CaO)_{12}$	−24
$H^+/OH^-/(CaO)_{12}$	−391

[a] Negative values denote exothermic energetics.

study of the interaction of water on rutile (110)[119] and α-Al_2O_3 (0001),[69] suggest that proper modeling of the interactions between adjacent water molecules as well as interactions between water molecules and the sorbent surface is of critical importance in predicting the behavior of water on metal oxide surfaces. It is interesting to note, however, that the study of water interactions on the rutile (110) surface[119] suggests that single water molecules with no immediate water neighbors dissociate, whereas the study of H_2O−MgO (100) interactions[63] suggests that interaction between adjacent water molecules is needed for dissociation to occur.

7.2.2. Transferring Molecular Modeling Results to Thermodynamic Models

One of the most complete examples of the approach of combining molecular and thermodynamic modeling is described in a series of papers by Rustad et al.[732−734] and Felmy and Rustad,[795] who developed a modeling capability for the ferric iron system. These studies began by introducing Fe^{3+} into the dissociating molecular dynamics water model of Halley et al.[796] by parametrizing the potential energy surface for Fe^{3+}−H_2O calculated by Curtiss et al.[797] This approach was then applied to progressively more complex systems beginning with an analysis of the mononuclear hydrolysis species of ferric iron in aqueous solution, progressing to studies of the iron oxide and oxyhydroxide minerals, continuing with calculations of proton binding to goethite crystal surfaces, and ending with thermodynamic calculations of the surface protonation of goethite.

Table 9. Predicted Site Protonation Values for Individual Sites on Goethite (α-FeOOH) (021) and (110)[a]

site type α-FeOOH (110)	percent protonated	site type α-FeOOH (021)	percent protonated
$(FeOH)^{-1/2}$	12.3	$(FeOH_A)^{-1/2}$	42.9
$(FeOH_2)^{1/2}$	46.2	$(FeOH_{2,A})^{1/2}$	20.6
$[(FeOH_2)^{1/2}\cdot Cl^-]^{-1/2}$	41.5	$[(FeOH_{2,A})^{1/2}\cdot Cl^-]^{-1/2}$	36.5
Fe_2O^-	14.3	$(FeOH_B)^{-1/2}$	13.7
Fe_2OH	80.7	$(FeOH_{2,B})^{1/2}$	31.2
$(Fe_2OH_2)^+$	5	$[(FeOH_{2,B})^{1/2}\cdot Cl^-]^{-1/2}$	55.1
$(Fe_3O_A)^{-1/2}$	21.7	$(Fe_2O_A)^-$	2.2
$(Fe_3OH_A)^{1/2}$	78.3	Fe_2OH_A	58.9
		$(Fe_2OH_{2,A})^+$	38.9
$(Fe_3O_B)^{-1/2}$	33.3	$(Fe_2O_B)^-$	5.3
$(Fe_3OH_B)^{1/2}$	66.7	Fe_2OH_B	49.4
		$(Fe_2OH_{2,B})^+$	45.3
$(Fe_3O_C)^{-1/2}$	67.3		
$(Fe_3OH_C)^{1/2}$	32.7		

[a] Letter designations are used to distinguish among the corresponding site types on each surface (see Figure 58). Values are reported as percentage of site type protonated.

Use of such a microscopically based model yields some interesting predictions of the differences in site protonation for the goethite (110) and (021) surfaces (Table 9). Although the total surface charge on the (110) and (021) surfaces is quite similar (see Figure 57), this model predicts quite different microscopic explanations for the charging behavior on the different surfaces. For example, almost twice as many oxo (hydroxo) coordinated sites are protonated on the (110) as on the (021) surface; the protonation of the 3-oxo (hydroxo) coordinated sites on the (110) surface varies from 33% to 78% depending on the individual

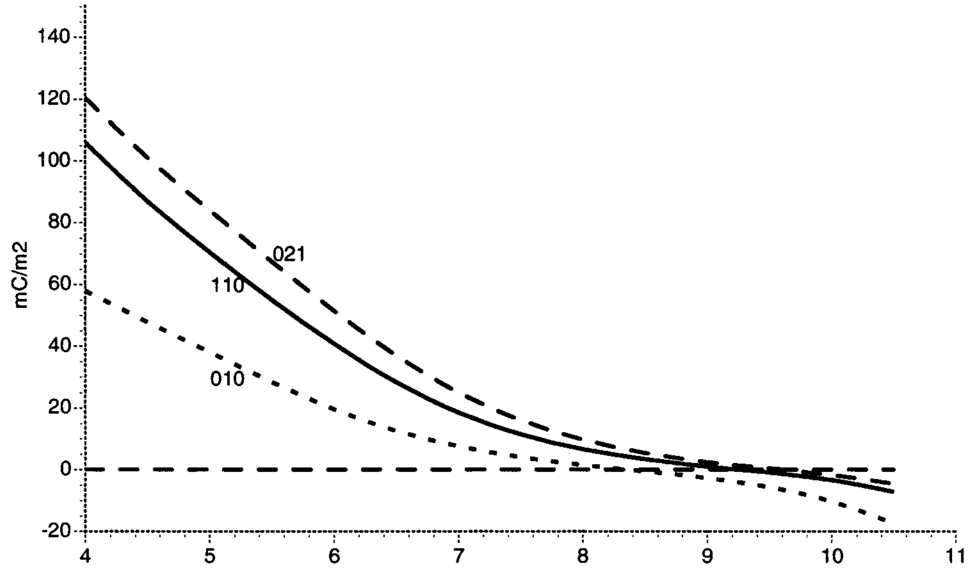

Figure 57. Calculated surface charge for different crystal faces of goethite (α-FeOOH).

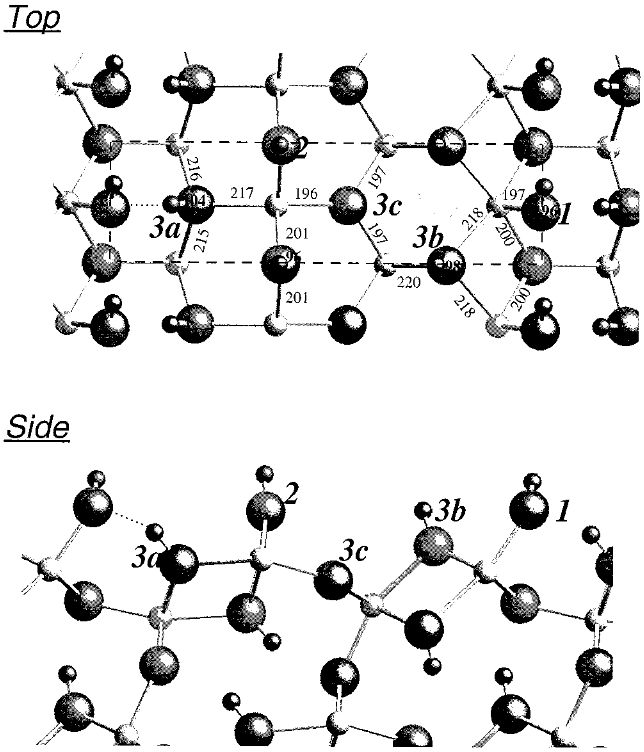

Figure 58. Goethite (α-FeOOH) (110).

site; and the oxo (hydroxo) coordinated sites on (021) protonate much more than the oxo (hydroxo) coordinated sites on (110). In particular, such studies indicate that even the same site type (i.e., same number of Fe−O bonds) on the same mineral surface can have quite different binding energies, depending upon the precise location of the protons which form a hydrogen-bonding network on the surface (Figure 58). This clearly demonstrates the potential effects of local molecular structure on proton binding energy. Such differences can have a significant impact on how adsorbate molecules will bind to the individual surfaces. These initial studies have been effective in demonstrating the usefulness of the overall approach and in suggesting new hypothesis and ideas as regards proton binding to ferric iron surfaces.

7.2.3. Thermodynamic Modeling

Recent work on thermodynamic models of the metal oxide−water interface has placed the triple-layer model on a predictive basis.[16,798−802] To do this, all the key parameters of the triple-layer model must be estimated. These include the surface protonation equilibrium constants K_1 and K_2 defined in eqs 25 and 26 and the electrolyte adsorption constants K_{M^+} and K_{L^-} (see eqs 29 and 30) for any electrolyte and metal oxide of interest. Finally, a site density for each oxide consistent with the equilibrium constants and the capacitance C_1 (eq 31), must be estimated. These parameters and the primary sources documenting the predictive methods are summarized below.

7.2.3.1. Prediction of Surface Protonation Equilibrium Constants. The variation of experimental surface protonation constants for a variety of different oxides can be accurately described by explicitly taking account of the Pauling electrostatic bond strength theory, together with a contribution from solvation of the aqueous adsorbing protons.[16,799] The standard Gibbs free energy of reaction is broken up into three contributions: an electrostatic proton interaction term ($\Delta G^0_{pi,\nu}$), a Born solvation term ($\Delta G^0_{s,\nu}$), and a term intrinsic to aqueous protons ($\Delta G^0_{ii,\nu}$) according to eq 38:

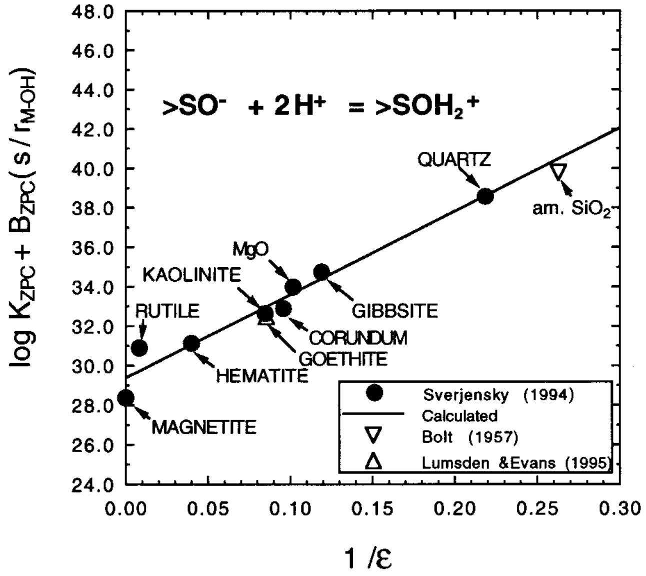

Figure 59. Example of the theoretically expected dependence of the logarithm of a surface protonation equilibrium constant (log K_{ZPC}) on the physical properties of the bulk solid ($s/\mathbf{r}$ is the Pauling bond strength per angstrom, and $1/\epsilon$ is the mean dielectric constant of the solid).

$$\Delta G^0{}_{r,\nu} = \Delta G^0{}_{pi,\nu} + \Delta G^0{}_{s,\nu} + \Delta G^0{}_{ii,\nu} \qquad (38)$$

Following Yoon et al.[803] for the electrostatic proton interaction term and James and Healy[603] for the solvation term, it has been shown that the logarithms of surface protonation equilibrium constants can be expressed by terms involving the inverse of the dielectric constant of the kth metal oxide ($1/\epsilon_k$) (from the solvation term in eq 38) and the Pauling bond strength per Ångstrom (s/r_{M-OH}). For example, at the pH_{PZC}, the surface of a metal oxide has a net zero charge. The surface equilibrium can be expressed by the sum of the logs of the equilibrium constants for eqs 23 and 24 according to eq 39, where pH_{PZC} and log K_{ZPC} are defined as in eqs 40 and 41, respectively:

$$>SO^- + 2H^+ \rightleftharpoons >SOH_2{}^+ \qquad (39)$$

$$pH_{PZC} = 0.5(\log K_1 + \log K_2) \equiv 0.5 \log K_{ZPC} = 0.5 \log \mathbf{a}_{>SOH^{2+}}/\mathbf{a}_{>SO^-}(\mathbf{a}_{H^+(aq)})^2 \qquad (40)$$

$$\log K_{PZC} = -(\Delta\Omega_{r,PZC}/2.303RT)(1/\epsilon_k) - B_{ZPC}(s/\mathbf{r}_{M-OH}) + \log K_{ii,PZC}'' \qquad (41)$$

The resulting correlation is shown in Figure 59. The numerical coefficients (e.g., $\Delta\Omega_{r,PZC}$, B_{PZC}, and log $K_{ii,PZC}''$) represent calibration with the experimentally derived equilibrium constants.[16] Similar equations for the log K_1 and log K_2 result in eqs 42 and 43:[799]

$$\log K_1 = -(\Delta\Omega_{r,1}/2.303RT)(1/\epsilon_k) - B_1(s/\mathbf{r}_{M-OH}) + \log K_{ii,1}'' \quad (42)$$

$$\log K_2 = -(\Delta\Omega_{r,2}/2.303RT)(1/\epsilon_k) - B_2(s/\mathbf{r}_{M-OH}) + \log K_{ii,2}'' \quad (43)$$

Again, the numerical coefficients (e.g., $\Delta\Omega_{r,1}$, B_1, and log $K_{ii,1}''$) represent calibration of the equations with experimentally derived equilibrium constants.[799] On the basis of eqs 42 and 43, numerous predictions of K_1 and K_2 for metal oxides, hydroxides, and silicates can be made.

7.2.3.2. Prediction of Surface Site Densities. Of all the experimentally based methods of measuring surface site densities, tritium exchange appears to give the most appropriate measurement for models of protonation and deprotonation reactions in water (see reviews by James and Parks[700] and Davis and Kent[2]). The site densities on which the surface protonation constants used to calibrate eqs 42 and 43 depend were derived experimentally using tritium-exchange methods.[382] Therefore, values of K_1 and K_2 predicted from eqs 42 and 43 must also be used with site densities derived from, or consistent with, the results of tritium-exchange measurements.[799]

Although tritium-exchange measurements have been reported for a range of metal oxides including quartz, amorphous silica, alumina, corundum, goethite, hematite, and rutile, few attempts have been made to explain the results theoretically.[2] The logical starting point is the bulk crystal structure as exposed at the surfaces of interest. How close is this to the real surface in water? Studies of oxide surfaces in high vacuum exhibit various degrees of relaxation relative to the bulk crystal structure.[15] As discussed in section 2.3, some have virtually no relaxation. Recent studies of the surface of hematite (see section 2.3.1.4) suggest that the relaxed surface in air actually recovers somewhat toward the bulk structure when in water.[129] Consequently, the bulk structure is our best clue, albeit an idealized one, as to the nature of the surface in water.[802]

A consistent, systematic approach to the problem of estimating site densities for both metal oxides and silicates in water has been developed by Koretsky et al.[802] The selection of the precise location of growth or cleavage planes in these structures has been specified by requiring that the total Brown−Shannon bond strengths were minimized on neutral or nearly neutral exposed surfaces. Using this criterion, unique planes for many crystallographic orientations have been identified for the first time in a wide variety of metal oxides and silicates of geochemical interest.[802] Based on these planes, the method that best matches the tritium-exchange results involves counting all dangling bonds on the surface (Figure 60), suggesting that the method could be used to estimate many more site densities for oxides in water that have yet to be studied experimentally.

7.2.3.3. Prediction of Electrolyte Adsorption Equilibrium Constants. The surface equilibrium constants K_{M^+} and K_{L^-} refer to adsorption of the electrolyte cation M^+ and anion L^- on the β-plane in the triple-layer model.[2] Based on Born solvation theory[798,799], it would be expected that sets of values of log K_M and log K_L on a range of different solids would correlate with $1/\epsilon$ of the solids. Such a correlation would be analogous to the correlations of log K with $1/\epsilon$ already developed for the adsorption of divalent metals on the β-plane in the triple-layer model.[798] This idea has been investigated with a wide range of solids covering an extreme range of values of the dielectric constant.[801] The results are consistent with equations of the form:

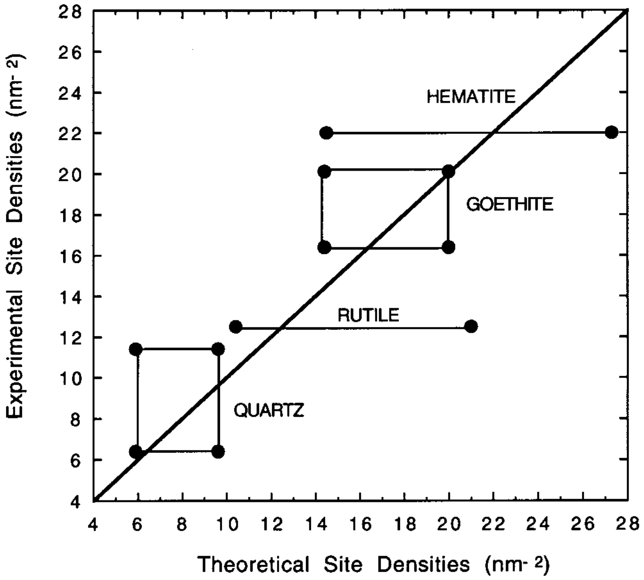

Figure 60. Experimental site densities based on tritium exchange with powders,[804] compared to theoretically estimated surface site densities.[802] The range of theoretical values for each mineral reflects a range of different crystal or cleavage faces (see text).

$$\log K_{M^+} = -(\Delta\Omega_{r,M^+}/2.303RT)(1/\epsilon_k) + \log K_{ii,M^+}'' \quad (44)$$

$$\log K_{L^-} = -(\Delta\Omega_{r,L^-}/2.303RT)(1/\epsilon_k) + \log K_{ii,L^-}'' \quad (45)$$

where the coefficients $\Delta\Omega r,M^+$, $\Delta\Omega_{r,L^-}$, K_{ii,M^+}'', and K_{ii,L^-}'' were calibrated with experimentally derived values of the electrolyte adsorption constants (e.g., Figure 61). Note that in eqs 44 and 45 for equilibrium constants referring to surface species on the β-plane, no dependence on the Pauling bond strength per Ångstrom ($s/\mathbf{r}_{M-OH}$) has been included (cf. eqs 41−43 referring to protons adsorbed on the zero plane). This result is to be expected if the interfacial dielectric constant appropriate to the β-plane is much larger than that for the zero plane (see Figure 1). Under such circumstances, the term $B(s/\mathbf{r}_{M-OH})$ for the electrolyte ions would be so small that it is apparently negligible.

From Born solvation theory, we would further expect that $\Delta\Omega_r$ is a function of the inverse of the effective electrostatic radii of the cations or anions,[798] which results in predictive equations for $\Delta\Omega_{r,M^+}$ and $\Delta\Omega_{r,L^-}$.[801] Similarly, the intrinsic equilibrium con-

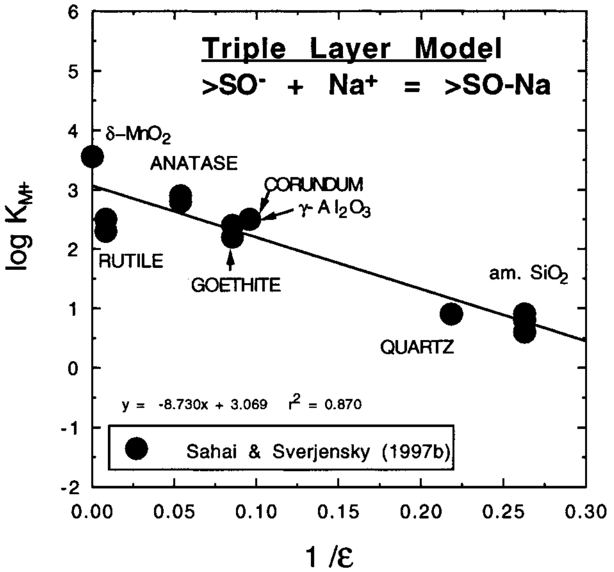

Figure 61. Example of the theoretically expected dependence of the logarithm of an electrolytic ion surface equilibrium constant on the inverse of the dielectric constant for a variety of different solids.

stants log K_{ii,M^+}'' and log K_{ii,L^-}'' correlate with the inverse of the effective electrostatic radii of the corresponding aqueous cations. Equations 43 and 44 thus permit prediction of the electrolyte adsorption constants for the triple-layer model for a wide variety of cations, anions, and solids.[801]

7.2.3.4. Prediction of Capacitance at the Oxide–Electrolyte Interface. The inner-layer capacitance (C_1) in the triple-layer model has long been a parameter obtained solely by regression of experimentally determined surface charge data as a function of pH and ionic strength.[2,3] Because of the great variety of assumptions used in such regressions, it has even been stated[385] (referring to the capacitance C_1 as C) that, “It would be extremely difficult to predict values of C, K_+, K_- by means independent of a surface hydrolysis experiment. These parameters can only be “adjustable parameters”, obtained by optimizing the fit of the model to experimental data.” Detailed sensitivity analyses of the TLM have examined the consequences of choosing different values of the capacitance during regression of experimental surface charge data and emphasized the development of internally consistent approaches.[805] Recent progress toward developing a predictive method for estimating C_1 values is summarized below.

The analogy between a parallel-plate capacitor and the triple-layer model of a mineral surface in water results in the expression of C_1 in terms of the dielectric constant in the double-layer region between the 0- and β-planes (ϵ_d) and the separation of these two planes (β) according to eq 46:

$$C_1 = \epsilon_d \epsilon_0 / \beta \tag{46}$$

where ϵ_0 is the permittivity of free space.[382] Although the value of ϵ_d is unknown, it can be hypothesized that the variation of ϵ_d with different electrolytes present would parallel the variation of the dielectric constant of bulk water in solutions with a variety of different salts. These considerations suggest that the capacitance C_1 associated with a particular electrolyte should be a function of the inverse of the product of the Born solvation coefficient and the effective electrostatic radius of the electrolyte. Such a correlation permits a first approximation to the estimation of capacitances.[801]

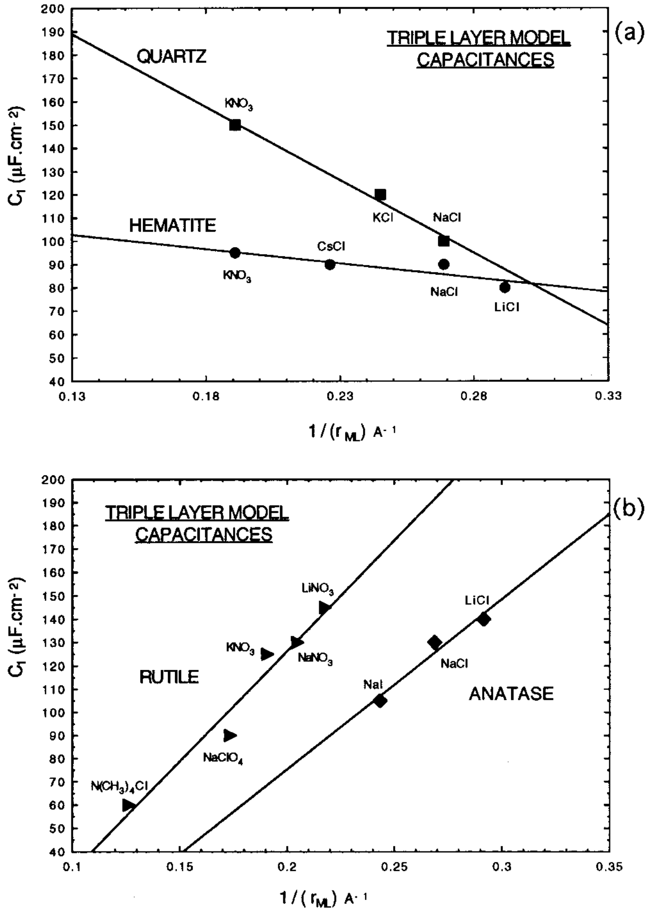

Figure 62. Triple-layer model capacitances as functions of the inverse of the effective electrostatic radii of the aqueous electrolytes. The capacitances were obtained by regression of experimentally derived surface charges over a range of pH values and ionic strengths using the extended triple-layer model. The capacitances were taken from ref 800 unless otherwise stated. The effective electrostatic radii of the electrolytes were taken from ref 806. (a) Correlation of decreasing capacitances for the insulators hematite and quartz with increasing inverse radii of the electrolytes. (b) Correlation of increasing capacitances for the semiconductors rutile and anatase with increasing inverse radii of the electrolytes [capacitances for rutile in $N(CH_3)_4Cl$ and $NaClO_4$ generated from current unpublished work].

A simpler, more accurate correlation exists between the capacitance C_1 and $1/\mathbf{r}_{e,ML}$, the inverse of the effective electrostatic radius of the electrolyte ML. For example, it can be seen in Figure 62a that C_1 values for the insulators hematite (Fe_2O_3) and quartz (α-SiO_2) decrease systematically with the $1/\mathbf{r}_{e,ML}$ values of a variety of electrolytes. This trend is similar to the trends with radius apparent in the capacitances of the Hg and AgI electrodes.[807] In the context of eq 46, the trend of the insulating oxides suggests that decreases in the value of C_1 are being strongly influenced by corresponding decreases in the interfacial dielectric constant, ϵ_d, between the 0- and β-planes. In contrast, it can be seen in Figure 62b that C_1 values for the semiconductors rutile (α-TiO_2) and anatase (β-TiO_2) increase systematically with the $1/\mathbf{r}_{e,ML}$ values of a variety of electrolytes. In other words, for semiconducting oxides the values of C_1 increase as the effective radius of the electrolyte decreases. In the context of eq 46, this trend suggests that the distance β is directly proportional to the size of the electrolyte for semiconducting oxides.

In summary, the above sections briefly describe how all the parameters in the triple-layer model can be predicted for any oxide in any 1:1 electrolyte solution at 298 K and 1 bar. This means that the surface charge and potential can be predicted for any oxide in a 1:1 electrolyte over a very wide range of ionic strengths. This gives the triple-layer model a unique status; it is now the only surface complexation model that can be used to make such general predictions. Other widely used surface complexation models (e.g., the constant capacitance and diffuse-double-layer models) can be placed on a predictive basis only for more restrictive ranges of conditions, because of the simplicity of the models.[799] They cannot be used to make predictions for many different electrolytes without experimental data. In contrast, now that the parameters in the triple-layer model have been placed on a predictive basis, it can be concluded that the triple-layer model is considerably more useful and flexible than any of the other models. This conclusion is quite different from those typically made when comparing surface complexation models used only for fitting experimental data.

8. Challenges and Future Directions

As is clear from the issues discussed above, metal oxide−aqueous solution interfaces are extremely complex. While significant steps have been taken in many areas to address their properties, there is a tremendous amount of important research yet to be performed before we can say that we really "understand" such interfaces. In the sections below we discuss some of the most important of those directions; however, our list is by no means exhaustive, and any imaginative approaches that might help to clarify any aspect of interfacial chemistry and physics should be attempted.

Perhaps the single most important requirement for rapid progress is the close collaboration of experiment and theory. Strong collaborations between the theoretical and experimental environmental science communities have already proven effective,[808] and they must be extended to all areas of aqueous, surface, and interface research.

Much of the motivation for the study of oxide mineral surface chemistry derives from the need to understand the reactivity of soil, sediment, groundwater, and other geochemical systems, whose surface chemical properties are dominated by composite oxide assemblages, including those of Al, Fe, Mn, Si, and Ti. There is also a great need to understand metal oxide catalysts and catalyst supports at a fundamental level in order to develop ways to improve their preparation, efficiency, and susceptibility to poisoning. It is thus imperative that fundamental studies (both experimental and theoretical) of single-crystal and chemically pure single-phase powdered oxides be performed with clear recognition of the types and nature of naturally occurring oxides and of metal oxide catalysts or catalyst supports. It is also essential that the results of these studies of model systems be integrated with studies of natural oxide particles and of metal oxide catalysts under reactive conditions. Such recognition and linkage are essential if the properties and reactivity of the natural systems are to be understood at a fundamental level. For example, natural oxides are often of small particle size (e.g., $<1\ \mu$m), contain extensive structural and surface impurities, are polycrystalline, are typically aggregated, and exhibit a range of solubilities, surface site energies, defects, and coatings. In attempting to extend molecular-level information and models of controlled oxide surfaces and phases to macroscopic situations, it is essential that the true characteristics of the target system be appreciated and taken into account at all levels of reductionism.

8.1. Surface Complexation Modeling Challenges

Surface complexation models (SCM) or their future variants will continue to be a primary computational tool through which molecular-scale information on oxide surface chemistry may be used to describe charge development, electrolyte binding, and sorption in oxide−water suspensions and to predict ion distributions in soil−water or rock−water systems containing oxide grain surfaces or coatings. Wide application and use of these models have shown both their strengths and weaknesses. New scientific developments and advances in the understanding of oxide surface chemistry and sorbate binding reactions that occur at the interface will provide the concepts and data needed to improve these models. Kinetic SCM codes have recently been developed and are in the initial stages of application by the environmental and geochemical community. Significant attention is now needed on the molecular phenomena controlling surface reaction kinetics on oxides as a basis to both rationalize and possibly predict rate constants for important surface-mediated reactions on oxide surfaces. The following represent important scientific questions pertaining to SCM:

- Should emphasis be placed on molecular or statistical descriptions of surface reaction processes?
- What are the reactive sites on hydrated oxide surfaces and how can molecular-level information on these be effectively integrated with macroscopic models?
- What is the role of "normal" versus defect sites as centers of reaction?
- How do surface structural variations impact or control adsorption and other surface reactions?
- What molecular-scale information about metal oxide surfaces and reactivity should be transferred to the macroscopic scale and above for environmental simulation?

Just as there are scientific questions and issues, there are many exciting opportunities in the area of surface complexation modeling for future research, including the following topics:

- distributed reaction surface complexation models and those with additional/key molecular constraints;
- characterizing and modeling multiple reaction networks on surfaces (e.g., kinetic phenomena);
- mechanistic basis for bacterially driven metal oxide reduction, including the electron-transfer reaction and surface chemistry/physiologic interrelationships;
- integration of SCM with microbially mediated reactions and phenomena; and
- linking molecular-scale studies of model oxide surfaces with comparable studies on analogous natural oxides isolated from soil or geological environments.

8.2. Experimental Challenges

There are a number of experimental challenges that must be overcome if progress is to be made in molecular-scale studies of the aqueous solution−metal oxide interface, including the following:

- high-spatial/depth resolution of contaminant distribution/speciation using new generation “microprobes” and analytical microscopies;
- improved spectroscopic interrogation techniques for heterogeneous materials (e.g., number of species, phase distribution);
- spatially resolved measurements of sorbate−surface bonding (e.g., X-ray microprobe) at scales over which surface structural defects occur ($<1\ \mu$m); and
- in situ, spatially resolved spectroscopic studies of sorption complexes in natural materials containing complex multi-oxide associations.

8.2.1. Atomic-Scale Geometric and Electronic Structure

At the most basic level, one of the major challenges for the future is to find ways to accurately determine the positions of atoms and ions on the surfaces of metal oxides in various media. One of the most important reasons to perform surface science measurements in vacuum on well-characterized surfaces is for comparison with theoretical calculations. Solid-state theory is not yet at the level of sophistication that will allow calculation of detailed electronic, geometric, or surface chemical properties of, for example, polycrystalline materials in a liquid environment. And yet our hopes for understanding surface physics and chemistry rest ultimately on our ability to explain observations theoretically. Some of the theoretical approaches that are being applied to the study of water−metal oxide interfaces are discussed in section 7. However, they must, of necessity, consider relatively simple, idealized systems. We can only approach such systems experimentally under the most carefully controlled conditions, which is one of the things that surface science can do well. A great deal has been learned over the past few years about aqueous solution−metal oxide interactions through an interplay between theory and experiment; such collaboration must continue and be strengthened.

Since many properties of a surface depend strongly on geometric structure, it is crucial that theoreticians and experimentalists are looking at the “same” surfaces. For example, ignoring relaxation at step edges can affect the predicted chemisorption behavior of a surface. At the same time, chemisorption—since it partially restores the coordinative saturation of surface ions—affects relaxation. STM appears to offer some hope in this area, partly because identical measurements can be performed in vacuum, atmospheric, or liquid environments. However, as discussed in section 2.3.1, the technique has not yet produced the necessary level of detail.

Scanning tunneling spectroscopy (STS) has the potential to determine the spectrum of both occupied and empty electronic levels within a few electron volts of the Fermi level at individual atomic sites on a surface, but this potential has not yet been realized in practice on metal oxides. In general, photoemission has given far more detailed pictures of even defect-site electronic structure than has STS, and inverse photoemission complements the unique electron-band-mapping capabilities of angle-resolved photoemission to explore unoccupied states at the surface; they cannot, of course, be used in aqueous environments. Continued effort should be devoted to trying to optimize STS for oxide samples in all environments.

One of the research areas that is most important for future progress in metal oxide surface chemistry is the characterization of all types of defects on oxide surfaces at the atomic level. STM and AFM offer some hope for success in this area, but much work remains before definitive determinations of surface defect structure (including relaxation, which affects electronic structure) can be made. A variety of other experimental techniques can also be applied, and computational methods for addressing complex defect systems must be expanded. It is particularly important to characterize defect populations before performing reactivity experiments, since chemical reactivity of metal oxide surfaces is very often dominated by defect sites.

Impurities on or in metal oxide surfaces, which can have very different electronic properties than the clean metal oxide, often play an even more important role in reactivity than do defects. Since very small impurity concentrations may be sufficient to dominate reactivity, higher photon and X-ray fluxes are needed in order to study lower coverages of species on surfaces. Such fluxes are now becoming available at recently completed, third-generation synchrotron X-ray sources.

Recent STM and AFM results on oxide surfaces are extremely encouraging,[25,795] and a great deal of effort, both in improving resolution and in interpreting images, should be expended in the future in applying STM, etc., to metal oxide−water interfaces.

The prospects for using STM, STS, and AFM as probes of the structure of both ordered and defective surfaces are a prime example of an area needing close cooperation between theory and experiment. The interpretation of STM images and STS spectra, for example, can only be made with the help of high-quality, independent information on electronic structure and the relationship between atomic and electronic structure; this is particularly true for defects. This knowledge must generally be coupled with a thorough understanding of conduction mechanisms for a given solid. An example is the recent advance in our understanding of STM images of hematite (section 3.1.5) in light of cluster and slab calculations.[129] Neither the initial STM interpretation[56] nor the calculated STM images[129] are "correct", but their interplay and usefulness in furthering our understanding are very important. Similarly, extending the usefulness of many in situ techniques for probing surface structures (e.g., SPM, NMR, XAFS, SHG, and SFG) will require attendant advances in the theoretical basis for interpreting spectroscopic results within the overall context of extended structures.

The application of synchrotron radiation techniques, particularly XAFS, to probing metal ion speciation in aqueous solution and at the aqueous–metal oxide interface has grown dramatically in the past decade (see sections 4.3.2.2 and 4.4.2.2) and is expected to play a major role in the foreseeable future. With future upgrades of existing synchrotron facilities and the completion of new synchrotron light sources worldwide, dramatic increases in brightness and flux density will make it possible to probe the speciation and distribution of metal ions in complex samples on length scales of approximately 1 μm or smaller. The increase in photon flux density provided by these new light sources will substantially improve the ability to characterize important reactions and transformations at the aqueous solution–metal oxide interface. As discussed in section 4.1, many studies of metal ions in aqueous systems are sensitive to the absolute concentrations of the metal ions. For example, aqueous Pb(II), Fe(II), or U(VI) solutes all occur predominantly as mononuclear species at typical concentration levels found in the environment. If the aqueous concentrations are increased, they can hydrolyze and oligomerize into large multimeric solution species, which react differently with the metal oxide surface. The expected increases in total flux from new synchrotron light sources and ongoing improvements in the sensitivity and throughput of X-ray detectors will make it possible to carry out XAFS studies of chemical interactions at aqueous solution–metal oxide interfaces at defect-level surface concentrations. These improvements should also make it possible to perform GI-XAFS experiments on high-quality oriented single crystals of metal oxides and to use oxidation-state-selective fluorescence yield XAFS on metal ions sorbed on metal oxide surfaces.

Although X-ray scattering and XSW methods have only been applied to a few aqueous solution–metal oxide interfaces,[87–89,359,423] these techniques can provide detailed information on atomic-scale geometric structure of simple model systems. We encourage such studies. These experiments can be used, for example, to test or validate theoretical approaches (section 7), such as the predicated surface structure of goethite (110) (see Figure 58). Furthermore, the surface geometric structure of α-Al_2O_3 (0001) in UHV has already been determined;[54,55] a similar approach should be used to measure the structure of a water–α-Al_2O_3 (0001) interface as well as other metal oxide–aqueous interfaces, since the water-exposed alumina surface is expected to have a different structure than the clean alumina surface, which will in turn affect its reactivity. Although future studies of the geometric and electronic structures of clean metal oxide surfaces are important in providing a basis for comparison of the effects of hydration or hydroxylation and the reaction of the surface with adsorbates, it is extremely important to couple such studies with similar ones on metal oxide surfaces in contact with, and after exposure to, aqueous solutions. It is also essential to explore the effects of impurities in a given metal oxide on reactivity. Without these steps, it will not be possible to transfer much information from detailed studies of clean metal oxide surfaces to "real" systems of importance in, for example, oxide-on-oxide catalysis or environmental chemistry.

8.2.2. Future Prospects for Experimental Studies of Interfacial Layers

8.2.2.1. Ion Distributions in the Electrical Double Layer. The success of XSW experiments that probe the ion distribution at metal–electrolyte interfaces suggests that comparable experiments at metal oxide–aqueous solution interfaces are possible, provided one can synthesize metal oxide–metal multilayers that are adequately smooth, have high enough reflectivities, and have controlled metal oxide stoichiometry. Additional research should be done to develop such materials and to optimize these experiments.

X-ray and neutron low-angle reflectivity experiments can also be designed to probe the diffuse-layer structure. For example, for a CsF electrolyte, the F(–I) anions are effectively invisible to this method, but the reflectivity will depend on the concentration of Cs(I) cations near the interface. Simulations show that for an alumina–aqueous CsF interface the X-ray reflectivity changes by about 10% when the interface is charged to $\approx$20 mC/cm^2 [assuming Gouy–Chapman behavior for the Cs(I) and F(–I) ion distributions]. Thus, this method can be used to directly test models of ion distribution in the diffuse layer.

In addition, the tip–sample interaction forces in AFM can be used to probe double-layer structure,[400–402] as well as the pH_{PZC} of individual faces on single-crystal metal oxides in contact with aqueous solution.

One can expect that NMR studies, based on metal cation and anion nuclei, will contribute new information on the electrical double layer. The application of NMR techniques based on magnetic field gradients should elucidate important features of ionic diffusion in the double layer. The use of modern NMR techniques for elucidating chemical structure and dynamics on solid surfaces is now well established. With the widespread and growing availability of excellent solid-state NMR spectrometers operating at frequencies approaching 1 GHz, one might expect that the relatively limited NMR studies of metal oxide surfaces to date might be extended with substantial success to a variety of high-surface-area metal oxide surfaces if persistent, extensive experimental efforts are focused in this direction. Such efforts can be expected to employ a variety of techniques based on hydrogen, oxygen, and metal isotopes and can be carried out at interfaces with air, vacuum, or aqueous media. The NMR study of adsorption of neutral organics on metal oxide surfaces from an aqueous phase is likely to be precluded in most cases because of the competition of water for adsorption sites; however, the use of NMR to examine metal ions adsorbed from aqueous phases to metal oxide surfaces is promising. It is surprising that little, if any, NMR work has been carried out on metal oxide−aqueous electrolyte interfaces via observation of nuclei of the anion, e.g., ^{19}F NMR observation of F^- ions, ^{31}P NMR observation of PO_4^{3-} ions, and ^{35}Cl NMR observation of ClO_4^- ions. The "simultaneous" observation of NMR signals for both the metal cation and a nuclide of the anion would a priori seem attractive, as does the use of magnetic field gradient techniques for characterizing ion diffusion at a metal oxide−aqueous solution interface. In general, one can expect an increasing importance of nuclear magnetic resonance in the study of such systems.

8.2.2.2. The Electrical Double Layer. The surface X-ray scattering method described in section 4.3.3.5 for water near Ag (111) should be applicable to metal oxide−aqueous solution interfaces. Indeed, the relatively low atomic number of many metal oxides will make the contrast between water and the substrate larger. It is important to find a substrate that is relatively simple from a structural standpoint and where the surface structure does not change much as the solution pH is varied over a broad range. Some early measurements have been reported for calcite $(10\bar{1}4)$ in calcite-saturated aqueous solutions.[88,423] These studies show that the calcite surface can be quite smooth, and they provide one of the first "direct" views of the ordering of water molecules in a discrete monolayer at an oxide−water interface.

8.2.3. Reaction Kinetics

It is unknown whether the kinetics of ligand exchange at sites in dissolved oligomers, such as the terminal water molecules on the $Al_{13}O_4(OH)_{24}(H_2O)_{12}^{7+}$(aq) complex (Figure 45a), can be quantitatively compared with the reactions at structurally similar sites on surfaces, such as on the (0001) surface of α-Al_2O_3 (Figure 45b). The promise of such a comparison is profound because, unlike for surfaces, well-established methods exist for determining rates of oxygen exchange in dissolved oligomers, such as ^{17}O NMR. It is clear that, at some point, transfer of information from the solution state to surfaces will fail, as structures differ and as unique solvent properties near the surface become important, but this point of failure is not known. The development of surface-sensitive probes of ligand-exchange kinetics at interfaces would be a great advance.

It is well known that some ligands bound to the surface have a labilizing effect on the metal atom coordinated to oxygens on monatomic steps at surfaces (see Figure 47). These ligands are assumed to be equilibrium adsorbates (although this is also an area that requires further study), and there appears to be consistency between the labilizing effect of ligands in dissolved metal−ligand complexes and in surface complexes. Obviously there must be structural similarity between the complexes in the two environments for this qualitative observation to be true. This comparison will break down when the symmetry of the surface complex is distorted from that found in solution because the bonding is changed.

Because the Brønsted properties of adsorbates may differ considerably from those of the corresponding dissolved metal complex, the coordination number of metal complexes in solution may not exhibit a similar pH dependence to those on surfaces. Hence, protonation states of surface complexes must be expected to differ from the dissolved model complex; however, the extent to which they differ can only be estimated with our current understanding. Likewise, the acidity of water molecules in oligomers is affected by strong intermolecular hydrogen bonding, commonly between the water molecule at one metal center and the hydroxyl bound at another or a hydroxyl bridge. For example, the pK_{a1}, and pK_{a2} values of water molecules in $(H_2O)(en)_2Cr(OH)Cr(en)_2(H_2O)$ differ by 10^7, a much larger value than expected from the monomers. This hydrogen bonding is present at metal oxide−water interfaces, but it is not measurable.[617]

Even if elementary rate constants cannot be transferred from sites on dissolved oligomers to sites at oxide mineral surfaces, one may be able to construct linear free energy relations (LFER) to predict rates of complicated processes (e.g., Figure 46). In addition, reactions at these oligomers are at the appropriate scale for cluster-based calculation of reaction properties based upon computer simulations (e.g., ref 796), which can then be extended to surfaces.

It has been pointed out (section 5.3) that direct evidence is lacking for oxide dissolution mechanisms involving monomer detachment from step sites, and experimental confirmation of this assumption would be useful.

In favorable cases, the dynamics of chemical reactions (e.g., site exchange) at the metal oxide−aqueous solution interface may be amenable to NMR measurements based on line shapes and/or relaxation experiments.

8.2.4. Particles, Colloids, and Nanostructured Materials

A particularly exciting area for new research on metal oxide surfaces and interfaces involves very small particles with nanometer to micrometer dimensions. As particle size decreases, the contribution of surface energy to the overall free energy increases and may become the dominant contribution for nanometer-sized particles, with accompanying changes in the properties of the nanoparticles, including reactivity and phase stability. For example, the influence of particle size on chemical reactivity of TiO_2 was recently investigated by Chen et al.,[621] who found that the unique photocatalytic reactivity of TiO_2 nanoparticles as small as 3 nm in diameter in reducing Cu(II) and Hg(II) can be explained by an increase in the number of surface Ti sites as well as possible corner defects. Surface effects are also important in the reactivity and phase stability of nanoparticle alumina. For example, McHale et al.[809] found that nanocrystalline Al_2O_3 sorbs water which could not be completely removed without particle coarsening. They also showed that when the surface area of nanocrystalline alumina exceeds about 125

m^2/g, the γ-Al_2O_3 form of alumina is stabilized relative to the α-Al_2O_3 form, which should be thermodynamically stable under all common pressure and temperature conditions.[298] This finding was attributed to the lower surface energy of the former. In general, little is known quantitatively about the surface energies of metal oxides or the molecular-scale reasons for changes in reactivity as particle size decreases into the nanometer range. We predict that there will be significant growth in this research area over the next few years because of the increasing technological applications being found for nanocrystalline oxides, as discussed below.

Significant advances in the fields of colloid and sol−gel chemistry in the last 2 decades now allow fabrication of micro- and nanosized structures using finely divided monodispersed colloidal particles.[810−821] There is a growing trend on the part of the scientific community to apply these concepts to develop systems of smaller dimensions. The homogeneous solid (three-dimensional) is giving way to multilayers with quasi-two-dimensional and quasi-one-dimensional structures, such as nanowires or clusters in an insulating matrix, and finally to porous nanocrystalline films. Nanocrystalline semiconductor films consist of a network of mesoscopic oxide particles, such as TiO_2, ZnO, Nb_2O_5, Fe_2O_3, WO_3, or Ta_2O_5, which are interconnected to allow for electronic conduction. The pores are filled with an electrolyte, or with a solid material such as an amorphous organic hole transmitter or a p-type semiconductor. In this way an electronic junction of extremely large contact area is formed, displaying very interesting and unique properties. Some important features of such mesoporous films are as follows:

•an extremely large internal surface area, the roughness factors (i.e., the true surface area of the film divided by the geometrically projected area) being in excess of 1000 for a film thickness of 8 μm;

•the ease of charge carrier percolation across the nanoparticle network, making this huge surface area electronically addressable;

•a very rapid and highly efficient interfacial charge transfer between the oxide and redox-active species anchored to the particle surface;

•the ability to form an accumulation layer under forward bias;

•for intrinsic or weakly doped oxides, the inability to form a depletion layer under reverse bias;

•the fast intercalation and release of Li^+ ions into the oxide; and

•the appearance of quantum confinement effects for certain oxides, such as ZnO, as the particle size decreases to a few nanometers or below.

Nanostructured materials offer many new opportunities to study fundamental surface processes in a controlled manner, and this in turn will lead to fabrication of new devices. The unique optical and electronic features of these films are being exploited to develop solar cells, photochromic displays and switches, optical switches, chemical sensors, intercalation batteries, capacitor dielectrics and supercapacitors, heat-reflecting and UV-absorbing layers, coatings to improve chemical and mechanical stability of glass, etc.; some recent articles[591−593] have outlined some of these novel applications. The properties of mesoporous films are intimately linked to their material content, chemical composition, structure, and surface morphology. Fortunately, colloid chemistry has advanced tremendously in the last 2 decades so that it is now possible to control the processing parameters such as precursor chemistry, hydrothermal growth temperature, binder addition, and sintering conditions and optimize the key parameters of the film, viz., porosity, pore size distribution, light scattering, electron percolation, etc.

The oxide material of choice for many of these systems has been TiO_2. With respect to material content and morphology, two crystalline forms of TiO_2 are important, anatase and rutile (the third form, brookite, is difficult to obtain). Anatase is the low-temperature stable form and yields mesoscopic films that are transparent and colorless. The predominant morphology of the particles is bipyramidal, exposing well-developed (101) faces. Rutile is the dominant form at high temperature, and its crystals are needle-shaped, similar to those of nanocrystalline Nb_2O_5.

8.2.5. Geomicrobiology

Geomicrobiology represents one of the great research opportunities in the chemistry of natural metal oxide surfaces; the two disciplines converge with regard to problems that need solving and techniques with sufficient resolution to allow the solutions. The material presented in section 6 and in ref 629 serves to point out how little we really know at both the macroscopic and mechanistic levels about the effect of microbial organisms on metal oxide surface chemistry, and there are many opportunities for chemists, geochemists, and geologists to begin interfacing with microbiologists in search of new insights in the areas of environmental mineral formation and dissolution. Some general areas of potential interest (which are extensions of the discussions in section 6) include the following:

•*cell attachment and biofilm formation*
  − properties of the biofilm communities
  − interactions of the communities with the substrata
  − molecular nature of microorganism attachment to oxide surfaces
•*community interactions*
  − types of organisms involved
  − dependency of community members on each other
  − importance of the geological/geochemical setting for proper community function
•*mechanisms of metal dissolution, reduction, and oxidation*
  − biochemistry/physiology/genetics
  − molecular architecture of the organism−oxide interface
  − mechanisms of electron and proton transfer from microorganisms to oxide surfaces
  − specific reducing agents (e.g., cytochromes?, quinones?)
  − dissolution enhancement via proton pumping, chelation, or reductive mechanisms

- *surface and structural properties of biogenic oxides and their reactivity*
  - structural polymorphs, size, morphology, and domain structure/length
  - reactivity comparisons to abiotic analogues
  - chemical reactivity within the oxide-organism interface: is it a hydrophobic or hydrophilic domain?
  - surface chemical mechanisms that link the oxide surface and the electron transport chain of metal-reducing bacteria

The most exciting and productive avenues for work may lie at the interfaces between new technological advances in surface chemistry and geochemistry on the one hand and between molecular biology and biophysics on the other. It is now possible to view both bacteria and metal oxides at levels of resolution unheard of a few years ago, and as these microscopic approaches are combined with in situ methods of organism identification and activity measurements, it may be possible to assign roles in mineral dissolution and formation to organisms in natural environments, something very seldom done with certainty. As these new approaches are juxtaposed and interfaced with the study of organisms already in culture, and with others that are continuously being isolated, new insights will almost certainly be achieved, and some of the paradigms now existing will be replaced by new, perhaps more accurately descriptive, ones.

8.3. Theoretical Challenges

Many of the advances that have been (and continue to be) made in computational chemistry and physics are making the examination of aqueous solution−metal oxide interface chemistry an approachable problem. The recent first-principles calculations on the interactions of water with MgO (100) by Giordano et al.[63], α-Al_2O_3 (0001) by Hass et al.,[69] and TiO_2 (110) (rutile) by Lindan et al.[119] are very encouraging because they produce results consistent with experiment. However, these calculations raise additional questions about the exact nature of the interactions between adjacent water molecules and of water molecules with different oxide surfaces and their effect on the dissociation of water: In the calculations by Giordano et al. on MgO (100), such interactions are required for the dissociation of water, whereas in the calculations by Lindan et al. on TiO_2 (110), apparently they are not required. Strong collaborations between the theoretical and experimental communities are essential and have proven very effective within the molecular environmental science community. Several theoretical, methodological, and computational challenges remain if we are to understand the fundamental chemistry and physics of aqueous solution−metal oxide interfaces. Advances in the field and new theoretical approaches are needed to:

- *treat the multiple time and length scales needed to determine the macroscopic properties of aqueous solution−metal oxide interfaces*

Research needs in this area include the development of quantum mechanical and molecular dynamics models capable of treating 100 → 100 000 atom systems and nanoseceond → second time frames. Methods are also needed to scale the information up from the molecular to the macroscopic scale so that thermodynamic observables can be predicted.

- *treat the chemical reactivity of bulk water and aqueous solutions*

Research needs in this area include improving the molecular dynamics models for liquid water in order to describe the dissociation reactions of water and development of methods capable of calculating the dielectric properties of interfacial and liquid water. These developments are necessary in order to better understand the fundamental parameters controlling the structure of the electrical double layer, the competition of protons for surface sites, the effects of pH on metal adsorption, the adsorption of organic molecules, and the nature of solvation at oxide−solution interfaces.

- *determine potential energy expressions for interactions at the metal oxide−aqueous solution interface*

Research needs in this area include deriving expressions for the interaction of water, metal ions, oxyanions, and other species with metal oxides. These potentials need to be sufficiently transferable that they can be used to predict a range of physical properties beyond those used in the fitting algorithms. The development of these potential energy functions is essential for describing the binding mechanisms and kinetics of sorption of metal cations and anions onto metal oxide surfaces.

- *treat relativistic effects in quantum mechanical calculations*

To compute the properties of heavy metals (high-Z transition metals, lanthanides, and actinides) using quantum mechanical methods, it is necessary to treat the relativistic effects by inclusion of spin−orbit coupling terms in the Dirac−Fock Hamiltonian. Simulations of the dynamical properties of heavy metals in solutions, in solids, and at interfaces must accurately reproduce the relativistic properties of these materials.

- *compute observable properties*

To make a direct comparison between theory and experiment, the theoretical methods need to be able to compute (compare and predict) empirical data (e.g., spectra) directly. This requires the development and refinement of methods that can transform the results of molecular-based and thermodynamic calculations into predictions of empirical data. These calculations are essential both to validate the computational methods as well as to provide help in interpreting empirical data. Important experimental methods where comparison with theory is crucial include XAFS, XANES, X-ray diffraction methods, photoemission spectroscopies (XPS and UPS), HREELS, IR spectroscopy, and measurements of the structural and elastic properties of bulk metal oxide phases.

- *develop multisite thermodynamic models of metal−ligand binding and surface protonation*

Improved thermodynamic models are needed that can explicitly calculate the effects of proton, metal, and ligand binding and charge development at specific molecular sites on surfaces. These approaches include the scaling up of molecular modeling calculations to the thermodynamic level and the extension of semiempirical theories developed for oxide phases (e.g., the application of Pauling electrostatic bond strength theory together with Born solvation theory) to different surfaces and sites. These methods need to address questions such as:

What mineral surfaces are present in the macroscopic experiments?

Should different capacitances be used for different surfaces?

How does one handle patchwise surfaces (i.e., does the electrical double layer overlap all surfaces and develop the same potentials, or should each "patch" develop a different potential)?

How do electrolyte ions bond to a metal oxide surface when many site types are present?

How are partial charges on each site calculated?

- *perform experimental studies of metal−ligand binding and surface protonation at elevated temperatures*

Improved thermodynamic models are needed to better understand metal oxide adsorption and dissolution reactions at elevated temperatures. The overall paucity of experimental data currently precludes the verification of models parametrized for lower temperatures to the high-temperature region.

- *perform dynamic modeling of reactions that are experimentally accessible*

A disproportionate amount of modeling of reaction rates has been conducted on systems that cannot be experimentally probed. Models of elementary reaction rates for ligand exchange, however, can be immediately compared with existing experimental results, thereby lending credibility to the ab initio models of surface reactions for which no data exist.

9. Acknowledgments

This is the first in a series of review articles sanctioned by the DOE Council on Chemical Sciences based on workshops sponsored by the Chemical Science Division, Office of Basic Energy Research, U.S. Department of Energy. We thank Dr. Robert Marianelli, Director, DOE−OBES Chemical Sciences Division, for sponsoring the workshop, held in Santa Fe, NM, in April 1997, from which this review article was generated. We also gratefully acknowledge the help of Drs. William Millman (Chemical Sciences Division) and Paula Davidson (Geosciences Program) in acting as DOE liaisons before and during the workshop. Ms. Leila Goslee, Oak Ridge Institute for Science and Education, is thanked for doing much of the organizational work involving accommodations and meals prior to the workshop. Drs. Neil Sturchio and Paul Fenter (Argonne National Laboratory) are thanked for providing preprints of their XSW and X-ray reflectivity work on calcite surfaces prior to publication. In addition, Prof. George Parks (Stanford University) is thanked by G.E.B. for many helpful discussions on metal oxide−aqueous solution interfaces over the past decade and for help in preparing Figure 29. Drs. Ping Liu and Tom Kendelewicz (Stanford University) are thanked for locating a number of references during the final revisions of this paper.

10. References

(1) Brown, G. E., Jr. In *Mineral−Water Interface Geochemistry*; Hochella, M. F., Jr., White, A. F., Eds.; Mineralogical Society of America: Washington, DC, 1990; Vol. 23.
(2) Davis, J. A.; Kent, D. B. In *Mineral−Water Interface Geochemistry*; Hochella, M. F., Jr., White, A. F., Eds.; Mineralogical Society of America: Washington, D. C., 1990; Vol. 23.
(3) Dzombak, D. A.; Morel, F. M. M. *Surface Complexation Modeling*; John Wiley and Sons: New York, 1990.
(4) Hochella, M. F., Jr.; White, A. F. In *Mineral−Water Interface Geochemistry*; Hochella, M. F., Jr., White, A. F., Eds.; Mineralogical Society of America: Washington, DC, 1990; Vol. 23.
(5) Sposito, G. *The Surface Chemistry of Soils*; Oxford University Press: New York, 1984.
(6) Schindler, P. W.; Stumm, W. In *Aquatic Surface Chemistry: Chemical Processes at the Particle−Water Interface*; Stumm, W., Ed.; John Wiley and Sons: New York, 1987.
(7) Stumm, W. *Chemistry of the Solid Water Interface*; John Wiley and Sons: New York, 1992.
(8) McBride, M. B. In *Minerals in Soil Environments*; Dixon, J. B., Weed, S. B., Eds.; Soil Science Society of America: Madison, WI, 1989.
(9) McBride, M. B. *Environmental Chemistry of Soils*; Oxford University Press: Oxford, 1994.
(10) Yan, B.; Meilink, S. L.; Warren, G. W.; Wynblatt, P. *IEEE Trans. Compon. Hybrids Manuf. Technol.* **1987**, *CHMT-10*, 247.
(11) Knözinger, H.; Ratnasamy, P. *Catal. Rev. − Sci. Eng.* **1978**, *17*, 31.
(12) Knözinger, H. In *Catalysis by Acids and Bases*; Imelik, B., Ed.; Elsevier: New York, 1985.
(13) Mariette, L.; Hemidy, J. F.; Cornet, D. In *Adsorption and Catalysis on Oxide Surfaces*; Che, M., Bond, G. C., Eds.; Elsevier: New York, 1985.
(14) Blonski, S.; Garofalini, S. H. *Surf. Sci.* **1993**, *295*, 263.
(15) Henrich, V. E.; Cox, P. A. *The Surface Science of Metal Oxides*; Cambridge University Press: Cambridge, 1994.
(16) Sverjensky, D. A. *Geochim. Cosmochim. Acta* **1994**, *58*, 3123.
(17) Wolery, T. J.; Daveler, S. A. *EQ3/6. A software package for geochemical modeling of aqueous systems: Package overview and installation guide, version 7.0*; Lawrence Livermore National Laboratory, 1992.
(18) *Semiconductors: Physics of II−IV and I−VII Compounds, Semimagnetic Semiconductors*; Madelung, O., Ed.; Springer-Verlag: Berlin, 1982; Vol. 17b.
(19) Welsh, I. D.; Sherwood, P. M. A. *Phys. Rev. B* **1989**, *40*, 6386.
(20) Condon, N. G.; Leibsle, F. M.; Lennie, A. R.; Murray, P. W.; Vaughan, D. J.; Thornton, G. *Phys. Rev. Lett.* **1995**, *75*, 1961.
(21) Sander, M.; Engel, T. *Surf. Sci.* **1994**, *302*, L263.
(22) Novak, D.; Garfunkel, E.; Gustafsson, T. *Phys. Rev. B* **1994**, *50*, 5000.
(23) Szabo, A.; Engel, T. *Surf. Sci.* **1995**, *329*, 241.
(24) Onishi, H.; Fukui, K.; Iwasawa, Y. *Bull. Chem. Soc. Jpn.* **1995**, *68*, 2447.
(25) Fischer, S.; Munz, A. W.; Schierbaum, K. D.; Göpel, W. *Surf. Sci.* **1995**, *337*, 17.
(26) Guo, Q.; Cocks, I.; Williams, E. M. *Phys. Rev. Lett.* **1996**, *77*, 3851.
(27) Berkó, A.; Solymosi, F. *Langmuir* **1996**, *12*, 1257.
(28) Martello, D. V.; Vecchio, K. S.; Diehl, J. R.; Graham, R. A.; Tamilia, J. P.; Pollack, S. S. *Geochim. Cosmochim. Acta* **1994**, *58*, 4657.
(29) Swartzentruber, B. S.; Mo, Y.-M.; Kariotis, R.; Lagally, M. G.; Webb, M. B. *Phys. Rev. Lett.* **1990**, *65*, 1913.
(30) Condon, N. G.; Murray, P. W.; Leibsle, F. M.; Thornton, G.; Lennie, A. R.; Vaughan, D. J. *Surf. Sci.* **1994**, *310*, L609.
(31) Jansen, R.; Brabers, V. A. M.; van Kempen, H. *Surf. Sci.* **1995**, *328*, 237.
(32) Woodruff, D. P.; Delchar, T. A. *Modern Techniques of Surface Science*, 2nd ed.; Cambridge University Press: Cambridge, 1994.
(33) Bonnell, D. A. *Prog. Surf. Sci.* **1998**, *57*, 187.
(34) Freund, H. J.; Kuhlenbeck, H.; Staemmler, V. *Rep. Prog. Phys.* **1996**, *59*, 283.
(35) Street, S. C.; Xu, C.; Goodman, D. W. *Annu. Rev. Phys. Chem.* **1997**, *48*, 43.
(36) Zangwill, A. *Physics at Surfaces*; Cambridge University Press: Cambridge, 1988.
(37) Heinz, K. *Prog. Surf. Sci.* **1988**, *27*, 239.
(38) VanHove, M. A.; Tong, S. Y. *Surface Crystallography by LEED*; Springer-Verlag: Berlin, 1979.
(39) Henzler, M. *Appl. Surf. Sci.* **1982**, *11/12*, 450.
(40) Henzler, M. *Surf. Sci.* **1996**, *357*, 809.
(41) Ascolani, H.; Cerda, J. R.; de Andres, P. L.; de Miguel, J. J.; Miranda, R.; Heinz, K. *Surf. Sci.* **1996**, *345*, 320.
(42) Watson, P. R.; Van Hove, M. A.; Herman, K. *NIST Surface Structure Database*, version 2.0; National Institutes of Standards and Technology: Gaithersburg, MD, 1996.

(43) Hochella, M. F., Jr.; Eggleston, C. M.; Elings, V. B.; Thompson, M. S. *Am. Mineral.* **1990**, *75*, 723.
(44) Renaud, G. *Surf. Sci. Rep.* **1998**, *32*, 1.
(45) Thevuthasan, S.; Kim, Y. J.; Yi, S. I.; Chambers, S. A.; Morais, J.; Denecke, R.; Fadley, C. S.; Liu, P.; Kendelewicz, T.; Brown, G. E., Jr. *Surf. Sci.*, submitted.
(46) Eggleston, C. M. In *Scanning Probe Microscopy of Clay Minerals*; Nagy, K. L., Blum, A. E., Eds.; Clay Minerals Society, 1994; Vol. 7.
(47) Fadley, C. S. In *Synchrotron Radiation Research: Advances in Surface and Interface Science: Techniques*; Bachrach, R. Z., Ed.; Plenum Press: New York, 1992; Vol. 1.
(48) Stern, E. A. *J. Vac. Sci. Technol.* **1977**, *14*, 461.
(49) Bianconi, A. *Appl. Surf. Sci.* **1980**, *6*, 392.
(50) Stöhr, J. *NEXAFS Spectroscopy*; Springer-Verlag: Berlin, 1992.
(51) Robinson, I. K.; Tweet, D. *Rep. Prog. Phys.* **1992**, *55*, 599.
(52) Newnham, R. E.; deHaan, Y. M. *Zeits. Kristallogr.* **1962**, *117*, 235.
(53) Blake, R. L.; Hessevick, R. E.; Zoltai, T.; Finger, L. W. *Am. Mineral.* **1966**, *51*, 123.
(54) Renaud, G.; Villette, B.; Vilfan, I.; Bourret, A. *Phys. Rev. Lett.* **1994**, *73*, 1825.
(55) Guenard, P.; Renaud, G.; Barbier, A.; Gautier-Soyer, M. *Mater. Res. Soc. Symp. Proc.* **1996**, *437*, 15.
(56) Eggleston, C. M.; Hochella, M. F., Jr. *Am. Mineral.* **1992**, *77*, 911.
(57) Gautier-Soyer, M.; Pollak, M.; Henriot, M.; Guittet, M. J. *Surf. Sci.* **1996**, *352−354*, 112.
(58) Eggleston, C. M. *Am. Mineral.* **1998**, submitted.
(59) Finnis, M. Personal communication.
(60) Lee, Y. C.; Tong, P.; Montano, P. A. *Surf. Sci.* **1987**, *181*, 559.
(61) Li, C.; Wu, R.; Freeman, A. J.; Fu, C. L. *Phys. Rev. B* **1993**, *48*, 8317.
(62) Guenard, P.; Renaud, G.; Villette, B. *Physica B* **1996**, *221*, 205.
(63) Giordano, L.; Goniakowski, J.; Suzanne, J. *Phys. Rev. Lett.* **1998**, *81*, 1271.
(64) Girardet, C.; Hoang, P. N. M.; Marmier, A.; Picaud, S. *Phys. Rev. B* **1998**, *57*, 11931.
(65) Liu, P.; Kendelewicz, T.; Brown, G. E., Jr.; Parks, G. A. *Surf. Sci.* **1998**, *412/413*, 287.
(66) Liu, P.; Kendelewicz, T.; Nelson, E. J.; Brown, G. E., Jr. *Surf. Sci.* **1998**, *415*, 156.
(67) Ahn, J.; Rabalais, J. W. *Surf. Sci.* **1997**, *388*, 121.
(68) Toofan, J.; Watson, P. R. *Surf. Sci.* **1998**, *410*, 162.
(69) Hass, K. C.; Schneider, W. F.; Curioni, A.; Andreoni, W. *Science* **1998**, *282*, 265.
(70) Puchin, V. E.; Gale, J. D.; Shluger, A. L.; Kotomin, E. A.; Günster, J.; Brause, M.; Kempter, V. *Surf. Sci.* **1997**, *370*, 190.
(71) Diebold, U.; Anderson, J. F.; Ng, K.-O.; Vanderbilt, D. *Phys. Rev. Lett.* **1996**, *77*, 1322.
(72) Charlton, G.; Howes, P. B.; Nicklin, C. L.; Steadman, P.; Taylor, J. S. G.; Muryn, C. A.; Harte, S. P.; Mercer, J.; McGrath, P.; Norman, D.; Turner, T. S.; Thornton, G. *Phys. Rev. Lett.* **1997**, *78*, 495.
(73) Wiesendanger, R.; Shvets, I. V.; Burgler, D.; Tarrach, G.; Guntherodt, H. J.; Coey, J. M. D.; Graser, S. *Science* **1992**, *255*, 583.
(74) Gaines, J. M.; Bloemen, P. J. H.; Kohlhepp, J. T.; Bulle-Lieuwma, C. W. T.; Wolf, R. M.; Reinders, A.; Jungblut, R. M.; van der Heiden, P. A. A.; van Eemeren, J. T. W. M.; van de Stegge, J.; De Jonge, W. J. M. *Surf. Sci.* **1997**, *373*, 85.
(75) Tarrach, G.; Burgler, D.; Schaub, T.; Wiesendanger, R.; Guntherodt, H. J. *Surf. Sci.* **1993**, *285*, 1.
(76) Chambers, S. A.; Joyce, S. A. *Surf. Sci. Lett.* **1998**, in press.
(77) Zhang, Z.; Jeng, S.-P.; Henrich, V. E. *Phys. Rev. B* **1991**, *43*, 12004.
(78) Woodruff, D. P.; Johnston, P. D.; Smith, N. V. *J. Vac. Sci. Technol. A* **1983**, *1*, 1104.
(79) Henrich, V. E.; Kurtz, R. L. *Phys. Rev. B* **1981**, *23*, 6280.
(80) Kröger, F. A. *Chemistry of Imperfect Crystals*; North-Holland: Amsterdam, 1974.
(81) Merchant, P.; Collins, R.; Kershaw, R.; Dwight, K.; Wold, A. *J. Solid State Chem.* **1979**, *27*, 307.
(82) Bjorkstein, U.; Moser, J.; Grätzel, M. *Chem. Mater.* **1994**, *6*, 858.
(83) Sherwood, P. M. A. *Chem. Soc. Rev.* **1985**, *14*, 1.
(84) Haupt, S.; Collisi, U.; Speckmann, H. D.; Strehblow, H. H. *J. Electroanal. Chem.* **1985**, *194*, 179.
(85) Hubbard, A. T. *Chem. Rev.* **1988**, *88*, 633.
(86) Hubbard, A. T. *Langmuir* **1990**, *6*, 97.
(87) Sturchio, N. C.; Chiarello, R. P.; Cheng, L.; Lyman, P. L.; Bedzyk, M. J.; Qian, Y.; You, H.; Yee, D.; Geissbuhler, P.; Sorensen, L. B.; Liang, Y.; Baer, D. R. *Geochim. Cosmochim. Acta* **1997**, *61*, 251.
(88) Chiarello, R. P.; Sturchio, N. C. *Geochim. Cosmochim. Acta* **1995**, *59*, 4557.
(89) Chiarello, R. P.; Sturchio, N. C.; Grace, J. D.; Geissbuhler, P.; Sorensen, L.; Cheng, L.; Xu, S. *Geochim. Cosmochim. Acta* **1997**, *61*, 1467.
(90) Henrich, V. E. *Surf. Sci.* **1993**, *284*, 200.
(91) Nilsson, A.; Weinelt, M. G.; Wiell, T.; Bennich, P.; Karis, O.; Wassdahl, N.; Stöhr, J.; Samant, M. G. *Phys. Rev. Lett.* **1996**, *78*, 2847.
(92) Idriss, H.; Pierce, K. G.; Barteau, M. A. *J. Am. Chem. Soc.* **1994**, *116*, 3063.
(93) Liu, P.; Kendelewicz, T.; Brown, G. E., Jr.; Parks, G. A.; Pianetta, P. *Surf. Sci.* **1998**, *416*, 326.
(94) Liu, P.; Kendelewicz, T.; Brown, G. E., Jr. *Surf. Sci.* **1998**, *412/413*, 315.
(95) Kendelewicz, T.; Liu, P.; Brown, G. E., Jr.; Nelson, E. J.; Pianetta, P. *Surf. Sci.* **1996**, *352−354*, 451.
(96) Scamehorn, C. A.; Harrison, N. M.; McCarthy, M. I. *J. Chem. Phys.* **1994**, *101*, 1547.
(97) Langel, W.; Parrinello, M. *Phys. Rev. Lett.* **1994**, *73*, 504.
(98) Refson, K.; Wogelius, R. A.; Fraser, D. G.; Payne, M. C.; Lee, M. H.; Milman, V. *Phys. Rev. B* **1995**, *52*, 10823.
(99) Langel, W.; Parrinello, M. *J. Chem. Phys.* **1995**, *103*, 3240.
(100) Ferry, D.; Glebov, A.; Senz, V.; Suzanne, J.; Toennies, J. P.; Weis, H. *J. Chem. Phys.* **1996**, *105*, 1697.
(101) Ferry, D.; Glebov, A.; Senz, V.; Suzanne, J.; Toennies, J. P.; Weiss, H. *Surf. Sci.* **1997**, *377/379*, 634.
(102) Peng, X. D.; Barteau, M. A. *Surf. Sci.* **1990**, *233*, 283.
(103) Heidberg, J.; Redlich, B.; Wetter, D. *Ber. Bunsen-Ges. Phys. Chem.* **1995**, *99*, 1333.
(104) Stirniman, M. J.; Haung, C.; Smith, R. S.; Joyce, S. A.; Kay, B. D. *J. Chem. Phys.* **1996**, *105*, 1.
(105) Xu, D.; Goodman, D. W. *Chem. Phys. Lett.* **1997**, *265*, 341.
(106) Jones, C. F.; Reeve, R. A.; Rigg, R.; Segall, R. L.; Smart, R. S. C.; Turner, P. S. *J. Chem. Soc., Faraday Trans. 1* **1984**, *80*, 2609.
(107) Knözinger, E.; Jacob, K. H.; Singh, S.; Hofmann, P. *Surf. Sci.* **1993**, *290*, 388.
(108) Kuroda, Y.; Yasugi, E.; Aoi, H.; Miura, K.; Morimoto, T. *Chem. Soc. Faraday Trans. 1* **1988**, *84*, 2421.
(109) Coluccia, S.; Marchese, L.; Lavagnino, S.; Anpo, M. *Spectrochim. Acta* **1987**, *43A*, 1573.
(110) Wogelius, R. A.; Refson, K.; Fraser, D. G.; Grime, G. W. *Geochim. Cosmochim. Acta* **1995**, *59*, 1875.
(111) Berry, A. J.; Fraser, D. G.; Grime, G. W.; Craven, J.; Sleeman, J. T. *Mineral. Mag.* **1998**, *62A*, 158.
(112) Liu, P.; Kendelewicz, T.; Brown, G. E., Jr.; Nelson, E. J.; Chambers, S. A. *Surf. Sci.* **1998**, *417*, 53.
(113) Liu, P.; Kendelewicz, T.; Brown, G. E., Jr.; Chambers, S. A. *Geochim. Cosmochim. Acta*, submitted.
(114) Nygren, M. A.; Gay, D. H.; Catlow, C. R. A. *Surf. Sci.* **1997**, *380*, 113.
(115) Lee, D. H.; Condrate, R. A., Sr. *Mater. Lett.* **1995**, *23*, 241.
(116) Lad, R. J.; Antonik, M. D. *Ceram. Trans.* **1991**, *24*, 359.
(117) Henrich, V. E.; Dresselhaus, G.; Zeiger, H. J. *Solid State Commun.* **1977**, *24*, 623.
(118) Kurtz, R. L.; Henrich, V. E. *Phys. Rev. B* **1982**, *26*, 6682.
(119) Lindan, P. J. D.; Harrison, N. M.; Gillan, M. J. *Phys. Rev. Lett.* **1998**, *80*, 762.
(120) Wang, L.-Q.; Baer, D. R.; Englehard, M. H.; Shultz, A. N. *Surf. Sci.* **1995**, *344*, 237.
(121) Hadjiivanov, K. I.; Klissurski, D. G. *Chem. Soc. Rev.* **1996**, 61.
(122) Linsebigler, A. L.; Lu, G.; Yates, J. T. *Chem. Rev.* **1995**, *95*, 735.
(123) Shklover, V.; Nazeeruddin, M.-K.; Zakeeruddin, S. M.; Barbé, C.; Kay, A.; Halbach, T.; Steurer, W.; Hermann, R.; Nissen, H.-U.; Grätzel, M. *Chem. Mater.* **1997**, *9*, 430.
(124) Morterra, C. *J. Chem. Soc., Faraday Trans.* **1987**, *84*, 1617.
(125) Vittadini, A.; Selloni, A.; Rotzinger, F.; Grätzel, M. *Phys. Rev. Lett.* **1998**, *81*, 2954.
(126) Primet, M.; Pichat, P.; Mathieu, M. V. *J. Phys. Chem.* **1971**, *75*, 1216.
(127) Eggleston, C. M. *Aquatic Sci.* **1993**, *55*, 240.
(128) Eggleston, C. M.; Stumm, W. *Geochim. Cosmochim. Acta* **1993**, *57*, 4843.
(129) Becker, U.; Hochella, M. F., Jr.; Apra, E. *Am. Mineral.* **1996**, *81*, 1301.
(130) Leland, J. K.; Bard, A. J. *J. Phys. Chem.* **1987**, *91*, 5076.
(131) Goodenough, J. B. *Prog. Solid State Chem.* **1972**, *5*, 145.
(132) Marcus, R. A.; Sutin, N. *Biochim. Biophys. Acta* **1985**, *811*, 265.
(133) Tao, N. J. *Phys. Rev. Lett.* **1996**, *76*, 4066.
(134) Abraham, R. J.; Fisher, J.; Loftus, P. *Introduction to Spectroscopy*; John Wiley and Sons: New York, 1988.
(135) Ernst, R. R.; Bodenhausen, G.; Wokaun, A. *Principles of Nuclear Magnetic Resonance in One and Two Dimensions*; Oxford University Press: Oxford, 1987.
(136) Maciel, G. E. *Science* **1984**, *226*, 282.
(137) Maciel, G. E.; Ellis, P. D. In *NMR Techniques in Catalysis*; Pines, A., Bell, A., Eds.; Marcel Dekker: New York, 1994.
(138) Waugh, J. S.; Huber, L. M.; Haeberlen, V. *Phys. Rev. Lett.* **1986**, *20*, 180.
(139) Burum, D. P.; Rhim, W. K. *J. Chem. Phys.* **1979**, *71*, 944.
(140) Gerstein, B. C.; Pembleton, R. G.; Wilson, R. C.; Ryan, L. J. *Chem. Phys.* **1977**, *66*, 361.
(141) Maciel, G. E.; Bronnimann, C. E.; Hawkins, B. L. In *Advances in Magnetic Resonance: The Waugh Symposium*; Warren, W. S., Ed.; Academic Press: San Diego, 1990; Vol. 14.

(142) Wooten, E. W.; Mueller, K. T.; Pines, A. *Acc. Chem. Res.* **1992**, *25*, 209.
(143) Ray, G. J.; Samoson, A. *Zeolites* **1993**, *13*, 410.
(144) Mueller, K. T.; Sun, B. Q.; Chingas, G. C.; Zwanziger, J. W.; Terao, T.; Pines, A. *J. Magn. Reson.* **1990**, *86*, 470.
(145) Mueller, K. T.; Wooten, E. W.; Pines, A. *J. Magn. Reson.* **1991**, *92*, 620.
(146) Bronnimann, C. E.; Ridenour, C. F.; Kinney, D. R.; Maciel, G. E. *J. Magn. Reson.* **1992**, *97*, 522.
(147) Frydman, L.; Harwood, J. S. *J. Am. Chem. Soc.* **1995**, *117*, 5367.
(148) Medek, A.; Harwood, J. S.; Frydman, L. *J. Am. Chem. Soc.* **1995**, *117*, 12779.
(149) Chang, W. K.; Liao, M. Y.; Gleason, K. K. *J. Phys. Chem.* **1996**, *100*, 19653.
(150) Gerstein, B. C.; Pruski, M.; Hwang, S.-J. *Anal. Chim. Acta* **1993**, *283*, 1059.
(151) Stejskal, E. O.; Tanner, J. E. *J. Chem. Phys.* **1965**, *42*, 288.
(152) Tanner, J. E.; Stejskal, E. O. *J. Chem. Phys.* **1968**, *49*, 1768.
(153) Callahan, P. T.; Gros, M. A. L.; Pinder, D. N. *J. Chem. Phys.* **1983**, *79*, 6372.
(154) Grandjean, J.; Laszlo, P. *J. Magn. Reson.* **1989**, *83*, 128.
(155) Levitt, M. H.; Raliegh, D. P.; Creuzet, F.; Griffin, R. G. *J. Chem. Phys.* **1990**, *92*, 6347.
(156) Spencer, R. G. S.; Halverson, K. J.; Auger, M.; McDermott, A. E.; Griffin, R. G.; Lansbury, P. T. *Biochemistry* **1991**, *30*, 10382.
(157) Gullion, T.; Schaefer, J. *J. Magn. Reson.* **1989**, *81*, 196.
(158) Schmidt, A.; McKay, R. A.; Schaefer, J. *J. Magn. Reson.* **1992**, *96*, 644.
(159) Yannoni, C. S.; Kendrick, R. D. *J. Chem. Phys.* **1981**, *74*, 747.
(160) Zimmerman, J. R.; Holmes, B. G.; Lasater, J. A. *J. Phys. Chem.* **1956**, *60*, 1157.
(161) Pearson, R. T.; Derbyshire, W. *J. Colloid Interface Sci.* **1974**, *46*, 232.
(162) Hanus, F.; Gillis, P. *J. Magn. Reson.* **1984**, *59*, 437.
(163) Silva, R. J. *Mater. Res. Soc. Symp. Proc.* **1992**, *257*, 323.
(164) Overloop, K.; Gerven, L. V. *J. Magn. Reson.* **1993**, *101*, 147.
(165) Hansen, E. W.; Schmidt, R.; Stocker, M.; Akporiaye, D. *J. Phys. Chem.* **1995**, *99*, 4148.
(166) Hansen, E. W.; Schmidt, R.; Stocker, M. *J. Phys. Chem.* **1996**, *100*, 11396.
(167) Bogdan, A.; Kulmala, M.; Gorbunov, B.; Kruppa, A. *J. Colloid Interface Sci.* **1996**, *177*, 79.
(168) Turov, V. V.; Leboda, R.; Bogillo, V. I.; Skubiszewska-Zieba, J. *Langmuir* **1997**, *13*, 1237.
(169) Gun′ko, V. M.; Zarko, V. I.; Turov, V. V.; Voronin, E. F.; Tischenko, V. A.; Chuiko, A. A. *Langmuir* **1995**, *11*, 2115.
(170) Gun′ko, V. M.; Turov, V. V.; Zarko, V. I.; Voronin, E. F.; Tischenko, V. A.; Dudnik, V. V.; Pakhlov, E. M.; Chuiko, A. A. *Langmuir* **1997**, *13*, 1529.
(171) Woessner, D. E.; Snowden, B. S., Jr. *J. Colloid Interface Sci.* **1969**, *30*, 54.
(172) Woessner, D. E. *Mol. Phys.* **1977**, *34*, 921.
(173) Woessner, D. E. *J. Magn. Reson.* **1980**, *39*, 297.
(174) Hougardy, J.; Stone, W. E. E.; Fripiat, J. J. *J. Chem. Phys.* **1976**, *64*, 3840.
(175) Hecht, A. M.; Geissler, E. *J. Colloid Interface Sci.* **1970**, *34*, 32.
(176) Hecht, A. M.; Geissler, E. *J. Colloid Interface Sci.* **1973**, *44*, 1.
(177) Fripiat, J.; Letellier, M. *J. Magn. Reson.* **1984**, *57*, 279.
(178) Majors, P. D.; Raidy, T. E.; Ellis, P. D. *J. Am. Chem. Soc.* **1986**, *108*, 8123.
(179) Majors, P. D.; Ellis, P. D. *J. Am. Chem. Soc.* **1987**, *109*, 1648.
(180) Fitzgerald, J. J.; Piedra, G.; Dec, S. F.; Seger, M.; Maciel, G. E. *J. Am. Chem. Soc.* **1997**, *119*, 7832.
(181) Kim, Y.; Cygan, R. T.; Kirkpatrick, R. J. *Geochim. Cosmochim. Acta* **1996**, *60*, 1041.
(182) Kim, Y.; Kirkpatrick, R. J.; Cygan, R. T. *Geochim. Cosmochim. Acta* **1996**, *60*, 4059.
(183) Weiss, G. A. J.; Kirkpatrick, R. J.; Altaner, S. P. *Am. Mineral.* **1990**, *75*, 970.
(184) Chu, P.-J.; Gerstein, B. C.; Nunan, J.; Klier, K. *J. Phys. Chem.* **1987**, *91*, 3588.
(185) Laperche, V.; Lambert, J. F.; Prost, R.; Fripiat, J. J. *J. Phys. Chem.* **1990**, *94*, 8821.
(186) Luca, V.; Cardile, C. M.; Meinhold, R. H. *Clay Minerals* **1989**, *24*, 115.
(187) Klogrogge, J. T.; Jansen, J. B. H.; Schuiling, R. D.; Geus, J. W. *Clays Clay Minerals* **1992**, *40*, 561.
(188) Lambert, J.-F.; Prost, R. *Clays Clay Minerals* **1992**, *40*, 253.
(189) Tinet, D.; Faugere, A. M.; Prost, R. *J. Phys. Chem.* **1991**, *95*, 8804.
(190) Bank, S.; Bank, J. F.; Ellis, P. D. *J. Phys. Chem.* **1989**, *93*, 4847.
(191) Piedra, G.; Fitzgerald, J. J.; Ridenour, C. F.; Maciel, G. E. *Langmuir* **1996**, *12*, 1958.
(192) Bigalow, A. I.; Gorte, R. J.; White, D. *J. Catal.* **1994**, *150*, 221.
(193) Gottlieb, H. E.; Luz, Z. *J. Magn. Reson.* **1983**, *54*, 257.
(194) Xu, T.; Munson, E. J.; Haw, J. F. *J. Am. Chem. Soc.* **1994**, *116*, 1962.
(195) Xu, T.; Torres, P. D.; Beck, L. W.; Haw, J. F. *J. Am. Chem. Soc.* **1995**, *117*, 8027.
(196) Tao, T.; Maciel, G. E. *J. Am. Chem. Soc.* **1995**, *117*, 12889.
(197) Munson, E.; Haw, J. F. *J. Am. Chem. Soc.* **1991**, *113*, 6030.
(198) Pan, V. Ph.D. Thesis, Colorado State University, 1996.
(199) Bernstein, T.; Michel, D.; Pfeifer, H.; Fink, P. *J. Colloid Interface Sci.* **1981**, *84*, 310.
(200) Slotfeldt-Ellingsen, D.; Bibow, B.; Pederson, B. Carbon-13 NMR investigation of acetone adsorbed on silica gel. In *Magnetic Resonance and Colloid and Interface Science*; NATO Adv. Study Inst. Ser., Ser. C, no. 61; Kluwer: Dordrecht; pp 571−576.
(201) Borovkov, V. Y.; Zaiko, A. V.; Kazansky, V. B.; Hall, W. K. *J. Catal.* **1982**, *75*, 219.
(202) Gay, I. D. *J. Phys. Chem.* **1974**, *78*, 38.
(203) Sindorf, D. W.; Maciel, G. E. *J. Am. Chem. Soc.* **1983**, *105*, 1487.
(204) Liu, C. C.; Maciel, G. E. *J. Am. Chem. Soc.* **1996**, *118*, 5103.
(205) Shatlock, M.; Maciel, G. E. *J. Chem. Phys.* **1984**, *81*, 895.
(206) Walter, T. H.; Turner, G. L.; Oldfield, E. *J. Magn. Reson.* **1988**, *76*, 106.
(207) Chuang, I.-S.; Kinney, D. R.; Bronnimann, C. E.; Zeigler, R. C.; Maciel, G. E. *J. Phys. Chem.* **1992**, *96*, 4027.
(208) Bronnimann, C. E.; Zeigler, R. C.; Maciel, G. E. *J. Am. Chem. Soc.* **1988**, *110*, 2023.
(209) Kinney, D. R.; Chuang, I.-S.; Maciel, G. E. *J. Am. Chem. Soc.* **1993**, *115*, 6786.
(210) Chuang, I.-S.; Kinney, D. R.; Maciel, G. E. *J. Am. Chem. Soc.* **1993**, *115*, 8695.
(211) Chuang, I.-S.; Maciel, G. E. *J. Phys. Chem.* **1997**, *101*, 3052.
(212) Chuang, I.-S.; Maciel, G. E. *J. Am. Chem. Soc.* **1996**, *118*, 401.
(213) Morris, H. D.; Ellis, P. D. *J. Am. Chem. Soc.* **1989**, *111*, 6045.
(214) Huggins, B. A.; Ellis, P. D. *J. Am. Chem. Soc.* **1992**, *114*, 2098.
(215) Coster, D.; Blumenfeld, A. L.; Fripiat, J. J. *J. Phys. Chem.* **1994**, *98*, 6201.
(216) Walter, T. H.; Oldfield, E. *J. Phys. Chem.* **1989**, *93*, 6744.
(217) Ripmeester, J. A. *J. Am. Chem. Soc.* **1983**, *105*, 2295.
(218) Haw, J. F.; Chuang, I.-S.; Hawkins, B. L.; Maciel, G. E. *J. Am. Chem. Soc.* **1983**, *105*, 7206.
(219) Baltusis, L.; Frye, J. S.; Maciel, G. E. *J. Am. Chem. Soc.* **1987**, *109*, 40.
(220) Hsi, C. K. D.; Langmuir, D. *Geochim. Cosmochim. Acta* **1985**, *49*, 1931.
(221) Langmuir, D. *Aqueous Environmental Geochemistry*; Prentice Hall: New Jersey, 1997.
(222) Stumm, W.; Morgan, J. J. *Aquatic Chemistry*, 2nd ed.; John Wiley and Sons: New York, 1996.
(223) Connors, K. A. *Binding Constants. The Measurement of Molecular Complex Stability*; John Wiley and Sons: New York, 1987.
(224) Baes, C. F.; Mesmer, R. E. *The Hydrolysis of Cations*; John Wiley and Sons: New York, 1976.
(225) Ohtaki, H.; Radnai, T. *Chem. Rev.* **1993**, *93*, 1157.
(226) Martell, A. E.; Motekaitis, R. J. *Determination and Use of Stability Constants*, 2nd ed.; VCH Publishers: New York, 1992.
(227) Ciavatta, L. *Ann. Chim. (Rome)* **1990**, *80*, 255.
(228) Grenthe, I.; Fuger, J.; Konigs, R. J. M.; Lemire, R. J.; Muller, A. B.; Nguyen-Trung, C.; Wanner, H. *Chemical Thermodynamics of Uranium*; Elsevier Science Publishing Co., Inc.: New York, 1992.
(229) Basolo, F.; Pearson, R. G. *Mechanisms of Inorganic Reactions. A Study of Metal Complexes in Solution*, 2nd ed.; John Wiley and Sons: New York, 1967.
(230) Morel, F. M. M.; Hering, J. G. *Principles and Applications of Aquatic Chemistry*; John Wiley and Sons: New York, 1993.
(231) Margerum, D. W.; Cayley, G. R.; Weatherburn, D. C.; Pagenkopf, G. K. In *Coordination Chemistry, Volume 2*; Martell, A. E., Ed.; ACS Monograph 174; American Chemical Society: Washington, DC, 1978.
(232) Richens, D. T.; Helm, L.; Pittet, P.-A.; Merbach, A. E.; Nicolo, F.; Chapuis, G. *Inorg. Chem.* **1989**, *28*, 1394.
(233) Crimp, S. J.; Spiccia, L.; Krouse, H. R.; Swaddle, T. W. *Inorg. Chem.* **1994**, *33*, 465.
(234) Wilkins, R. G. *Kinetics and Mechanism of Reactions of Transition Metal Complexes*, 2nd ed.; VCH Publishers: New York, 1991.
(235) Phillips, B. L.; Casey, W. H.; Neugebauer-Crawford, S. *Geochim. Cosmochim. Acta* **1997**, *61*, 3041.
(236) Felmy, A. R.; Rai, D.; Fulton, R. W. *Radiochim. Acta* **1990**, *50*, 193.
(237) Itagaki, H.; Nakayama, S.; Tanaka, S.; Yamawaki, M. *Radiochim. Acta* **1992**, *58/59*, 61.
(238) Neck, V.; Kim, J. I.; Kanellakopulos, B. *Radiochim. Acta* **1992**, *56*, 25.
(239) Rai, D.; Ryan, J. L. *Inorg. Chem.* **1985**, *24*, 247.
(240) Wood, S. A.; Tait, C. D.; Vlassopoulos, D.; Janecky, D. R. *Geochim. Cosmochim. Acta* **1994**, *58*, 625.
(241) Giordano, T. H.; Drummond, S. E. *Geochim. Cosmochim. Acta* **1991**, *55*, 2401.
(242) Grenthe, I.; Lagerman, B. *Radiochim. Acta* **1993**, *61*, 169.
(243) Wesolowski, D. J.; Palmer, D. A. Water-Rock Interactions. *Proc. Seventh Int. Symp., Chem. Div.*; Oak Ridge Natl. Lab.: Oak Ridge, TN, 1992; p 185.
(244) Hofslagare, O.; Sjoeberg, S.; Samuelsson, G. *Chem. Speciation Bioavail.* **1994**, *6*, 95.

(245) Lis, S.; Choppin, G. R. *Conf. Coord. Chem.* **1995**, *15*, 185.
(246) Palmer, D. A.; Nguyen-Trung, C. *J. Solution Chem.* **1995**, *24*, 1281.
(247) Ciavatta, L.; Iuliano, M. *Ann. Chim. (Rome)* **1996**, *86*, 1.
(248) Shenker, M.; Hadar, Y.; Chen, Y. *Soil Sci. Soc. Am. J.* **1996**, *60*, 1140.
(249) Breault, R. F.; Colman, J. A.; Aiken, G. R.; McKnight, D. *Environ. Sci. Technol.* **1996**, *30*, 3477.
(250) Lu, W.; Smith, E. H. *Geochim. Cosmochim. Acta* **1996**, *60*, 3363.
(251) Turner, G. D.; Zachara, J. M.; McKinley, J. P.; Smith, S. C. *Geochim. Cosmochim. Acta* **1996**, *60*, 3399.
(252) Brendler, V.; Geipel, G.; Bernhard, G.; Nitsche, H. *Radiochim. Acta* **1996**, *74*, 75.
(253) Morris, D. E.; Chisholm-Brause, C. J.; Barr, M. E.; Conradson, S. D.; Eller, P. G. *Geochim. Cosmochim. Acta* **1994**, *58*, 3613.
(254) Clark, D. L.; Conradson, S. D.; Ekberg, S. A.; Hess, N. J.; Janecky, D. R.; Neu, M. P.; Palmer, P. D.; Tait, C. D. *New J. Chem.* **1996**, *20*, 211.
(255) Hauser, W.; Goetz, R.; Klenze, R.; Kim, J. I. *Proc. SPIE-Int. Soc. Opt. Eng.* **1996**, *2778*, 598.
(256) Richmann, M. K.; Reed, D. T. *Mater. Res. Soc. Symp. Proc.* **1996**, *412*, 623.
(257) Wood, S. A.; Tait, C. D.; Janecky, D. R.; Constantopoulos, T. L. *Geochim. Cosmochim. Acta* **1995**, *59*, 5219.
(258) Berg, J. M.; Tait, C. D.; Morris, D. E.; Woodruff, W. H. *Mater. Res. Soc. Symp. Proc.* **1991**, *212*, 531.
(259) Kim, J. I.; Stumpe, R.; Klenze, R. *Top. Curr. Chem.* **1990**, *157*, 129.
(260) Beitz, J. V.; Bowers, D. L.; Doxtader, M. M.; Maroni, V. A.; Reed, D. T. *Radiochim. Acta* **1988**, *44*−*45*, 87.
(261) Nakayama, S.; Kimura, T. *J. Nucl. Sci. Technol.* **1991**, *28*, 780.
(262) Okajima, S.; Reed, D. T.; Mazer, J. J.; Sabau, C. A. *Mater. Res. Soc. Symp. Proc.* **1990**, *176*, 583.
(263) Geipel, G.; Brachmann, A.; Brendler, V.; Bernhard, G.; Nitsche, H. *Radiochim. Acta* **1996**, *75*, 199.
(264) Moulin, C.; Decambox, P.; Mauchien, P.; Pouyat, D.; Couston, L. *Anal. Chem.* **1996**, *68*, 3204.
(265) Brendler, V.; Geipel, G.; Brachmann, A. *Determination of stability constants for aqueous uranyl phosphate complexes at low ionic strengths with time-resolved laser-induced fluorescence spectroscopy (TRLFS) and potentiometry*; Inst. Radiochem., Forschungszent. Rossedorf e.V.: Dresden, Germany, 1996.
(266) Beitz, J. V. In *Separations of f Elements [Proc. Am. Chem. Soc. Symp.]*; Nash, K. L., Ed.; Plenum: New York, 1995.
(267) Moulin, V. M.; Moulin, C. M.; Dran, J. C. *Book of Abstracts*; 210th ACS National Meeting, Chicago, IL, Aug 20−24, 1995; Section Geochemistry, DCC, Fontenay-aux-Roses, France, p I&EC-005.
(268) Moulin, C.; Decambox, P.; Moulin, V.; Decaillon, J. G. *Anal. Chem.* **1995**, *67*, 348.
(269) Moulin, C.; Briand, A.; Decambox, P.; Fleurot, B.; Lacour, J. L.; Mauchien, P.; Remy, B. *Radioprotection* **1994**, *29*, 517.
(270) Kim, J. I.; Rhee, D. S.; Wimmer, H.; Buckau, G.; Klenze, R. *Radiochim. Acta* **1993**, *62*, 35.
(271) Bidoglio, G.; Gibson, P. N.; Haltier, E.; Omenetto, N.; Lipponen, M. *Radiochim. Acta* **1992**, *58*−*59*, 191.
(272) Kumpulainen, H. *Actinide Speciation by Laser Spectroscopic Methods*; VTT Chem. Technol.: Finland, 1995.
(273) Wimmer, H.; Kim, J. I.; Klenze, R. *Radiochim. Acta* **1992**, *58*−*59*, 165.
(274) Fritzsche, M.; Elvingson, K.; Rehder, D.; Pettersson, L. *Acta Chem. Scand.* **1997**, *51*, 483.
(275) Fraval, S.; Bottero, J. Y.; Stone, W. E. E.; Broekaert, P.; Masin, F.; Pirotte, P.; Mosnier, F. *Langmuir* **1997**, *13*, 2550.
(276) Heath, S. L.; Jordan, P. A.; Johnson, I. D.; Moore, G. R.; Powell, A. K.; Helliwell, M. *J. Inorg. Biochem.* **1995**, *59*, 785.
(277) Faust, B. C.; Labiosa, W. B.; Dai, K. H.; MacFall, J. S.; Browne, B. A.; Ribeiro, A. A.; Richter, D. D. *Geochim. Cosmochim. Acta* **1995**, *59*, 2651.
(278) Harris, W. R.; Berthon, G.; Day, J. P.; Exley, C.; Flaten, T. P.; Forbes, W. F.; Kiss, T.; Orvig, C.; Zatta, P. F. *J. Toxicol. Environ. Health* **1996**, *48*, 543.
(279) Elvingson, K.; Fritzache, M.; Rehder, D.; Pettersson, L. *Acta Chem. Scand.* **1994**, *48*, 878.
(280) Jordan, P. A.; Clayden, N. J.; Heath, S. L.; Moore, G. R.; Powell, A. K.; Tapparo, A. *Coord. Chem. Rev.* **1996**, *149*, 281.
(281) Kobayashi, A.; Yagasaki, A. *Inorg. Chem.* **1997**, *36*, 126.
(282) Tokunaga, T. K.; Pickering, I. J.; Brown, G. E., Jr. *Soil Sci. Soc. Am. J.* **1996**, *60*, 781.
(283) Lytle, C. M.; Lytle, F. W.; Smith, B. N. *J. Environ. Qual.* **1996**, *25*, 311.
(284) Frank, P.; Kustin, K.; Robinson, W. E.; Linebaugh, L.; Hodgson, K. O. *Inorg. Chem.* **1995**, *34*, 5942.
(285) Pickering, I. J.; Brown, G. E., Jr.; Tokunaga, T. K. *Environ. Sci. Technol.* **1995**, *29*, 2456.
(286) Nitsche, H. *J. Alloys Compd.* **1995**, *223*, 274.
(287) Bertsch, P. M.; Hunter, D. B.; Sutton, S. R.; Bajt, S.; Rivers, M. L. *Environ. Sci. Technol.* **1994**, *28*, 980.
(288) Farges, F.; Sharps, J. A.; Brown, G. E., Jr. *Geochim. Cosmochim. Acta* **1993**, *57*, 1243.
(289) Smith, R. M.; Martell, A. E. *Critical Stability Constants*; Plenum: New York, 1989.
(290) Smith, R. M.; Martell, A. E. *Critical Stability Constants*; Plenum: New York, 1982.
(291) Smith, R. M.; Martell, A. E. *Critical Stability Constants*; Plenum: New York, 1977.
(292) Smith, R. M.; Martell, A. E. *Critical Stability Constants*; Plenum: New York, 1976.
(293) Smith, R. M.; Martell, A. E. *Critical Stability Constants*; Plenum: New York, 1975.
(294) Smith, R. M.; Martell, A. E. *Critical Stability Constants*; Plenum: New York, 1974.
(295) Sivla, R. J.; Bidoglio, G.; Rand, M. H.; Robouch, P. B.; Wanner, H.; Puigdomenech, I. *Chemical Thermodynamics of Americium*; Elsevier: New York, 1995.
(296) Allison, J. D.; Brown, D. S.; Novo-Gradac, K. J. *MINTEQA2/PRODEFA2, a Geochemical Assessment Model for Environmental Systems: version 3.0 Users Manual*; Environmental Research Laboratory, Office of Research and Development, U.S. Environmental Protection Agency: Washington, DC, 1991.
(297) Helgeson, H. C.; Delany, J. M.; Nesbitt, H. W.; Bird, D. K. *Am. J. Sci.* **1978**, *278A*, 1.
(298) McHale, J. M.; Auroux, A.; Perrotta, A. J.; Navrotsky, A. *Science* **1997**, *277*, 788.
(299) Gratz, A. J.; Manne, S.; Hansma, P. K. *Science* **1991**, *251*, 1343.
(300) Sunagawa, I. In *Morphology of Crystals*; Sunagawa, I., Ed.; Terra Scientific Publishing Co., 1987.
(301) Burton, W. K.; Cabrera, N.; Frank, F. C. *Philos. Trans. R. Soc. London Ser. A* **1951**, *243*, 40.
(302) Davey, R. J. *J. Cryst. Growth* **1976**, *34*, 109.
(303) Biber, M. V.; Dos Santos Afonso, M.; Stumm, W. *Geochim. Cosmochim. Acta* **1994**, *58*, 1999.
(304) Stumm, W. *Colloids Surf.* **1997**, *120*, 143.
(305) De Yoreo, J. J.; Land, T. A.; Dair, B. *Phys. Rev. Lett.* **1994**, *73*, 838.
(306) Frank, F. C. *Acta Crystallogr.* **1951**, *4*, 497.
(307) Gilmer, G. H. *J. Cryst. Growth* **1977**, *42*, 3.
(308) Blum, A. E.; Lasaga, A. C. In *Aquatic Surface Chemistry*; Stumm, W., Ed.; John Wiley and Sons: New York, 1987.
(309) Murr, L. W.; Hiskey, J. B. *Metall. Trans.* **1981**, *12B*, 255.
(310) Casey, W. H.; Carr, M. J.; Graham, R. A. *Geochim. Cosmochim. Acta* **1988**, *52*, 1545.
(311) Brantley, S. L.; Crane, S. R.; Crerar, D. A.; Hellmann, R.; Stallard, R. *Geochim. Cosmochim. Acta* **1986**, *50*, 2349.
(312) Lussiez, P.; Osseo-Asare, K.; Simkovich, G. *Metall. Trans. B* **1981**, *23*, 651.
(313) Jones, C. F.; Segall, R. L.; Smart, R. S. C.; Turner, P. S. *J. Chem. Soc., Faraday Trans. 1* **1977**, *73*, 1710.
(314) Pease, W. R.; Segall, R. L.; Smart, R. S. C.; Turner, P. S. *J. Chem. Soc., Faraday Trans. 1* **1986**, *82*, 759.
(315) Blesa, M. A.; Morando, P. J.; Regazzoni, A. E. *Chemical Dissolution of Metal Oxides*; CRC Press: Boca Raton, FL, 1994.
(316) Parks, G. A. *J. Geophys. Res.* **1984**, *89*, 3997.
(317) Parks, G. A. In *Mineral−Water Interface Geochemistry*; Hochella, M. F., Jr., White, A. F., Eds.; Mineralogical Society of America: Washington, DC, 1990; Vol. 23.
(318) Gruber, E. E.; Mullins, W. W. *J. Phys. Chem. Solids* **1967**, *28*, 875.
(319) Kandel, D.; Weeks, J. D. *Phys. Rev. Lett.* **1995**, *74*, 3632.
(320) Frenkel, J. *J. Phys. USSR* **1945**, *9*, 392.
(321) Bosbach, D.; Rammensee, W. *Geochim. Cosmochim. Acta* **1994**, *58*, 843.
(322) Adamson, A. W. *Physical Chemistry of Surfaces*; John Wiley and Sons: New York, 1982.
(323) Hering, J.; Stumm, W. *Langmuir* **1991**, *7*, 1567.
(324) Feidenhans'l, R. *Surf. Sci. Rep.* **1989**, *10*, 105.
(325) Vleig, E.; Robinson, I. K. In *Synchrotron Radiation Crystallography*; Coppens, P., Ed.; Academic Press: New York, 1992.
(326) You, H.; Nagy, Z. *Curr. Top. Electrochem.* **1993**, *2*, 21.
(327) Toney, M. F.; Melroy, O. R. In *Electrochemical Interfaces: Modern Techniques for In Situ Characterization*; Abruna, H., Ed.; VCH Verlag Chemical: Berlin, 1991.
(328) Toney, M. F.; Ocko, B. M. *Synch. Rad. News* **1993**, *6*, 22.
(329) *Synchrotron Radiation Crystallography*; Coppens, P., Ed.; Academic Press: New York, 1992.
(330) Toney, M. F.; Howard, J. N.; Richer, J.; Borges, G. L.; Gordon, J. G.; Melroy, O. R.; Wiesler, D. G.; Yee, D.; Sorensen, L. B. *Nature* **1994**, *368*, 444.
(331) Toney, M. F.; Howard, J. N.; Richer, J.; Borges, G. L.; Gordon, J. G.; Melroy, O. R.; Wiesler, D. G.; Yee, D.; Sorensen, L. B. *Surf. Sci.* **1995**, *335*, 326.
(332) Robinson, I. K.; Whiteaker, K. L.; Walko, D. A. *Physica B* **1996**, *221*, 70.
(333) Renaud, G.; Fuoss, P. H.; Ourmazd, A.; Bevk, J.; Freer, B. S.; Hahn, P. O. *Appl. Phys. Lett.* **1991**, *58*, 1044.
(334) Brown, G. E., Jr.; Parks, G. A.; O'Day, P. A. In *Mineral Surfaces*; Vaughan, D. J., Pattrick, R. A. D., Eds.; Chapman and Hall: London, 1995.
(335) Chen, J. G. *Surf. Sci. Rep.* **1997**, *30*, 1.

(336) Zabinsky, S. I.; Rehr, J. J.; Ankudinov, A.; Albers, R. C.; Eller, M. J. *Phys. Rev. B* **1995**, *52*, 2995.

(337) Ankudinov, A. L.; Ravel, B.; Rehr, J. J.; Conradson, S. D. *Phys. Rev. B* **1998**, *58*, 7565.

(338) Farges, F.; Brown, G. E., Jr.; Rehr, J. J. *Geochim. Cosmochim. Acta* **1996**, *60*, 3023.

(339) Farges, F.; Brown, G. E., Jr.; Navrotsky, A.; Gan, H.; Rehr, J. J. *Geochim. Cosmochim. Acta* **1996**, *60*, 3039.

(340) Farges, F.; Brown, G. E., Jr.; Rehr, J. J. *Phys. Rev. B* **1997**, *56*, 1809.

(341) O'Day, P. A.; Rehr, J. J.; Zabinsky, S. I.; Brown, G. E., Jr. *J. Am. Chem. Soc.* **1994**, *116*, 2938.

(342) Heald, S. M.; Keller, E.; Stern, E. A. *Phys. Rev. Lett.* **1984**, *103A*, 155.

(343) Lytle, F. W.; Sandstrom, D. R.; Marques, E. C.; Wong, J.; Spiro, C. L.; Huffman, G. P.; Huggins, F. E. *Nucl. Instr. Methods* **1984**, *226*, 542.

(344) Waychunas, G. A.; Brown, G. E., Jr. *Adv. X-Ray Anal.* **1994**, *37*, 607.

(345) Heald, S. M.; Chen, H.; Tranquada, J. M. *Phys. Rev. B* **1988**, *38*, 1016.

(346) Bargar, J. R.; Towle, S. N.; Brown, G. E., Jr.; Parks, G. A. *J. Colloid Interface Sci.* **1997**, *85*, 473.

(347) Bargar, J. R.; Brown, G. E., Jr.; Parks, G. A. *Geochim. Cosmochim. Acta* **1997**, *61*, 2639.

(348) Andersen, S. K.; Golovchenko, J. A.; Mair, G. *Phys. Rev. Lett.* **1976**, *37*, 1141.

(349) Cowan, P. L.; Golovchenko, J. A.; Robins, M. F. *Phys. Rev. Lett.* **1980**, *44*, 1680.

(350) Zagenhagen, J.; Patel, J. R.; Freeland, P. E.; Chen, D. M.; Golovchenko, J. A.; Bedrosian, P.; Northrup, J. E. *Phys. Rev. B* **1989**, *39*, 1298.

(351) Golovchenko, J. A.; Patel, J. R.; Kaplan, D. R.; Cowan, P. L.; Bedzyk, M. J. *Phys. Rev. Lett.* **1982**, *49*, 560.

(352) Woodruff, D. P.; Seymour, D. L.; McConville, C. F.; Riley, C. E.; Crapper, M. D.; Prince, N. P.; Jones, R. G. *Surf. Sci.* **1988**, *195*, 237.

(353) Kendelewicz, T.; Woicik, J. C.; Miyano, K. E.; Herrera-Gomez, A.; Cowan, P. L.; Karlin, B. A.; Bouldin, C. E.; Pianetta, P.; Spicer, W. E. *Phys. Rev. B* **1992**, *46*, 7276.

(354) Kendelewicz, T.; Woicik, J. C.; Miyano, K. E.; Cowan, P. L.; Karlin, B. A.; Bouldin, C. E.; Pianetta, P.; Spicer, W. E. *J. Vac. Sci. Technol.* **1991**, *B9*, 2290.

(355) Batterman, B. W.; Cole, H. *Rev. Mod. Phys.* **1964**, *36*, 681.

(356) Batterman, B. W. *Phys. Rev.* **1964**, *133*, A759.

(357) Materlik, G.; Frahm, A.; Bedzyk, M. J. *Phys. Rev. Lett.* **1984**, *52*.

(358) Cheng, L.; Lyman, P. F.; Sturchio, N. C.; Bedzyk, M. J. *Surf. Sci.* **1997**, *382*, L690.

(359) Cheng, L.; Sturchio, N. C.; Woicik, J. C.; Kemner, K. M.; Lyman, P. F.; Bedzyk, M. J. *Surf. Sci. Lett.* **1998**, *415*, L976.

(360) Kendelewicz, T.; Liu, P.; Brown, G. E., Jr.; Nelson, E. J. *Surf. Sci.* **1998**, *411*, 10.

(361) Patel, J. R.; Berreman, D. W.; Sette, F.; Citrin, P. H.; Rowe, J. E.; Cowan, P. L.; Jach, T.; Karlin, B. *Phys. Rev. B* **1989**, *40*, 1330.

(362) Little, L. H. *Infrared Spectra of Adsorbed Species*; Academic Press: New York, 1966.

(363) Hair, M. L. *Infrared Spectroscopy in Surface Chemistry*; Marcel Dekker: New York, 1967.

(364) Pemberton, J. E. In *Electrochemical Interfaces: Modern Techniqus for In Situ Interface Characterization*; Abruna, H. C., Ed.; VCH Publishers: New York, 1991.

(365) Stole, S. M.; Popenoe, D. D.; Porter, M. D. In *Electrochemical Interfaces: Modern Techniques for In Situ Interface Characterization*; Abruna, H. C., Ed.; VCR Publishers: New York, 1991.

(366) Koretsky, C. M.; Sverjensky, D. A.; Salisbury, J. W.; D'Aria, D. M. *Geochim. Cosmochim. Acta* **1997**, *61*, 2193.

(367) Russell, J. D.; Parfitt, R. L.; Fraser, A. R.; Farmer, V. C. *Nature* **1974**, *248*, 220.

(368) Harrick, N. J. *Internal Reflection Spectroscopy*; John Wiley and Sons: New York, 1967.

(369) Harrick, N. J. *Internal Reflection Spectroscopy − Review and Supplement*; Harrick Scientific Co.: Ossining, NY, 1985.

(370) Mirabella, F. M., Jr. *Appl. Spectrosc. Rev.* **1985**, *21*, 45.

(371) Tejedor-Tejedor, M.; Anderson, M. A. *Langmuir* **1986**, *2*, 203.

(372) Sperline, R. P.; Muralidharan, S.; Freiser, H. *Langmuir* **1987**, *3*, 198.

(373) Hug, S. J.; Sulzberger, B. *Langmuir* **1994**, *10*, 3587.

(374) Hagfeldt, A.; Grätzel, M. *Chem. Rev.* **1995**, *95*, 49.

(375) Tachibana, Y.; Moser, J. E.; Grätzel, M.; Klug, D. R.; Durrant, J. R. *J. Phys. Chem.* **1996**, *100*, 20056.

(376) Guyot-Sionnest, P.; Chen, W.; Shen, Y. R. *Phys. Rev. B* **1986**, *33*, 8254.

(377) Shen, Y. R. *Nature* **1989**, *337*, 519.

(378) Corn, R. M.; Higgins, D. N. *Chem. Rev.* **1994**, *94*, 107.

(379) Higgins, D. A. Ph.D. Thesis, University of Wisconsin, 1993.

(380) Higgins, D. A.; Abrams, M. B.; Byerly, S. B.; Corn, R. M. *Langmuir* **1992**, *8,* 1994.

(381) Russell, T. P. *Mater. Sci. Rep.* **1990**, *5*, 171.

(382) Davis, J. A.; James, R. O.; Leckie, J. O. *J. Colloid Interface Sci.* **1978**, *63*, 480.

(383) Sposito, G. In *Mineral−Water Interface Geochemistry*; Hochella, M. F., Jr., White, A. F., Eds.; Mineralogical Society of America: Washington, DC, 1990; Vol. 23.

(384) Haworth, A. *Adv. Colloid Interface Sci.* **1990**, *32*, 43.

(385) Westall, J. C.; Hohl, H. *Adv. Colloid Interface Sci.* **1980**, *12*, 265.

(386) Adamson, A. W.; Gast, A. P. *Physical Chemistry of Surfaces*, 6th ed.; New York, 1997.

(387) Israelachvili, J. N. *Intermolecular and Surface Forces*, 2nd ed.; Academic Press: New York, 1992.

(388) Bockris, J. O. M.; Conway, B. E.; Yeager, E. *Comprehensive Treatise of Electrochemistry*; Plenum Press: New York, 1980.

(389) Lee, C. Y.; McCammon, J. A.; Rossky, R. J. *J. Chem. Phys.* **1984**, *80*, 4448.

(390) Patey, G. N.; Torrie, G. M. *Chem. Scr.* **1989**, *29A*, 39.

(391) Schmickler, W.; Henderson, D. *Prog. Surf. Sci.* **1986**, *22*, 323.

(392) Price, D.; Halley, J. W. *Phys. Rev. B* **1988**, *38*, 9357.

(393) Gosli, J. N.; Philpott, M. R. *J. Chem. Phys.* **1992**, *96*, 6962.

(394) Spohr, E. *J. Chem. Phys* **1989**, *93*, 6171.

(395) Raghavan, K.; Foster, K.; Berkowitz, M. *Chem. Phys. Lett.* **1991**, *177*, 426.

(396) Nagy, G.; Heinzinger, K. *J. Electroanal. Chem.* **1992**, *327*, 25.

(397) Aloisi, G.; Foresti, M. L.; Guidelli, R.; Barnes, P. *J. Chem. Phys.* **1989**, *91*, 5592.

(398) Philpott, M. R.; Glosli, J. N.; Zhu, S.-B. *Surf. Sci.* **1995**, *335*, 422.

(399) Thiel, P. A.; Madey, T. E. *Surf. Sci. Rep.* **1987**, *7*, 221.

(400) Butt, H.-J. *Biophys. J.* **1991**, *60*, 1438.

(401) Ducker, W. A.; Senden, T. J.; Pashley, R. M. *Nature* **1991**, *353*, 239.

(402) Ducker, W. A.; Senden, T. J.; Pashley, R. M. *Langmuir* **1992**, *8*, 1831.

(403) Hillier, A. C.; Kim, S.; Bard, A. J. *J. Phys. Chem.* **1996**, *100*, 18808.

(404) Eggleston, C. M.; Jordan, G. *Geochim. Cosmochim. Acta* **1998**, *62*, 1919.

(405) Fokkink, L. G. J.; de Keizer, A.; Lyklema, J. *J. Colloid Interface Sci.* **1987**, *127*, 116.

(406) Marti, A.; Hahner, G.; Spencer, N. D. *Langmuir* **1995**, *11*, 4632.

(407) Ong, S.; Zhao, X.; Eisenthal, K. B. *Chem. Phys. Lett.* **1992**, *191*, 327.

(408) Du, Q.; Freysz, E.; Shen, Y. R. *Phys. Rev. Lett.* **1994**, *72*, 238.

(409) Eisenthal, K. B. *Chem. Rev.* **1996**, *96*, 1343.

(410) Bedzyk, M. J.; Bommarito, G. M.; Caffrey, M.; Penner, T. L. *Science* **1990**, *248*, 52.

(411) Abruna, H. D.; Bommarito, G. M.; Acevedo, D. *Science* **1990**, *250*, 69.

(412) Trainor, T.; Fitts, J. P.; Brown, G. E., Jr. Unpublished data.

(413) Pashley, R. M.; Israelachvili, J. N. *J. Colloid Interface Sci.* **1984**, *101*, 511.

(414) McGuggan, P. M.; Israelachvili, J. N. *J. Phys. Chem.* **1988**, *92*, 1235.

(415) Israelachvili, J. N.; Pashley, R. M. *Nature* **1983**, *306*, 249.

(416) Porter, J. D.; Zinn, A. S. *J. Chem. Phys.* **1993**, *97*, 1190.

(417) Zettlemoyer, Z. C.; Micale, F. J.; Klier, K. In *Water: A Comprehensive Treatise*; Franks, F., Ed.; Plenum: New York, 1975; Vol. 5.

(418) McCafferty, E.; Pravdic, V.; Zettlemoyer, Z. C. *Trans. Faraday Soc.* **1970**, *66*, 1720.

(419) Durkhin, S. S. In *Surface and Colloid Science*; Matijevic, E., Ed.; American Chemical Society: Washington, DC, 1971; Vol. 3.

(420) Texter, J.; Klier, K.; Zettlemoyer, A. C. In *Progress in Membrane and Surface Science*; Cadenhead, D. A., Danielli, J. F., Eds., 1978; Vol. 12.

(421) Conway, B. E. *Ionic Hydration in Chemistry and Biophysics*; Elsevier: New York, 1981.

(422) Davies, C. W. *Ion Association*; Butterworth: London, 1962.

(423) Fenter, P.; Geissbühler, P.; DiMasi, E.; Srajer, G.; Sorensen, L.; Sturchio, N. Unpublished data.

(424) de Leeuw, N. H.; Parker, S. C.; Rao, K. *Langmuir* **1998**, *14*, 5900.

(425) Bockris, J. O. M.; Reddy, A. K. N. *Modern Electrochemistry*; Plenum Press: New York, 1970.

(426) Porter, J. D.; Zinn-Warner, A. S. *Phys. Rev. Lett.* **1994**, *73*, 2279.

(427) Johnsson, P. A.; Eggleston, C. M.; Hochella, M. F., Jr. *Am. Mineral.* **1991**, *76*, 1442.

(428) Maurice, P. A.; Hochella, M. F., Jr.; Parks, G. A.; Sposito, G.; Schwertmann, U. *Clays Clay Minerals* **1995**, *43*, 29.

(429) Schindler, P. W. In *Mineral−Water Interface Geochemistry, Reviews in Mineralogy*; Hochella, M. F., Jr., White, A. F., Eds.; Mineralogical Society of America: Washington, DC, 1990; Vol. 23.

(430) Benjamin, M. M.; Leckie, J. O. *Environ. Sci. Technol.* **1981**, *15*, 1050.

(431) Woodward, J. T.; Ulman, A.; Schwartz, D. K. *Langmuir* **1996**, *12*, 3626.

(432) Fenter, P.; Sturchio, N. C. *Geochim. Cosmochim. Acta*, submitted.

(433) Chambers, S. A.; Thevuthasan, S.; Kim, Y. J.; Herman, G. S.; Wang, Z.; Tober, E.; Ynzunza, R.; Morais, J.; Peden, C. H. F.; Ferris, K.; Fadley, C. S. *Chem. Phys. Lett.* **1997**, *267*, 51.
(434) Girvin, D. C.; Glassman, P. L. *Soil Sci. Soc. Am. J.* **1993**, *57*, 1.
(435) Zachara, J. M.; Smith, S. C.; Kuzel, L. S. *Geochim. Cosmochim. Acta* **1995**, *59*, 4825.
(436) Davis, J. A. *Geochim. Cosmochim. Acta* **1982**, *46*, 2381.
(437) Zachara, J. M.; Smith, S. C.; Kuzel, L. S. *Geochim. Cosmochim. Acta* **1994**, *58*, 553.
(438) Cheah, S.-F.; Brown, G. E., Jr.; Parks, G. A. In *Aqueous Chemistry and Geochemistry of Oxides, Oxyhydroxides, and Related Matrials*; Voigt, J. A., Bunker, B. C., Casey, W. H., Wood, T. E., Crossey, L. J., Eds.; Materials Research Society: Pittsburgh, PA, 1997; Vol. 432.
(439) Bourg, A. C. M.; Schindler, P. W. *Chimia* **1978**, *32*, 166.
(440) Bourg, A. C. M.; Schindler, P. W. *Inorg. Nucl. Chem. Lett.* **1979**, *15*, 225.
(441) Bourg, A. C. M.; Joss, S.; Schindler, P. W. *Chimia* **1978**, *33*, 19.
(442) Barteau, M. A. *Chem. Rev.* **1996**, *96*, 1413.
(443) Hayes, K. F.; Leckie, J. O. *J. Colloid Interface Sci.* **1987**, *115*, 564.
(444) James, R. O. Ph.D. Thesis, University of Melbourne, 1971.
(445) Kobol, I.; Hesleitner, P.; Matijevic, E. *Colloid Interface* **1988**, *33*, 167.
(446) Chisholm-Brause, C. J. Ph.D. Thesis, Stanford University, 1991.
(447) Parks, G. A. *Chem. Rev.* **1965**, *65*, 177.
(448) Sposito, G. In *Geochemical Processes at Mineral Surfaces*; Davis, J. A., Hayes, K. F., Eds.; American Chemical Society: Washington, DC, 1986; Vol. 323.
(449) Hayes, K. F.; Katz, L. E. In *Chemistry and Physics of Mineral Surfaces*; Brady, P. V., Ed.; CRC Press: Boca Raton, FL, 1996.
(450) Brown, G. E., Jr.; Parks, G. A.; Chisholm-Brause, C. J. *Chimia* **1989**, *43*, 248.
(451) Brown, G. E., Jr.; Parks, G. A. *Rev. Geophys.* **1989**, *27*, 519.
(452) Manceau, A.; Charlet, L.; Boisset, M. C.; Didier, B.; Spadini, L. *Appl. Clay Sci.* **1992**, *7*, 201.
(453) Chisholm-Brause, C. J.; Hayes, K. F.; Roe, A. L.; Brown, G. E., Jr.; Parks, G. A.; Leckie, J. O. *Geochim. Cosmochim. Acta* **1990**, *54*, 1897.
(454) Chisholm-Brause, C. J.; O'Day, P. A.; Brown, G. E., Jr.; Parks, G. A. *Nature* **1990**, *348*, 528.
(455) Chisholm-Brause, C. J.; Conradson, S. D.; Buscher, C. T.; Eller, P. G.; Morris, D. E. *Geochim. Cosmochim. Acta* **1994**, *58*, 3625.
(456) Roe, A. L.; Hayes, K. F.; Chisholm-Brause, C. J.; Brown, G. E., Jr.; Parks, G. A.; Leckie, J. O.; Hodgson, K. O. *Langmuir* **1991**, *7*, 367.
(457) O'Day, P. A.; Brown, G. E., Jr.; Parks, G. A. *J. Colloid Interface Sci.* **1994**, *165*, 269.
(458) O'Day, P. A.; Parks, G. A.; Brown, G. E., Jr. *Clays Clay Minerals* **1994**, *42*, 337.
(459) O'Day, P. A.; Chisholm-Brause, C. J.; Towle, S. N.; Parks, G. A.; Brown, G. E., Jr. *Geochim. Cosmochim. Acta* **1996**, *60*, 2515.
(460) Persson, P.; Parks, G. A.; Brown, G. E., Jr. *Langmuir* **1995**, *11*, 3782.
(461) Peterson, M. L.; Brown, G. E., Jr.; Parks, G. A. *Colloids Surf.* **1996**, *107*, 77.
(462) Towle, S. N.; Bargar, J. R.; Brown, G. E., Jr.; Parks, G. A. *J. Colloid Interface Sci.* **1997**, *187*, 62.
(463) Bargar, J. R.; Towle, S. N.; Brown, G. E., Jr.; Parks, G. A. *Geochim. Cosmochim. Acta* **1996**, *60*, 3541.
(464) Bargar, J. R.; Brown, G. E., Jr.; Parks, G. A. *Geochim. Cosmochim. Acta* **1997**, *61*, 2617.
(465) Charlet, L.; Manceau, A. *J. Colloid Interface Sci.* **1992**, *148*, 443.
(466) Waychunas, G. A.; Rea, B. A.; Fuller, C. C.; Davis, J. A. *Geochim. Cosmochim. Acta* **1993**, *57*, 2251.
(467) Waite, T. D.; David, J. A.; Payne, T. E.; Waychunas, G. A.; Xu, N. *Geochim. Cosmochim. Acta* **1994**, *58*, 5465.
(468) Fendorf, S. E.; Lamble, G. M.; Stapleton, M. G.; Kelley, M. J.; Sparks, D. L. *Environ. Sci. Technol.* **1994**, *28*, 284.
(469) Spadini, L.; Manceau, A.; Schindler, P. W.; Charlet, L. *J. Colloid Interface Sci.* **1994**, *168*, 73.
(470) d'Espinose de la Caillerie, J.-B.; Kermarec, M.; Clause, O. *J. Am. Chem. Soc.* **1995**, *117*, 11471.
(471) Scheidegger, A. M.; Lamble, G. M.; Sparks, D. L. *Environ. Sci. Technol.* **1996**, *30*, 548.
(472) Papelis, C.; Hayes, K. F. *Colloids Surf.* **1996**, *107*, 89.
(473) Chisholm-Brause, C. J.; Brown, G. E., Jr.; Parks, G. A. In *XAFS VI, Sixth International Conference on X-ray Absorption Fine Structure*; Hasnain, S. S., Ed.; Ellis Horwood, Ltd.: London, 1991.
(474) Towle, S. N.; Bargar, J. R.; Brown, G. E., Jr.; Parks, G. A.; Barbee, T. W. In *Structure and Properties of Interfaces in Ceramics*; Bonnell, D. A., Chowdhry, U., Rühle, M., Eds.; Materials Research Society: Pittsburgh, PA, 1995; Vol. 357.
(475) Pauling, L. *The Nature of the Chemical Bond*; Cornell University Press: Cornell, 1960.
(476) Scheidegger, A. M.; Lamble, G. M.; Sparks, D. L. *J. Colloid Interface Sci.* **1997**, *186*, 118.
(477) Towle, S. N.; Bargar, J. R.; Brown, G. E., Jr.; Parks, G. A. *J. Colloid Interface Sci.*, submitted.
(478) Hiemstra, T.; Van Riemsdijk, W. H.; Bolt, G. H. *J. Colloid Interface Sci.* **1989**, *133*, 91.
(479) Hiemstra, T.; Wit, J. C. M. D.; Van Riemsdijk, W. H. *J. Colloid Interface Sci.* **1989**, *133*, 105.
(480) Hiemstra, T.; Van Riemsdijk, W. H. *J. Colloid Interface Sci.* **1996**, *179*, 488.
(481) Brown, I. D.; Shannon, R. D. *Acta Crystallogr.* **1973**, *A29*, 266.
(482) Brown, I. D.; Altermatt, D. *Acta Crystallogr.* **1985**, *B41*, 244.
(483) Ziolkowski, J. *J. Catal.* **1983**, *84*, 317.
(484) Edwards, J. O.; Monacelli, F.; Ortaggi, G. *Inorg. Chim. Acta* **1974**, *11*, 47.
(485) Dyrek, K.; Che, M. *Chem. Rev.* **1997**, *97*, 305.
(486) McBride, M. B. *Clays Clay Minerals* **1976**, *24*, 88.
(487) McBride, M. B. *Soil Sci.* **1978**, *126*, 200.
(488) McBride, M. B. *Soil Sci. Soc. Am. J.* **1979**, *43*, 693.
(489) McBride, M. B. *Soil Sci. Soc. Am. J.* **1980**, *44*, 495.
(490) McBride, M. B. *Clays Clay Minerals* **1982**, *30*, 200.
(491) McBride, M. B.; Fraser, A. R.; McHardy, W. J. *Clays Clay Minerals* **1984**, *32*, 12.
(492) McBride, M. B.; Bouldin, D. R. *Soil Sci. Soc. Am. J.* **1984**, *48*, 56.
(493) McBride, M. B. *Clays Clay Minerals* **1985**, *33*, 397.
(494) McBride, M. B. *J. Colloid Interface Sci.* **1986**, *120*, 419.
(495) McBride, M. B. *Clays Clay Minerals* **1995**, *43*, 383.
(496) Clark, C. J.; McBride, M. B. *Clays Clay Minerals* **1984**, *32*, 300.
(497) Harsh, J. B.; Doner, H. E.; McBride, M. B. *Clays Clay Minerals* **1984**, *32*, 407.
(498) Bleam, W. F.; McBride, M. B. *J. Colloid Interface Sci.* **1985**, *103*, 124.
(499) Bleam, W. F.; McBride, M. B. *J. Colloid Interface Sci.* **1986**, *110*, 335.
(500) Xia, K.; Mehadi, A.; Taylor, R. W.; Bleam, W. F. *J. Colloid Interface Sci.* **1997**, *185*, 252.
(501) Xia, K.; Taylor, R. W.; Bleam, W. F.; Helmke, P. A. *J. Colloid Interface Sci.* **1998**, *199*, 77.
(502) Weesner, F. J.; Bleam, W. F. *J. Colloid Interface Sci.* **1997**, *196*, 79.
(503) Motschi, H. *Natuerwissenschaften* **1983**, *70*, 519.
(504) Rudin, M.; Motschi, H. *J. Colloid Interface Sci.* **1984**, *98*, 385.
(505) Motschi, H. *Colloids Surf.* **1984**, *9*, 333.
(506) Motschi, H. In *Aquatic Surface Chemistry*; Stumm, W., Ed.; Wiley-Interscience: New York, 1987.
(507) Persson, P.; Lovgren, L. *Geochim. Cosmochim. Acta* **1996**, *60*, 2789.
(508) Hug, S. J. *J. Colloid Interface Sci.* **1997**, *188*, 415.
(509) Parfitt, R. L.; Russell, J. D.; Farmer, V. C. *J. Chem. Soc., Faraday Trans. 1* **1976**, *72*, 1082.
(510) Russell, J. D.; Paterson, E.; Fraser, A. R.; Farmer, V. C. *J. Chem. Soc., Faraday Trans.* **1975**, *171*, 1623.
(511) Atkinson, R. J.; Posner, A. M.; Quirk, J. P. *J. Inorg. Nucl. Chem.* **1972**, *34*, 2201.
(512) Atkinson, R. J. Ph.D. Thesis, University of Western Australia, Perth, 1969.
(513) Yates, D. E.; Healy, T. W. *J. Colloid Interface Sci.* **1975**, *52*, 222.
(514) Hingston, F. J.; Posner, A. M.; Quirk, J. P. *J. Soil Sci.* **1974**, *25*, 16.
(515) Persson, P.; Nilsson, N.; Sjöberg, S. *J. Colloid Interface Sci.* **1996**, *177*, 263.
(516) Parfitt, R. L.; Russell, J. D. *J. Soil Sci.* **1977**, *28*, 297.
(517) Eggleston, C. M.; Hug, S.; Stumm, W.; Sulzberger, B.; Dos Santos Afonso, M. *Geochim. Cosmochim. Acta* **1998**, *62*, 585.
(518) Parfitt, R. L.; Smart, R. S. C. *J. Chem. Soc., Faraday Trans. 1* **1977**, *73*, 796.
(519) Parfitt, R. L.; Smart, R. S. C. *Soil Sci. Soc. Am. J.* **1978**, *42*, 48.
(520) Harrison, J. B.; Berkheiser, V. E. *Clays Clay Minerals* **1982**, *30*, 97.
(521) Turner, L. J.; Kramer, J. R. *Soil Sci.* **1991**, *152*, 226.
(522) Biber, M. V.; Stumm, W. *Environ. Sci. Technol.* **1994**, *28*, 763.
(523) Nordin, J.; Persson, P.; Laiti, E.; Sjöberg, S. *Langmuir* **1997**, *13*, 4085.
(524) Persson, P.; Laiti, E.; Ohman, L.-O. *J. Colloid Interface Sci.* **1997**, *190*, 341.
(525) Tejedor-Tejedor, M. I.; Yost, E. C.; Anderson, M. A. *Langmuir* **1990**, *6*, 981.
(526) Tejedor-Tejedor, M. I.; Yost, E. C.; Anderson, M. A. *Langmuir* **1992**, *8*, 525.
(527) Yost, E. C.; Tejedor-Tejedor, M. I.; Anderson, M. A. *Environ. Sci. Technol.* **1990**, *24*, 822.
(528) Bargar, J. R.; Persson, P.; Brown, G. E., Jr. *Geochim. Cosmochim. Acta*, submitted.
(529) Nowack, B.; Sigg, L. *Geochim. Cosmochim. Acta* **1997**, *61*, 951.
(530) Higgins, S. H.; Eggleston, C. M. Unpublished data.
(531) Schwertmann, U.; Taylor, R. M. In *Minerals in Soil Environments*, 2nd ed.; Dixon, J. B., Weed, S. B., Eds.; Soil Science Society of America: Madison, 1989; Vol. 1.
(532) Colombo, C.; Barron, V.; Torrent, J. *Geochim. Cosmochim. Acta* **1994**, *58*, 1261.

(533) Sample, E. C.; Soper, R. J.; Racz, G. J. In *The Role of Phosphorus in Agriculture*; Khasawneh, F. E., Sample, E. C., Kamprath, E. J., Eds.; American Society of Agronomy, Crop Science Society of America, Soil Science Society of America: Madison, WI, 1980.
(534) Borggaard, O. K. *J. Soil Sci.* **1983**, *34*, 333.
(535) Bunker, B. C.; Rieke, P. C.; Tarasevich, B. J.; Campbell, A. A.; Fryxell, G. E.; Graff, G. L.; Song, L.; Liu, J.; Virden, J. W.; McVay, G. L. *Nature* **1994**, *264*, 48.
(536) Alvarez, R.; Fadley, C. S.; Silva, J. A. *Soil Sci. Soc. Am. J.* **1980**, *44*, 422.
(537) Lookman, R.; Grobet, P.; Merckx, R.; Vlassak, K. *Eur. J. Soil Sci.* **1994**, *45*, 37.
(538) Busca, G.; Ramis, G.; Lorenzelli, V.; Rossi, P. F. *Langmuir* **1989**, *5*, 911.
(539) Barrow, N. J. *Adv. Agron.* **1985**, *38*, 183.
(540) Torrent, J. *Aust. J. Soil Res.* **1991**, *29*, 69.
(541) Hingston, F. J.; Atkinson, R. J.; Posner, A. M.; Quirk, J. P. *Nature* **1967**, *215*, 1459.
(542) Martin, R. R.; Smart, R. S. C. *Soil Sci. Soc. Am. J.* **1987**, *51*, 54.
(543) Martin, R. R.; Smart, R. S. C.; Tazaki, K. *Soil Sci. Soc. Am. J.* **1988**, *52*, 1492.
(544) Nooney, M. G.; Campbell, A.; Murrell, T. S.; Lin, X.-F.; Hossner, L. R.; Chusuei, C. C.; Goodman, D. W. *Langmuir* **1998**, *14*, 2750.
(545) Nooney, M. G.; Murrell, T. S.; Corneille, J. S.; Rusert, E. I.; Hossner, L. R.; Goodman, D. W. *J. Vac. Sci. Technol. A* **1996**, *14*, 1359.
(546) Leung, L.-W.; Gregg, T. W.; Goodman, D. W. *Rev. Sci. Instrum.* **1991**, *62*, 1857.
(547) Marcus, R. A. *J. Chem. Phys.* **1965**, *43*, 679.
(548) Cui, D.; Eriksen, T. E. *Environ. Sci. Technol.* **1996**, *30*, 2259.
(549) White, A. F.; Peterson, M. L. *Geochim. Cosmochim. Acta* **1996**, *60*, 3799.
(550) Valverde, N. *Ber. Bunsen-Ges. Phys. Chem.* **1976**, *80*, 333.
(551) Oblonsky, L. J.; Davenport, A. J.; Ryan, M. P.; Isaacs, H. S.; Newman, R. C. *J. Electrochem. Soc.* **1997**, *144*, 2398.
(552) Peterson, M. L.; White, A. F.; Brown, G. E., Jr.; Parks, G. A. *Environ. Sci. Technol.* **1997**, *31*, 1573.
(553) Davies, S. H. R.; Morgan, J. J. *J. Colloid Interface Sci.* **1989**, *129*, 63.
(554) Motschi, H.; Rudin, M. *Colloid Polym. Sci.* **1984**, *262*, 579.
(555) Wehrli, B.; Stumm, W. *Langmuir* **1988**, *4*, 753.
(556) Wehrli, B. In *Aquatic Chemical Kinetics*; Stumm, W., Ed.; Wiley Interscience: New York, 1990.
(557) Tamura, H.; Goto, K.; Nagayama, M. *Corrosion Sci.* **1976**, *26*, 197.
(558) Stone, A. T. *Environ. Sci. Technol.* **1987**, *21*, 979.
(559) Stumm, W.; Sulzberger, B. *Geochim. Cosmochim. Acta* **1992**, *56*, 3233.
(560) Blesa, M. A.; Borghi, E. B.; Maroto, A. J. G.; Regazzoni, A. E. *J. Colloid Interface Sci.* **1984**, *98*, 295.
(561) Borghi, E. B.; Regazzoni, A. E.; Maroto, A. J. G.; Blesa, M. *J. Colloid Interface Sci.* **1988**, *130*, 299.
(562) Waite, T. D.; Morel, F. M. M. *J. Colloid Interface Sci.* **1984**, *102*, 121.
(563) Litter, M. I.; Blesa, M. A. *J. Colloid Interface Sci.* **1988**, *125*, 679.
(564) McKnight, D. M.; Kimball, B. A.; Bancala, K. E. *Science* **1988**, *240*, 637.
(565) Siffert, C. L.; Sulzberger, B. *Langmuir* **1991**, *7*, 1627.
(566) Kendelewicz, T.; Liu, P.; Doyle, C.; Brown, G. E., Jr.; Nelson, E. J.; Chambers, S. A. *Surf. Sci.*, in press.
(567) Cominellis, C. *Electrochim. Acta* **1994**, *39*, 1857.
(568) O'Regan, B.; Grätzel, M. *Nature* **1991**, *335*, 737.
(569) Vlachopoulos, N.; Liska, P.; Augustynski, J.; Grätzel, M. *J. Am. Chem. Soc.* **1988**, *110*, 1216.
(570) Liska, P.; Vlachopoulos, N.; Nazeeruddin, M. K.; Comte, P.; Grätzel, M. *J. Am. Chem. Soc.* **1988**, *110*, 3686.
(571) DeSilvestro, J.; Grätzel, M.; Kavan, L.; Moser, J.; Augustynski, J. *J. Am. Chem. Soc.* **1985**, *107*, 2988.
(572) Amadelli, R.; Argazzi, R.; Bignozzi, C. A.; Scandola, F. *J. Am. Chem. Soc.* **1990**, *112*, 7099.
(573) Heimer, T. A.; Bignozzi, C. A.; Meyer, G. J. *J. Phys. Chem.* **1993**, *97*, 11987.
(574) Argazzi, R.; Bignozzi, C. A.; Heimer, T. A.; Castellano, F. N.; Meyer, G. J. *Inorg. Chem.* **1994**, *33*, 5741.
(575) Bignozzi, C. A.; Argazzi, R.; Schoonover, J. R.; Meyer, G. J.; Scandola, F. *Solar Energy Mater. Sol. Cells* **1995**, *38*, 187.
(576) Murakoshi, K.; Kano, G.; Wada, Y.; Yanagida, S.; Miyazaki, H.; Matsumoto, M.; Murasawa, S. *J. Electroanal. Chem.* **1995**, *396*, 27.
(577) Hagfeldt, A.; Lindquist, S.; Grätzel, M. *Sol. Energy Mater. Sol. Cells* **1994**, *32*, 245.
(578) Hagfeldt, A.; Didriksson, B.; Palmquist, T.; Lindström, H.; Sodergren, S.; Rensmo, H.; Lindquist, S. *Sol. Energy Mater. Sol. Cells* **1994**, *31*, 481.
(579) Knödler, R.; Sopka, J.; Harbach, F.; Grünling, H. W. *Sol. Energy Mater. Sol. Cells* **1993**, *30*, 277.
(580) Smestad, G.; Bignozzi, C. A.; Argazzi, R. *Sol. Energy Mater. Sol. Cells* **1994**, *32*, 273.
(581) *Theory of Photographic Processes*; 4th ed.; James, T. H., Ed.; MacMillan: New York, 1977.
(582) Weigl, J. W. *Angew. Chem., Int. Ed.* **1977**, *16*, 374.
(583) Willig, F. *Top. Curr. Chem.* **1976**, *61*, 31.
(584) Memming, R. In *Photochemistry and Photophysics*; Rabek, J. F., Ed.; CRC Press: Boca Raton, FL, 1992.
(585) Parkinson, B. A.; Spitler, M. T. *Electrochim. Acta* **1992**, *37*, 943.
(586) *Photoinduced Electron Transfer*; Fox, M. A., Channon, M., Eds.; Elsevier: Amsterdam, 1988.
(587) Moser, J.; Punchihewa, S.; Infelta, P. P.; Grätzel, M. *Langmuir* **1991**, *7*, 3012.
(588) Houlding, V.; Grätzel, M. *J. Am. Chem. Soc.* **1983**, *105*, 5695.
(589) Vrachnou, E.; Vlachopoulos, N.; Grätzel, M. *J. Chem. Soc., Chem. Commun.* **1987**, 868.
(590) Frei, H.; Fitzmaurice, D.; Grätzel, M. *Langmuir* **1990**, *6*, 198.
(591) Hagfeldt, A.; Vlachopoulos, N.; Grätzel, M. *J. Electrochem. Soc.* **1994**, *142*, L82.
(592) Mayor, M.; Hagfeldt, A.; Grätzel, M.; Walder, L. *Chimia* **1996**, *50*, 47.
(593) Gerfin, T.; Grätzel, M.; Walder, L. *Prog. Inorg. Chem.* **1996**, *44*, 346.
(594) Grätzel, M. *Heterogeneous Photochemical Electron Transfer*; CRC Press: Boca Raton, FL, 1989.
(595) Hunter, R. J. *Introduction to Modern Colloid Science*; Oxford University Press: Oxford, 1993.
(596) Marcus, R. A. *J. Phys. Chem.* **1990**, *94*, 1050.
(597) Eggleston, C. M.; Ehrhardt, J. J.; Stumm, W. *Am. Mineral.* **1996**, *81*, 1036.
(598) Hipps, K. W.; Lu, X.; Wang, X. D.; Mazur, U. *J. Phys. Chem.* **1996**, *100*, 11207.
(599) Schmickler, W. In *Nanoscale Probes of the Solid/Liquid Interface*; Gewirth, A. A., Siegenthaler, H., Eds.; Kluwer: Boston, 1995.
(600) Luttrull, D. K.; Graham, J.; DeRose, J. A.; Gust, D.; Moore, T. A.; Lindsay, S. M. *Langmuir* **1992**, *8*, 765.
(601) Tao, N. J.; Cardenas, G.; Cunha, F.; Shi, Z. *Langmuir* **1995**, *11*, 4445.
(602) Farley, K. J.; Dzombak, D. A.; Morel, F. M. M. *J. Colloid Interface Sci.* **1985**, *106*, 226.
(603) James, R. O.; Healy, T. W. *J. Colloid Interface Sci.* **1972**, *40*, 65.
(604) Stumm, W.; Furrer, F.; Kunz, B. *Croat. Chem. Acta* **1983**, *56*, 593.
(605) Eary, L.; Rai, D. *Am. J. Sci.* **1989**, *289*, 180.
(606) Peterson, M. L.; Brown, G. E., Jr.; Parks, G. A.; Stein, C. L. *Geochim. Cosmochim. Acta* **1997**, *61*, 3399.
(607) Junta, J. L.; Hochella, M. F., Jr. *Geochim. Cosmochim. Acta* **1994**, *58*, 4985.
(608) Dove, P.; Chermak, J. In *Scanning Probe Microscopy of Clay Minerals*; Nagy, K. L., Blum, A. E., Eds.; 1994.
(609) Wachs, I. E. *Catal. Today* **1996**, *27*, 437.
(610) Gates, B. C. *Catalytic Chemistry*; John Wiley and Sons: New York, 1992.
(611) Wachs, I. E.; Weckhuysen, B. M. *Appl. Catal. A* **1997**, *157*, 67.
(612) Lambert, J.-F.; Che, M. In *Dynamics of Surfaces and Reaction Kinetics in Heterogeneous Catalysis*; Froment, G. F., Waugh, K. C., Eds.; Elsevier Science B.V.: New York, 1997.
(613) Fujishima, A.; Honda, K. *Nature* **1972**, *238*, 37.
(614) Kalyanasundaram, K. *Solar Cells* **1985**, *15*, 93.
(615) Rothenberger, G.; Moser, J.; Grätzel, M.; Serpone, N.; Sharama, D. K. *J. Am. Chem. Soc.* **1985**, *107*, 8054.
(616) Hoffmann, M. R.; Martin, S. T.; Choi, W.; Bahenemann, D. W. *Chem. Rev.* **1995**, *95*, 69.
(617) Bandara, J.; Kiwi, J.; Pulgarin, C.; Peringer, P.; Pajonk, G.-M.; Elaloui, A.; Albers, P. *Environ. Sci. Technol.* **1996**, *30*, 1261.
(618) Sulzberger, B.; Laubscher, H.; Karametaxas, G. In *Aquatic and Surface Chemistry*; Helz, G. R., Zepp, R. G., Crosby, D. G., Eds.; Lewis: Boca Raton, FL, 1994.
(619) Foster, N. S.; Lancaster, A. N.; Noble, R. D.; Koval, C. A. *Ind. Eng. Chem. Res.* **1995**, *34*, 3865.
(620) Rajh, T.; Ostafin, A. E.; Micic, O. I.; Tiede, D. M.; Thurnauer, M. C. *J. Phys. Chem. B* **1996**, *100*, 4538.
(621) Chen, L. X.; Rajh, T.; Wang, Z.; Thurnauer, M. C. *J. Phys. Chem. B* **1997**, *101*, 10688.
(622) Foster, A. L.; Brown, G. E., Jr.; Parks, G. A. *Environ. Sci. Technol.* **1998**, *32*, 1444.
(623) Furrer, G.; Stumm, W. *Geochim. Cosmochim. Acta* **1986**, *50*, 1847.
(624) Casey, W. H.; Westrich, H. R. *Nature* **1992**, *355*, 157.
(625) Hachiya, K.; Sasaki, M.; Ikeda, T.; Mikami, N.; Yasunaga, T. *J. Phys. Chem.* **1984**, *88*, 27.
(626) Ludwig, C.; Casey, W. H.; Rock, P. A. *Nature* **1995**, *375*, 44.
(627) Ludwig, C.; Devidal, J.-L.; Casey, W. H. *Geochim. Cosmochim. Acta* **1996**, *60*, 213.
(628) Springborg, J. *Adv. Inorg. Chem.* **1988**, *32*, 55.
(629) *Geomicrobiology: Interactions between Microbes and Minerals*; Banfield, J. F., Nealson, K. H., Eds.; Mineralogical Society of America: Washington, DC, 1997; Vol. 35.

(630) Characklis, W. G.; Marshall, K. C. *Biofilms*; Wiley-Interscience: New York, 1990.
(631) Wimpenny, J. W. T.; Colasanti, R. *FEMS Microbiol. Ecol.* **1997**, *22*, 1.
(632) Caldwell, D. E.; Korber, D. R.; Lawrence, J. R. In *Advanced Microbiology and Ecology*; Marshall, K., Ed.; Plenum: New York, 1992.
(633) Caldwell, D. E.; Korber, D. R.; Lawrence, J. R. *J. Microbiol. Methods* **1992**, *15*, 249.
(634) Lewandowski, Z.; Altobelli, S. A.; Fukushima, E. *Biotechnology* **1993**, *9*, 40.
(635) DeBaer, D.; Stoodley, P.; Roe, F.; Lewandowski, Z. *Bioengineering* **1994**, *43*, 1131.
(636) Costerton, J. W.; Lewandowski, Z.; Caldwell, D. E.; Korber, D. R.; Lappin-Scott, H. M. *Annu. Rev. Microbiol.* **1995**, *49*, 711.
(637) Little, B.; Wagner, P.; Hard, K.; Ray, R.; Lavoie, D.; Nealson, K.; Aguilar, C. *Corrosion 97*; Houston, TX, 1997; p 1.
(638) Little, B.; Wagner, P.; Ray, R.; Pope, R.; Sheetz, R. *J. Indust. Microbiol.* **1991**, *8*, 213.
(639) Amann, R. I.; Stromley, J.; Devereux, R.; Key, R.; Stahl, D. *Appl. Environ. Microbiol.* **1992**, *58*, 614.
(640) Rissati, J. B.; Capman, W.; Stahl, D. *Proc. Natl. Acad. Sci. U.S.A.* **1994**, *91*, 10173.
(641) Batchelor, S.; Cooper, M.; Chhabra, S.; Glover, L.; Stewart, G.; Williams, P.; Prosser, J. *Appl. Environ. Microbiol.* **1997**, *63*, 2281.
(642) Nealson, K. H. *Annu. Rev. Earth Planet. Sci.* **1997**, *25*, 403.
(643) Neilands, J. B. In *Metal Ions and Bacteria*; Beveridge, T. J., Doyle, R. J., Eds.; John Wiley and Sons: New York, 1989.
(644) Larsen, I.; Little, B.; Nealson, K. H.; Ray, R.; Stone, A.; Tian, J. *Am. Mineral.* **1998**, *98*, in press.
(645) Kostka, J. E.; Luther, G. W., III; Nealson, K. H. *Geochim. Cosmochim. Acta* **1994**, *59*, 885.
(646) Burdige, D. J.; Nealson, K. H. *Geomicrobiology J.* **1986**, *4*, 361.
(647) Burdige, D. J.; Dhakar, S. P.; Nealson, K. H. *Geomicrobiol.* **1992**, *10*, 27.
(648) Arnold, R. G.; Hoffman, M. R.; DiChristina, T. J.; Picardal, F. W. *Appl. Environ. Microbiol.* **1990**, *56*, 2811.
(649) Arnold, R. G.; DiChristina, T. J.; Hoffman, M. *Biotechnol. Bioeng.* **1988**, *32*, 1081.
(650) Roden, E. E.; Zachara, J. M. *Environ. Sci. Technol.* **1996**, *30*, 1618.
(651) Kostka, J. E.; Nealson, K. H. *Environ. Sci. Technol.* **1995**, *29*, 2535.
(652) Gates, W. P.; Wilkinson, H. T.; Stucki, J. W. *Clays Clay Minerals* **1993**, *41*, 360.
(653) Kostka, J. E.; Stucki, J. W.; Nealson, K. H.; Wu, J. *Clays Clay Minerals* **1996**, *44*, 522.
(654) Fude, L.; Harris, B.; Urrutia, M. M.; Beveridge, T. J. *Appl. Environ. Microbiol.* **1994**, *60*, 1525.
(655) Gorby, Y.; Lovley, D. R. *Environ. Sci. Technol.* **1991**, *26*, 205.
(656) Ferrenkopf, A. M.; Dollhopf, M. E.; Chadhain, S. N.; Luther, I.; Nealson, K. H. *Mar. Chem.* **1997**, *57*, 347.
(657) Oremland, R. S.; Blum, J. S.; Culbertson, C. W.; Visscher, P. T.; Miller, L. G.; Dowdle, P.; Strohmaier, F. E. *Appl. Environ. Microbiol.* **1995**, *60*, 3011.
(658) Ahmann, D.; Krumholz, L. R.; Hemond, H. H.; Lovley, D. R.; Morel, F. M. *Environ. Sci. Technol.* **1997**, *31*, 2923.
(659) Stone, A. T.; Morgan, J. J. *Environ. Sci. Technol.* **1984**, *18*, 450.
(660) LaKind, J. S.; Stone, A. T. *Geochim. Cosmochim. Acta* **1989**, *53*, 961.
(661) Lovley, D. R.; Coates, J. D.; Blunt-Harris, E. L.; Phillips, E. J. P.; Woodward, J. C. *Nature* **1996**, *382*, 445.
(662) Seeliger, S.; Cord-Ruwisch, R.; Schink, B. *J. Bacteriol.* **1998**, *180*, 3686.
(663) Myers, C. R.; Myers, J. M. *J. Bacteriol.* **1992**, *174*, 3429.
(664) Lovley, D. R.; Widman, P. K.; Woodward, J. C.; Phillips, E. J. P. *Appl. Environ. Microbiol.* **1993**, *59*, 3572.
(665) Tsapin, A. I.; Nealson, K. H.; Meyer, T.; Cusanovich, M. A.; VanBeeuman, J.; Crosby, L. D.; Feinberg, B. A.; Zhang, C. *J. Bacteriol.* **1996**, *178*, 6386.
(666) Lovley, D. R.; Phillips, E. J. P.; Lonergan, D. J. *Environ. Sci. Technol.* **1991**, *25*, 1062.
(667) Burdige, D. J.; Nealson, K. H. *Appl. Environ. Microbiol.* **1985**, *50*, 491.
(668) Nealson, K. H.; Rosson, R.; Myers, C. In *Metal Ions and Bacteria*; Beveridge, T., Doyle, R., Eds.; John Wiley and Sons: New York, 1989.
(669) DiChristina, T. J. *J. Bacteriol.* **1992**, *174*, 1891.
(670) Myers, C. R.; Nealson, K. H. *Science* **1988**, *240*, 1319.
(671) Nealson, K. H.; Saffarini, D. *Annu. Rev. Microbiol.* **1994**, *48*, 311.
(672) Lonergan, D. J.; Jenter, H. L.; Coates, J. D.; Phillips, E. J. P.; Schmidt, T. M.; Lovley, D. R. *J. Bacteriol.* **1996**, *178*, 2402.
(673) DiChristina, T. J.; DeLong, E. F. *J. Bacteriol.* **1994**, *176*, 1468.
(674) Saffarini, D. A.; Nealson, K. H. *J. Bacteriol.* **1993**, *175*, 7938.
(675) Myers, C. R.; Myers, J. M. *Microbiol. Lett.* **1993**, *108*, 15.
(676) Myers, C. R.; Myers, J. M. *J. Bacteriol.* **1997**, *179*, 1143.
(677) Pealing, S. L.; Black, A. C.; Manson, F. D.; Ward, F. B.; Chapman, S. K.; Reid, G. A. *Biochemistry* **1992**, *31*, 12132.
(678) Nealson, K. H. In *The Prokaryotes*, 2nd ed.; Balows, A., Trueper, H. G., Dworkin, M., Harder, W., Schleifer, K.-H., Eds.; Springer-Verlag: New York, 1991; Vol. 1.
(679) Nealson, K. H.; Tebo, B. M.; Rosson, R. A. *Adv. Appl. Microbiol.* **1988**, *33*, 279.
(680) vanWaasbergen, L.; Hildebrand, M.; Tebo, B. M. *J. Bacteriol.* **1996**, *178*, 3527.
(681) Corstjens, P.; deVrind, J. P. M.; Goosen, T.; deVrind-deJong, E. W. *Geomicrobiol. J.* **1997**, *14*, 91.
(682) Siering, P. L.; Ghiorse, W. C. *Geomicrobiol. J.* **1997**, *14*, 109.
(683) Tebo, B. M.; Ghiorse, W. C.; Waasbergen, L. B. v.; Siering, P. L.; Caspi, R. In *Geomicrobiology: Interactions between Microbes and Minerals*; Banfield, J. F., Nealson, K. H., Eds.; Mineralogical Society of America: Washington, DC, 1997; Vol. 35.
(684) Mandernack, K. W.; Post, J.; Tebo, B. M. *Geochim. Cosmochim. Acta* **1995**, *59*, 4393.
(685) Ehrenreich, A.; Widdel, F. *Appl. Environ. Microbiol.* **1994**, *60*, 45517.
(686) Straub, K. L.; Benz, M.; Schink, B.; Widdel, F. *Appl. Environ. Microbiol.* **1996**, *62*, 1458.
(687) Frankel, R. B.; Blakemore, R. P. *Iron Biominerals*; Plenum Press: New York, 1991.
(688) Bazylinski, D. A.; Moskowitz, B. M. In *Geomicrobiology: Interactions between Microbes and Minerals*; Banfield, J. F., Nealson, K. H., Eds.; Mineralogical Society of America: Washington, DC, 1997; Vol. 35.
(689) Mortimer, R. J. G.; Coleman, M. L. *Geochim. Cosmochim. Acta* **1997**, *61*, 1705.
(690) Fredrickson, J. K.; Zachara, J. M.; Kennedy, D. W.; Dong, H.; Onstott, T. C.; Hinman, N. W.; Li, S. *Geochim. Cosmochim. Acta* **1998**, in press.
(691) Zachara, J. M.; Fredrickson, J. K.; Li, S.; Kennedy, D. W.; Smith, S. C.; Gassman, P. L. *Am. Mineral.* **1998**, in press.
(692) Gouy, G. *J. Phys. Chem.* **1910**, *9*, 451.
(693) Chapman, D. L. *Philos. Mag.* **1913**, *25*, 475.
(694) Stern, O. *Electrochemistry* **1924**, *30*, 508.
(695) Parsons, R. *Chem. Rev.* **1990**, *90*, 813.
(696) Charmas, R.; Piasecki, W.; Rudzinski, W. *Langmuir* **1995**, *11*, 3199.
(697) Van Riemsdijk, W. H.; de Wit, J. C. M.; Koopal, L. K.; Bolt, G. H. *J. Colloid Interface Sci.* **1987**, *116*, 511.
(698) Hiemstra, T.; Venema, P.; Van Riemsdijk, W. H. *J. Colloid Interface Sci.* **1996**, *184*, 680.
(699) Rudzinski, W.; Charmas, R.; Partyka, S.; Bottero, J. Y. *Langmuir* **1993**, *9*, 2641.
(700) James, R. O.; Parks, G. A. In *Surface and Colloid Science*; Matijevic′, E., Ed.; Plenum Press: New York, 1982; Vol. 12.
(701) Hunter, R. J. *Foundations of Colloid Science, Vol. 1*; Oxford University Press: New York, 1986.
(702) Hunter, R. J. *Foundations of Colloid Science, Vol. 2*; Oxford University Press: New York, 1989.
(703) Bérubé, Y. G.; de Bruyn, P. L. *J. Colloid Interface Sci.* **1968**, *28*, 305.
(704) Tewari, P. H.; McLean, A. W. *J. Colloid Interface Sci.* **1972**, *40*, 267.
(705) Tewari, P. H.; Campbell, A. B. *J. Colloid Interface Sci.* **1976**, *55*, 531.
(706) Blesa, M. A.; Figliolia, N. M.; Maroto, A. J. G.; Regazzoni, A. E. *J. Colloid Interface Sci.* **1984**, *101*, 410.
(707) Fokkink, L. G. J.; de Keizer, A.; Lyklema, J. *J. Colloid Interface Sci.* **1987**, *118*, 454.
(708) Fokkink, L. G. J. Ph.D. Thesis, Wageningen University, 1987.
(709) van den Vlekkert, H.; Bousse, L.; de Rooij, N. *J. Colloid Interface Sci.* **1988**, *122*, 336.
(710) Brady, P. V. *Geochim. Cosmochim. Acta* **1992**, *56*, 2941.
(711) Kosmulski, M.; Matysiak, J.; Szczypa, J. *J. Colloid Interface Sci.* **1994**, *164*, 280.
(712) Machesky, M. L.; Palmer, D. A.; Wesolowski, D. J. *Geochim. Cosmochim. Acta* **1994**, *58*, 5627.
(713) Griffiths, D. A.; Furstenau, D. W. *J. Colloid Interface Sci.* **1981**, *80*, 271.
(714) Machesky, M. L.; Anderson, M. A. *Langmuir* **1986**, *2*, 582.
(715) Mehr, S. R.; Eatough, D. J.; Hansen, L. D.; Lewis, E. A. *Thermochim. Acta* **1989**, *154*, 129.
(716) de Keizer, A.; Fokkink, L. G. J.; Lyklema, J. *Colloids Surf.* **1990**, *49*, 149.
(717) Machesky, M. L.; Jacobs, P. F. *Colloids Surf.* **1991**, *53*, 297.
(718) Machesky, M. L.; Jacobs, P. F. *Colloids Surf.* **1991**, *53*, 315.
(719) Casey, W. H.; Cheney, M. A. *Aquatic Sci.* **1993**, *55*, 304.
(720) Casey, W. H. *J. Colloid Interface Sci.* **1994**, *163*, 407.
(721) Skipper, N. T.; Chang, F. C.; Sposito, G. *Clays Clay Minerals* **1995**, *43*, 285.
(722) Skipper, N. T.; Sposito, G.; Chang, F. C. *Clay Clay Minerals* **1995**, *43*, 294.
(723) Lasaga, A. C.; Gibbs, G. V. *Am. J. Sci.* **1990**, *290*, 263.
(724) Lasaga, A. C. *Rev. Geophys.* **1992**, *30*, 269.
(725) Xiao, Y. T.; Lasaga, A. C. *Geochim. Cosmochim. Acta* **1996**, *60*, 2283.

(726) Cygan, R. T.; Nagy, K. L.; Brady, P. V. In *Sorption of Metals by Earth Materials*; Jenne, E. A., Ed.; Academic Press: New York, 1990.
(727) Kubicki, J. D.; Xiao, D. Y.; Lasaga, A. C. *Geochim. Cosmochim. Acta* **1993**, *57*, 3847.
(728) Kubicki, J. D.; Sykes, D. *Geochim. Cosmochim. Acta* **1995**, *59*, 4791.
(729) Kubicki, J. D.; Apitz, S. E.; Blake, G. A. *Geochim. Cosmochim. Acta* **1996**, *60*, 4987.
(730) Kubicki, J. D.; Blake, G. A.; Apitz, S. E. *Am. Mineral.* **1996**, *81*, 265.
(731) Kubicki, J. D.; Itoh, M. J.; Schroeter, L. M.; Apitz, S. E. *Environ. Sci. Technol.* **1997**, *31*, 1151.
(732) Rustad, J. R.; Hay, B. P.; Halley, J. W. *J. Chem. Phys.* **1995**, *102*, 427.
(733) Rustad, J. R.; Hay, B. P. *Geochim. Cosmochim. Acta* **1995**, *59*, 1251.
(734) Rustad, J. R.; Felmy, A. R.; Hay, B. P. *Geochim. Cosmochim. Acta* **1996**, *60*, 1553.
(735) Feuston, B. P.; Garofalini, S. H. *J. Phys. Chem.* **1990**, *94*, 5351.
(736) Wasserman, E.; Rustad, J. R.; Felmy, A. R.; Hay, B. P.; Halley, J. W. *Surf. Sci.* **1997**, *385*, 217.
(737) Teppen, B. J.; Rasmussen, K.; Bertsch, P. M.; Miller, D. M.; Schager, L. *J. Phys. Chem.* **1997**, *101*, 1579.
(738) *Advances in Molecular Electronic Structure Theory: Molecular Approaches to Materials Chemistry*; Dunning, T. H., Jr., Ed.; Jai Press: Greenwich, CT, 1994; Vol. 2.
(739) *Cluster Models for Surface and Bulk Phenomena*; Paccioni, G., Bagus, P. S., Parmigiani, F., Eds.; Plenum Press: New York, 1992.
(740) *Electronic Properties of Solids Using Cluster Methods*; Kaplan, T. A., Mahanti, S. D., Eds.; Plenum Press: New York, 1995.
(741) Pisani, C.; Dovesi, R.; Roetti, C. *Hartree−Fock Ab Initio Treatment of Crystalline Systems*; Springer-Verlag: Berlin, 1988.
(742) Jones, R. O.; Gunnarsson, O. *Rev. Mod. Phys.* **1989**, *61*, 689.
(743) Kryachko, E. S.; Ludena, E. B. *Energy Density Functional Theory of Many-Electron Systems*; Kluwer: Boston, 1990.
(744) Causa, M.; Dovesi, R.; Pisani, C.; Colle, R.; Fortunelli, A. *Phys. Rev. B* **1987**, *36*, 891.
(745) Causa, M.; Colle, R.; Fortunelli, A.; Dovesi, R.; Pisani, C. *Phys. Scr.* **1988**, *38*, 194.
(746) De Vita, A.; Gillan, M. J.; Lin, J. S. *Phys. Rev. Lett.* **1992**, *68*, 3319.
(747) Andrews, S. B.; Burton, N. A.; Gillan, M. J. *Chem. Phys. Lett.* **1996**, *261*, 521.
(748) Gillan, M. J.; Manassidis, I.; De Vita, A. *Philos. Mag. B* **1994**, *69*, 879.
(749) Gillan, M. *Phys. World* **1996**, *9*, 31.
(750) Hernandez, E.; Gillan, M. J. *Phys. Rev. B* **1995**, *51*, 10157.
(751) Hernandez, E.; Gillan, M. J.; Goringe, C. M. *Phys. Rev. B* **1996**, *53*, 7147.
(752) Jaffe, J. E.; Hess, A. C. *J. Chem. Phys.* **1996**, *105*, 10983.
(753) Stefanovich, E. V.; Truong, T. N. *J. Chem. Phys.* **1996**, *104*, 2946.
(754) Lafemina, J. P. *Crit. Rev. Surf. Chem.* **1994**, *3*, 297.
(755) *Reviews in Computational Chemistry 6*; Lipkowitz, K. B., Boyd, D. B., Eds.; VCH Publishers: New York, 1995.
(756) *Molecular Dynamics Simulations*; Yonezawa, F., Ed.; Springer-Verlag: New York, 1990.
(757) *Computer Modelling of Fluids Polymers and Solids*; Catlow, C. R. A., Parker, S. C., Allen, M. P., Eds.; Kluwer: Boston, 1988; Vol. 293.
(758) Allen, M. P.; Tildesley, D. J. *Computer Simulation of Liquids*; Clarendon Press: Oxford, 1987.
(759) *Simulation Approach to Solids: Molecular-Dynamics of Equilibrium Crystals and More*; Ronchetti, M., Jacucci, G., Eds.; Kluwer: Milan, 1990.
(760) Sykes, D.; Kubicki, J. D.; Farrar, T. C. *J. Phys. Chem.* **1997**, *101*, 2715.
(761) Sherman, D. M. *Am. Mineral.* **1990**, *75*, 256.
(762) Pelmenschikov, A. G.; Morosi, G.; Gamba, A. *J. Phys. Chem.* **1992**, *96*, 7422.
(763) Mejias, J. A.; Oviedo, J.; Fernandez, S. F. *Chem. Phys.* **1995**, *191*, 133.
(764) Truong, T. N.; Stefanovich, E. V. *Chem. Phys. Lett.* **1995**, *240*, 253.
(765) Truong, T. N.; Stenfanovich, E. V. *Chem. Phys. Lett.* **1996**, *256*, 348.
(766) Hill, J. R.; Sauer, J. *J. Phys. Chem.* **1995**, *99*, 9536.
(767) Catlow, C. R. A.; George, A. R.; Freeman, C. M. *Chem. Commun.* **1996**, *N11*, 1311.
(768) Balint, I.; Aika, K.-I. *J. Chem. Soc., Faraday Trans.* **1995**, *91*, 1805.
(769) Coluccia, S.; Lavagnino, S.; Marchese, L. *Mater. Chem. Phys.* **1988**, *18*, 445.
(770) Goni-Elizalde, S.; Garcia-Clavel, M. E. *Solid State Ionics* **1991**, *45*, 15.
(771) Gotoh, T.; Takagi, S. *Surf. Sci.* **1993**, *287/288*, 31.
(772) Onishi, H.; Egawa, C.; Aruga, T.; Iwasawa, Y. *Surf. Sci.* **1987**, *191*, 479.
(773) Karolewski, M. A.; Cavell, R. G. *Surf. Sci.* **1992**, *271*, 128.
(774) Peng, X. D.; Barteau, M. A. *Langmuir* **1991**, *7*, 1426.
(775) Picaud, S.; Hoang, P. N. M.; Girardet, C. *Surf. Sci.* **1992**, *278*, 339.
(776) Wu, M.-C.; Estrada, C. A.; Goodman, D. W. *Phys. Rev. Lett.* **1991**, *67*, 2910.
(777) Wu, M.-C.; Estrada, C. A.; Corneille, J. S.; Goodman, D. W. *J. Chem. Phys.* **1992**, *96*, 3892.
(778) Wu, M. C.; Goodman, D. W. *Catal. Lett.* **1992**, *15*, 1.
(779) Zhou, X. L.; Cowin, J. P. *J. Phys. Chem.* **1996**, *100*, 1055.
(780) Anchell, J. L.; Hess, A. C. *J. Phys. Chem.* **1996**, *100*, 18317.
(781) Chacon-Taylor, M. R.; McCarthy, M. I. *J. Phys. Chem.* **1996**, *100*, 7610.
(782) de Leeuw, N. H.; Watson, G. W.; Parker, S. C. *J. Phys. Chem.* **1995**, *99*, 17219.
(783) de Leeuw, N. H.; Watson, G. W.; Parker, S. C. *J. Chem. Soc., Faraday Trans.* **1996**, *92*, 2081.
(784) De Vita, A.; Gillan, M. J. *J. Phys.: Cond. Matter* **1991**, *3*, 6225.
(785) Goniakowski, J.; Gillan, M. J. *Surf. Sci.* **1996**, *350*, 145.
(786) Johnson, M. A.; Stefanovich, E. V.; Truong, T. N. *J. Phys. Chem.* **1997**, *101*, 3196.
(787) Kantorovich, L. N.; Holender, J. M.; Gillan, M. J. *Surf. Sci.* **1995**, *343*, 221.
(788) Kantorovich, L. N.; Gillan, M. J.; White, J. A. *J. Chem. Soc., Faraday Trans.* **1996**, *92*, 2075.
(789) McCarthy, M. I.; Schenter, G. K.; Scamehorn, C. A.; Nicholas, J. B. *J. Phys. Chem.* **1996**, *100*, 16989.
(790) Nada, R.; Hess, A. C.; Pisani, C. *Surf. Sci.* **1995**, *336*, 353.
(791) Scamehorn, C. A.; Hess, A. C.; McCarthy, M. I. *J. Chem. Phys.* **1993**, *99*, 2786.
(792) Stefanovich, E. V.; Truong, T. N. *J. Chem. Phys.* **1995**, *102*, 5071.
(793) Szymanski, M. A.; Gillan, M. J. *Surf. Sci.* **1996**, *367*, 135.
(794) Almeida, A. L.; Martins, J. B. L.; Taft, C. A.; Longo, E.; Lester, W. A., Jr. *J. Chem. Phys.* **1998**, *109*, 3671.
(795) Felmy, A. R.; Rustad, J. R. *Geochim. Cosmochim. Acta* **1998**, *62*, 25.
(796) Halley, J. W.; Rustad, J. R.; Rahman, A. *J. Chem. Phys.* **1993**, *98*, 4110.
(797) Curtiss, L. A.; Halley, J. W.; Hautman, J.; Rahman, A. *J. Chem. Phys.* **1987**, *86*, 2319.
(798) Sverjensky, D. A. *Nature* **1993**, *364*, 776.
(799) Sverjensky, D. A.; Sahai, N. *Geochim. Cosmochim. Acta* **1996**, *60*, 3773.
(800) Sahai, N.; Sverjensky, D. A. *Geochim. Cosmochim. Acta* **1997**, *61*, 2827.
(801) Sahai, N.; Sverjensky, D. A. *Geochim. Cosmochim. Acta* **1997**, *61*, 2801.
(802) Koretsky, C. M.; Sverjensky, D. A.; Sahai, N. *Am. J. Sci.* **1998**, *298*, 349.
(803) Yoon, R. H.; Salman, T.; Donnay, G. *J. Colloid Interface Sci.* **1979**, *70*, 483.
(804) Yates, D. E.; Grieser, F.; Cooper, R.; Healy, T. W. *Austral. J. Chem.* **1977**, *30*, 1655.
(805) Hayes, K. F.; Redden, G.; Ela, W.; Leckie, J. O. *J. Colloid Interface Sci.* **1991**, *142*, 448.
(806) Helgeson, H. C.; Kirkham, D. H.; Flowers, G. C. *Am. J. Sci.* **1981**, *281*, 1241.
(807) Lyklema, J.; Overbeck, J. T. G. *J. Colloid Sci.* **1961**, *16*, 595.
(808) McCarthy, M. I.; Schenter, G. K.; Chacon-Taylor, M. R.; Rehr, J. J.; Brown, G. E., Jr. *Phys. Rev. B* **1997**, *56*, 9925.
(809) McHale, J. M.; Navrotsky, A.; Perrotta, A. J. *J. Phys. Chem. B* **1997**, *101*, 603.
(810) Brinker, C. J.; Scherer, C. W. *Sol−Gel Science: The Physics and Chemistry of Sol−Gel Processing*; Academic Press: San Diego, 1990.
(811) Xu, Q.; Anderson, M. A. *J. Am. Ceram. Soc.* **1977**, *77*, 1939.
(812) *Sol−Gel Technology for Thin Films, Fibres, Preforms, Electronics and Speciality Shapes*; Klein, L. C., Ed.; Noyes: New Jersey, 1988.
(813) Klein, L. C. *Sol−Gel Optics − Processing and Applications*; Kluwer: Boston, 1994.
(814) Gesser, H. D.; Goswami, P. C. *Chem. Rev.* **1989**, *89*, 765.
(815) Matijevic, E. *Mater. Res. Soc. Bull.* **1989**, *4*, 18.
(816) Matijevic, E. *Mater. Res. Soc. Bull.* **1990**, *5*, 16.
(817) Matijevic, E. *Langmuir* **1994**, *10*, 8.
(818) Matijevic, E. *Langmuir* **1986**, *2*, 12.
(819) Matijevic, E. *Chem. Mater.* **1993**, *5*, 412.
(820) Matijevic, E. *Annu. Rev. Mater. Sci.* **1985**, *15*, 485.
(821) Mehrotra, R. *Struct. Bonding* **1992**, *77*, 1.
(822) Wang, X.-G.; Weiss, W.; Shaikhutdinov, Sh. K.; Ritter, M.; Petersen, M.; Wagner, F.; Schlögel, R.; Scheffler, M. *Phys. Rev. Lett.* **1998**, *81*, 1038.
(823) Elam, J. W.; Nelson, C. E.; Cameron, M. A.; Tolbert, M. A.; George, S. M. *J. Phys. Chem. B* **1998**, *102*, 7008.
(824) Nelson, C. E.; Elam, J. W.; Cameron, M. A.; Tolbert, M. A.; George, S. M. *Surf. Sci.* **1998**, *416*, 341.
(825) Laiti, E.; Persson, P., Öhman, L.-O. *Langmuir* **1998**, *14*, 825.

CR980011Z